Towards integrating strain rates in PSHA source models in Europe : testing the compatibility between seismic and geodetic moment rates

Bénédicte Donniol Jouve

▶ **To cite this version:**

Bénédicte Donniol Jouve. Towards integrating strain rates in PSHA source models in Europe : testing the compatibility between seismic and geodetic moment rates. Applied geology. Université Grenoble Alpes [2020-..], 2024. English. NNT : 2024GRALU006 . tel-04862320

HAL Id: tel-04862320

https://theses.hal.science/tel-04862320v1

Submitted on 3 Jan 2025

HAL is a multi-disciplinary open access archive for the deposit and dissemination of scientific research documents, whether they are published or not. The documents may come from teaching and research institutions in France or abroad, or from public or private research centers.

L'archive ouverte pluridisciplinaire **HAL**, est destinée au dépôt et à la diffusion de documents scientifiques de niveau recherche, publiés ou non, émanant des établissements d'enseignement et de recherche français ou étrangers, des laboratoires publics ou privés.

THÈSE

Pour obtenir le grade de

DOCTEUR DE L'UNIVERSITÉ GRENOBLE ALPES

École doctorale : STEP - Sciences de la Terre de l'Environnement et des Planètes
Spécialité : Sciences de la Terre et de l'Environnement
Unité de recherche : Institut des Sciences de la Terre

Vers l'intégration des taux de déformation dans les modèles de source PSHA en Europe : test de la compatibilité entre les taux de moment sismique et géodésique

Towards integrating strain rates in PSHA source models in Europe: testing the compatibility between seismic and geodetic moment rates

Présentée par :

Bénédicte DONNIOL JOUVE

Direction de thèse :

Céline BEAUVAL directrice de recherche, Université Grenoble Alpes	Directrice de thèse
Anne SOCQUET, PHYSICIENNE, Université Grenoble Alpes	Co-directrice de thèse

Rapporteurs :

Nicola D'AGOSTINO
SENIOR SCIENTIST, Istituto Nazionale Geofisica e Vulcanologia
Laurentiu DANCIU
SENIOR SCIENTIST, Ecole polytechnique fédérale de Zurich

Thèse soutenue publiquement le **9 février 2024**, devant le jury composé de :

Andréa WALPERSDORF, PHYSICIENNE, Université Grenoble Alpes	Présidente
Céline BEAUVAL, DIRECTRICE DE RECHERCHE, IRD délégation régionale Sud Est	Directrice de thèse
Anne SOCQUET, PHYSICIENNE, Université Grenoble Alpes	Co-directrice de thèse
Nicola D'AGOSTINO, SENIOR SCIENTIST, Istituto Nazionale Geofisica e Vulcanologia	Rapporteur
Laurentiu DANCIU, SENIOR SCIENTIST, Ecole polytechnique fédérale de Zurich	Rapporteur
Fabrice COTTON, FULL PROFESSOR, Universität Potsdam	Examinateur

Invités :

Adrien Pothon
INGENIEUR DOCTEUR, AXA GROUP RISK MANAGEMENT

PhD thesis

Bénédicte Donniol Jouve

March 15, 2024
Version: Defended

Université Grenoble Alpes

Université Grenoble Alpes
Institut des Sciences de la Terre
ISTerre

Earth Sciences

PhD thesis

Bénédicte Donniol Jouve

1. Reviewer Nicola D'Agostino
Sezione Centro Nazionale Terremoti
Istituto Nazionale Geofisica e Vulcanologia

2. Reviewer Laurentiu Danciu
Swiss Seismological Service
ETH Zurich

Supervisors Céline Beauval and Anne Socquet

March 15, 2024

Bénédicte Donniol Jouve
PhD thesis
Earth Sciences, March 15, 2024
Reviewers: Nicola D'Agostino and Laurentiu Danciu
Supervisors: Céline Beauval and Anne Socquet

Université Grenoble Alpes
ISTerre
Institut des Sciences de la Terre
Université Grenoble Alpes
1381 Rue de la Piscine
38610 and Gières (France)

Abstract

National and international seismic regulations commonly mandate the assessment of seismic hazard through probabilistic seismic hazard assessment (PSHA) methods. PSHA serves as a fundamental tool for authorities in establishing a framework from which to consider ground motions for earthquake-resistant design. To effectively utilize PSHA, knowledge regarding seismic sources and potential magnitudes must be translated into probabilities of occurrence within specified future time window, forming what is known as the source model. This source model, when coupled with a ground-motion model, facilitates the determination of exceedance probabilities for ground-motion levels at specific sites over forthcoming time windows. The primary objective of this research is to explore how geodetic monitoring can provide valuable constraints to enhance the accuracy of the source model. In low-to moderate seismicity areas, seismic activity is dispersed, hindering the identification of active faults and the incorporation of realistic fault geometries into seismic hazard assessments. Earthquake catalogs, merging instrumental and historical data, serve as the foundation for establishing recurrence models. However, despite spanning several centuries, these catalogs often have short observation time windows compared to the recurrence times of moderate-to-large events, resulting in weakly constrained recurrence models. To overcome this limitation, GPS measurements offer a promising alternative by providing estimates of deformation rates and valuable insights into the anticipated rate of seismicity. The Conservation of Moment theorem forms the theoretical basis of this study, asserting that seismic and geodetic moment rates should equate, modulo a certain percentage of aseismic deformation.

Leveraging geodetic strain rate maps for Europe derived by Piña Valdes et al. (2020) and the recently released ESHM20 seismic hazard model by Danciu et al. (2021) presents a valuable opportunity. This enables the comparison of the ESHM20 source model with geodetic moment rates across a geographically extensive region characterized by heterogeneous seismic activity. In consequence, this thesis has centered around a pivotal question: to what extent can geodetic moment rates serve as a reliable proxy for seismic moment rates in Europe, spanning from high-deformation zones to regions with low to moderate deformation?

We assess the agreement between seismic and geodetic moment rates across Europe, considering epistemic uncertainties, with seismogenic thickness identified as a

pivotal parameter for geodetic moment rates. In high-activity zones, primary compatibility is evident, yet local disparities underscore the importance of source zone scale; broader zones enhance the overlap between geodetic and seismic moment rates distributions. Discrepancies arise in low-to-moderate activity zones, particularly in areas affected by Scandinavian Glacial Isostatic Adjustment, where geodetic moment rates are much larger than seismic moment rates. However, in some zones where the ESHM20 recurrence models are well-constrained, we note an overlap in the distributions of seismic and geodetic moments, offering hope for the integration of geodetic data even in regions with low deformation. Subsequently, we investigate whether the disparity between seismic and geodetic moments may stem from the seismic catalog not representing the long-term average seismicity rate. Leveraging the work of Marsan and Tan (2020), we generate synthetic earthquake catalogs reflecting a zone's seismicity, introducing geodetic moments to balance earthquake moment release over the long term. We develop a methodology to anchor the model parameters to the zone's long-term seismicity and apply it to a region (southern Switzerland) with conflicting geodetic and seismic moment rates. Our findings suggest that, in low-deformation regions like southwestern Switzerland, the seismic catalog may not be representative of the seismic moment rate released over the long term (millena). Under that hypothesis, even if it includes historical earthquakes as old as a few centuries, the seismic catalogue may represent only a snapshot of the average seismic moment rate over the long term, and could explain the difference in seismic and geodetic moment rates.

Résumé

Les réglementations sismiques nationales et internationales exigent couramment l'évaluation de l'aléa sismique par des méthodes d'évaluation probabiliste de l'aléa sismique (PSHA). Le PSHA sert d'outil pour les autorités afin d'établir un cadre pour la conception parasismique. En pratique, la connaissance des sources sismiques et des magnitudes potentielles doit être traduite en probabilités d'occurrence dans des fenêtres de temps futures, formant ce que l'on appelle le modèle de source. Ce modèle de source, associé à des équations de prévision du mouvement du sol, permet la détermination des probabilités de dépassement de niveaux de mouvement du sol, pour un site spécifique, dans une fenêtre temporelle future. L'objectif principal de cette recherche est d'explorer comment la surveillance géodésique peut apporter des nouvelles contraintes pour améliorer la précision des modèles de source. Dans les zones de sismicité faible à modérée, l'activité sismique est dispersée, entravant l'identification de failles actives et l'intégration de géométries de failles réalistes dans les évaluations de l'aléa sismique. Les catalogues de séismes, fusionnant des données instrumentales et historiques, servent de base à l'établissement de modèles de récurrence. Ces catalogues incluent souvent plusieurs siècles de données ce qui est cependant peu comparé au temps de récurrence des séismes de magnitude modérées à grandes. Les modèles de récurrences peuvent alors être mal contraints. Pour surmonter cette limitation, les mesures géodésiques offrent une alternative prometteuse en fournissant des estimations des taux de déformation et des informations sur les potentiels taux de sismicité futurs. Le théorème de conservation des moments forme le cadre théorique utilisé dans cette étude. Il postule que les taux de moments géodésiques et sismiques devraient être égaux, modulo un certain pourcentage de déformation asismique.

Deux études ont été récement publiées à l'échelle de l'europe : les cartes de taux de déformation géodésique établies par Piña Valdes et al. (2020), ainsi que le modèle d'aléa sismique ESHM20 par Danciu et al. (2021). Cela nous donne l'opportunité de comparer le modèle source ESHM20 avec des valeurs de moments gédésiques dans une région géographiquement étendue caractérisée par des contextes sismotectoniques divers. En conséquence, cette thèse s'est centrée autour d'une question cruciale : dans quelle mesure les taux de moment géodésique peuvent-ils servir de

proxy fiable pour les taux de moment sismique en Europe, depuis des zones de forte déformation aux régions présentant une déformation faible à modérée ?

Nous évaluons l'accord entre les taux de moment sismique et géodésique à travers l'Europe, en prenant en compte les incertitudes épistémiques qui leurs sont associées. Nous observons que l'épaisseur sismogénique prise en compte dans le calcul du moment géodésique est un paramètre clé controlant son incertitude. Dans les zones de forte déformation, une compatibilité est globalement mise en évidence, bien que dans le détail des divergences soient observées. Nous observons que le fait de considérer des plus grandes zones augmente la superposition entre les distributions des taux de moments sismiques et géodésiques. Des divergences apparaissent dans les zones d'activité faible à modérée, notamment dans les zones affectées par le rebond post-glaciaire scandinave, où les taux de moment géodésique sont nettement plus élevés que les taux de moment sismique. Dans certaines zones où les modèles de récurrence proposés par ESHM20 sont bien contraints, nous constatons un chevauchement entre les distributions des taux de moments sismiques et géodésiques, offrant des perspectives pour l'utilisation des données géodésiques même dans des régions de plus faible déformation.

Ensuite, nous questionnons si la disparité entre les moments sismiques et géodésiques pourrait découler du fait que le catalogue sismique ne représente pas le taux moyen de sismicité à long terme, à travers une zone exemple (au sud-ouest de la Suisse). En utilisant le modèle de Marsan et Tan (2020), nous générons des catalogues sismiques synthétiques qui utilisent le taux de moment géodésique moyen de la zone pour équilibrer la libération de moment sismique sur le long terme. Nous développons une méthodologie pour ancrer les paramètres du modèle sur la sismicité à long terme de la zone. Nous appliquons cette approche à une région (le sud de la Suisse) présentant des taux de moment géodésique et sismique contradictoires. Nos résultats suggèrent que, dans les régions à faible déformation comme le sud-ouest de la Suisse, le catalogue sismique peut ne pas être représentatif du taux de moment sismique libéré sur le long terme (millénaires). Selon cette hypothèse, même s'il inclut des séismes historiques datant de quelques siècles, le catalogue sismique pourrait représenter seulement un instantané du taux moyen de moment sismique sur le long terme, ce qui pourrait expliquer la différence entre les taux de moment sismique et géodésique.

Acknowledgement

First and foremost, I would like to express my gratitude to my two thesis advisors, Anne and Céline. Céline, thank you for your assistance and efficiency in the work and your always insightful suggestions. Anne, thank you for your deep support during this thesis and for giving me the opportunity to participate in the one-month GNSS field mission in Peru, which enriched me immensely. Thank you, of course, for all your valuable advice and reviews.

I also want to thank both of you for giving me the opportunity to develop this project and grow personally. Additionally, participating in numerous conferences allowed me to share my work and benefit from the work of others and their feedback.

Moving on to the thesis supervisors, I would like to warmly thank David, with whom I had the pleasure of working in this last year on synthetic catalogs. A special thank you for your kindness, which really helped me progress quickly and enjoyably on this topic. Thank you for your trust, guidance, and reviews. I would also like to express my gratitude to Jesùs Piña-Valdés for sharing his codes and for his assistance.

For the other people who contributed to the completion of this project, I would like to extend my sincere thanks to the members of my thesis committee, Fabrice Cotton, Frédéric Masson, and Philippe Gueguen. For their presence, availability, advice, and corrections, but also for their listening, which brought fluidity to this project.

Next, I would like to express my sincere thanks to my two reviewers, Laurentiu Danciu and Nicola D'Agostino, for the time they spent reviewing this document. Thanks also to the other members of my thesis jury, Andréa Walpersdorf, Fabrice Cotton, and Adrien Pothon, for their presence in this important step.

Behind the science, there are also funders who made this research project possible. I would like to thank the Axa Research Fund for funding this thesis and Philippe Gueguen for facilitating the process.

Now that I have officially thanked those directly involved, I would like to express my gratitude to all the other people with whom I had the chance to interact over these past three years.

First and foremost, I would like to extend immense thanks to Judith for your absolutely essential help. For your support, your listening, and also for your reviews. I was really fortunate that you made yourself available every time I needed help. Next, I would like to thank Mai-Linh for your support and listening.

Then, I would like to thank Julia and Pascale for giving me the incredible opportunity to teach in geology and supervise field trips. It enriched me both professionally and personally and I really appreciated the teaching experience.

Next, of course, I would like to thank all the members of the cycle team for our very interesting exchanges. I would also like to thank all the people who make research possible at ISTerre, the human resources, administrative and technical department, and the cleaning staff.

Finally, on a more personal note, I would like to thank my friends and family for being there, making me laugh, and spending wonderful years. Special thanks to all the fellow doctoral friends (whom I won't list here) and especially to Juliette and Subash for their reviews.

I would like to extend special thanks to the members of my family for their support, and particularly to Léonore for dedicating hours to very effective coaching over the phone.

Finally, thank you to my partner, William. Thank you for carrying and supporting me during this thesis. I am really happy to flourish alongside you day after day, and I look forward to undertaking all the new projects we will do together in future.

Contents

1 Introduction

1.1 Motivation and Problem Statement

In Europe, we have all been deeply affected by the widely disseminated images of seismic catastrophes that occurred around the Mediterranean in 2023. The seismic sequence in Kahramanmaras, Turkey, extending from January to March 2023, culminated in the Pazarcik earthquake ($M_W 7.8$), resulting in the tragic loss of just under 60,000 lives. These events inflicted substantial damages in Turkey, Syria, and, to a lesser extent, neighboring countries, with estimated costs surpassing 100 billion US dollars. Another noteworthy seismic event occurred in Morocco on September 9, 2023. The Al Haouz earthquake, with a moment magnitude of 6.8, occurred near Marrakesh, leading to the unfortunate loss of nearly 3,000 lives, injuries to 6,000 individuals, damage or destruction of 60,000 homes and 585 schools as reported by the US Geological Survey (*USGS.gov | Science for a changing world* 2023). These disasters, occurring as I was actively engaged in the research for this thesis, served as a poignant reminder of the critical importance and utility of endeavors aimed at preventing such calamities.

Earthquakes stand out as among the most destructive, lethal, and unpredictable natural hazards. Among natural catastrophes, earthquakes accounted for approximately one-fifth of economic losses between 1900 and 2018, resulting in an average of 20 thousand fatalities annually (Silva et al., 2019). Illustrating the gravity of their impact, seven out of the ten deadliest natural catastrophes recorded from 2000 were attributed to earthquakes, as documented in the EM-DAT disaster database. Notably, the $M_W 7$ earthquake that struck Haiti in 2010 stands as a poignant example, resulting in over 220,000 lives lost and economic losses exceeding 8 billion US dollars. Another notable event is the 2004 $M_W 9.1$ Sumatra-Andaman earthquake in Indonesia, which triggered a tsunami, claiming more than 165,000 lives and causing an economic loss of 4.5 billion US dollars.

In Figure 1.1, as illustrated by Elliott et al., 2016, the distribution of earthquakes in South Asia from 1900 to 2015, leading to more than 1000 fatalities, is presented. The size of the circle corresponds to the number of fatalities, while the color indicates the magnitude. Notably, the largest circles, representing around 250,000 fatalities, are

situated in China, specifically for the Tangshan earthquake on July 1976 (depicted in yellow), and the Haiyuan earthquake (depicted in orange). These incidents are linked to earthquakes with magnitudes ranging from 7 to 8. Alternatively, we observe other earthquakes of similar magnitude associated with significantly fewer casualties, as seen in Iran or northern India, for example. Another noteworthy observation is that even earthquakes of moderate magnitude (between 6 and 7) can result in tens of thousands of fatalities, as exemplified in southern India. In essence, this observation highlights that the number of victims is not directly proportional to the magnitude of an earthquake.

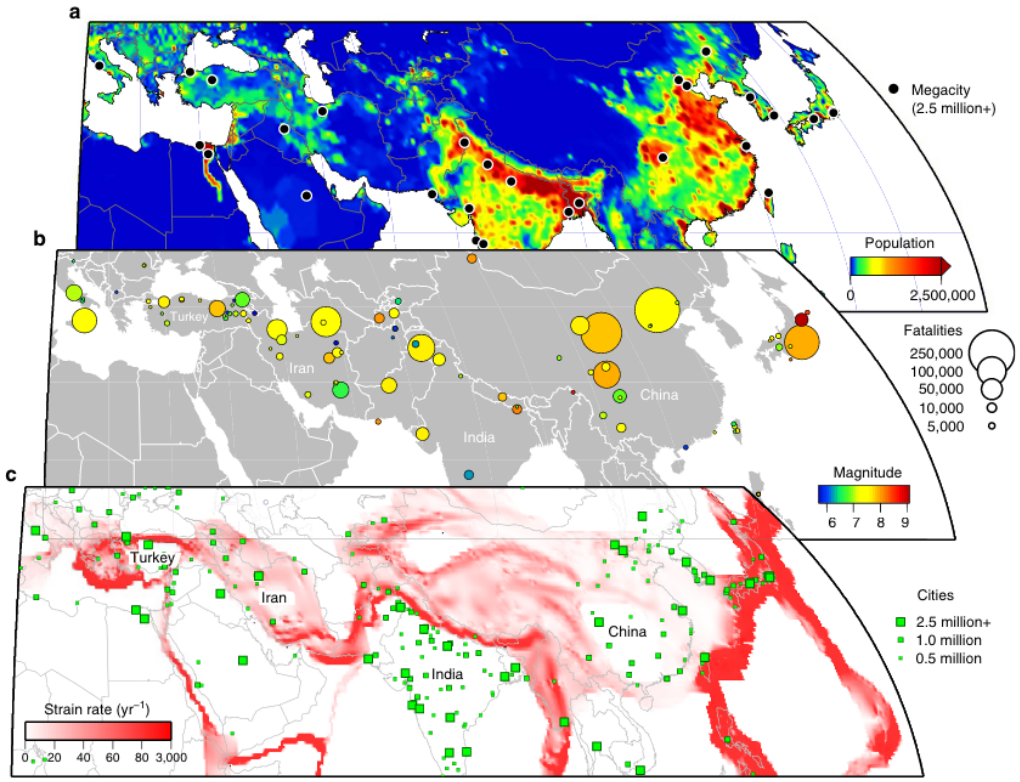

Fig. 1.1: **From Elliott et al., 2016** : Distribution of current population relative to past fatal earthquakes and crustal strain across Eurasia. (a) Population count on a half-degree by half-degree grid for 2005. Megacities with populations over 2.5 million are marked by black circles. (b) Locations of past earthquakes in the period 1900–2015 resulting in more than 1,000 fatalities are denoted by circles coloured by magnitude and scaled in size by the number of fatalities. (c) Global Strain Rate Model (v2.1) showing the second invariant of the strain rate tensor. This model is based on measurements from over 22,000 GNSS sites around the world. Large cities are overlayed (green) and scaled by population size.

This example illustrates that seismic hazard is distinct from seismic risk. Seismic hazard can be defined as the potential extent and frequency of ground motion in a specific region, while seismic risk can be defined as the likelihood of humans

experiencing loss of life and means of sustenance when exposed to a seismic hazard with a specific probability of occurrence. Broadly speaking, this relationship can be qualitatively represented by the equation: Seismic Risk = Seismic Hazard x Vulnerability x Exposure.

Exposure encompasses all individuals and assets susceptible to the impact of a seismic hazard. Returning to the previous example, this is exemplified by the fact that the earthquakes in China occurred in areas with high population density, as reported by the *USGS.gov | Science for a changing world* 2023. The quantity of individuals susceptible to being affected by each earthquakes was consequently significant.

These elements are further distinguished by their vulnerability, which is defined as the degree of susceptibility to loss, ranging from 0% to 100%, following the occurrence of an event of a specific severity. In the context of constructions, a seismic vulnerability function is a correlation that outlines the anticipated damage for portfolio as a function of a designated ground motion parameter representing the seismic hazard.

In this thesis, we will focus on seismic hazard. A result frequently employed in seismic hazard assessment is a map where ground motion, typically expressed in terms of peak ground acceleration, spectral acceleration, macroseismic intensity, etc, is presented, with a target probability of being exceeded within a future time window.

To obtain this type of information, Probabilistic Seismic Hazard Assessment (PSHA) models have gradually become an international reference. These models integrate a source model, providing information about where and when future earthquakes are likely to occur, along with a ground motion prediction model. The ground motion prediction model determines how seismic waves are expected to propagate through the Earth—whether they will attenuate, amplify, and to what extent—yielding estimates of ground motions at each point in space. In this thesis, the focus is specifically on source models.

What is an earthquake ? In simple terms, an earthquake is a geological phenomenon that occurs when a fault remains locked (by friction) while stress slowly accumulates. This phase is called the interseismic phase and is associated with deformation in the vicinity of the fault. Then earthquakes occur when the fault suddenly ruptures, releasing the stored-up stress. Energy is released in the form of seismic waves which propagate throughout the Earth, leading to ground motion. This theory is known as the elastic rebound theory (Reid, 1910). The moment magnitude (M_W) scale is

commonly used to quantify the size of an earthquake, providing a measure of its amplitude.

The source models often rely on seismicity catalogs. An important point to note at this stage is that seismicity can be divided into two distinct components. The first part encompasses earthquakes that occur independently of preceding seismic events, primarily attributed to long-term tectonic loading. These events are distinguished from those interrelated earthquakes, such as aftershocks, which result from static or dynamic stress changes induced by prior seismic events. Various scaling laws and models (e.g., the Epidemic-Type Aftershock Sequence model introduced by Ogata, 1988) have been proposed to describe seismic activity and its temporal variability. The most famous scaling law is known as the Gutenberg and Richter law and dates back to 1944. It states that the logarithm of the cumulative number of events ($N(M)$) with respect to magnitude (M) follows a straight line with an ordinate at the origin, the productivity, as a constant a, and a slope, the exponential coefficient, as a second constant b, often around 1. It is noteworthy that several researchers have introduced deviations from this line, particularly at lower and higher magnitudes, as will be discussed later. For each seismic zone, this relationship, known as the magnitude-frequency distribution (or Gutenberg-Richter curve), can be fitted to the earthquakes recorded.

The challenge arises in how we fit the magnitude-frequency distributions with the events included in the considered earthquake catalog. The issue lies in the fact that the number of known earthquakes depends on various parameters, particularly the time period for which we have information. This, in turn, depends on how long records have been kept and the manner in which information has been preserved, varying significantly across different regions of the world. Additionally, the number of known earthquakes is influenced by the seismic activity of the region. In seismically active zones, over the same time span, one is likely to record a greater number of earthquakes compared to a less active region. This aspect influences the robustness of recurrence models, providing better constraints in seismically active areas.

In regions where active faults are thoroughly characterized, their inclusion is imperative in seismic hazard assessments (e.g., Stirling et al., 2012; Field et al., 2014; Beauval et al., 2018). These fault models predominantly rely on geological data, encompassing temporal scales far beyond those covered by available earthquake catalogs. Consequently, fault models provide valuable insights into earthquake generation, supplementing catalog-based earthquake forecasts. Nonetheless, it is acknowledged that fault databases exhibit inherent incompleteness, even in regions with robust characterizations. Unforeseen earthquakes may manifest on unknown

faults, as illustrated by historical seismic events such as the 2002 $M_W 5.7$ Molise earthquakes in Italy (Valensise et al., 2004) or the Darfield $M_W 7.1$ earthquake in New Zealand (Hornblow et al., 2014).

In this context, Probabilistic Seismic Hazard Assessment (PSHA) tends towards incorporating progressively additional data sets. Geodetic data, have undergone significant advancements in the past two decades. One notable study was conducted by Soudarin and Cazenave, 1995. They expressed displacement rates based on the NUVEL-1 worldwide geological model (DeMets et al., 1990) and compared them with displacement rates measured by geodesy (DORIS solution). They obtained a linear relationship between the two, with a correlation coefficient of 0.98. At a first approximation, this suggests a very good agreement between geological and geodetic displacement rates. On the scale of tectonic plates, this provides support for the argument that displacements have remained relatively constant over the past millions of years. While GPS velocities typically capture long-term tectonic motion, they can be influenced by variations such as Slow Slip Events (SSE) and post-seismic effects. These variations are typically removed during the analysis of the time series to isolate the long-term tectonic signals, although variations of coupling have been evidenced at various subduction plates notably before the Tohoku earthquake in japan (Heki and Mitsui, 2013; Mavrommatis et al., 2014; Marill et al., 2021).

Geodesy, therefore the advantage to provides an approach that we can assume is representative of plate movement over the long term. Another advantage of this technique is that the amount of data obtained in a region depend on the station coverage. For instance, in Europe, Figure 1.2a illustrates the seismic locations from ESHM20 (Danciu et al., 2021) earthquake catalog, revealing concentrations in specific zones with higher seismic activity, primarily in southern Spain, Italy, the Balkans, Greece, and Turkey. In comparison, regions with lower activity have significantly fewer seismic events to constrain recurrence models based on seismicity catalogs. Contrastingly, Figure 1.2b displays the locations of stations used to constrain geodetic models, indicating that many stations are situated in areas with lower seismic activity. This example highlights the complementarity between seismicity and geodesy data, where information can be obtained even from regions with lower seismic activity—provided that sensors are strategically placed.

In practical terms, one method of leveraging geodetic data to provide new constraints on seismicity involves deriving surface deformation from GPS measurements. This surface deformation is expressed as strain rates, computed from the velocity gradient tensor. Geodetic strain rate data can then be compared with earthquake-induced strain or assessed in terms of geodetic moment. The fundamental concept is based on

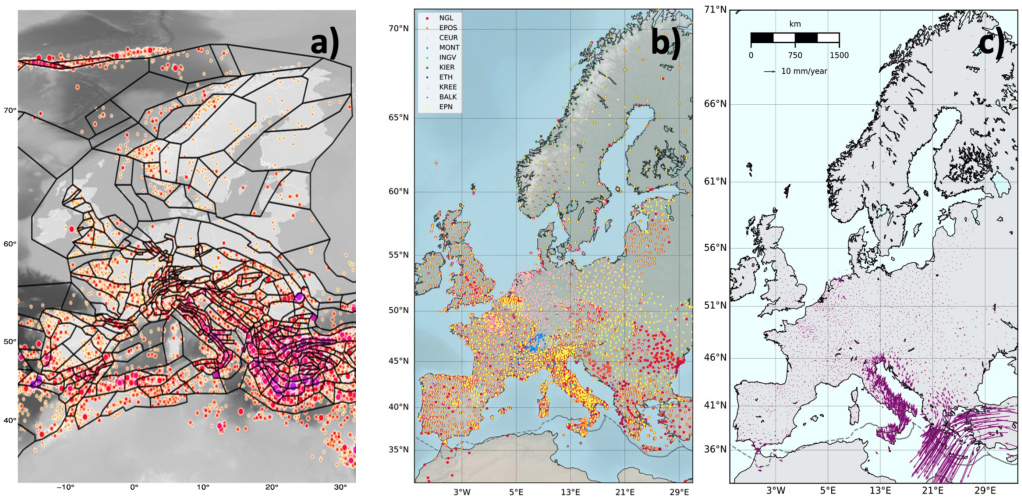

Fig. 1.2: Comparison between earthquake locations and GNSS (Global Navigation Satellite System) station locations in Europe. a) Earthquake locations in Europe sourced from Danciu et al., 2021, utilized for the ESHM20 source model. b) GNSS station locations derived from Piña-Valdés et al., 2022, representing the best models for strain rate maps. c) Velocity field in Europe obtained from Piña-Valdés et al., 2022.

the notion that the seismic moment released should equal the accumulated moment measured by geodesy (i.e., the energy accumulated in the elastic part of the crust, measurable at the surface through interseismic GNSS velocities). It is important to note that this equality holds true when the influence of aseismic deformation can be neglected (a point we will delve into in detail). However, in other cases, the percentage of aseismic deformation needs to be taken into account.

Numerous studies at a regional scale have validated the equality between seismic and geodetic moment, particularly in active zones (Kreemer and Young, 2022; D'Agostino, 2014; Mohapatra et al., 2014; Middleton et al., 2018). However, challenges persist in standardizing its application, especially in areas characterized by lower deformation. Many researchers, for example, have noted disparities between seismic and geodetic moments in several regions where geodetic moments surpass seismic moments (for example Ojo et al., 2021, Sparacino et al., 2020 in most of the zones considered in Maghreb, Ward, 1998a in Turkey, Chousianitis et al., 2015 for most of the Aegean zone, Clarke et al., 1997, Masson et al., 2004 for southern Iran, Mazzotti et al., 2011 for Western Canada).

In Europe, the new European PSHA model, ESHM20, was published in 2021 and offers a compilation of all current data on earthquakes and faults, which have been compiled and harmonized. Additionally, Piña-Valdés et al., 2022 recently proposed a strain model compiled from harmonized velocity fields for Europe. Europe is

also characterized by diverse seismotectonic contexts, ranging from regions with moderate to high deformation and seismicity as highlighted by the earthquake location and velocity field in Figure 1.2 (Southern Spain, Greece, Italy, Turkey) to areas with low to moderate deformation (Scandinavia, France, Germany). Therefore, it provides an excellent playground for comparing geodetic and seismic moment in various contexts.

The main question investigated in this thesis is as follows: In Europe, ranging from areas of high to low deformation, can geodetic moment rates be effectively utilized as a reliable proxy for seismic moment rates? Additionally, the research aims to identify the reasons behind potential divergences between geodetic and seismic moments, elucidate the parameters governing uncertainties, and establish best practices in addressing these disparities.

1.2 Thesis Structure

Chapter 2 :

In this section, we review the methods and challenges associated with integrating geodesy into Probabilistic Seismic Hazard Assessment (PSHA) models. We will introduce the concept of PSHA before providing some principles of seismology and geodesy that form the basis for this thesis. Subsequently, we explain how geodesy and seismicity are related, encompassing the elastic rebound theory, the conservation of moments theorem, and elastic dislocation theory.

Then, we will observe that numerous authors have identified a strong correspondence between geodesy and seismicity in terms of strain and moment, particularly in regions of heightened seismic activity. However, this alignment gives way to discrepancies in various other zones, especially in areas characterized by lower deformation. Subsequently, we will explore explanations presented in the literature for these divergences. Finally, we examine the various approaches proposed by different authors to practically incorporate geodesy into PSHA models.

Chapter 3 :

In this section, we provide a comprehensive review of existing studies on the seismic-tectonic context in Europe and present ESHM20 model.

The section 3.2 is written in the form of a paper in preparation for the Geophysical Journal International and makes a comparison in terms of moment at the European scale, between the strain rate estimates from Piña-Valdés et al., 2022 and

the ESHM20 source model (Danciu et al., 2021). We aim to address the following questions:

1. Are the ESHM20 seismic moment rates, inferred from the long-term magnitude frequency distributions, consistent with the geodetic moment rates in Europe in regions of high deformation?
2. Can it be extended to areas of low to moderate deformation, and under what conditions?
3. How can uncertainties arising from the spatial inversion of data be accounted for in the geodetic moment calculation, using the method employed by Piña-Valdés et al., 2022? What parameters control this uncertainty?
4. What is the impact of utilizing different ESHM20 geometries and models on the moment balance?

To answer these questions, we propose a methodology for calculating geodetic moments rates while accounting for the epistemic uncertainties, thereby obtaining a distribution of geodetic moments rates. We then estimate the seismic moment rates that correspond to the ESHM20 source model, built to be representative of long-term seismicity. Then we compare these two quantities in Europe.

Chapter 4 :

This final section, is written in the form of a paper in preparation for Seismological Research Letters and aim to explore whether, the divergence between seismic and geodetic moments could be explained by the assumption that the seismic catalogue does not represent the long term average seismicity rate.

To address this question, we focus on a ESHM20 polygon characterized by significantly higher geodetic moments rates than seismic moments rates. Subsequently, we generate synthetic seismicity catalogs based on the model developed by Marsan and Tan, 2020. This model enables the creation of synthetic catalogs representative of a zone's seismicity, allowing the introduction of a moment (constrained, for example, by geodetic data) into the system that should balance the earthquake moment release through time. We develop a methodology to anchor the seismicity parameters of this model in the long-term seismicity of the zone. The analysis of the generated catalogs provide insights into the representativity of the seismicity catalog.

2 How to integrate geodesy into PSHA model : A State of the Art Review

2.1 Introduction to Probabilistic Seismic Hazard Assessment (PSHA)

The aim of this section is to provide a brief overview of PSHA, how it is calculated, and the challenges associated with integrating new datasets, such as geodetic information, to better constrain source models. The majority of information presented in the first two points has been extracted and synthesized from the theses of Mariniere, 2020; Mathey, 2020; Aristizabal, 2018.

2.1.1 Objectives

The Probabilistic Seismic Hazard Assessment (PSHA) was introduced by two authors in the 1960s: Esteva, 1967 and Cornell, 1968. Since then, it has evolved into the reference model for the majority of national and international seismic regulations. The objective of PSHA is to provide a framework for assessing potential ground movements that must be considered in earthquake-resistant design. This estimation is applicable to both private entities (residential areas, industries, insurance companies, etc.) and public agencies, serving to evaluate societal and economic risks.

PSHA aims to be integrative, encompassing all possible earthquakes and their spatial and temporal probabilities of occurrence based on magnitude. One of the primary outputs of PSHA is hazard maps, which can be defined at regional, national, or international scales. These maps represent, at each point, the probability of ground movement (typically expressed in terms of peak ground acceleration, spectral acceleration, macroseismic intensity, etc) or the ground movement at each point with a given probability of being exceeded. An example of such a map is presented in Figure 2.1 for the ESHM20 model. The represented value is the Peak

Ground Acceleration (PGA) with a 10% probability of being exceeded in the next 50 years. This representation is commonly used in PSHA, such as the hazard map for France.

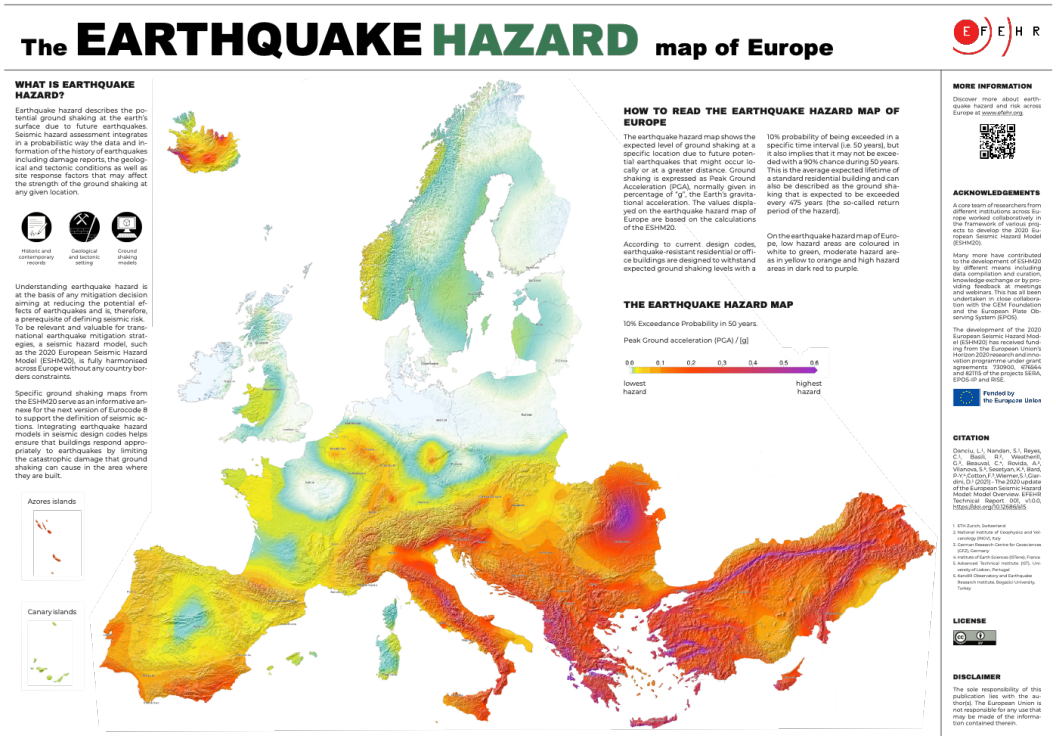

Fig. 2.1: European Seismic Hazard Model 2020 (ESHM20) from Danciu et al., 2021. The color represent the ground motion in term of Peak Ground Acceleration (PGA) (in g) that has 10% of probability to be exceeded in the next 50 years.

2.1.2 Implementation

The implementation of the PSHA models involves four steps (Reiter, 1990), as presented in Figure 2.2, modified from Mariniere, 2020 :

1. **Source Definition**: This step involves identifying locations susceptible to producing earthquakes. Sources can be modeled with three different geometries (e.g., OpenQuake by Pagani et al., 2023): point, planar (faults), or volumetric (area source zone) defined by a surface polygon and depth.

2. **Modeling Earthquake Occurrence Rate**: The occurrence rate of earthquakes is modeled based on their magnitudes. These relationships are derived from the work of Gutenberg and Richter, 1944, who observed an exponential decrease in earthquake frequencies as a function of magnitude.

3. **Estimation of Ground Motion**: This step involves predicting ground motion in response to seismic sources. A first category is the Ground Motion Prediction Equations (GMPEs) describe the path of seismic waves through the subsurface to the target site, expressing the probability density function of ground motion based on magnitude and distance. A second category, known as site effects, seeks to describe the impact of geology and topography on the earthquake experienced at the surface around the site of interest. For example, an often-used parameter is VS_{30}, representing the harmonic mean of S-wave velocities in the top 30 meters.

4. **Determination of Ground Motion Exceedance Rates**: This step combines the previous information to define hazard curves, representing the annual rates of exceeding target accelerations at a site. Another output is hazard maps, illustrating accelerations with a target probability of being exceeded over a future time window (t).

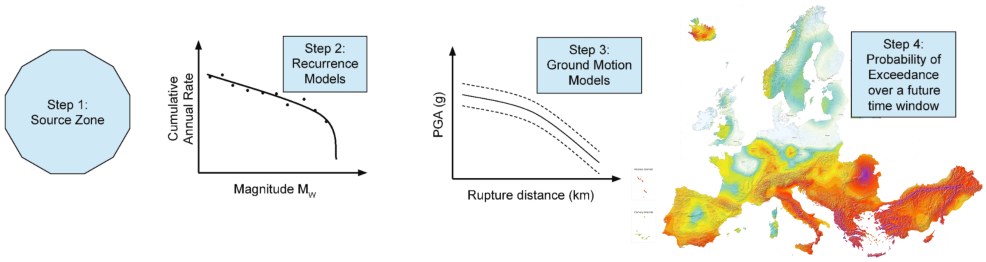

Fig. 2.2: Modified from Mariniere, 2020 : illustration of the four steps used in the definition of the PSHA approach.

Multiple models are frequently considered for each of the first three categories to account for uncertainties in modeling and data. Typically, all envisaged scenarios are represented in a logical tree. Logical trees, introduced by Kulkarni et al., 1984, stand as the most widely employed method for incorporating uncertainties in PSHA models. An example of the logic tree utilized by ESHM20 for the source model is presented in Figure 2.2 and allow the integration of a plausible range of values for the different components (a, b, M_{max}, choice of the equation) . The concept involves associating all plausible branches with probabilities for the three aforementioned aspects (Source, Earthquake Recurrence and Ground Motion models).

In the frame of this thesis we will only focus on the two first steps.

2.1.3 Source models datasets and future challenges

In contemporary probabilistic seismic hazard assessments, source models are constructed by integrating both past seismicity and active tectonics datasets. In regions where active faults are well-characterized, their inclusion becomes imperative in hazard estimations (Stirling et al., 2012; Field et al., 2014; Beauval et al., 2018). Fault models predominantly rely on geological information, offering insights over much larger temporal scales than available earthquake catalogs. Consequently, fault models provide additional perspectives on earthquake generation that complement catalog-based forecasts. Nevertheless, it is acknowledged that fault databases may be incomplete, even in extensively studied regions, and seismic events might occur on undiscovered faults.

Although the incorporation of geodetic data into source models has been limited thus far, the use of deformation rates derived from Global Navigation Satellite Systems (GNSS) velocities presents a promising avenue for constraining earthquake recurrence models (Jenny et al., 2004; Shen et al., 2007).

2.1.4 A brief introduction to the 2020 European Seismic Hazard source model (ESHM20)

The aim of this point is to provide a brief introduction for the ESHM20 source model used in this thesis. The information presented has been synthesized from the article Danciu et al., 2021, to which we recommend referring for more detailed information.

The 2020 European Seismic Hazard Model (ESHM20) by Danciu et al., 2021 is an integral component of a seismic risk model developed under the EU-funded project "Seismology and Earthquake Engineering Research Infrastructure Alliance for Europe" (SERA). Comprising both a source model and a ground motion prediction model, our focus in this discussion will be solely on the source model. It integrates crustal, deep and subduction sources.

The ESHM20 source model relies on several updated datasets (Danciu et al., 2021):

1. A historical seismicity catalogue covering earthquakes from 1000 to 1899;
2. An instrumental earthquake catalogue from 1900 to 2014;
3. Active faults datasets, encompassing their geometry and slip characteristics, referred to as the European Fault-Source Model 2020 (EFSM20).

Several hazard models are combined to capture the spatial and temporal uncertainty of earthquake rate forecasts in Europe.

Firstly, Danciu et al., 2021, propose an Area Source Model. It is based on cross-border polygons, called area source zones, where the seismic activity rates are assumed to follow a Poisson process. The magnitude-frequency distributions are computed, taking into account the uncertainties.

The second model proposed by ESHM20 is a fault source model (labeled 'Active Faults' in figure 3.7). It is combined with a smoothed seismicity model that proposes an earthquake recurrence model on a grid based on background seismic activity. In the vicinity of active faults, the smoothed seismicity model is combined with the fault model. Earthquakes below a moment magnitude threshold are assigned to the smoothed seismicity, whereas others are considered to be taken into account by the fault model.

In conclusion, ESHM20 incorporates information from both earthquake catalogs and active fault datasets. Consideration and synthesis of uncertainties in data quality and earthquake recurrence models are depicted through the logic tree presented in figure 3.7.

In the upcoming sections, we will delve into the characteristics of the two types of datasets used in this thesis : seismicity and geodesy. Following that, we will outline the theoretical models that form the foundation for establishing a connection between them. Then, we will highlight the successes and challenges that persist in adopting geodesy as a proxy for seismicity, both in regions of high and low deformation. Finally, we will explore how geodesy is practically employed in probabilistic seismic hazard assessment (PSHA) source models.

2.2 Seismicity: from data to seismic moment calculation

In this section, we will first explore the fundamental statistics used to model the observed seismicity recorded in earthquake catalogs. Subsequently, we will delve into the calculation of seismic moment from these data and models.

2.2.1 From data to models

The objective of this section is not to be exhaustive but to offer a concise overview of key points that will facilitate understanding in the subsequent sections of this

thesis. We will present both the equations commonly employed for PSHA and those that will be utilized in the final chapter. A substantial portion of the information has been extracted and synthesized from Reverso, 2015 thesis, to which we recommend referring for more detailed insights.

Scaling laws

In the early 20^{th} century, Galitzin developed the first electromagnetic seismometer, laying the foundation for modern seismometers. These instruments facilitated the establishment of seismicity catalogs worldwide, forming the basis for empirical relationships. These catalogs contributed to the formulation of scaling laws, which we will discuss in the context of this thesis.

Productivity Law

This law defines the number of aftershocks generated for an earthquake of magnitude m:

$$k = k_0 \exp(\alpha(m - M_t)) \tag{2.1}$$

where, k_0 and α are constants, where k_0 depends on the region, and α is approximately 2 and M_t, the threshold magnitude, is the minimum magnitude from which the vast majority of seismic events will be detected.

Omori-Utsu Law

At the end of the 19^{th} century, Fusakichi Omori observed a decrease in the aftershock rate of the Nobi earthquake in Japan in 1891 over time. He expressed the number of aftershocks (n), over time (t), with an empirical law. Utsu later modified and universalized Omori's law, resulting in the well-known Omori-Utsu law:

$$n(t) = k/(t + c)^p \tag{2.2}$$

where p is a constant describing the temporal decay, typically ranging between 0.8 and 2.

Gutenberg-Richter Law

One of the most well-known scaling laws is the Gutenberg-Richter law, proposed by Gutenberg and Richter in 1944 based on the analysis of Californian earthquake

catalogs. It states that the logarithm of the cumulative number of events ($N(M)$) with respect to magnitude (M) follows a straight line with an ordinate at the origin, the productivity, as a constant a, and a slope, the exponential coefficient, as a second constant b, often around 1. This relation can be expressed as :

$$log_{10}N(M) = a - bM \tag{2.3}$$

Since 1944, several discussions have unfolded, particularly concerning various models that have attempted to better constrain the behavior of this law in the highest magnitudes ranges. These variations have been extensively deliberated in the context of seismic moment calculations, and they will be presented in the following section.

ETAS Models

Seismicity can be modeled as the superposition of two processes described by distinct components: background seismicity μ and a term accounting for interaction between earthquakes, denoted ν. The occurrence rate of earthquakes in space and time $\lambda(x, y, t)$

$$\lambda(x, y, t) = \mu(x, y, t) + \nu(x, y, t) \tag{2.4}$$

The term $\mu(x, y, t)$ is independent of previous seismicity and is related to spontaneous seismic activity, varying across different zones. The probabilistic distinction between these components was introduced by Kagan and Knopoff, 1978, stating that the background rate is stationary and homogeneous for a given region.

Ogata, 1988; Ogata, 1998 proposed a method based on clustering models, known as the ETAS model (Epidemic-Type Aftershock Sequence). It is a stochastic method aimed at 1) determining the background seismicity rate, assuming spatial homogeneity and stationarity, and 2) modeling the interaction term between earthquakes.

The second term depends on empirical laws described earlier (Gutenberg-Richter law, Omori law, productivity law, spatial distribution of aftershocks). Marsan and Tan, 2020 adapted this model to allow input of a moment that could be released within the system over time by using the Hanks and Kanamori, 1979 relationship expressing the moment released by an earthquake in terms of its magnitude.

2.2.2 Seismic moment computation

The seismic moment is computed in two ways in the literature.

The first commonly used approach, the Kostrov, 1974 summation, involves summing the contributions of earthquakes in the earthquake catalog, utilizing the formula of Hanks and Kanamori, 1979 to convert the earthquake moment magnitude (M_W) obtained from the catalog to scalar seismic moment (M_o).

$$M_{0S} = 10^{cM_W+d} \tag{2.5}$$

where $c = 1.5$ and $d = 9.1$. Certain authors employ values of $d = 9.0$ or $d = 9.05$, choosing between them based on the rounding conventions applied to coefficients in the equation linking moment and moment magnitude (refer to Pancha, 2006). As indicated by Mariniere, 2020, opting for $d = 9.0$ instead of $d = 9.1$ results in a 20% reduction in the calculated moment rate for a given magnitude.

The Kostrov summation has been used in studies conducted by Ward, 1998b; Ward, 1998a; Masson et al., 2004; Palano et al., 2018; Ojo et al., 2021. The seismic moment rate is obtained by summing the contributions of each event in the catalog and is represented by the following equation :

$$\dot{M}_{0S} = 1/t \sum_{i=1}^{N} 10^{cM_W(i)+d} \tag{2.6}$$

where N is the total number of earthquakes and t the time interval. The second commonly employed method integrates the contributions of earthquakes over magnitude-frequency distributions, relying on the Poissonian behavior of earthquake recurrence (Gutenberg and Richter, 1944). A common approach is to combine these functions with the Hanks and Kanamori, 1979 equation 2.5.

Various equations have been proposed, differing in their form at high magnitudes. The three subsequent forms are illustrated by Figure 2.3 The two primary solutions are commonly found in studies comparing geodetic and seismic moment rates and have been proposed by Anderson and Luco, 1983. One such equation is the truncated Gutenberg-Richter (GR), also known as Anderson and Luco form 1. This equation is frequently employed in studies that compare geodetic and seismic moment rates, and it finds widespread use (Main et al., 1998; Mazzotti et al., 2005; Ojo et al., 2021; Palano et al., 2018; D'Agostino, 2014; Avouac, 2015; Stevens and Avouac, 2016; Stevens and Avouac, 2017).

It states that the number of earthquakes with a magnitude greater than M follows the relation:

$$N(m) = 10^{a-bm} \text{ for m} \leq M_{max} \tag{2.7}$$

When integrated, the seismic moment rates can be computed following the equation (Mariniere et al., 2021):

$$\dot{M}_{0S} = \frac{c}{(c-b)} 10^{a+d+(c-b)M_{max}} \tag{2.8}$$

Another form is the Anderson and Luco, 1983 form 2. It is the most commonly used in PSHA studies (Beauval et al., 2014; Mariniere et al., 2021) and is the one implemented in OpenQuake (Pagani et al., 2023, "Truncated Gutenberg–Richter MFD").

$$N(m) = 10^{a-b*m} + 10^{a-bM_{max}} \text{ for m} \leq M_{max} \tag{2.9}$$

Giving (Mariniere et al., 2021):

$$\dot{M}_{0S} = \frac{b}{(c-b)} 10^{a+d+(c-b)M_{max}} \tag{2.10}$$

Another function proposed by Kagan, 2002 introduces a corner magnitude (M_C) influencing a decrease in the function:

$$N(m) = \alpha * 10^{2/3b*c(M_t-m)} * \exp(10^{c(M_t-M_c)} - 10^{(m-M_c)}) \tag{2.11}$$

with M_t the magnitude threshold (taken as the minimum magnitude considered) and α the occurrence rate for earthquakes with a moment magnitude M_t and greater.

$N(m)$ can be integrated over the higher magnitudes by:

$$\dot{M}_{0S} = M_C^{(1-\beta)} * \alpha * M_t^{\beta} * \Gamma(2-\beta)/(1-\beta) \tag{2.12}$$

with Γ, the gamma function (defined as $\Gamma(x) = \int_0^{\infty} t^{x-1}e^{-t}dt$), and $\beta = b * ln(10)$. Other equations, albeit not extensively utilized, are found in the literature, such as the Gaussian function (Main et al., 1998) or the Anderson and Luco, 1983 form 3. The Weichert, 1980 maximum-likelihood method allows for the determination of the Gutenberg–Richter recurrence parameters from magnitude intervals with varying time windows of completeness (productivity a and exponential coefficient b, (Gutenberg and Richter, 1944)). The parameter that is the most challenging to evaluate in this case is the one governing the behavior near the maximum magnitude M_{max}. There are three definitions of M_{max} (Main et al., 1998):

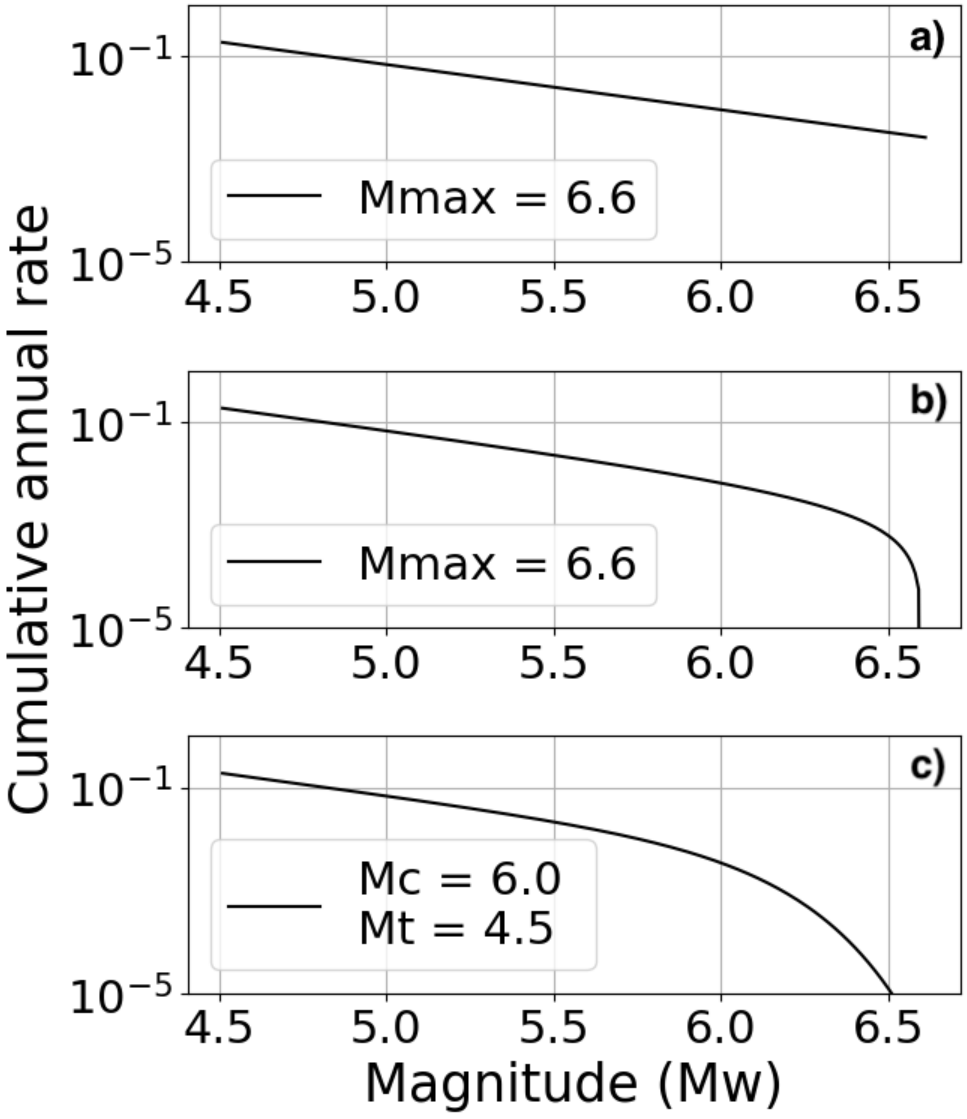

Fig. 2.3: Three distinct representations of varying forms applied within the highest magnitude range, where constants a and b are fixed at 3.2 and 0.9, respectively. a) Illustrates the curve modeled by the Anderson and Luco form1 equation, employing Mmax = 6.6 (Equation 2.7). b) Depicts the curve modeled using Anderson and Luco Form 2 with Mmax = 6.6 (Equation 2.9). c) Presents the curve modeled by the equation 2.11, representing the Tapered Pareto form of the function, Mc = 6.0, Mt = 4.5

1. The maximum historical earthquake, providing a lower bound for the maximum size.

2. The maximum 'credible' earthquake, based on a 'reasonable' assessment of the maximum earthquake potential with respect to the ambient tectonic regime. The definition of 'credible' and 'reasonable' is not fixed; it depends on the state of knowledge and is based on expert opinions, for example on the known faults. It is less than or equal to the maximum possible earthquake (defined below) but greater than or equal to the maximum historical earthquake.

3. The maximum possible magnitude that could occur in a given time interval and tectonic regime, providing an absolute though improbable upper-bound earthquake.

In litterature, maximum magnitudes are estimated using scaling laws, geological and geomophological studies, or comparisons with other regions with the same tectonic context. One way is to use the information from fault (or fault zones) to constrain M_{max}. Empirical relationships have been formulated, linking fault parameters, such as surface rupture length, earthquake moment magnitude, rupture area, and displacement, with earthquake magnitude (Wells and Coppersmith, 1994; Hanks, 2002; Hanks and Bakun, 2008; Wesnousky, 2008). To ascertain the maximum magnitude (M_{max}) associated with a particular fault or fault zone, these empirical equations can be integrated with details concerning the overall length of the fault susceptible to rupture and the potential width or seismogenic thickness capable of undergoing rupture. For an illustrative example, one may refer to the work of Whitney and Hengesh, 2013.

We have discussed how seismic moment can be calculated from earthquake catalogs. Now, our focus turns to the calculation of geodetic moment from GNSS data.

2.3 Geodesy: from data to geodetic moment calculation

In a manner similar to seismicity, we will first explore how geodetic data is acquired and interpreted in terms of strain rates maps. Subsequently, we will delve into how these strain data are employed to calculate a representative geodetic moment for a given region.

2.3.1 From data to models

The objective here is not to provide an exhaustive overview but to present the concept of strain rates map creation, setting the stage for the thesis challenges. The majority of the information is extracted and synthesized from the theses of Masson et al., 2019; Mariniere, 2020; Tarayoun, 2018; Pagani, 2021 as well as from Shen et al., 2015 article on VISR software.

The GPS, developed in 1973 for military purposes and made publicly available in 2000, marks a significant advancement in precise location determination. GPS constellation includes 24 operational satellites orbiting 20,000 km above Earth's surface in 12-hour circular orbits. Subsequent developments in satellite navigation systems, collectively known as Global Navigation Satellite Systems (GNSS), include the Russian GLONASS and European GALILEO systems.

The creation of strain maps from GNSS data involves several phases outlined in Figure 2.4 which are 1) Station Position Calculation, 2) Velocity Derivation from position time Series, and 3) Strain Rates Map Generation from Station Velocities. Theses 3 items will be detailed in the next points.

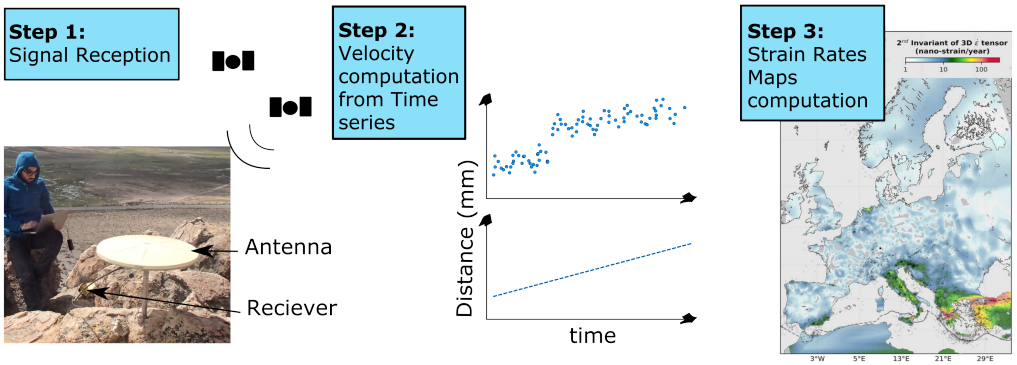

Fig. 2.4: Illustration of the 3 steps used to compute strain rate maps. Steps 1 depict the equipment used to receive location data, with an example of a campaign GNSS. Step 2 shows two panels: the first one displays an initial time serie, each dot representing a location recorded over time, and the bottom panel illustrates the overall interseismic movement of the station across time after removing transient parasitic signals. Step 3 provides an example of a strain rate map computed from several stations. In this example, the map shows the Piña-Valdés et al., 2022 second invariant of the strain rate tensor, termed the 'best model', computed from the VISR algorithm (Shen et al., 2015) and a combined velocity field for Europe.

Station Position Calculation

We have GNSS stations and aim to determine their locations. These stations consist of ground-based receivers equipped with antennas linked to a receiver, as illustrated in Figure 2.4a. They capture signals from satellites, and the positions of GNSS stations are obtained through the inversion of phase arrivals. Typically, for monitoring tectonic movements and intracontinental deformation, we rely on static positions estimated from 24 hours of observation, then georeferenced. The evolution of these positions over time can be tracked through the analysis of time series of positions. This approach enables the monitoring of changes in station locations, providing valuable insights into tectonic movements and intracontinental deformation.

Velocity Derivation from position time Series

Once the precise daily positions are estimated, repeated measurements over time yield time series of position (Figure 2.4b). These position time series are affected by various phenomena like seasonal variations, co-seismic jumps, antenna changes, or postseismic relaxation, that necessitate the removal of parasitic terms to reveal the station's motion associated with the linear trend usually supposed to represent the interseismic loading and possibly the secular tectonic movement of the stations. Conventionally, the method used is to subtract functions representing these transient variations from the signal, for example, using trajectory models approaches (Bevis and Brown, 2014; Marill et al., 2021). This is illustrated in Figure 2.4, step 3. The top panel of the figure depicts a noisy signal that can be obtained as input. The bottom panel represents the component of the signal corresponding to the movement made by the station, once these transient variations have been removed. Alternative methods, such as statistical analysis of the position time series such as MIDAS Blewitt et al., 2016, also lead to a robust estimate of the linear long-term velocity at the station, with a lower sensitivity to unknown jumps in the time series. Because of its robustness, this approach is the one used by NGL (http://geodesy.unr.edu/) and by EPOS (https://www.resif.fr/) to compute their velocity products.

Strain Rates Map Generation from Station Velocities

In this section, we will start by providing a definition of strain rate, utilizing a 1D scenario. Subsequently, we will explore the derivation of the strain rate tensor from a velocity gradient tensor within a 2D context. Most of the information of the two first point is extracted from Calais classes (Calais, 2023). Following this, we

will exemplify the spatial inversion process using Shen et al., 2015's VISR software, illustrating how strain rates can be obtained across a grid from discretized GNSS stations. The rationale for presenting this example lies in its adoption as the primary method in this thesis. Lastly, we will delve into alternative approaches for computing strain rate maps that have been developed in the existing literature.

1) 1D case : Strain rate definition

Let's consider a 1D case with two stations $A(x)$ and $B(x+dx)$, very close to each other, in a coordinate system (O, x).

Assuming infinitesimal displacements, the two stations are now located at A' and B' with $u(x)$ and $u(x+dx)$ representing the displacements at A and B, respectively.

As the displacement dx is infinitesimal, therefore:

$$u(x+dx) = u(x) + \frac{\partial u}{\partial x} dx \tag{2.13}$$

Strain is defined as the ratio of the change in length to the original length :

$$\varepsilon_x = \frac{\Delta L}{L} \tag{2.14}$$

with L as the distance between the two stations and ΔL as the change in length between them. Then we can write:

$$\varepsilon_x = \frac{\Delta L}{L} = \frac{A'B' - AB}{AB} = \frac{dx + \left(u(x) + \frac{\partial u}{\partial x} dx\right) - u(x) - dx}{dx} = \frac{\partial u}{\partial x} \tag{2.15}$$

Infinitesimal strain can be expressed as the gradient of the displacement.

2) 2D Case : Strain rate tensor from velocity gradient tensor

We consider a 2D Cartesian frame (O, x, y) and infinitesimal displacements. The velocity along the two coordinates can be expressed as a function of the position X in the following manner.

$$v_x(X + \delta X) = v_x(X) + \frac{\partial v_x}{\partial x} \delta x + \frac{\partial v_x}{\partial y} \delta y \tag{2.16}$$

$$v_y(X + \delta X) = v_y(X) + \frac{\partial v_y}{\partial x} \delta x + \frac{\partial v_y}{\partial y} \delta y \tag{2.17}$$

So

$$v(X + \delta X) = v(X) + \nabla V \delta X \tag{2.18}$$

With

$$\nabla V = \begin{pmatrix} \frac{\partial v_x}{\partial x} & \frac{\partial v_x}{\partial y} \\ \frac{\partial v_y}{\partial x} & \frac{\partial v_y}{\partial y} \end{pmatrix} \tag{2.19}$$

With ∇V the velocity gradient tensor. The theory of tensors states that second-rank tensors can be decomposed into a symmetric and an antisymmetric tensor. So,

$$\nabla V = 1/2[\nabla V + \nabla V^T] + 1/2[\nabla V - \nabla V^T] \tag{2.20}$$

Which can be written as :

$$\nabla V = \begin{pmatrix} \frac{\partial v_x}{\partial x} & \frac{1}{2}(\frac{\partial v_x}{\partial y} + \frac{\partial v_y}{\partial x}) \\ \frac{1}{2}(\frac{\partial v_x}{\partial y} + \frac{\partial v_y}{\partial x}) & \frac{\partial v_y}{\partial y} \end{pmatrix} + \begin{pmatrix} 0 & \frac{1}{2}(\frac{\partial v_x}{\partial y} - \frac{\partial v_y}{\partial x}) \\ \frac{1}{2}(\frac{\partial v_x}{\partial y} - \frac{\partial v_y}{\partial x}) & 0 \end{pmatrix} \tag{2.21}$$

With the left part being the symmetric tensor and the right part being the antisymmetric tensor. The strain rate tensor is defined as the symmetric part of the velocity gradient tensor. The antisymmetric part is the rigid rotation tensor and is denoted as W. We have the strain rate tensor E:

$$E = \begin{pmatrix} \dot{\varepsilon}_{xx} & \dot{\varepsilon}_{xy} \\ \dot{\varepsilon}_{xy} & \dot{\varepsilon}_{yy} \end{pmatrix} \tag{2.22}$$

with $\dot{\varepsilon}_{xx} = \frac{\partial v_x}{\partial x}$, $\dot{\varepsilon}_{yy} = \frac{\partial v_y}{\partial y}$ and $\dot{\varepsilon}_{xy} = \frac{1}{2}(\frac{\partial v_x}{\partial y} + \frac{\partial v_y}{\partial x})$

One way to represent the strain is to use the eigenvectors (principal axes of the strain rate tensor) and eigenvalues (principal strain rates). Here are the equations to find the eigenvalues and principal angle.

$$\dot{\varepsilon}_{max} = MAX\left(\frac{\dot{\varepsilon}_{xx} + \dot{\varepsilon}_{yy}}{2} + \sqrt{\left(\frac{\dot{\varepsilon}_{xx} - \dot{\varepsilon}_{yy}}{2}\right)^2 + \dot{\varepsilon}_{xy}^2}; \frac{\dot{\varepsilon}_{xx} + \dot{\varepsilon}_{yy}}{2} - \sqrt{\left(\frac{\dot{\varepsilon}_{xx} - \dot{\varepsilon}_{yy}}{2}\right)^2 + \dot{\varepsilon}_{xy}^2}\right) \tag{2.23}$$

$$\dot{\varepsilon}_{min} = MIN\left(\frac{\dot{\varepsilon}_{xx} + \dot{\varepsilon}_{yy}}{2} + \sqrt{\left(\frac{\dot{\varepsilon}_{xx} - \dot{\varepsilon}_{yy}}{2}\right)^2 + \dot{\varepsilon}_{xy}^2}; \frac{\dot{\varepsilon}_{xx} + \dot{\varepsilon}_{yy}}{2} - \sqrt{\left(\frac{\dot{\varepsilon}_{xx} - \dot{\varepsilon}_{yy}}{2}\right)^2 + \dot{\varepsilon}_{xy}^2}\right) \tag{2.24}$$

$$tan(2\theta) = \frac{2\dot{\varepsilon}_{xy}}{\dot{\varepsilon}_{xx} - \dot{\varepsilon}_{yy}} \tag{2.25}$$

By convention, extension is taken as positive. In Figure 2.5, we will have $\dot{\varepsilon}_{min}$ as the width of the rectangle (under compression) in the e2 direction, and $\dot{\varepsilon}_{max}$ as the length of the rectangle (in the e1 direction).

We need a spatial inversion method to obtain the strain rate tensor in each point of the space (not only xhere there are GNSS stations). To present the method, we

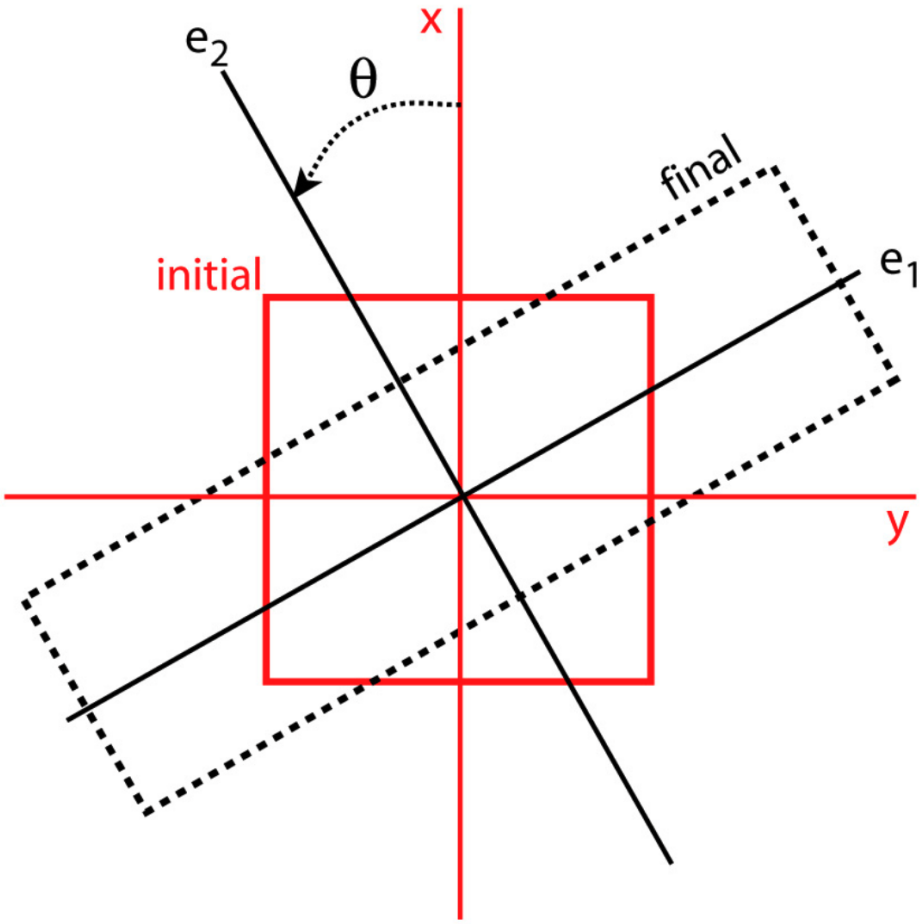

Fig. 2.5: **From Calais classes:** representation of the transformation of a square (in red) from an initial state in the Cartesian coordinate system (O, x, y) to a final state following deformation in a frame defined by the principal directions of the strain rate tensor, $e1$ and $e2$. The values of extension $\dot{\varepsilon}_{max}$ and compression $\dot{\varepsilon}_{min}$ are given by the length and width of the black rectangle, respectively. Θ represents the rotation between the two frames (O, x, y) and $(O, e1, e2)$.

will follow the approach of Shen et al., 2015, as this algorithm is used in this thesis. Later, we will explore other possibilities presented in the literature.

3) Spatial inversion used in VISR software Shen et al., 2015

At each interpolation coordinate R, the horizontal strain rates and displacement field can be linked to the velocities of the neighboring GNSS stations, considering only the case of horizontal strain rates.

$$d = Am + \epsilon \tag{2.26}$$

with d is the data vector, m is the vector of unknowns (translation, rotation and strain) A is the partial derivative matrix and ϵ is the error vector. It can also be written as :

$$\begin{pmatrix} v_{x_1} \\ v_{y_1} \\ v_{x_2} \\ v_{y_2} \\ \dots \\ v_{x_n} \\ v_{y_n} \end{pmatrix} = \begin{pmatrix} 1 & 0 & dy_1 & dx_1 & dy_1 & 0 \\ 0 & 1 & -dx_1 & 0 & dx_1 & dy_1 \\ 1 & 0 & dy_2 & dx_2 & dy_2 & 0 \\ 0 & 1 & -dx_2 & 0 & dx_2 & dy_2 \\ \dots & \dots & \dots & \dots & \dots & \dots \\ 1 & 0 & dy_n & dx_n & dy_n & 0 \\ 0 & 1 & -dx_n & 0 & dx_n & dy_n \end{pmatrix} \begin{pmatrix} U_x \\ U_y \\ \omega \\ \dot{\varepsilon}_{xx} \\ \dot{\varepsilon}_{xy} \\ \dot{\varepsilon}_{yy} \end{pmatrix} + \begin{pmatrix} \epsilon_{x_1} \\ \epsilon_{y_1} \\ \epsilon_{x_2} \\ \epsilon_{y_2} \\ \dots \\ \epsilon_{x_n} \\ \epsilon_{y_n} \end{pmatrix} \tag{2.27}$$

With U_x and U_y the translation in x and y direction, ω the rotation, $\dot{\varepsilon}_{xx}$, $\dot{\varepsilon}_{xy}$ and $\dot{\varepsilon}_{yy}$ the component of the strain rate tensor in the cartesian reference frame. v_{x_i} and v_{y_i} are the displacement component of the i^{th} GNSS station at location r_i. dx_i and dy_i are the vector components of $dR_i = r_i - R$

If we assume the error matrix is $\epsilon \sim N(0, C)$ and C is the covariance matrix of the velocity data, the preceding equation can then be solved using the least-squares method:

$$m = (A^T C^{-1} A)^{-1} A^T C^{-1} d \tag{2.28}$$

The preceding equations hold for the mean strain field of the entire region. Consequently, the data is reweighted to give more weight to sites closer to R. To achieve this, they reconstruct the covariance matrix C by multiplying a weighting function to each of its diagonal terms C_i, and the weighting is given as $C_i \leftarrow C_i G_i^{-1}$. The weighting function is $G_i = L_i \times Z_i$, in which L_i and Z_i are functions dependent on distance and spatial coverage, respectively.

For distance-dependent weighting, they proposed two equations, Gaussian or quadratic (refer to Shen et al., 2015 for further details). The primary difference lies in how the Gaussian function diminishes weight more rapidly with distance ΔR_i compared to the quadratic function. The choice between them depends on data quality; the Gaussian function may yield a finer resolution of the interpolation result when dealing with clean and smooth data. Conversely, if the data exhibit heterogeneity, the quadratic function tends to be more conservative, offering a smoother solution, particularly in regions with sparsely distributed data.

The Z_i function is designed to compensate for the often unevenly distributed data points, offering two alternatives. The first is termed the 'azimuthal weighting function', which assigns a weight to the i^{th} station based on the station coverage per azimuthal bin. The second involves the use of Voronoi cells. In this case, the surface area of the Voronoi cells is utilized as a reweighting coefficient.

4) Other examples in literature

In performing spatial inversion to obtain deformation measurements, the literature addresses several major issues following the acquisition of a well-defined velocity field, including tectonic discontinuities and their boundary conditions, as well as variations in station density. For the first question, some authors have proposed creating multiple subsets on which they calculate strains and then combine them afterward. However, this approach sometimes poses challenges in terms of how to effectively merge them (e.g., Frank, 1966). Regarding classical smoothing issues, there were two main approaches until now. One involves spatially interpolating the locally measured displacement rates at GNSS stations to obtain a continuous field. This approach involves an arbitrary level of smoothing defined by the user (example: the SPARSE code by Beavan and Haines, 2001). Alternatively, one can invert from GNSS data without needing a velocity interpolation scheme (Shen et al., 1996). In this case, a grid is defined, and at each point, a system of linear equations can relate displacement and deformation at that point with the velocities of GPS stations at neighboring points. GNSS velocities can then be inverted using a standard least-square scheme to recover deformation at each point. This second method has been refined over the years (Shen et al., 1996; Shen et al., 2015) and is widely used in the literature (Piña-Valdés et al., 2022; Ojo et al., 2021, ect). Other alternatives exist. Some of these methods rely on geophysical models, such as elastic or viscoelastic block models with predefined faults (e.g., McCaffrey et al., 2013 or Parsons, 2006), to calculate surface velocities and deformation rates. Additionally, recent methods propose novel techniques, such as Pagani, 2021, who suggest inverting geodetic data to create strain maps based on a Bayesian approach.

This study exclusively adopts the VISR model, used by Pina Valdes et al. to produce European-scale strain maps. The investigation aims to meticulously consider the impact of different model parameters on geodetic moment uncertainties, excluding alternative approaches.

2.3.2 Geodetic moment equations

The generation of strain maps involves various uncertainties, stemming from the GNSS measurements themselves and the spatial inversion techniques employed for these data. Here we review the various methodologies employed in the computation of the geodetic moment derived from strain rate tensors.

The formulation for computing the geodetic moment is not singular and varies particularly in the manner of integrating the strain component. Hereafter are presented the most common ones.

A primary equation, employed by numerous researchers (**pagani_bayesian_2021**; Ward, 1998a; Ward, 1998b; Ward, 1994; D'Agostino, 2014; D'Agostino et al., 2009; Adly et al., 2018), is expressed as follows:

$$\dot{M}_{0G} = 2\mu AH\dot{\varepsilon}_{max} \tag{2.29}$$

Where, μ is the shear modulus (second Lamé coefficient) of the considered elastic layer, expressed in $N.m^{-1}$ or in GPa ($1N.m^{-1} = 10^{-9}GPa$). Classical values for the crust are $33GPa$ and $30GPa$ (Dziewonski and Anderson, 1981; Burov, 2011) as it will be detailed in the subsequent point, H is the seismogenic thickness, A the area of the zone, and $\dot{\varepsilon}_{max}$ the maximum principal component of the strain rate tensor.

An alternative proposal was put forth by the Working Group on California Earthquake Probabilities, 1995 :

$$\dot{M}_{0G} = 2\mu AH(\dot{\varepsilon}_{max} - \dot{\varepsilon}_{min}) \tag{2.30}$$

In this equation, $\dot{\varepsilon}_{min}$ represents the second principal component of the strain rate tensor

Savage and Simpson, 1997 demonstrated that the approach based on surface strain accumulation leads to a non-unique determination, primarily resulting in underestimation, of the scalar moment rate. This non-uniqueness stems from the inherent

limitation that a 2-D strain rate tensor typically does not correspond to a double-couple mechanism. The authors argue that attempting to deduce a unique scalar moment rate from such strain rate data is challenging due to the complexities of resolving the moment tensor into multiple double-couple mechanisms, each with its own scalar moment rate. In response to this challenge, they proposed an alternative equation, formulated as the minimal energy effectively accumulated in the crust, as a more robust method for estimating the scalar moment rate.

$$\dot{M}_{0G} = 2\mu AHMAX(|\dot{\varepsilon}_{max}|, |\dot{\varepsilon}_{min}|, |\dot{\varepsilon}_{max} - \dot{\varepsilon}_{min}|) \tag{2.31}$$

This approach has found extensive use in literature (Ojo et al., 2021; Mazzotti et al., 2011; D'Agostino et al., 2009).

Recently, Stevens and Avouac, 2021 introduced an additional approach to address this issue, using the second invariant of the strain tensor, which reflects the magnitude of the total strain:

$$\dot{M}_{0G} = C_g \mu AH \sqrt{\dot{\varepsilon}_{NN}^2 + \dot{\varepsilon}_{EE}^2 + 2\dot{\varepsilon}_{NE}^2} \tag{2.32}$$

with $\dot{\varepsilon}_{NN}$, $\dot{\varepsilon}_{EE}$, and $\dot{\varepsilon}_{NE}$ as the components of the strain tensor in the North, East, and North East directions, $\sqrt{\dot{\varepsilon}_{NN}^2 + \dot{\varepsilon}_{EE}^2 + 2\dot{\varepsilon}_{NE}^2}$ the second invariant of the strain rate tensor and C_g as a geometric coefficient.

The choice of the parameters used to compute the geodetic moment is detailed in the subsequent point.

Definition and values of the parameters used to compute the geodetic moment

The estimation of the geodetic moment can be viewed either as a best-model or as a distribution, exploring the various parameters listed below to account for their uncertainties. Different approaches have been proposed to integrate these uncertainties. For instance, D'Agostino et al., 2009 explored several equations and seismogenic thicknesses, comparing the resulting distribution with the seismic moment. Mazzotti and Adams, 2005 suggested several alternative geodetic moment computations integrated in a tree of uncertainty prospecting inspired by the logic-tree approach for Probabilistic Seismic Hazard Assessment (PSHA). Hodge et al., 2015 incorporated uncertainties by conducting Monte Carlo simulations.

The shear modulus μ is commonly considered as the bulk shear modulus for the crust. In the context of continental regions, two values serve as the reference, namely $33GPa$ and $30GPa$ (Dziewonski and Anderson, 1981; Burov, 2011), and find widespread use (Palano et al., 2018; Stevens and Avouac, 2021; Hyndman et al., 2003 for $33GPa$, and Ward, 1998a; Working Group on California Earthquake Probabilities, 1995 for $30GPa$). However, certain authors have proposed broader ranges of values, such as Mazzotti et al., 2011 ($23 - 37GPa$, from Turner, 2002) or smaller values such as Bird, 2004 ($27.7GPa$).

Another contentious parameter is the seismogenic thickness. According to Mazzotti and Adams, 2005, it can be defined either as the seismogenic thickness or as an effective seismic thickness. In the former case, the extent may be constrained by the minimum and maximum earthquake depths. The latter definition corresponds to the thickness over which 100% of the deformation is seismic. They highlighted that strictly adhering to the first definition might lead to significant approximations, primarily because the initial kilometers of the crust do not predominantly produce earthquakes, and secondarily because some deep-seated earthquakes are a consequence of local mechanical properties that do not reflect the mechanical state of the surrounding rocks. Most authors adapt this first definition, viewing it as the depth at which the majority of earthquakes occur (Hodge et al., 2015; Palano et al., 2018; D'Agostino, 2014; Pancha, 2006; Masson et al., 2004).

Mazzotti and Adams, 2005 proposed a methodology to apply the second definition. They suggest that H can be approximated by utilizing the depth distribution of the number of earthquakes as a proxy for the distribution of seismic moment. The effective seismic thickness is then defined as the height of a rectangle which has an area equivalent to the depth distribution and a width defined by the peak in the distribution (as depicted in Figure 2.6 below). The figure demonstrates that in the case of Charlevoix in Western Quebec, the resulting effective seismogenic thickness (second definition) is approximately one third (12 km vs. 30 km) of the seismogenic thickness computed from the strict first definition.

Other propositions have been put forth in the literature for this coefficient. For instance, Ojo et al., 2021 consider it as one third of the Moho depth in their study on Canada. Another approach was presented by Bird, 2004. They estimate the so-called 'coupled thickness' by solving the moment conservation principle for different types of plate boundaries on a global scale. Their results have been incorporated in various studies, such as those from Carafa et al., 2017; Rong et al., 2016 and Bird and Kreemer, 2015.

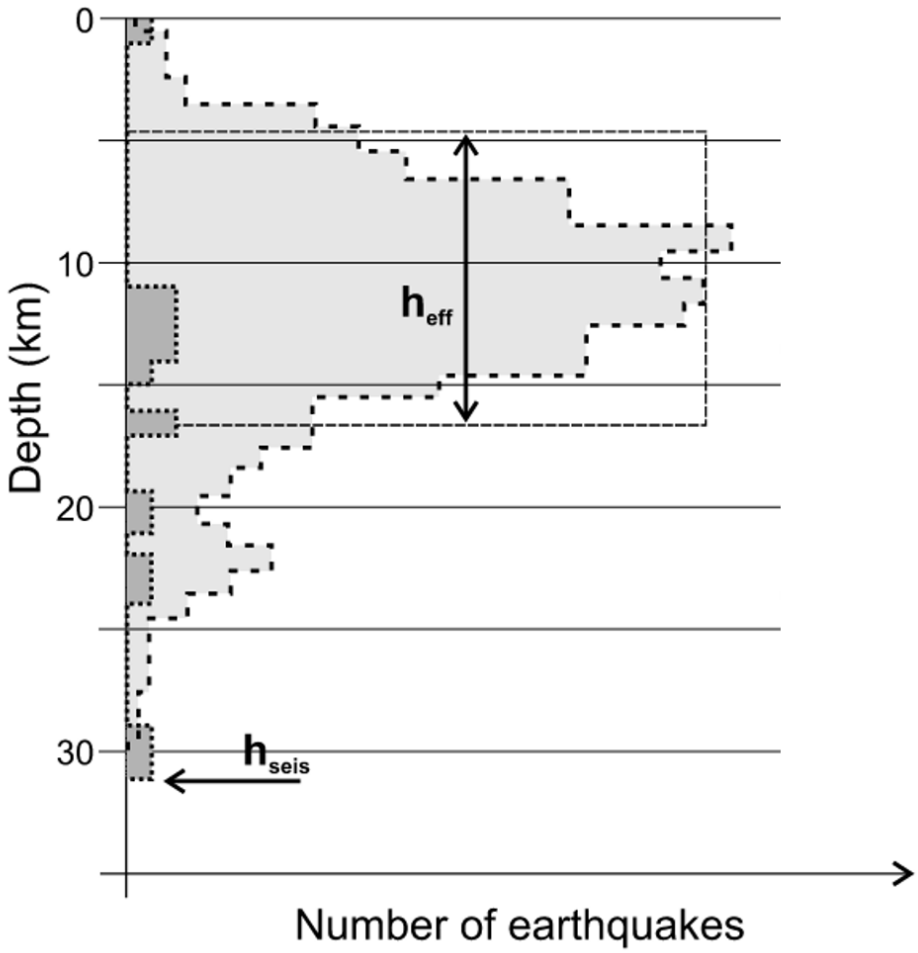

Fig. 2.6: **Adapted from Mazzotti and Adams, 2005**: Earthquake depth distribution is illustrated in their example in the Charlevoix and West Quebec seismic zones respectively. Dashed and dotted lines depict the depth distribution of earthquakes in these zones. 'h_{eff}' and 'h_{seis}' denote respectively effective seismic thickness and seismogenic thickness.

The coefficient C_g is a geometric coefficient that depends on the orientation and dip angle (δ) of the fault plane accommodating the strain. Following Stevens and Avouac, 2021, for dip-slip faults with uniaxial compression, $C_g = 1/(sin(\delta)cos(\delta))$. A dip angle of 45° is associated with a geometric coefficient of 2, a value adopted by the Working Group on California Earthquake Probabilities, 1995 and Savage and Simpson, 1997, as well as in a significant portion of the literature (e.g., Ward, 1998a; Jenny et al., 2004; Bird and Liu, 2007; D'Agostino, 2014). In their recent investigation of the Himalayan region, Stevens and Avouac, 2021 incorporate two values, corresponding to dips ranging from 45° ($C_g = 2$) to 15° ($C_g = 4$), to accommodate the presence of low-angle thrust faults in the area. This parameter is rarely explored in the estimation of geodetic moment rates.

We have thus far explored the geodetic and seismic datasets and calculation of moments. Now, our focus shifts to theoretical framework establishing connection between these two quantities.

2.4 Theoretical framework: Establishing the connection between geodesy and seismicity

In this section, we will present the major models that serve as the foundation for comparing seismicity with geodesy, forming the basis of the scientific literature on this subject. Additionally, we will highlight the assumptions underlying these analyses, facilitating a discussion on their validity in Section 2.5.2.

2.4.1 Elastic rebound theory

The triggering of earthquakes is a complex process involving mechanisms that generate both millimeter-scale and multi-kilometer-scale ruptures. As presented in figure 2.7, during the interseismic phase, loading occurs at asperities present on the superficial part of the fault, which remains locked by friction. The deformation in the vicinity of the fault is characterized by a specific shape in surface which correspond to an arc-tangent in the case of a strike slip fault in a homogeneous elastic half space model, has presented in figure 2.7b. Earthquakes occur when the accumulation of interseismic deformation reaches a critical stress level (σc) that surpasses the threshold of friction along a fault. It releases the stored-up stress. This phase is known as the coseismic phase. Once the released energy becomes too low to sustain

rupture propagation, the sliding stops, and the system begins to accumulate stresses again. Some deformation occurs in the vicinity of the rupture zone just after an earthquake. This last phase is known as the post-seismic phase.

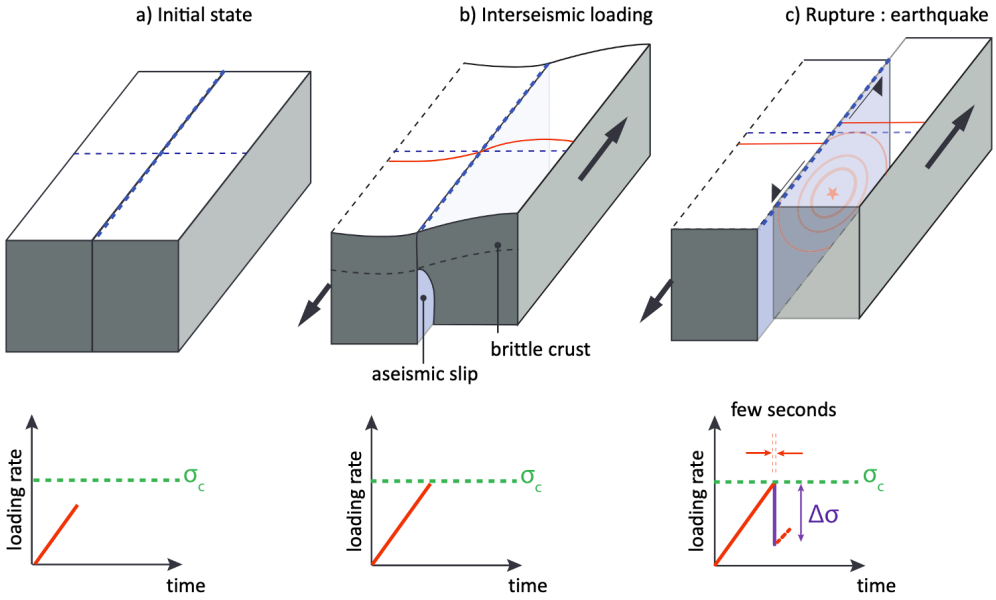

Fig. 2.7: **Translated from Reverso, 2015** : Simplified diagram of a classical seismic cycle. The fault plane (blue) is represented on the surface. Over time, the present forces induce displacement (interseismic displacement) affecting the area and a portion of the fault, but it remains locked at the brittle crust level. When the forces become too intense, an earthquake occurs (red star) and propagates along the fault, generating displacement along the fault (co-seismic displacement) accommodating the subsurface movement.

In this thesis, we focus on two measurable observation that characterized this seismic cycle : firstly, the seismic waves characterizing the co-seismic phase, and secondly, the permanent interseismic regional displacement measured by GNSS (or InSAR). Within the existing literature, the link between these two observations is generally rooted in the elastic rebound theory, that has been developed following the geodetic study of the 1906 California earthquake, by Reid, 1910. They propose that the surface deformation on both sides of the associated fault resulted from the earthquake. In essence, this theory postulates that an earthquake releases the accumulated elastic strain over the long term preceding its occurrence.

Several hypothesis (hereafter enumerated as Hn) are necessary to apply this theory effectively.

H1: The interseismic velocities recorded extracted from geodesy are representative of the region. This implies that the record by GNSS is sufficiently long to ensure

reliability, and their distribution sufficiently dense to provide a comprehensive understanding of the deformation in the area.

H2: The crust's rheology can be conceptualized by an homogeneous elastic layer of a certain thickness (approximately 15 km in the figure 2.8) overlaying a ductile layer represented as the lower crust. The deformation accumulates in this elastic segment and is subsequently released seismically.

H3: Inter-seismic loading remains stationary through time and the period of measurement is not affected by major transient motion.

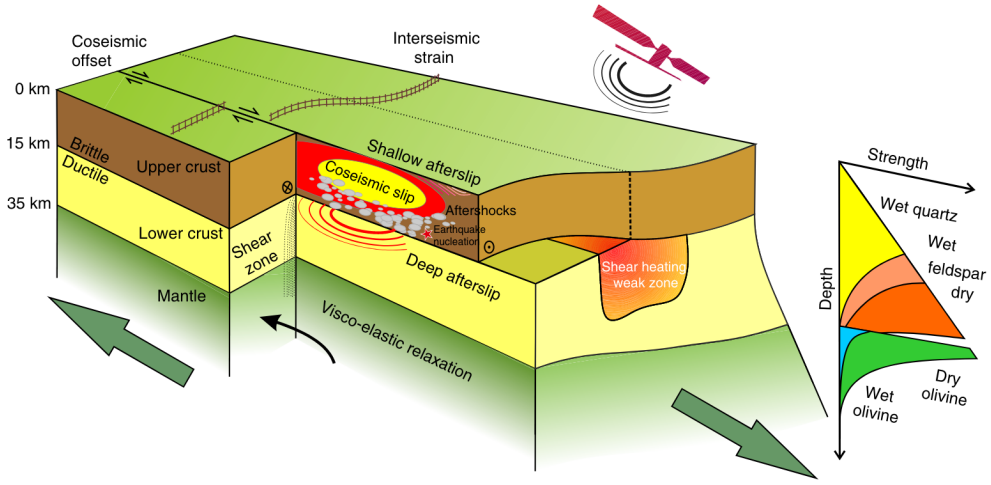

Fig. 2.8: **From Eliott et al. 2015**: Conceptual cartoon of deformation in the crust and uppermost mantle. Satellite geodesy offers the opportunity to measure the complete earthquake cycle: first, coseismic slip in the seismogenic upper crust, its relationship with aftershocks and fault segmentation; second, postseismic deformation localized on fault structures as shallow and deep afterslip, or more widely distributed through the ductile lower crust and upper mantle flow as viscoelastic relaxation; and third, interseismic strain accumulation across fault zones between earthquakes.

If we look in the vicinity of faults, this theory has evolved over time and enables monitoring of where and when faults are likely to break.

2.4.2 The elastic dislocation theory

The aim is to examine how the field of deformation can be linked to the mechanical properties of faults at depth. Tectonic geodesy has facilitated the development of models illustrating the evolution of slip on faults during the different stages of the seismic cycle, with the widely utilized model being the elastic dislocation theory (Avouac, 2015).

This approach stems from the observation of disparities between velocities recorded near the fault and the far field velocities, often considered as the plate boundary velocity (plates motions). Faults can either be locked by friction at asperities present on the superficial part of the fault, or exhibit aseismic slip and the ratio between fault creep and fault velocities is interpreted in terms of fault locking.

In literature, a widely adopted method to interpret this concept involves defining a coupling coefficient. The interseismic coupling coefficient X_i is determined as the ratio of the slip rate deficit during the interseismic period to the long-term slip rate.

$$X_i = 1 - \frac{v_{creep}}{v_{plate}} \tag{2.33}$$

with v_{creep} the velocity of the creep along the fault and v_{plate} the long term velocity of the tectonic plate. This coefficient serves as a quantitative measure of the degree of locking within the fault zone. A value of $X_i = 1$ indicates a fully locked patch, while $X_i = 0$ represents a patch exhibiting full creep at the plate convergence rate.

The concept of 'fault coupling' has emerged, describing the ratio between fault creep and and long term fault velocity along the fault. Coupling typically signifies a state of no or low current slip. If a fault is completely locked, it can be described as "coupled". Conversely, if a plate boundary fault is creeping at the long-term plate convergence rate, it is regarded as "decoupled". Fault segments that creep at a rate slower than the plate convergence rate are categorized as "partially" coupled (Wang and Dixon, 2004).

During the interseismic phase, loading occurs at asperities present on the superficial part of the fault, which remains locked by friction. Earthquakes occur when the accumulation of interseismic deformation reaches a critical stress level that surpasses the threshold of friction along a fault.

The illustrative figure 2.9, as presented in Avouac, 2015, delineates a comprehensive representation of this coefficient, employing the instance of a fully locked subduction zone. As demonstrated in panel a), the interface is observed to be locked within a thickness (z_d), characterized by a coupling coefficient of 1. At farther depths, the

subduction interface is creeping at the plate convergence rate, corresponding to a coupling coefficient of 0. This frictional profile is reflected in the velocity profiles showcased in panel b), displaying the interseismic phase (depicted in blue) that counterbalances the coseismic and post-seismic displacement represented in red.

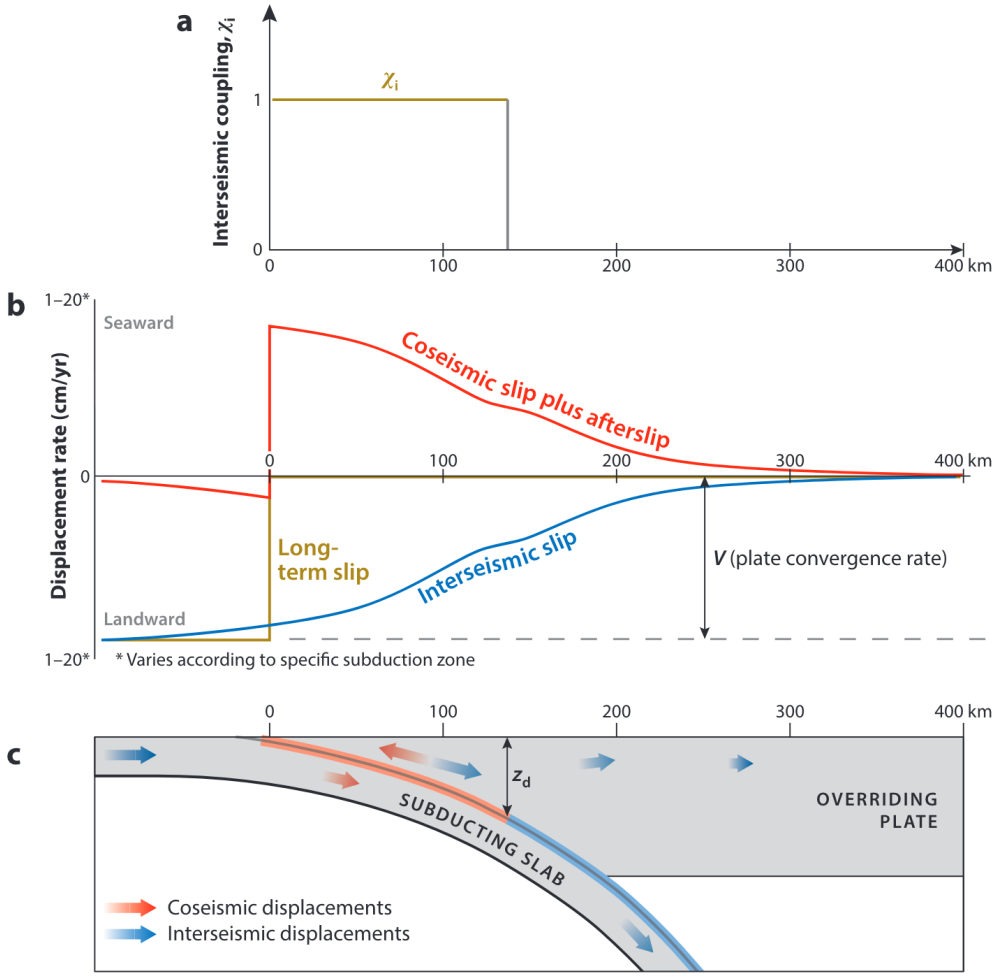

Fig. 2.9: **From Avouac, 2015**: Simple two-dimensional model of the seismic cycle on a subduction zone. The model assumes that, in the long run, plate convergence is entirely absorbed by slip along the subduction interface (the so-called megathrust). (a) Interseismic coupling. (b) Displacements at the surface. The blue line represents the theoretical surface displacement rate relative to the stable overriding plate. The dark yellow line represents the long-term surface displacement rate. The difference between the two curves, depicted by the red line, represents the contribution of transient slip events. (c) Displacements at depth, indicated by red arrows (coseismic) and blue arrows (cumulated over the interseismic period). The shallower portion of the megathrust, highlighted in red, is assumed to slip only during transient slip events (interplate earthquakes, afterslip, or slow slip events) and is fully locked during the interseismic period between these transients ($X_i = 1$ in panel a). The deeper part of the interface (beyond depth z_d), highlighted in blue, creeps at the plate convergence rate, V ($X_i = 0$ in panel a).

Since the coupling coefficient is often interpreted in terms of the frictional state on the fault interface, it is commonly utilized as a proxy for the mechanical properties of the fault interface, highlighting areas or patches exhibiting either rate-strengthening, which inhibits rupture, or rate-weakening, which facilitates the propagation of rupture (Avouac, 2015). The presence of rate-weakening patches, also known as 'asperities', is a widely utilized method for identifying regions where the next earthquakes are most likely to occur, providing valuable insights into their potential magnitudes that can be used to estimate the seismic hazard.

What has been explained earlier is applicable to a known fault where deformation is concentrated. In areas of low deformation, this approach becomes obsolete (unknown or insufficiently active faults, distributed deformation, etc.). In such cases, the approach used is to perform a moment balance at the regional scale, utilizing the 'moment conservation principle', as we will present in the next point.

2.4.3 Moment Conservation Theorem

The concept of moment conservation has been utilized since 40 years (Molnar, 1979). It directly stems from the elastic rebound theory (Reid, 1910) and posits that the accumulated strain corresponds to an elastic potential energy budget within the seismogenic crust. This approach asserts that the rate of elastic strain accumulation should be equal to the rate of strain release during earthquakes.

It implies that the release seismic moment should be equal to the accumulated moment measured by geodesy (accumulated in the elastic part of the crust, measurable at the surface through interseismic GNSS velocities). However, it is imperative to first scrutinize the conditions under which this equivalence holds and the parameters influencing this correlation.

Let us consider the hypothetical case of an ideal polygon situated on a continental crust satisfying H1, H2, and H3 (i.e., GNSS representative of the deformation, a crust well-modeled by an elastic layer overlying a more ductile layer as represented in Figure 2.8, interseismic loading stationary). We can expect the moment budget to be balanced if the following hypothesis are also validated:

H4: The considered region must be consistent from a seismotectonic perspective. It should be sufficiently large to avoid being affected by deformation signals in the direct vicinity of faults and should form a coherent unit from a tectonic viewpoint.

H5: The seismic moment must be representative of the interseismic phase of the seismic cycle.

In essence, as in this thesis, we will focus on a heterogeneous zone ranging from high-activity areas (Turkey, Greece) to lower-activity zones (as northern Europe), by comparing geodetic and seismic moment rates. The following section will present results from the comparison between geodesy and seismicity. Initially, we will elaborate on studies demonstrating agreement between the two datasets in high-activity regions, followed by an examination of studies indicating disagreement, especially in low-to moderate activity areas.

2.5 Comparisons between geodesy and seismology for earthquake potential evaluation

In this section, we will cover several aspects. Firstly, we will focus on areas of higher activity, revealing that numerous studies have demonstrated agreement between data derived from seismicity and geodesy. Following this, we will delve into the persisting challenges in systematizing their use, particularly in regions of lower deformation. We will preferentially focus on areas outside of Europe. This choice is made as we plan to present a synthesis on active deformation and seismicity in Europe in Section 3.1.

2.5.1 Agreement between seismicity and geodesy in regions with high seismic activity

Time and space-dependent approach: When geodesy provides insights into potential locations and timing of future seismic events thanks to interseismic coupling calculation

Let's first focus on high-activity zones, which are well-monitored and have known faults. In this case, we will see that the use of geodetic data provides information on potential locations and timing of future seismic events on the fault zone.

1. Pioneering studies in the 1980s.

In the 1980s, pivotal investigations marked the genesis of research in seismic patch identification. One notable study in California assessed interseismic strain by measuring variations in length along trilateration lines near Parkfield along the San Andreas Fault, interpreted as a locked segment (Harris and Segall, 1987). Concurrently, Savage, 1983 contributed significantly to establishing a methodological framework for studying subduction zones during this era.

2. Evolution of methods illustrated with the example of the Main Himalayan Thrust.

The Main Himalayan Thrust (MHT) in Nepal, forming the boundary between the Eurasian and Indian plates, serves as an exemplary case to illustrate the evolution of techniques. It has been extensively studied because it exhibits an exceptionally high seismic hazard, notably highlighted by the 2015 $M_W 7.8$ Gorkha earthquake

(Avouac et al., 2015) and the 1950 $\sim M_W 8.7$ Assam and 1934 $\sim M_W 8.4$ Nepal-Bihar earthquakes (Chen and Molnar, 1977).

Historically, the use of interseismic coupling facilitated the initial identification of potential seismic patches, evolving and improving over time. Studies by Pandey et al., 1995; Bilham et al., 1997; Bilham et al., 2001; Ader et al., 2012; Stevens and Avouac, 2015 and Bilham, 2019 provide early evidence of detecting asperities using geodetic and seismic data in the region. Their work emphasizes the necessity of large-magnitude earthquakes.

Subsequently, methods for evaluating maximum magnitudes were established (see part 2.6 for the methodology), stressing the need for earthquakes exceeding magnitude 8 (Ader et al., 2012) , and Stevens and Avouac, 2016 argue for millennial occurrences of $M_W 9$ events to counterbalance the accumulated slip deficit. Then another approach was proposed by Michel et al., 2021 by incorporating physic based model on the fault slip. They obtained a frequency of $M_W 8.7$ earthquakes every 200 years.

3. Method Validation.

This section highlights the efficacy of the method through:

- The increase in earthquake probability with the level of coupling as demonstrated by Kaneko et al., 2010 who developed a numerical simulation model showing that the probability of generating an earthquake is a function of coupling on a locked patch.

- Concrete examples of identifying patches predicting subsequent earthquakes. Findings by Moreno et al., 2010 revealed a correlation between the slip during the Maule earthquake and the pre-seismic locking of the Andean subduction zone (as also observed by Loveless and Meade, 2011 in Japan and by Métois et al., 2016 in Chile for example). Furthermore, Protti et al., 2014 demonstrated that the 2012 earthquake in Costa Rica ruptured a fault patch previously identified through geodetic observations.

Figure 2.10, adapted from Moreno et al., 2010, presents the interseismic coupling depicted in panel a), observed during the decade preceding the Maule earthquake. Panel b) illustrates the distribution of pre-seismic locking in the study area, represented by isolines, superimposed on the coseismic slip distributions computed from GNSS inversion for the 2010 Maule earthquake. Notably, the figure shows a strong correspondence between the coupling and the co-seismic slip distribution,

revealing that a significant portion of the slip of the earthquake occurred in regions characterized by high coupling coefficients.

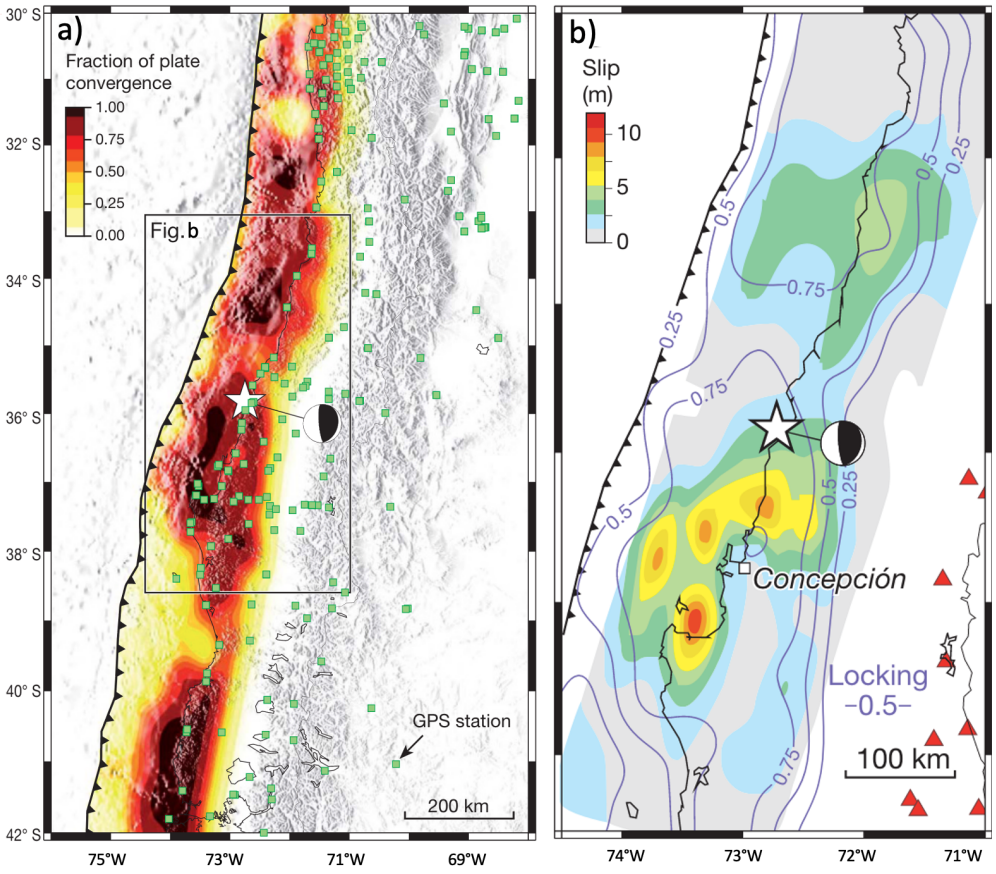

Fig. 2.10: **Adapted from Moreno et al., 2010**: Correlation between interseismic coupling and co-seismic Slip prior to the 2010 Maule Earthquake. a) Distribution of coupling coefficient along the Andean Subduction Zone Megathrust before the 2010 Maule Earthquake, with the epicenter (white star) and focal mechanism (beach ball) of the 2010 event. b) Pre-seismic locking distribution (isolines) superimposed on preliminary coseismic slip patterns of the 2010 Maule earthquake.

4. Global Application to Known Faults. The practice of estimating interseismic coupling and its spatial variations, with the goal of identifying asperities, comprehending the nature of coupling, and pinpointing regions that may harbor future earthquakes, has found extensive application across various renowned faults worldwide.

These studies have been particularly important for subduction zones where populations reside on the overriding plate. Notable research contributions include Lundgren et al., 1999 for Costa Rica, Sagiya, 1999, Mazzotti et al., 2000 in Japan, Chlieh et al., 2004; Métois et al., 2012; Métois et al., 2013b; Métois et al., 2013a in Chile, Chlieh et al., 2008 in Malaysia, Cross and Freymueller, 2007 for the Aleutian subduction zone (Alaska), Chlieh et al., 2011 for the Central Andes, Hsu et al., 2016 in the Philippines, and Mariniere et al., 2021 in Ecuador.

Similar studies have been conducted on other significant faults within intracontinental regions, such as Western India (Szeliga et al., 2012) and Taiwan (Thomas et al., 2014).

Collectively, these studies underscore the widespread adoption and utility of this method.

These studies are applicable in cases where we have a well-defined and monitored fault zone. In the next section, we will explore how geodesy is employed when fault traces are unknown or when the GNSS network is not dense enough to highlight coupling patches.

Time-independent approach for earthquake potential evaluation : geodesy utilized as a proxy for long-term seismic behavior

If we assume that fault traces in the area are inaccessible, what alternative parameters can be utilized to leverage geodesy and enhance our understanding of long-term seismic behavior?

The insight provided by Figure 2.11 reveals that, in two highly active regions, Turkey (panels a to c) and California (panels d to f), areas with the highest strain rates (exceeding 200 nanostrain per year) align with regions exhibiting seismic moments greater than $10^{17} N.m.km^{-2}$ (calculated from the cumulative earthquake moments in the catalog since 1000 AD). These locations also display a correlation with seismicity rates, as indicated by the 'a' values. It is important to note that this zoning correlation is a first-order approximation. Upon closer examination, variations become apparent (for instance, the highest strain rates are observed in the northern fault zone in Turkey, while the zones with the highest seismic moments and earthquake rates are situated in the southern zone).

This figure, illustrating a correlation between geodetic strain rates, seismic moment, and seismicity rates in active regions, underscores that several alternative parameters can be effectively employed, as we will further explore below.

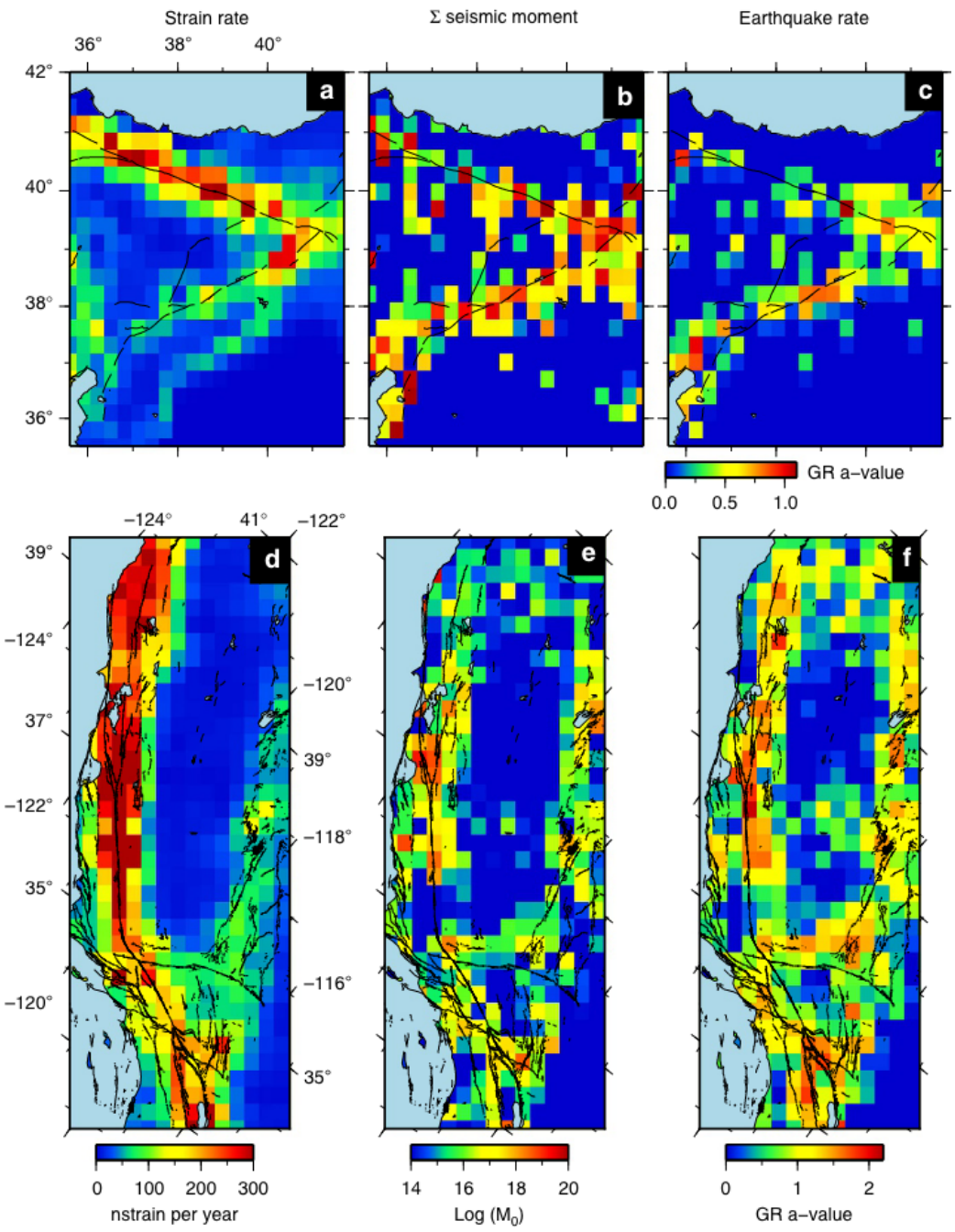

Fig. 2.11: **From Elliott et al., 2016** : Comparison of geodetic strain rate against seismic moment and earthquake rate. (a) Second invariant of the horizontal geodetic strain-rate tensor for Eastern Turkey, showing localized strain on the North and East Anatolian Faults (NAF and EAF respectively). Active fault traces are denoted by black lines. (b) The log of the summed seismic moment since 1000 AD, derived from declustered historical and instrumental seismic catalogue and calculated at 0.25° resolution. (c) The Gutenberg-Richter a-value calculated at the same resolution from the same data. d–f show the same for California and the San Andreas Fault Zone, with seismic parameters derived from declustered UCERF3 seismic catalogue. Fault traces show structures assumed active since the late Quaternary from the USGS. For both Eastern Turkey and California, there is a clear relationship between geodetic strain-rate and both seismic moment and earthquake rate.

1. Correlation between strain rate and seismicity rate

Some authors compare geodetic and seismic data by examining seismicity rates and geodetic strain tensors, obtaining a correlation between the two values in active areas:

- Shen et al., 2007 in California conducted a comparison between geodetic strain rates and seismic rates, observing a significant correlation when considering only events of $M_W 5$ and above.
- Zeng et al., 2018 in California studied the relationship between strain rates inferred from GNSS data and seismicity, revealing a strong correlation suggesting a close connection between the two.
- Stevens and Avouac, 2021, in the Himalayas, compared seismicity rates and geodetic strain rates in different zones defined by ranges of homogeneous geodetic strain rates. They demonstrated a strong correlation, analyzing it both linearly and non-linearly.

2. Comparison of seismic and geodetic strain rate tensors

Other studies indicate that in certain highly active regions, the deformation tensors derived from geodetic measurements and those computed from seismicity (using the Kostrov summation, 1974) could be compatible in terms of both orientations and magnitudes:

- Jenny et al., 2004 conducted a study in the Eastern Mediterranean, where they compared the horizontal seismic strain rate field, recorded over a 500-year historical catalog, with the tectonic strain rate field measured geodetically. They found that the two strain rates exhibit very similar characteristics in style across all magnitude ranges. With the exception of the region along the Hellenic Arc, the amplitudes of the strain rates are also consistent, further enhancing the coherence between the geodetic and seismic measurements in the area.
- Masson et al., 2004 in Iran compared strain tensors obtained from GNSS and those derived from seismicity, distinguishing seismic and aseismic deformation. They found that in areas of significant deformation, the two tensors were collinear. Moreover, their magnitudes were compatible in northern Iran (Geodetic/Seismic ratio between 30% and 100%). Note that other zones, notably in southern Iran, exhibited significantly higher geodetic strain rates compared to seismic strain rates, which will be further discussed in a subsequent point (2.5.2).

- Middleton et al., 2018 analyzed seismic and geodetic strains in the Ordos Plateau in China, revealing a strong agreement in both orientation and magnitude of strain.

This comparison reveals that the assumption of equality between seismic and geodetic strain measurement appears to be validated in specific active zones. Consequently, it suggests that geodetic deformation measurements may provide information consistent with seismicity, enhancing the estimation of seismic hazard.

3. Nearly balanced moment budget in active zones

In the last section we presented the potential of agreement between geodetic and seismic strain rates, here we want to emphasize studies that have compared seismicity and geodesy in term of moment. In active zones, numerous studies conducting moment balances have demonstrated that seismic and geodetic moments are of the same order of magnitude. We can note here that many studies have shown that the geodetic moment can be significantly greater than the seismic moment, as we will detail in Section 2.5.2. Here, we focus only on studies that demonstrate agreement between these two values or highlight a slightly higher geodetic moment compared to the seismic moment, attributing the minor moment deficit to potential forthcoming major earthquakes. Comparing these studies is challenging due to the evolving methodologies used to compare geodetic and seismic data over time. The aim here is just to provides some examples. Notably, these studies encompass various active zones worldwide.

In North America:

- Field et al., 1999 found that adjusting catalog b values, magnitude-moment relations, or magnitude estimates in California could match geodetic and catalog moment rates.

- Ward, 1998a in California compared geodetic and seismic moments, suggesting that the divergence between the two values could be attributed to an impending high-magnitude earthquake, thereby potentially aligning the two.

- Hyndman et al., 2003 studied crustal earthquakes in the western United States, estimating occurrence rates of large future earthquakes from geodetic moments, indicating the existence of plausible scenarios.

- Mazzotti et al., 2005 in Eastern North America reported a ratio of approximately 1 from GNSS to earthquake catalog moment rates.

- Pancha, 2006 in the Basin and Range Province, USA, computed seismic moments from seismicity catalogs and compared them with geodetic moments. They showed good agreement between the two quantities, accounting for uncertainties.

In other parts of the world:

- Déprez et al., 2013 conducted a comparison between seismic moments (integrated from recurrence models) and geodetic moments in the East African Rift in Africa. They discussed potential causes for differences, indicating that the Western Rift exhibited a $\dot{M}_{0G}/\dot{M}_{0S}$ ratio close to 1, while the slight prevalence of geodetic moment over seismic moment in the Malawi Rift could be explained by plausible future earthquakes.

- Palano et al., 2018 analyzed the ratios between seismic and geodetic moments in northern Iran. They found that in the northern Zagros and on the Turkish-Iranian Plateau, a moderate to large fraction of the deformation measured by the geodetic moment is released seismically, although this was not the case in other parts of the study region as we will see later (in section 2.5.2).

- Grunewald and Stein, 2006 in Japan reported a ratio of approximately 1 from GNSS to earthquake catalog moment rates.

These studies collectively underscore the importance of comparing geodetic and seismic moments. From these examples, it is evident that the correspondence between seismic and geodetic moments has been demonstrated in several active zones worldwide. However, it is noteworthy that, even in these high deformation zones, many authors (sometimes the same) have found differences, notably with a geodetic moment exceeding the seismic moment. We will now review the challenges that have been emphasized in the literature and need to be overcome.

To conclude, we have seen that in high-activity zones, geodesy is used to provide information about potential locations for future seismic events along fault zones. Additionally, at a regional scale, numerous studies have highlighted similar seismic and geodetic strain tensors, both in terms of orientation and amplitude. Moreover, in many regions, seismic and geodetic moments are of the same order of magnitude. In the next section, we will explore the persistent challenges in systematically implementing their usage, particularly in low-strain areas.

2.5.2 Remaining challenges, particularly in low strain/seismicity zones

Numerous active regions worldwide exhibited geodetic and seismic moments of comparable magnitudes, providing encouragement for utilizing this technique as a proxy for future PSHA studies. However several counterexamples exists with a discrepancy between these two quantities (for example Ojo et al., 2021, Sparacino et al., 2020 in most of the zones considered in Maghreb, Ward, 1998a in Turkey, Chousianitis et al., 2015 for most of the Aegean zone, Clarke et al., 1997, Masson et al., 2004 for southern Iran, Mazzotti et al., 2011 for Western Canada). In these cases, authors usually emphasize that the study area did not meet one of the initial assumptions outlined in the section 2.4. In this section, we try to analyze the challenges associated with each of these assumptions.

H1: Is the GNSS always representative of the deformation ?

Several challenges persist in understanding the uncertainties associated with GNSS data, propagating throughout the chain leading up to geodetic moment calculations. Firstly, in regions of low deformation, extracting a signal out of the noise is challenging. According to Mazzotti et al., 2005, the uncertainties associated with GNSS are typically of the same order of magnitude as the deformation signal in areas of low deformation (that they defined as strain inferior of $10^{-10}/yr$). Furthermore, a prolonged acquisition period may be necessary to stabilize the signal over time, as demonstrated by Walpersdorf et al., 2015, who showed that sub-millimeter velocities in the southwestern Alps converged after a 15-year acquisition period.

Additionally, the velocities derived from GNSS undergo spatial inversion to be analyzed in terms of strain rates. A well-distributed spatial coverage is essential, which can be challenging, particularly when a portion of the region is offshore. For instance, in their study on the Betics and the Maghreb, Sparacino et al., 2020 highlighted a limitation in their interpretation of the areas north of Algeria due to the exclusion of offshore (highly active) deformation in that region. The impact of this inversion is often absent from the analyses in various studies. Only a few authors (Mazzotti et al., 2011; D'Agostino et al., 2009) have investigated the influence of smoothing coefficients on geodetic moment results, showing that this impact is not negligible. However, we have not found any studies that comprehensively discuss all stages of the inversion chain on the moment budget.

H2: Can the crust be accurately represented by a simple elastic layer overriding a ductile layer?

The hypothesis of an elastic layer with a thickness H, accumulating deformation and situated above a ductile layer (see Figure 2.8), is a key assumption that is frequently debated in regions exhibiting a seismic moment deficit. Many authors interpret this difference in terms of 'aseismic deformation' (for instance, Elliott et al., 2016; Sparacino et al., 2020, for the Betics and Morocco; Ward, 1998b, in Turkey; Chousianitis et al., 2015, for the western Gulf of Corinth in Greece; Masson et al., 2004, for the Zagros region in Iran; Mazzotti et al., 2011, for Western Canada) which can be attributed to several processes (viscous flow in the lower crust, asthenospheric mantle, creep or afterslip on faults, magmatic deformation, etc.), as we will discuss here.

Under the assumption of non-neglectable aseismic deformation, the conservation theorem of moments can be rephrased as follows:

$$\dot{M}_{0S} = \alpha \dot{M}_{0G} \tag{2.34}$$

with α as the proportion of aseismic deformation.

The aseismic deformation assumption is due to several reasons. First and foremost, as discussed in section 2.3.2, estimating the seismogenic layer's thickness is complex and necessitates a well-constrained catalog where the earthquakes depths are precisely known, which is not always the case. Since the method and definition of this layer vary among authors, this leads to different results and considerable uncertainty in estimating this parameter.

Secondly, the interpretation of the crust as a purely elastic layer has been a subject of discussion, suggesting that it might be an oversimplified representation (Burov, 2011). Certain geological contexts are associated with specific rheologies, leading authors to question the assumption of a purely elastic crust. For example, in Malawi, Déprez et al., 2013 argue that the moment deficit in the Main Ethiopian rift is due to potential volcanic activity. Similarly, in Iran, Palano et al., 2018 argue that the formation of the Hormuz evaporites is responsible for aseismic deformation in the associated zone. Similar arguments are put forth by numerous other studies. Some tectonic contexts are almost systematically associated with a significant moment deficit interpreted as aseismic deformation, such as those affected by viscoelastic mantle flow (as Glacial Isostatic Adjustment (GIA)) (we will detail in the next point), by volcanic activity or by certain lithology (evaporites, smectites, serpentinites).

Thirdly, even in areas where the geology can be reasonably approximated with a simple crustal model (Figure 2.8), moment may be released in the fault zone in an aseismic manner in the form of creep (Rosen et al., 1998), afterslip, or slow slip events (Behr and Bürgmann, 2021). This moment dissipation is not always accounted for in the seismic moment calculation and thus leads to a moment deficit. Although this type of long-term creep has been proposed as an explanation for the difference between GNSS and seismic rates in some areas (Working Group on California Earthquake Probabilities, 1995; Masson et al., 2004; Barani et al., 2010), most studies remain susceptible to limitations due to catalog completeness or geodetic strain rate resolution, which makes it difficult to obtain accurate quantitative resolution of seismic moment under these conditions.

Fourthly, the alignment between the orientation of the seismic and geodetic strain tensors is observed in many contexts, validating the assumption that the measured deformation is representative of the stress field on the fault (Rontogianni, 2010; Middleton et al., 2018). There is a general agreement in both orientation and magnitude between the time-averaged seismic and geodetic strain rate tensors, in regions large enough where short-term variations in seismicity rate are not significant (Ekström and England, 1989). Conversely, the crust breaks in areas of pre-existing weaknesses, i.e., fault zones, which might have originated from ancient tectonic processes. The orientation of faults relative to the stress field determines whether they are in a favorable stress regime for rupture. For instance, Damon et al., 2022 investigation in the Paris Basin, a region characterized by minimal deformation, revealed that the considered GIA could induce significant stress perturbations capable of potentially reactivating faults. However, it was observed that known fault structures in the eastern Paris Basin are more likely to be immobilized when integrating these stress perturbations into the ambient crustal stresses. The pre-existing structures within the Earth's crust can significantly influence the release of aseismic deformation.

The approximation of the zone's geology by a simple elastic layer is one of the greatest source of uncertainty in the geodetic moment calculation and would benefit from better constraints. Some solutions have been proposed in the literature.

Firstly, some authors (Bird, 2004; Bird and Liu, 2007; Bird et al., 2010) propose calculating the seismogenic thickness globally by introducing a 'coupled thickness'. They separate plate boundaries into different types and calculate global geodetic strain rates and associated seismic moments from seismicity catalogs considered representative due to their global scale and thus constrained by numerous earthquakes. This approach allows the resolution the coupled thickness. Their estimates have been widely used in the literature (Carafa et al., 2017; Rong et al., 2016; Bird

and Kreemer, 2015). However, some issues persist, as even if seismicity catalogs are more comprehensive at a global scale, are they complete and representative of the long-term seismic cycle (especially in intracontinental environments)? Moreover, authors linking the percentage of aseismic behavior to the local geology show that a local parameter's contribution can be significant (e.g., evaporite formation, volcanism). Working on a global scale, while very interesting generally and in the context of creating global PSHA maps, may not be a universal resolution to aseismic deformation issues.

Another occasionally discussed solution is regional rescaling. This was the approach taken by Ward, 1994 and Lotfi et al., 2022. In essence, they solve equation 2.34 to obtain the percentage of aseismic on a regional scale. Once the proportion of aseismic behavior is quantified, they discuss local variations.

Finally, another branch of research is crustal deformation model, aiming to consider precisely the rheology of rocks in a given area. Takeuchi and Fialko, 2012, for instance, proposed a deformation model along the San Andreas Fault to better understand the seismicity of this area. Shen and Bird, 2022 also achieved promising results by comparing the rates of seismicity from a crustal deformation model constrained by fault data, GNSS, and crustal stress orientation with the current seismic model.

In conclusion, understanding what occurs in the deforming Earth's crust is a primary source of uncertainty in establishing the moment budget.

H3: Is the interseismic loading always stationary ?

The notion that interseismic strain remains stationary finds support in the congruity of geodetic and geological evaluations of slip rates on various continental faults (Meade et al., 2013).

However, there are instances that contradict this hypothesis. We will cite three examples hereafter :

- First, Peltzer et al., 2001 highlighted that the strain accumulation rate in the East California Shear Zone is currently three times its average, whereas the Garlock fault exhibits no present signs of strain accumulation, despite its average slip rate of $7\,\mathrm{mm}\cdot\mathrm{yr}^{-1}$ over the Holocene. This illustration implies that interactions between faults could induce notable temporal variations in strain rates.

- Another aspect to consider is viscoelastic relaxation following an earthquake, which can extend over several decades Wang et al., 2012 (e.g., over 60 years in the case of the 1960 Valdivia earthquake in Chile Wang et al., 2007). The impact of this phenomenon can potentially extend to regional scales (Chéry et al., 2001).

- Similarly, the case of GIA presents a pertinent example. Craig et al., 2016 have shown that the reverse-faulting earthquakes (described by Arvidsson, 1996) occurred in Scandinavia during a period of extensional strain, suggesting that the elastic lithosphere might accumulate strain over long periods.

Stevens and Avouac, 2021, proposed a sanity-check to assess whether the interseismic loading is stationary in their study of the Himalayas. They stated that "Earthquakes release elastic strain built up over a duration much longer than the period covered by geodetic measurements." As a result, temporal variations in the strain rate tensor would manifest as geometric discrepancies between geodetic strain and coseismic strain. Validating the geometric consistency between these tensors could confirm the stationarity of interseismic loading.

H4: At what spatial scale should we integrate the strain rates?

The calculation of strain over zones is motivated by the observations of Amelung and King, 1997, who demonstrate that strain release computed from earthquakes tends to follow the regional pattern of tectonic deformation when averaged over a regional scale. The geometry of the zones over which geodetic and seismic moments are compared varies between studies, integrating over grids (Ojo et al., 2021; Masson et al., 2004; Jenny et al., 2004) or polygons. Polygons are often defined based on criteria of tectonic coherence, such as "homogeneous spatial and temporal seismicity distribution; consistent tectonic and stress patterns; consistent GNSS strain rate style (and amplitude)" (Mazzotti et al., 2011). An alternative approach proposed by Stevens and Avouac, 2021 involves basing polygons on criteria of constant strain. The zoning used for strain integration varies depending on the approach, impacting the calculation of geodetic and seismic moments. Some studies have incorporated the impact of zone geometry on moment balance. Rontogianni, 2010, for example, investigated the compatibility between geodesy and seismicity on both grids and polygons in Greece. It would be beneficial to further quantify the impact of selecting specific zones in such studies.

H5: Is the seismic moment representative of the long-term seismic cycle ?

Earlier it was observed that there are different approaches to calculating seismic moment. Two major contrasting methods include using Kostrov summation on the catalog and employing recurrence models. Several authors have utilized both approaches to compare them (Palano et al., 2018; Ojo et al., 2021) and have found that the seismic moment computed using Kostrov sums is generally lower than that obtained from recurrence models. A limitation of using Kostrov sums is the incompleteness of seismicity catalogs over the considered time period, leading to an underestimation of the seismic moment. In contrast, considering recurrence models attempts to capture long-term seismicity (Palano et al., 2018). For authors relying on estimating seismic moment from recurrence models, a significant challenge is properly accounting for uncertainties, especially in integrating the behavior near M_{max}. Mariniere et al., 2021 demonstrated that the shape of the curve at high magnitudes and the values of M_{max} were the parameters that most influenced the seismic moment. Having representative models of long-term seismicity and its uncertainties is, therefore, a challenge in these studies.

Moreover, the majority of studies that uses the traditional approach of computing earthquakes recurrence model from Weichert, 1980 methodology (see 2.2), neglect the contribution of aftershocks. This is grounded in research, such as that conducted by Beauval et al., 2006, which quantified the contribution of aftershocks to seismic hazard. Their findings indicate that, on average, aftershocks contribute less than 5% to the probabilistic hazard, with an upper bound reaching around 18% in the Pyrenees region in France. However, Rollins and Avouac, 2019 noted that there is uncertainty about whether to decluster the instrumental catalog first, which method to use if so, whether declustering should yield a smaller b-value, and how this may affect the inferred long-term model. Another limitation has been pointed out by Stein and Liu, 2009 who showed that in intracontinental areas, a considerable portion of intracontinental earthquakes may constitute aftershock sequences originating from events occurring centuries ago. Stevens and Avouac, 2021 applied this argument in their study of the Himalayas, arguing that there might be clusters corresponding to aftershocks of main shocks that are not documented in the instrumental catalog they utilized. Consequently, these clusters are not eliminated during the declustering process. This may skew the average rate of small earthquakes, leading to an overall upward shift in the seismic curve.

Other works have proposed alternatives to incorporate aftershocks in such studies. Rollins and Avouac, 2019 developed moment-balanced synthetic catalogs including seismicity with aftershocks. Similarly, Marsan and Tan, 2020 proposed models that

utilize moment-balanced synthetic catalogs, which include aftershocks, indicating a promising avenue for research.

Traditionally, PSHA models are based on instrumental and historical seismic catalogs to compute recurrence models. However, this approach is limited in regions where the average recurrence interval is greater than the length of historical seismicity, as is the case in the majority of continental areas worldwide (Elliott et al., 2016). Consequently, the issue of whether earthquake catalogs are long enough to capture the long-term seismicity or not remains a crucial concern. Ward, 1998a argued that the completeness of a seismic catalog depends on the duration of observation and the regional strain rate, with regions experiencing slower strain requiring a proportionally longer observation period. He modeled catalog completeness using gamma distributions based on the ratio of observed seismic moment to geodetic moment, demonstrating that it would take between 200 and 300 years of seismic data to represent the long term seismicty in regions with a strain rate of $10^{-7}yr^{-1}$, similar to that of Southern California. Conversely, regions with a strain rate of 10^{-9} yr^{-1}, such as the Southeastern United States, would require over 20,000 years of seismic data to achieve a similar level of completeness. Similarly, Pancha, 2006 proposed introducing a factor that would indicate whether the catalog duration is sufficient to represent the seismic cycle based on the geodetic moment, defined as the product of the duration of the earthquake record, the area of the region, and the average strain rate, as estimated by space geodetic methods.

In conclusion, the methods used for calculating seismic moments, the behavior of recurrence models for high magnitudes, the consideration or neglect of aftershocks, and the representativeness of seismicity catalogs are significant limitations for seismic moments to accurately represent the long-term seismic cycle.

The particular case of areas affected Glacial Isostatic Adjustment (GIA), and other contexts impacted by visco-elastic deformation

In this section, we will delve into the specific case of Glacial Isostatic Adjustment (GIA) before extending our discussion to other types of context characterized by viscoelastic deformation. In contrast to the rest of this section, we will incorporate European examples to illustrate these concepts.

The GIA is a geodynamic process associated with glacial cycles. During a glacial period, substantial amounts of water are locked in the form of ice on continents, resulting in an overload on the continental lithosphere. This induces a large-scale

bending of this elastic lithosphere, which sinks into the underlying viscous asthenospheric mantle. The viscoelastic relaxation of the mantle–lithosphere system following the ice cap's melting leads to a movement, recorded in GNSS data, characterized by uplift velocities of several millimeters per year (up to 11 mm/year in Scandinavia for example). The maximum uplift rates occurs where the ice cap had its greatest thickness. Uplift rates decrease away from this central zone, and the uplifted area may be surrounded by a subsiding region (Nocquet, 2005). Horizontal velocities can exhibit a radial pattern, with velocities pointing outward from the zone of maximum uplift rates.

The regions influenced by GIA are characterized by a persistent prevalence of geodetic moment over seismic moment, representing a substantial order of magnitude disparity that cannot be solely attributed to data uncertainties, issues of catalog completeness or aseismic deformation (Ojo et al., 2021 in Canada, Mazzotti et al., 2011 for the western United States, James and Bent, 1994 in North America, Mazzotti et al., 2005 for western Canada, excluding the Charlevoix region, Keiding et al., 2015 for Scandinavia).

We found 4 hypotheses have been posited in scientific literature to elucidate this disparity.

First, James and Bent, 1994, conducted a comparative study in North America, contrasting strains derived from a GIA model with seismicity data. Their findings suggest that, in most instances, deglaciation appears to be unrelated to seismic activity. They offer two potential explanations. Firstly, they argue that the rapid and cyclical nature of post-glacial loading and unloading on a geological timescale could trigger crustal yielding under significant strains over prolonged time periods. Secondly, they propose that the orientations of strains originating from GIA do not seem aligned to amplify the observed deviatoric stress field.

Another hypothesis has also been raised in Fennoscandia, where Keiding et al., 2015 and Craig et al., 2016 have shown that contemporary seismicity likely releases both elastic strain accumulated from postglacial relaxation and ongoing tectonic strain. Consequently, the modern geodetic strain rate tensor may not be in alignment with the accumulated elastic strain available for release via seismic events.

Finally, one hypothesis highlights the role of the lithosphere's visco-elastic response to postglacial rebound as a primary source of aseismic strain (Mazzotti et al., 2011) due to viscous flow in the astheosphere.

It is noteworthy that other contexts characterized by large-scale viscoelastic mantle processes are also associated with aseismic deformation. For instance, the slab

detachment that occurred in the Vrancea region in Romania (Nemcok et al., 1998) exhibits significant post-seismic visco-elastic deformation, with substantial strain but a low occurrence of shallow seismic events. Another example is the case of the Alps. In the Alps, three tectonic processes can induce viscoelastic mantle deformation characterized by aseismic deformation: (1) Post-glacial rebound (Mey et al., 2016), (2) Erosion, where the removal of material (reduced weight) leads to isostatic adjustments, (3) Slab detachment.

In this section, we observed that geodesy can function as a reliable proxy for seismicity in high-activity areas. However, challenges persist in systematizing its use, especially in low-activity regions. The following section will delve into how geodesy is practically integrated into Probabilistic Seismic Hazard Assessment (PSHA) models.

2.6 How is Geodesy Practically Integrated into PSHA Source Models?

The use of geodetic data by various researchers in an attempt to better constrain the probabilities and locations of future seismic events has been previously discussed. The diversity of approaches in utilizing geodetic data to enhance the understanding of the seismic cycle mirrors the variety of ways it is integrated into PSHA source models.

It will be shown that numerous PSHA source models already incorporate geodetic data, typically as a proxy for the available long-term seismic energy. This incorporation serves to constrain fault slip rates and is also integrated into area source zone models. Additionally, some studies have suggested a more nuanced use of geodetic data in PSHA by incorporating coupling concepts into these models, as will be discussed subsequently.

2.6.1 To constrain fault slip rates

Geodesy provides precise information to constrain fault slip rates when combined with other data types such as geochronology and paleoseismicity (Elliott et al., 2016). It is frequently used in fault-based PSHA source models.

Its application in fault zones dates back several decades, with Molnar, 1979 establishing a relationship between fault slip rates and the available moment in the region, calculated from seismicity or geodetic data. Since then, various methods have been developed. One straightforward approach is to utilize the relative horizontal velocities between pairs of GNSS stations situated on opposite sides of the fault, positioned sufficiently far from the fault trace to minimize the elastic contribution from the locked fault segment (Beauval et al., 2014). Another commonly employed method involves the inversion of geodetic data using block models (Meade and Loveless, 2009).

Numerous PSHA models incorporate these data, including those by Field et al., 2014 in California, Petersen, 2014 covering other parts of the United States, Beauval et al., 2014 in Ecuador, and Basili et al. in press. for Europe (ESHM20).

2.6.2 At the regional scale, integration in area source zone model

The integration of geodetic data into PSHA models has a long history. Papastamatiou, 1980 discussed the general incorporation of crustal deformation data into PSHA models. Ward, 1994 then proposed the first PSHA source model based on geodesy, which combined seismological, geodetic and geological data in a recurrence model for forecasting earthquake frequencies in seismic hazard assessments. This proposition was subsequently integrated into the model put forward by the Working Group on California Earthquake Probabilities, 1995 for California.

How is this done? There are several possibilities. One major approach involves the development of hybrid models combining seismology and geodetic data. In such cases, seismic events constrain a part of the recurrence curve, while geodetic data anchors the other part. This is commonly achieved through the estimation of maximum magnitudes (M_{max}), which are challenging to determine (but it can also be used to constrain the a value in areas where M_{max} is well constrained). Various methods have been proposed in the literature, such as resolving the moment conservation equation and expressing M_{max} as a function of recurrence parameters. As already detailed in part 2.5.2, various factors can influence the uncertainties associated with this method, including the b-value, the choice of magnitude-frequency distribution, and the precise moment-magnitude definition used (Field et al., 1999). Nonetheless, the shape of the curve near M_{max} has the most significant impact on the derived M_{max} values (Mariniere et al., 2021).

This method of obtaining M_{max} has been extensively utilized in litterature. For instance, Main et al., 1998 in the UK used a mixture of geodetic and isostatic models

to constrain the magnitude-frequency distribution. Similarly, Koravos et al., 2003 constrained M_{max} for the Aegean region using tectonic moments and regional seismicity. Pancha, 2006 in the United States compared different forms of Anderson and Luco, 1983 equations to estimate M_{max}. Other studies, including Mazzotti et al., 2005 in Canada, Mohapatra et al., 2014 in northern India, and Stevens and Avouac, 2021 in the Himalayas, also relied on geodetic data to anchor M_{max} values.

Several comprehensive PSHA source models have been constructed based on the aforementioned approach. Rong et al., 2020 developed a hybrid PSHA model for China, which exhibited favorable alignment with previous PSHA models. Lotfi et al., 2022 introduced a novel PSHA model for Iran, also grounded on similar principles. Additionally, other hybrid models have been proposed, including Field et al., 2014 in California, Kastelic et al., 2016 in the Dinarides, Hodge et al., 2015 and Williams et al., 2023 in Malawi.

Various techniques have been proposed to capture the maximum magnitude, integrating the uncertainties associated with the process. We can underline that Stevens and Avouac, 2017 proposed a recursive approach to determine M_{max} from geodetic data and observed earthquake occurrence rates, which accounts for aftershocks. This method was employed in the PSHA source model developed for Nepal by Stevens et al., 2018, where a hybrid PSHA source model was created. The maximum magnitude earthquake (M_{max}) was estimated using a combination of earthquake catalogs, moment conservation principles and comparisons with other tectonic regions.

Rollins and Avouac, 2019 also developed an alternative approach to constrain recurrence models using geodetic data by creating synthetic moment-balanced catalogs that incorporate both Gutenberg-Richter models and aftershock models (Bath law). They selected models that appeared to be consistent with the seismicity of the considered zones, enabling the estimation of M_{max} and b-values as probability distributions. Their method is well illustrated in the figure 2.12 for the example of California. The moment-balanced recurrence models from synthetic catalogs are represented in blue and grey, while the brown and white curves depict the G-R model from the recorded instrumental catalogs including or not aftershocks. This method proves to be highly valuable for obtaining distributions on the parameters of recurrence models for various zones, thus providing potential application in future PSHA models.

Moreover, Avouac, 2015 notably proposed an approach that was further investigated by Mariniere et al., 2021 in their case study in Ecuador. Essentially, this technique involves integrating coupling coefficient into the moment conservation principle and incorporating it into the computation of M_{max}.

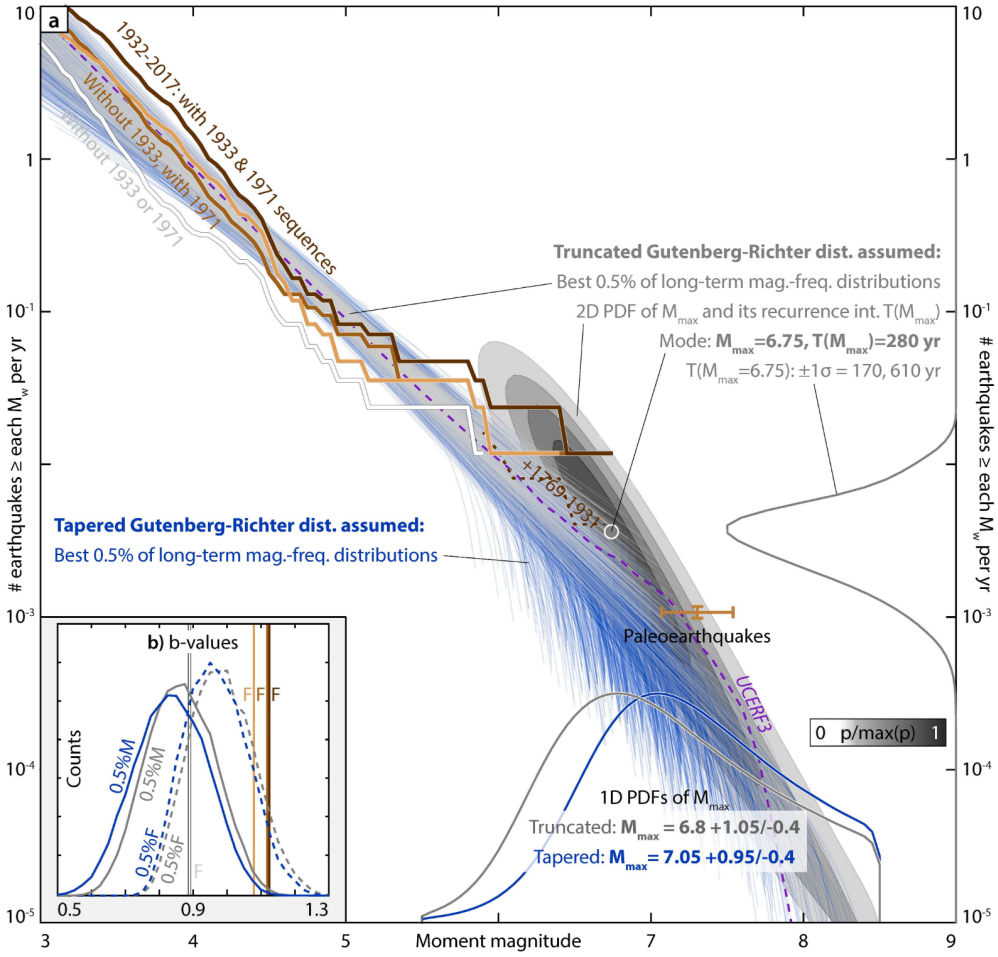

Fig. 2.12: **From Rollins and Avouac, 2019** : (a) Preferred estimates of long-term-average earthquake likelihoods (in Gutenberg-Richter space), assuming that mainshocks obey a truncated (gray) or tapered (blue) Gutenberg-Richter (G-R) magnitude-frequency distribution (MFD) and are accompanied by aftershocks plus postseismic deformation. The brown lines are cumulative MFDs of the four versions of the instrumental catalog. Thin translucent lines are full MFDs (including aftershocks) of the best fit ting 0.5percent of models in the truncated (gray) and tapered (blue) cases. The gray shape is the 2-D probability density function (PDF) of the maximum earthquake's magnitude and recurrence interval assuming a truncated G-R distribution. The brown error bars show aggregate recurrence interval and magnitudes of paleoearthquakes. The dashed purple line is cumulative MFD from all faults in study area. (b) Histograms of b-values in the best fitting 0.5percent of truncated (gray) and tapered (blue) models. The solid lines are intrinsic model parameter b that governs mainshocks (M) and individual aftershock sequences; the dashed lines are maximum-likelihood b-values of the full (F) long-term MFDs of the same models (including aftershocks) at $M_c = 3.5$; the brown lines are maximum-likelihood b-values of four versions of the instrumental catalog at $M_c = 3.5$.

Another major approach is to develop PSHA source models independent of seismicity data. This was proposed by Shen and Bird, 2022 in California. Essentially, they constructed a crustal deformation model using the Neokinema software, incorporating data from faults, GPS and crustal stress orientation. Subsequently, they derived seismicity rates from this model and compared them with existing seismic models. They observed that the long-term seismicity rates obtained from their model showed good agreement with the observed seismicity rates, except in the Cascadia region where the instrumental seismicity rates over 45 years were significantly quieter than the projections from their long-term model.

2.6.3 At global scale

In this section, we briefly overview the research conducted in the aftermath of the Seismic Hazard Inferred from Tectonics (SHIFT) project. Our objective here is not to delve into the intricacies of the method (as it was not applied in this thesis) but to acknowledge its existence and reference the relevant articles. The primary aim of the SHIFT project was to enhance the reliability of long-term seismicity forecasts beyond those primarily grounded in local instrumental and/or historical records, incorporating plate tectonic models and strain data.

Bird, 2003 initiated the process with a comprehensive literature review on plate tectonics, classifying every plate-boundary step into seven types, as cited in Table 2.1.

Following this, Bird, 2004 utilized these classifications to assign 95% of shallow earthquakes to appropriate plate boundaries, estimating seismicity parameters in concordance with tectonic constraints. They introduced a novel parameter, the 'coupled thickness,' representing the fraction of seismogenic thickness that is coupled. The main result is a table associating each plate boundary with various parameters, such as coupled thickness or the shearing coefficient. This table (table 2.1) is presented hereafter, extracted from the subsequent article for ease of use.

Subsequently, Bird and Liu, 2007 refined the model and introduced a method to estimate long-term average seismicity for any region. This approach relies on geodetic strain rates and the earlier global calibration of plate-boundary seismicity established in Bird, 2004. Essentially, the procedure involves calculating the geodetic moment by combining geodetic strain rates with the remaining parameters (mu, seismogenic thickness, considered as the coupled thickness) obtained from global-scale statistics, as outlined in Table 2.1. This resulting geodetic moment is then utilized to conduct moment budgets at a regional scale. The application of this method to California yielded a long-term seismicity forecast exceeding the levels observed in several 20th-century catalogs. Notably, this method has been embraced in the literature, including contributions by Carafa et al., 2017 and Rong et al., 2016.

Subsequently, Bird, 2009 created a long-term seismicity forecast map by applying the Bird and Liu, 2007 method on a global scale. To achieve this, they initiated the process by creating a strain rates map (called GRSM Global Strain Rate Model) on a global scale based on GNSS data before utilizing their method to develop long-term worldwide seismicity models.

Tab. 2.1: **From Bird and Liu, 2007 (truncated) : Seismicity Parameters for Discrete Faults**, with the 7 plate boundary types defined by Bird, 2003: CRB, continental rift boundary; CTF, continental transform fault; CCB, continental convergent boundary; OSR, oceanic spreading ridge; OTF, oceanic transform fault; OCB, oceanic convergent boundary; SUB, subduction zone; <cz>, the coupled thickness ; θ the fault dip ; μ, the shear modulus

Subduction Zone?	Crust Type	Fault Type	Slip Rate, mm a^{-1}	Plate Boundary Analog	<*cz*>, km*	θ, deg.*	*μ*, GPa*
Yes	**(Mixed)**	**All (merged)**	**any**	SUB	18	14	49
No	**Continental**	**Thrust**	**any**	CCB	18	20	
		Strike-slip	**any**	CTF	8.6	73	27.7
		Normal	**any**	CRB	3	55	
	Oceanic	**Thrust**	**any**	OCB	3.8	20	49
		Strike-slip	**<39.5**	slow OTF	13		
			39.5–68.5	medium OTF	1.8	73	25.7
			>68.5	fast OTF	1.6		
		Normal	**any**	OSR/normal	eq. (3)	55	25.7

* Based on Bird and Kagan (2004), table 5.

Finally, the Global Earthquake Activity Rate Model (GEAR) models developped by Bird et al., 2015 propose a method to develop hybrid models between seismicity and strain rate maps.

These articles are noteworthy as they offer global statistics to constrain the calculation of geodetic moment. Additionally, they provide a valuable initial global perspective on potential long-term seismicity rates, particularly useful for estimating hazard in areas where no models have been developed yet. However, these models were not employed in this thesis, as calibrating geodetic moment parameters based on global data ultimately renders them dependent on global seismicity catalogs. In our approach, we aimed to consider geodetic strain rates as a dataset entirely independent of seismic catalogs.

3 Comparison between seismic moment rates from ESHM20 model and geodetic estimates

3.1 Active deformation and seismicity in Europe

Hereafter, we present a succinct synthesis of recognized deformation patterns in Europe. Our approach involves a systematic description of the deformation characteristics in each zone, with insights primarily drawn from review works by Jean-Mathieu Nocquet (2012), Piña-Valdés et al. (2022), and J.-M. Nocquet and Calais (2003; 2004). Throughout this discussion, we will reference pertinent studies that have leveraged geodetic data to enhance our understanding of seismic behavior within these zones.

High activity areas

In Europe, regions of high strain are positioned along plate boundaries, particularly between Nubia and Eurasia in the western part of the continent and between Nubia, Anatolia, and Eurasia in the east, owing to the relative movement of these plates. The study made by Ward, 1998b, one of the early works in Europe, calculated the geodetic moment in active zones based on strain rates and compared it with a seismic moment calculated as the sum of earthquake moments in a 100-year catalog. They obtained a ratio M_{0G}/M_{0S} between 0.5 and 0.7 in active European zones, except for Turkey (0.22). The authors argued that improved geological fault databases, longer historical earthquake catalogs, and the densification of the continent's space geodetic network would clarify the roles of aseismic deformation versus statistical quiescence.

In a more recent study, Rong et al., 2016 focused on active zones in Europe (excluding intraplate regions). They initially compared geodetic and seismic moments for ESHM13 (Woessner et al., 2015) area sources grouped by proposed M_{max} ranges. The study revealed a good agreement between these two values in the Apennines,

Dinarides, and most of the eastern Mediterranean. However, for the Betics, Alps, and Pannonian Basin zones, they demonstrated that the geodetic moment exceeded the seismic moment. In these cases, the authors argued that this inequality validates the decisions of ESHM13 modelers to set M_{max} values above observed historical seismicity. A similar observation was made in areas around the North Anatolian Fault.

Now, let's present the major deformation patterns from west to east.

1) Westernmost part of Europe and Betics range

To the west of the Gibraltar Strait, the oceanic-oceanic plate boundary between Nubia and Eurasia transitions into a continent-continent type, with an increase of deformation from west to east (Nocquet, 2012). According to Nocquet and Calais, 2004; Serpelloni et al., 2007, more than 90% of the convergence in the westernmost part of Europe is accommodated through the Maghrebide (figure 3.1). In our study area, the Betics Mountains (figure 3.1), located in the southwest of Spain, constitute the primary deforming region along the dextral strike-slip Betics fault system, which accommodates a 4mm/year dextral strike slip movement. Koulali et al., 2011 proposed that the southern Betics can be modeled as a block, including the Rif, moving southeastward relative to stable Eurasia. This zone also concentrates the majority of seismicity in the region, both in terms of the number of earthquakes and their magnitudes.

Sparacino et al., 2020 focused on the Maghreb and Betics, defined source zones and analysed seismic/geodetic moment ratios. The findings revealed that, in the Betics, most of the region exhibited a seismic-to-geodetic ratio (M_{0S}/M_{0G}) below 23%, while certain areas, particularly those in the east, presented an intermediate ratio between 35% and 60%. The authors interpreted this difference as indicative of the proportion of aseismic deformation present in this region.

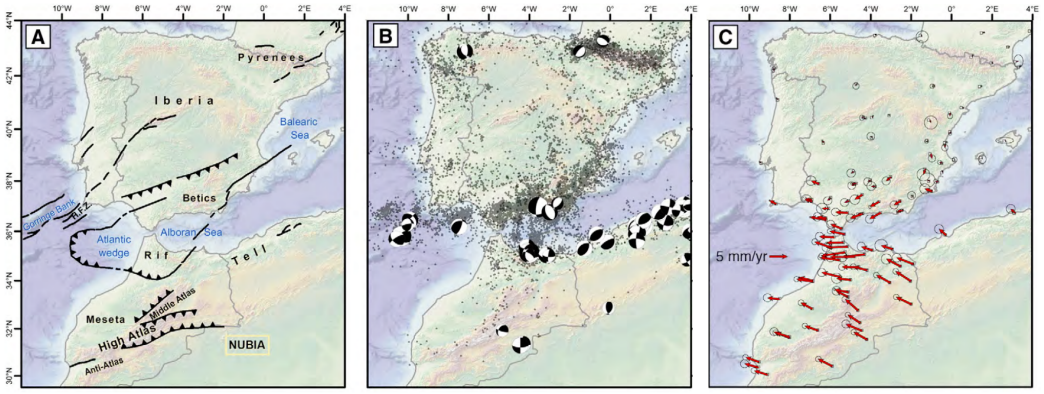

Fig. 3.1: **From Nocquet, 2012**: A: Tectonic map of Iberia and Morocco, H.F.Z.: Horsehoe upper case names surrounded by the yellow rectangle indicate main tectonic plates. H.F.: Horseshoe fracture zone. B: Seismicity distribution (NEIC catalog, 1976–2010) and CMT focal mechanisms (http://www.globalcmt.org, 1976–2011); C: velocity field in a Eurasia fixed reference frame. Error ellipses show 1-sigma (67%) confidence level.

2) The Appenines

Looking east, the counterclockwise rotation of Adria/Apulia (figure 3.2a) plate with respect to stable Europe results in a north-eastward motion visible in Italian peninsula (Piña-Valdés et al., 2022; Nocquet, 2012) as it can be seen in the figure 3.2c. Their relative motion is accommodated by a set of active faults which has an extensional play in the Apennines range (as shown in the kinematic models figure 3.2d). This region accommodates up to 4mm/yr of horizontal velocities and 1-2mm/yr uplift. The figure 3.2b shows that the Apennines range presents an abundant seismicity, mainly extensive.

The Italian Peninsula has garnered considerable attention in research due to the abundance of rich, reliable, and consistently updated historical earthquake and seismogenic fault databases, coupled with the dense network of permanent GPS stations.

Firstly, the Apennines have been a extensively studied region, and the correlation between seismicity and strain evolution can be conducted in a highly detailed manner, as demonstrated by these two studies.

D'Agostino et al., 2009 performed a moment budget in the Apennines, revealing a moment deficit in the northern Apennines. They suggested that this deficit could be filled by forthcoming seismicity or explained by aseismic deformation (see section 2.5.2).

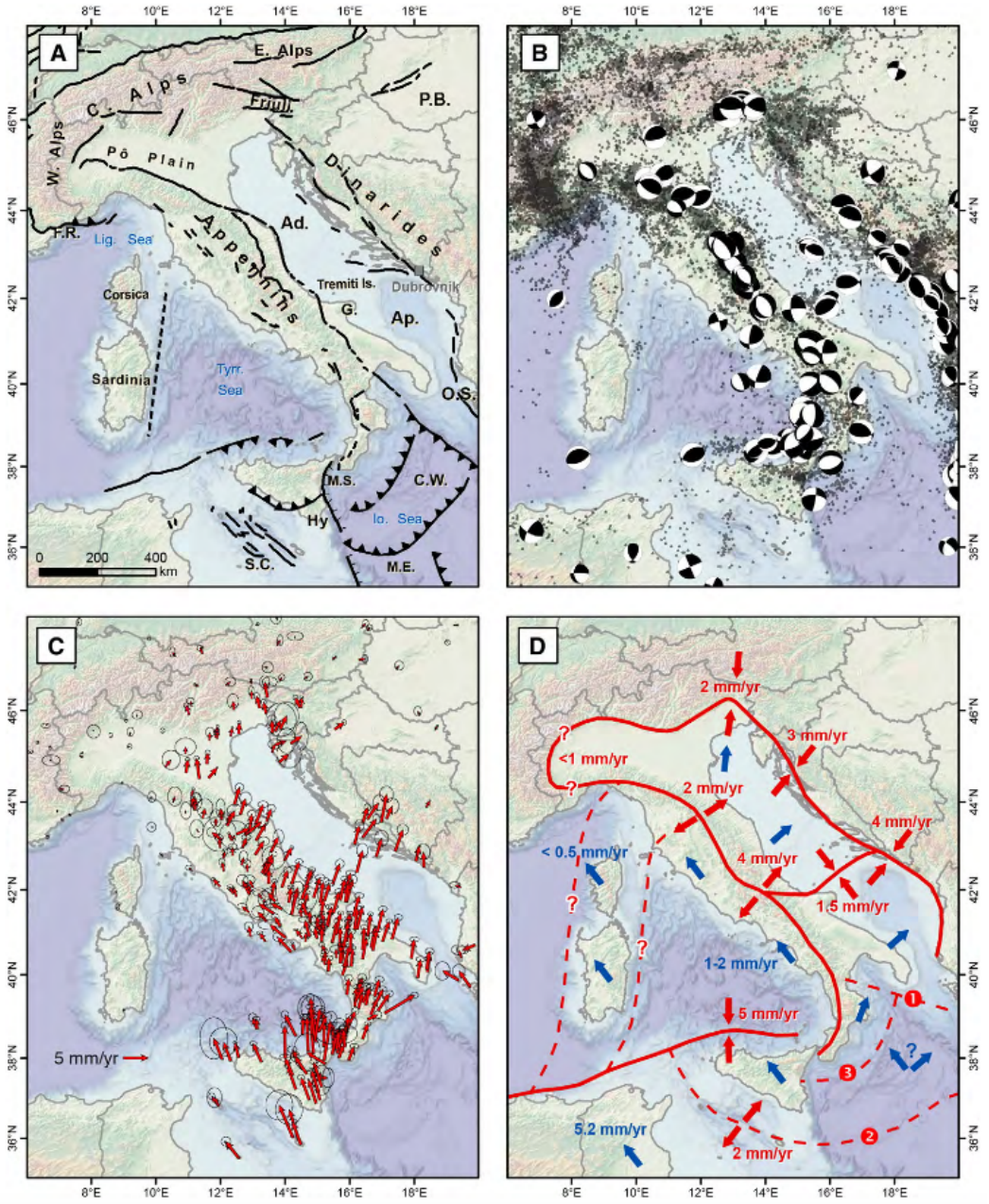

Fig. 3.2: **From Nocquet, 2012**: A: Tectonic map of central Mediterranean. W. Alps: western Alps, C. Alps, central Alps, F.R.: French Riviera, P.B. Pannonian basin, Lig. Sea, Ligurian Sea, Tyr. Sea, Tyrrhenian Sea, Io. Sea, Ionian Sea, Ad., Adria, G: Gargano, O.S.: Otranto Strait, AP. Apulia, M.S. Messina strait, C.W, Calabrian wedge, Hy. Hyblean plateau, M.E, Malta escarpment, S.C: Siculy Channel. B: Seismicity distribution (NEIC catalog, 1976–2010) and CMT focal mechanisms ; C: velocity field in a Eurasia fixed reference frame. Error ellipses show 1—sigma (67%) confidence level. D: Kinematics models 1, 2, 3 indicate the boundary between Apulia and Nubia favored by different authors (see Nocquet, 2012 for more information).

D'Agostino, 2014 conducted a comprehensive analysis of the geodetic and seismic moment accumulation over time in the central Apennines, demonstrating that the geodetic moment accumulation coincides with the seismic moment accumulation without the need for invoking aseismic processes. They also identified spatial patterns where seismic moment release occurred in areas with a previous moment deficit, suggesting the presence of a spatial window capable of generating a 6.5 magnitude earthquake.

The figure 3.3 provides a comprehensive visualization of the findings. The plot depicting the cumulative moment release (b) from earthquakes in the area (illustrated in c) reveals that the total moment release reaches a plateau corresponding to the long-term geodetic moment across the Apennines, except for specific areas identified as a spatial windows (a). This observation suggests that the occurrence of a major earthquake in these spatial windows is anticipated compared to other parts of the Apennines.

Several other studies combining seismicity and geodesy have been conducted in southern Italy, offering novel insights into deformation patterns and stress states in the region.

Jenny et al., 2006, in southern Italy, incorporated constraints on the style and rate of deformation from geological and geodetic data at the seismotectonic source zone scale. They demonstrated that in the majority of southern Italy, seismic coupling appears to be broad, even complete, in most zones, indicating good compatibility between geodetic and seismicity data. The only exception is within the Southern Tyrrhenian thrust zone, where they identified aseismic deformation ranging from 25% to almost 100% for the Aeolian Islands.

Angelica et al., 2013 presented a comprehensive analysis of the seismic potential distribution across the Apennines and southern Italy, examining the variations in space-time seismic strain rates in comparison to cumulated geodetic strain rates. The study demonstrated that deformation rates derived from seismic and geodetic data exhibit similar styles of deformation and coherent kinematics in areas where both datasets provide enough information. The southern Apennines exhibited the highest seismic potential, revealing a significantly lower seismicity in the last two decades despite being subjected to the highest total strain rates. In contrast, the central–northern Apennines and the northern offshore region of Sicily demonstrated a lower seismic potential than the central–southern Apennines, possibly influenced by more recent seismic activity in these areas. The Messina Straits and eastern Sicily displayed significant seismic potential, along with the Calabrian arc (see figure 3.2a for the locations).

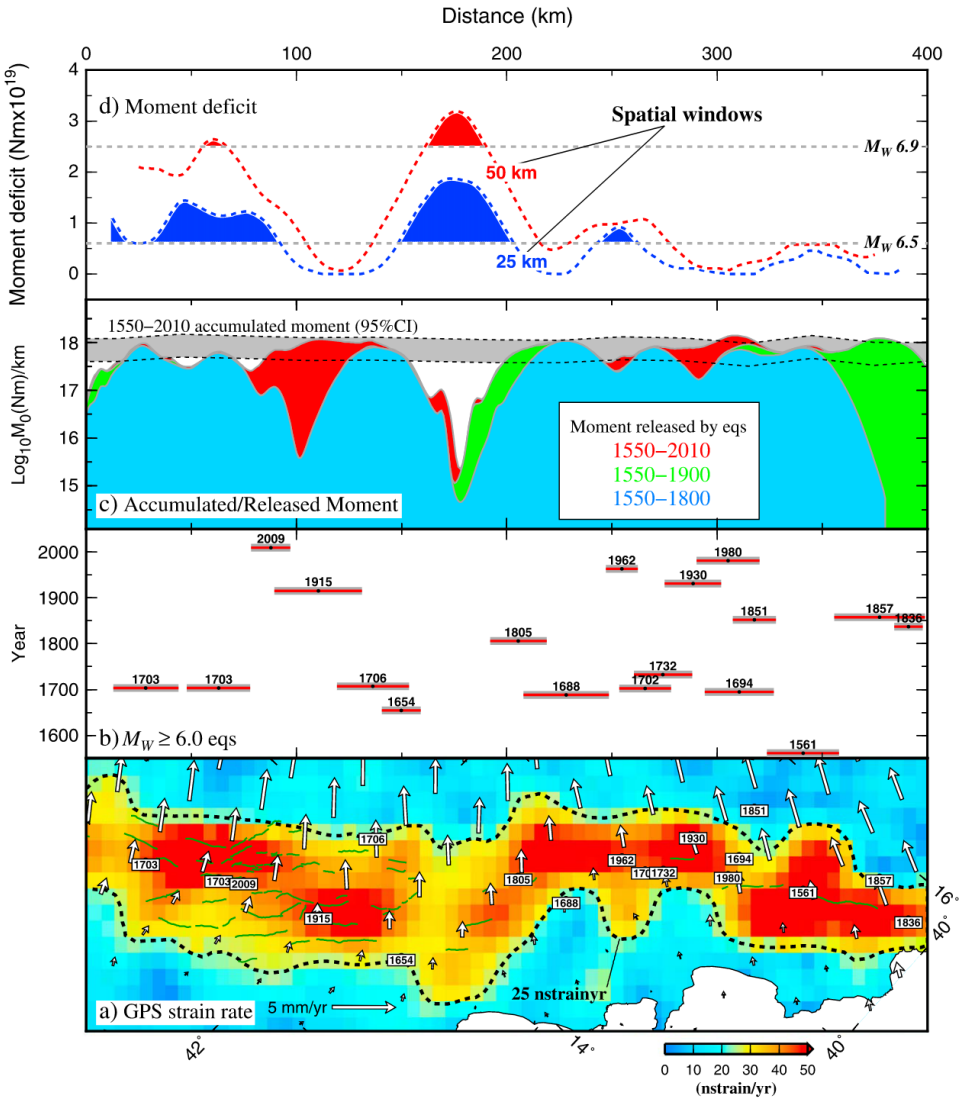

Fig. 3.3: **From D'Agostino, 2014** : a) Second invariant of the strain rate tensor with model velocities (white vectors), labeled dates of $M_W \geq 6$ seismic events and active faults. (b) $M_W \geq 6$ seismic events ordered in temporal sequence from bottom to top are shown as horizontal red bars scaled to the length of rupturing faults. (c) Distribution of smoothed seismic moment released by earthquakes in various time frames compared with the 1550–2010 seismic moment buildup from GPS (95% confidence interval). (d) Deficit of seismic moment release calculated in moving spatial windows of 25 and 50 km (assuming a zero strain level prior to 1550).

Carafa et al., 2018 investigated the subduction of the Ionian seafloor beneath Calabria. Historically, Calabria has experienced significant crustal earthquakes, but there is no evidence available regarding the activity of the underlying megathrusts. The key question they addressed, is whether the subduction interface is creeping, posing no additional threat to the region, or if it is locked and capable of rare but major earthquakes. Through numerical 3D modeling of crustal and subduction-related deformation constrained by GNSS velocities, they demonstrated that Southern Calabria may represent a "geodetic gap", where subduction-related strains are temporarily offset by crustal strains. This suggests that the subduction may indeed be locked.

Finally, it is worth noting a recent study that provided new constraints on the state of faults at the scale of the entire Italy. Carafa et al., 2017 analyzed fault catalogs, earthquake catalogs, and geodetic data to enhance the understanding of coupling on different types of faults (extensional, strike-slip, compressional). They have demonstrated that seismic coupling is twice as large for extensional faults compared to compressional faults, implying that the most significant earthquakes occur in extensional settings, while compressional faults host comparatively smaller events.

3) The Alps

Toward the north, the Alps show low strain rates. In the western Alps, inframillimetrics horizontal velocities underline extension where the highest relief takes place. In central and eastern Alps, the 2mm/yr of convergence between Adria and Europe (5-10 nanostrain/yr) is principally localized in the south of the Dolomites. This region has been studied by several authors :

Firstly, Barba et al., 2013 estimated the seismic potential in this region by fitting a rheological model with GPS data. They interpreted the comparison between the deformation provided by the model and seismicity rates in terms of coupling coefficients on different faults in this area. They showed that certain structures in this zone, such as the Massano Thrust, are prone to be characterized by aseismic deformation, whereas others, like the Bassano Thrust, may be locked and thus prone to produce major events.

Then, Cheloni et al., 2014 estimated the seismic potential in this region using geodetic data, suggesting that a magnitude 7.5 earthquake would balance the moment budget and align with the fault zone's geometry in the region.

4) The Dinarides

The Dinarides region, as depicted in Figure 3.4, serves as a focal point for significant seismic activity in the examined area, as illustrated in Figure 3.4b. This zone plays a

crucial role in absorbing a substantial portion of the Italian peninsula's movement towards the northeast relative to Europe, with a rate of 3mm/yr compared to the overall convergence rate of 4mm/yr, as evidenced in Figures 3.4c and d. The residual northeastward velocities are accommodated in the Pannonian basin towards the east.

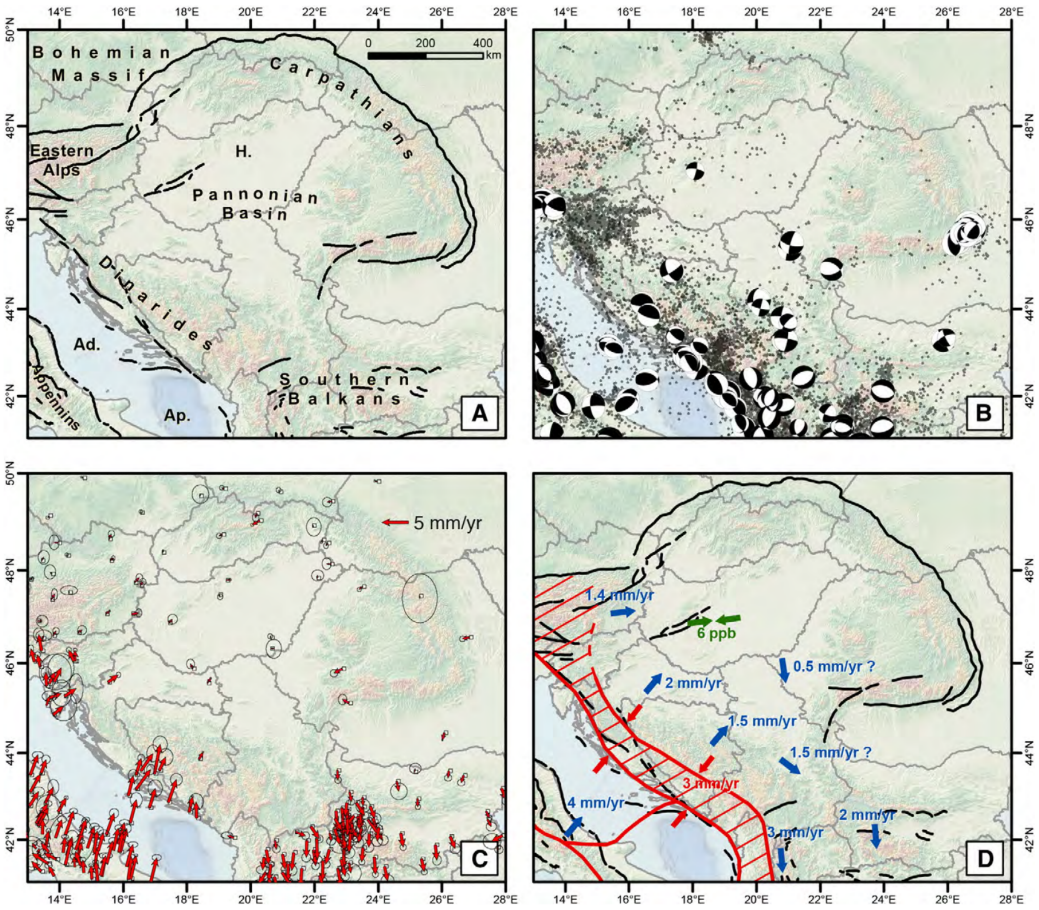

Fig. 3.4: **From Nocquet, 2012**: A: Tectonic map of central Mediterranean. Ad. Adria, AP. Apulia, H Hungary. B: Seismicity distribution and CMT focal mechanisms ; C: velocity field in a Eurasia fixed reference frame. Error ellipses show 1-sigma (67%) confidence level. D: Kinematics model. Dashed area shows the area accommodating the deformation. Green arrows show the average strain rate (nstrain/year) for the Pannonian basin.

In the Dinarides the study of Kastelic et al., 2016 assesses the efficacy of geodynamic models in comparison to traditional Probabilistic Seismic Hazard Assessment (PSHA) models based on seismicity. Utilizing various geodynamic models constrained by fault data and GPS measurements, the authors demonstrate a notable consistency with conventional PSHA models. Seismic hazard calculations derived from geodynamic models exhibit coherence with those from classic seismicity-based models.

Moreover, the variability in results, quantified in terms of Peak Ground Acceleration (PGA), is found to be comparable to that arising from ground motion prediction models. This comparative analysis underscores the efficacy of geodynamic models in addressing seismic uncertainties, providing a complementary approach to conventional seismicity-based methodologies.

5) Eastern Mediterranean

The figure 3.5 from Nocquet, 2012 shows that the eastern Mediterranean pattern of deformation is due to a combination between the relative movement of Nubia wrt Eurasia at convergence rates of 5.5 to 6 mm per year in the direction N322-332E, and between the movement of Arabia wrt stable Eurasia of 1.5cm/yr in a direction N340 (Nocquet, 2012). Both movement result in a counterclockwise rotation of Anatolia. The principal deforming areas are at its borders. We can highlight the subduction of Nubia beside Eurasia which occur in the Hellenic trench with a convergence rate around 3.5cm/yr, the dextral strike slip motion of 2.5cm per year along the north Anatolian Fault and the dextral strike slip Kephalonia fault (2cm/yr). Despite the high velocities at its border, high deformation rates are also recorded inside Anatolia. Several studies have been done in the Aegean : Firstly, Clarke et al., 1997 performed a moment budget analysis in the Gulf of Corinth, indicating agreement between the geodetic and seismic values to the east of the gulf. However, a seismic moment deficit was observed in the central and western parts, suggesting a requirement for several $M_W 6.5$ earthquakes to balance the budget.

Secondly, in their study focusing on Greece, Rontogianni, 2010 undertake a comparative analysis of geodetic and seismic strain rates. Their investigation reveals a remarkable consistency in the orientations of these deformation measures, thereby bolstering the reliability of geodetic data. Employing a strain budgeting approach, the authors juxtapose the amplitude of geodetic strain, assessed across polygons and a grid, against seismic strain derived from recorded seismic events. The findings uncover a pervasive seismic strain deficit across all examined regions in Greece. The researchers interpret this deficit as indicative of latent seismic potential, suggesting that accumulated deformation may be discharged through future seismic events. Alternatively, they entertain the possibility of aseismic deformation.

Thirdly, Vernant et al., 2014 explored the Hellenic subduction by employing GNSS data to fit a block model. Their objective was to assess the coupling properties along the main structures. They demonstrated that a low coupling (10 percent) for the Hellenic Trench is in agreement with the observations.

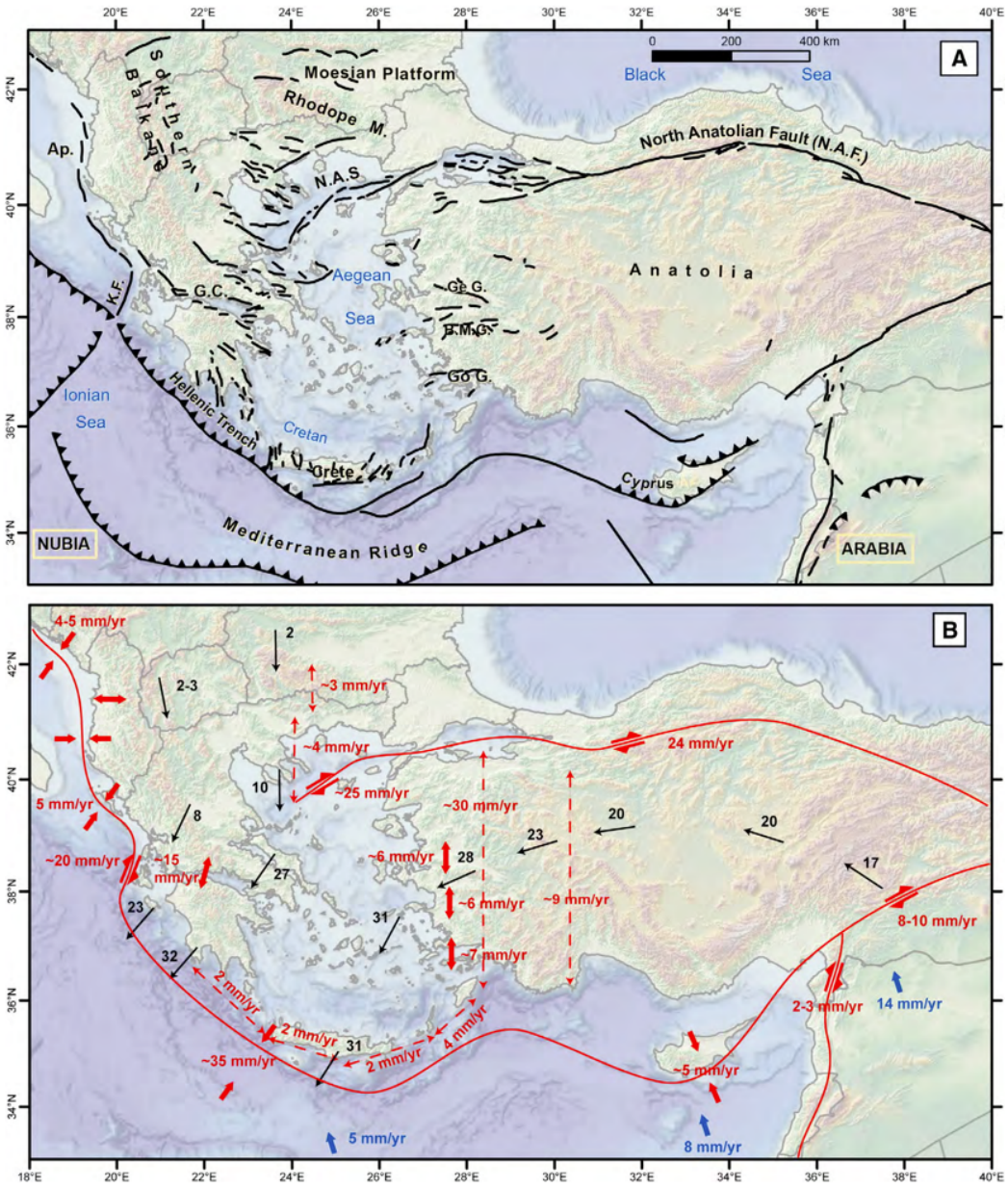

Fig. 3.5: **From Nocquet, 2012**: A: Tectonic map of the Aegean and Anatolia. K.F., Kephalonia fault, Ge.G., Gediz graben, B.M.G. Buyuk Menderes graben, Go. G. Gökova gulf. B: Kinematics sketch. Dashed double-arrow lines show integrated relative motion over a given area. Thin black arrows are velocities at selected locations.

Finally, in their investigation Chousianitis et al., 2015 on the Aegean scale, the authors explored the moment budget, revealing that in the central Ionian Sea, the geodetic moment is entirely released seismically. However, across the majority of the study area, geodetic moment rates exceeded earthquake-based rates by at least a twofold margin. This disparity was primarily attributed to the limitations in earthquake catalog representativeness over extended periods, or suggesting a potential contribution from aseismic deformation. Particularly in the western part of the Gulf of Corinth, the authors identified deficits in seismic moment rates reaching 60% to 70% of the total deformation budget. They interpreted this incongruity not solely as attributable to future seismic events but rather as necessitating a component of aseismic deformation.

In our study region, specifically in Turkey, another noteworthy investigation is the study by Meghraoui et al., 2021. They conducted a compelling study on the Marmara Fault (the western termination of the North Anatolian Fault in Turkey), performing a moment budget using seismic and paleoseismic data. They calculated the moment deficit compared with geodesy and concluded that it can be balanced by an earthquake of magnitude 7.4/7.5.

Low to moderate activity areas

In intracontinental Europe, the most important movement recorded by GNSS, is due to the Glacial Isostatic Rebound (GIA) in Fennoscandia. During the Last Glacial Maximum ($\sim$ 20 ka), an ice cap, which had a maximum thickness of 2 to 4km covered northern Europe and a large part of Britain island (Steffen and Wu, 2011). As a result, the visco-elastic relaxation of the mantle lithosphere system following the melting of the ice cap causes an uplift which as a maximum ($\sim$ 11mm/yr) in the gulf of Bothnia and progressively decreases until reaching subsidence of 0.4mm per year in the northermost Europe (Nocquet, 2005). Horizontal velocities are organized in radial pattern and reach 2mm per year. The strain is mainly extensional in the center of Fennoscandia whereas a shortening is observed in the surrounding regions.

This region demonstrates a disparity between geodetic and seismic strain rates in both orientations and magnitude (Keiding et al., 2015; Craig et al., 2016). We recommend referring to Section 2.5.2 for more details.

Except for GIA, other places in Europe are known as potentially seismic active areas. It is the case in the Armorican fault system in France, in the Roer-Rhine graben system (between France and Germany), in the Eifel hotspot in Germany and in

the Pyreneans mountains strike slip fault system at the border between Spain and France.

3.2 Article. Towards integrating strain rates in PSHA models in Europe: Comparison between seismic moment rates from ESHM20 model and geodetic estimates

This article is a work in progress currently undergoing revision with the intention of submission to the Geophysical Journal International in the coming months.

3.2.1 Introduction

Nowadays, source models in up-to-date probabilistic seismic hazard studies are based both on past seismicity and active tectonics datasets. For example, the source model logic tree in the European Seismic Hazard Model 2013 (Woessner et al., 2015) and its update the European Seismic Hazard Model 2020 (Danciu et al., 2021) include two main branches, an area source model and a fault model. In regions where active faults are rather well-characterized, they must be accounted for in the hazard estimations (e.g. Stirling et al., 2012; Field et al., 2014; Beauval et al., 2018). Fault models are mostly based on geologic information, covering much larger time windows than the available earthquake catalogs. Fault models thus bring insights on the generation of earthquakes that complement the catalog-based earthquake forecasts. However, fault databases are known to be incomplete, even in the best characterized regions, and earthquakes may occur on unknown faults, as demonstrated by several earthquakes in the past (e.g. the two 2002 Mw 5.7 Molise earthquakes (Valensise et al., 2004) in Italy; or the Darfield Mw 7.1 earthquake in New Zealand (Hornblow et al., 2014).

The use of geodetic data in the building of source models has been limited up to now, although deformation rates based on velocities from the Global Navigation Satellite Systems (GNSS) constitutes a promising perspective for constraining earthquake recurrence models (Jenny et al., 2004; Shen et al., 2007). GNSS stations measure the present-day displacements at the surface of the earth. A convenient way to characterize the ground deformation is to invert the surface velocities measured by GNSS to compute strain rate maps, that are independent from the reference frame. The accuracy of the estimated strain rates depends on the spatial density of GNSS stations, on the quality of the sites, and on the duration of the recordings (Mathey et al., 2018). Along major interplate faults, such as subduction zones or lithospheric strike slip faults, interseismic velocities measured by GNSS are now

commonly used to constrain the slip deficit on the fault associated with locking in between large seismic events (also referred to as interseismic coupling). In such highly active tectonic boundary regions, the interseismic slip deficit may be combined with the earthquake catalog to constrain earthquake recurrence (Avouac, 2015; Mariniere et al., 2021). In plate interiors, where the faults are moving more slowly and where the fault mapping might not be exhaustive, strain rate models can provide constraints on the seismic potential.

Indeed, the tectonic loading recorded by geodesy should be proportional to the energy released during earthquakes, under the assumption that the earth's crust behaves elastically. If this assumption is true and if other factors such as aseismic deformation are not significant, then the rate at which energy is released during earthquakes (represented by the seismic moment rate) and the rate at which tectonic forces build up between earthquakes (represented by the geodetic moment rates) should be equal (Stevens and Avouac, 2021). This balance can be used to constrain magnitude-frequency distributions. In the last 30 years, a number of studies have analyzed the catalog-based magnitude-frequency distributions with respect to the tectonic loading measured by geodesy. In the Hellenic arc, Jenny et al., 2004, found that the maximum magnitudes required for the earthquake recurrence models to be moment-balanced were unrealistic and concluded that a large part of the strain is released in aseismic processes. In the India-Asia collision zone, Stevens and Avouac, 2021 highlighted a correlation between earthquake rates and strain rates. They established moment-balanced recurrence models that fit both past seismicity and the geodetic moment, bounded by maximum magnitudes compatible with those expected in the region.

Determining the extent to which the methods used to study highly active tectonic regions can be applied to areas with lower levels of seismic activity is an open research question. The present study is at the scale of the whole European continent, that is very heterogeneous in terms of tectonic activity. Southern Europe, with regions such as the Apennines, Greece and Turkey, is characterized by a high seismic activity; whereas northern and central Europe is characterized by a low to moderate seismic activity. We take advantage of two new studies performed at the scale of Europe: the release of the new probabilistic seismic hazard model for Europe (ESHM20, Danciu et al., 2021); and the strain rates models computed by Piña-Valdés et al., 2022. Our objective is to compare the ESHM20 earthquake forecast with the deformation rates obtained from the GNSS velocities, giving special attention to the estimation of uncertainties.

In a first step, we present the datasets and methods used to compute the seismic and geodetic moments integrated in space and time and to explore the uncertainties. Then we compare the estimated seismic and geodetic moments in the different source zones of the ESHM20 model that covers the whole of Europe. We then discuss the parameters that influence the most the compatibility in both high and low-to moderate activity.

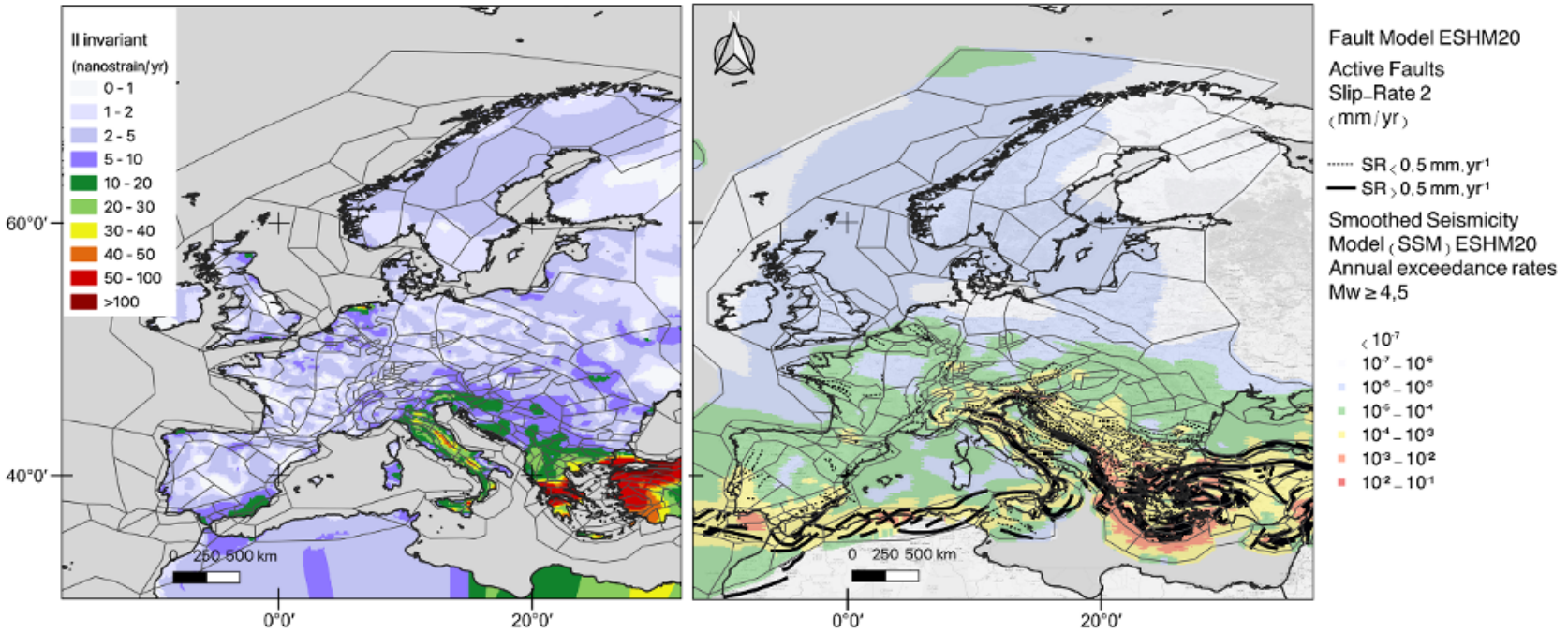

Fig. 3.6: Strain rate model for Europe and ESHM20 earthquake forecast (smoothed seismicity and fault model branch). a) II invariant of the strain rate tensor (Piña-Valdés et al., 2022), with area sources from ESHM20 source model superimposed; b) Smoothed seismicity model, earthquakes rates $M_W \geq 4.5$, faults included in the model are superimposed (Danciu et al., 2021)

3.2.2 Seismic moment: moment distribution associated with the ESHM20 source model logic tree

The 2020 European Seismic Hazard Model (ESHM20) aims at delivering seismic hazard levels throughout Europe, using harmonized datasets and applying homogeneous methodologies (Danciu et al., 2021). The hazard model is made of a source model logic tree and a ground-motion logic tree. The present study deals with the source model component. The earthquake forecast includes all earthquake types, ie crustal, deep, and subduction earthquakes. In this paper we focus on the contribution of crustal seismic sources, that can be easily compared to surface strain rate.

The ESHM20 source model is based on several updated datasets (Danciu et al., 2021): an earthquake catalog, covering the time window 1000-2014, including both historical and instrumental periods, and a fault database including potentially active faults, with their geometry and geologic or geodetic slip rates (European Fault-Source Model 2020 EFSM20, Basili et al. in press.). The source model logic tree accounts for alternative source models to capture the spatial and temporal uncertainty of the earthquake rate forecast in Europe. It includes two main branches : an area source model and a fault model associated to a smoothed seismicity model.

The area source model is made of area sources which geometry is guided by seismotectonic evidence such as potentially active faults, geologic features, seismicity pattern (Danciu et al., 2021). For every area source, a Gutenberg magnitude-frequency distribution (Gutenberg and Richter, 1944) has been established from the earthquake catalog taking into account time windows of completeness. Two alternative models have been considered to account for the uncertainty in forecasting earthquake rates in the upper magnitude range:

- a magnitude-frequency distribution truncated at a maximum magnitude M_{max}, corresponding to form 2 in Anderson and Luco, 1983 :

$$N(m) = 10^{a-b*m} + 10^{a-bM_{max}} \text{ for m} \leq M_{max} \tag{3.1}$$

- a tapered Pareto distribution (Kagan, 2002) which includes a bending of the recurrence model from a magnitude called the corner magnitude (M_c).

As an alternative to the area source model, a fault model has been built, associated with off-fault smoothed seismicity (Fig 3.7). For each fault, a moment-balanced

magnitude-frequency distribution has been established, that accommodates the moment inferred from the slip rate and the geometry of the fault, assuming moment conservation principle. The maximum magnitude is obtained applying the Leonard, 2015, scaling relationship to the length, the width and the area of the fault (Basili et al. in press). The smoothed seismicity model relies on the earthquake catalog. To avoid double-counting, a buffer zone is applied around each fault (see Danciu et al., 2021).

The source model logic tree explores the uncertainty on the definition of the maximum (or corner) magnitude both in the area source model and in the fault model (Figure 3.7). For the area source model, the uncertainty on the estimation of a- and b- values is also considered (Gutenberg-Richter model branch). For the fault model, the uncertainty on the slip rate estimates is explored. Overall, the exploration of the logic tree leads to 21 alternative recurrence models, with different weights.

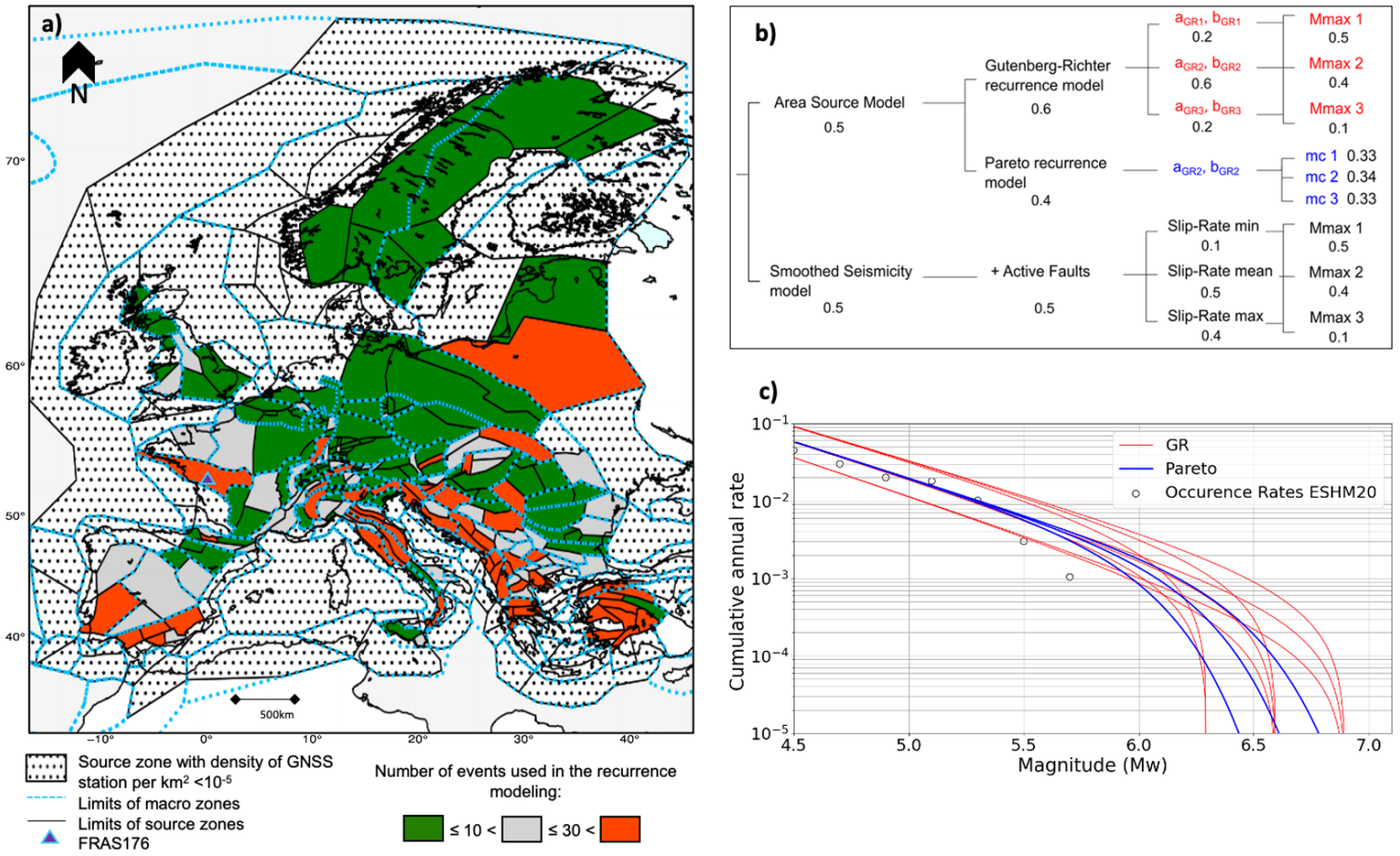

Fig. 3.7: ESHM20 source model (Danciu et al., 2021): a) area sources (black polygons), and larger macrozones (dashed blue) used to infer the b-value in regions with poor earthquake data; orange: sources with at least 30 events used to establish the recurrence model, green: with less than 10 events, black dots: area sources not considered in the study (poorly constrained strain rates). b) Source model logic tree, with the weights associated to the different branches. c) Alternative earthquake recurrence models for the example source zone FRAS176 (southern Brittany in France, blue triangle), colors correspond to the branch combinations in the area source model, Fig. 2b

For every area source zone, 21 alternative estimates for the seismic moment are computed from the 21 alternative source models. Considering the recurrence models Gutenberg-Richter and Pareto, the total annual moment rate corresponds to the integral under the curve in terms of moment. In the case of the Gutenberg-Richter model (form 2 in Anderson and Luco, 1983), the moment can be estimated using the equation (Mariniere et al., 2021) :

For every area source zone, 21 alternative estimates for the seismic moment are computed from the 21 alternative source models. Considering the recurrence models Gutenberg-Richter and Pareto, the total annual moment rate corresponds to the integral under the curve in terms of moment. In the case of the Gutenberg-Richter model (form 2 in Anderson and Luco, 1983), the following equation is used (Mariniere et al., 2021) :

$$\dot{M}_{0S} = \frac{b}{(c-b)} * 10^{a+d+(c-b)M_{max}} \tag{3.2}$$

with $c = 1.5$ and $d = 9.1$ the parameters used in the calculation of the seismic moment from the moment magnitude, Hanks and Kanamori, 1979.

To compute the annual seismic moment rate from the smoothed seismicity and fault model, we sum the seismic moments associated to every spatial cell within the area source zone (one magnitude-frequency distribution per cell). When a fault straddles several zones, the seismic moment associated to the source zone is proportional to the length of the fault within the source zone.

For each source zone, a distribution of 21 seismic moments is obtained, representative of the uncertainties considered in the ESHM20 source model logic tree. A weighted mean seismic moment is calculated considering the weights associated to every branch combination (Fig 3.7). Besides, approximate 16^{th} and 84^{th} percentiles are inferred from the discrete distributions.

3.2.3 Geodetic moment computation from strain rates maps and uncertainty exploration

Our aim is to use strain rates evaluated at the scale of Europe to estimate the geodetic moment rate within every area source of the ESHM20 source model. We rely on the work done by Piña-Valdés et al., 2022. They combined ten GNSS velocity fields with different spatial coverage in Europe. After filtering the velocity field obtained to remove stations with highest uncertainties, they applied the VISR algorithm

(Shen et al., 2015) to produce a strain rate map for Europe (a best estimate model). The algorithm VISR calculates horizontal strains through interpolation of geodetic velocities. It is an undetermined inverse problem; the algorithm uses as inputs the discretized geodetic observations and delivers smoothed distributed strain rates. Key decisions need to be taken on the exact weighting scheme to apply, that may impact the interpolation and the final strain rate estimates. In our case, rather than a best estimate, we need a distribution for the geodetic moment rate that is representative of the uncertainties.

Uncertainties on the strain rate estimates

Ideally, only the stations with the best constrained velocity estimates should be included for deriving strain rates, however a compromise must be obtained between discarding poorly constrained stations and keeping a reasonable number of stations for the analysis. Piña-Valdés et al., 2022 have classified the 4863 available stations into 4 categories A, B, C, and remaining stations, depending on their noise level (increasing uncertainty on the velocity, with A the stations with lowest uncertainty). To derive their best model, they finally decided to include all stations falling into categories A, B and C. Here, we are interested in quantifying how much this decision impacts the strain rate estimates and we explore the uncertainty related to the use of only class A stations (3377), of both A and B stations (4091), or all stations A, B and C (4468).

For the strain rates to be reliable, anomalous velocities must be identified and removed from the combined velocity field. Piña-Valdés et al., 2022 proposed to detect outliers based on an analysis of the spatial consistency of the velocities. For every station, the distribution of the velocities within a circular region around the station is obtained; stations with velocities in the tails of the distribution are considered outliers. Piña-Valdés et al., 2022 tested 4 different radius (50, 100, 150 and 200km) and showed that when the radius is increased, the number of outliers decreases. They used 150km for deriving their best estimate model, considering this radius a compromise between the number of stations left (4238) and a reduction of the variance obtained on the final solution. Here, we keep track of the uncertainty associated with this decision, and we use alternatively the 4 different radii to evaluate strain rates.

While applying the algorithm VISR, a number of decisions are required that may impact horizontal strain rates estimates. Shen et al., 2015 show that the distance-dependent weighting can be achieved by employing either a Gaussian or a Quadratic

decay function, and that for the spatially-dependent weighting either an Azimuthal weighting or a Voronoi cell area weighting function can be applied. Another crucial parameter is the weighting threshold, which governs the smoothing of the inversion process. Here we include in the analysis both the uncertainty on the smoothing function and on the spatially dependent weighting, as well as three alternative weighting thresholds values (6, 12 and 24; see Shen et al., 2015).

Estimation of the geodetic moment rate within an area source zone

For each area source of the EHSM20 model, we determine a distribution for the geodetic moment rate. Figure 3.8 illustrates the different steps for the source zones in Northwestern France.

First, for each component of the strain rate tensor ($\dot{\varepsilon}_{xx}$, $\dot{\varepsilon}_{yy}$, $\dot{\varepsilon}_{xy}$), we determine the mean component from all grid cells falling within the source zone (Figs. 3.8a and 3.8b) :

$$\overline{\dot{\varepsilon}_{xx}}^2 = \frac{\sum_{i=1}^{ncells} \dot{\varepsilon}_{xx}(i)}{n} \tag{3.3}$$

Then we calculate the principal components (eigenvalues) of the strain rate tensor within the area source :

$$\overline{\dot{\varepsilon}_{max}} = MAX\left(\frac{\overline{\dot{\varepsilon}_{xx}} + \overline{\dot{\varepsilon}_{yy}}}{2} + \sqrt{\left(\frac{\overline{\dot{\varepsilon}_{xx}} - \overline{\dot{\varepsilon}_{yy}}}{2}\right)^2 + \overline{\dot{\varepsilon}_{xy}}^2}; \frac{\overline{\dot{\varepsilon}_{xx}} + \overline{\dot{\varepsilon}_{yy}}}{2} - \sqrt{\left(\frac{\overline{\dot{\varepsilon}_{xx}} - \overline{\dot{\varepsilon}_{yy}}}{2}\right)^2 + \overline{\dot{\varepsilon}_{xy}}^2}\right) \tag{3.4}$$

$$\overline{\dot{\varepsilon}_{min}} = MIN\left(\frac{\overline{\dot{\varepsilon}_{xx}} + \overline{\dot{\varepsilon}_{yy}}}{2} + \sqrt{\left(\frac{\overline{\dot{\varepsilon}_{xx}} - \overline{\dot{\varepsilon}_{yy}}}{2}\right)^2 + \overline{\dot{\varepsilon}_{xy}}^2}; \frac{\overline{\dot{\varepsilon}_{xx}} + \overline{\dot{\varepsilon}_{yy}}}{2} - \sqrt{\left(\frac{\overline{\dot{\varepsilon}_{xx}} - \overline{\dot{\varepsilon}_{yy}}}{2}\right)^2 + \overline{\dot{\varepsilon}_{xy}}^2}\right) \tag{3.5}$$

As underlined by previous authors (e.g. Ward, 1998a; Pancha, 2006), the conversion of surface strain to a scalar moment rate bears large uncertainties and there is no unique method. We use three different equations for calculating the moment rate, to propagate this uncertainty up to the final moment estimate:

- The Working Group on California Earthquake Probabilities, 1995, uses the difference between the principal strain rates:

$$\dot{M}_{0G} = 2\mu AH(\overline{\dot{\varepsilon}_{max}} - \overline{\dot{\varepsilon}_{min}}) \tag{3.6}$$

- Savage and Simpson, 1997, propose that the scalar moment rate is at least as large as:

$$\dot{M}_{0G} = 2\mu AHMAX(|\overline{\dot{\varepsilon}_{max}}|, |\overline{\dot{\varepsilon}_{min}}|, |\overline{\dot{\varepsilon}_{max}} - \overline{\dot{\varepsilon}_{min}}|) \tag{3.7}$$

- Stevens and Avouac, 2021, uses the second invariant, which reflects the magnitude of the total strain rate:

$$\dot{M}_{0G} = C_g \mu AH \sqrt{\overline{\dot{\varepsilon}_{xx}}^2 + \overline{\dot{\varepsilon}_{yy}}^2 + 2\overline{\dot{\varepsilon}_{xy}}^2} \tag{3.8}$$

With μ the shear modulus and H the seismogenic thickness. C_g is a geometric coefficient, it depends on the orientation and dip angle (δ) of the fault plane accommodating the strain. Following Stevens and Avouac, 2021, for dip-slip faults with uniaxial compression, $C_g = 1/[sin(\delta).cos(\delta)]$. A dip of 45° corresponds to a geometric coefficient equal to 2, which is the value assumed by Working Group on California Earthquake Probabilities, 1995 and Savage and Simpson, 1997, as well as in a large part of the literature (e.g. Ward, 1998a; Jenny et al., 2004; Bird and Liu, 2007; D'Agostino, 2014). In their study focused on the Himalayan region, Stevens and Avouac, 2021 consider two values, corresponding to dips between 45° ($C_g = 2$) and 15° ($C_g = 4$), to account for the low-angle thrust faults in the region. Here we consider two values 2 and 2.6, which is the range corresponding to a dip between 25° and 65°.

The uncertainty on the shear modulus is also taken into account, including two alternative values $3.3 * 10^{10} N.m^{-2}$ and $3.0 * 10^{10} N.m^{-2}$ (e.g. Dziewonski and Anderson, 1981). Whereas for the seismogenic thickness (H in Equations 3.6 to 3.8), as there is considerable uncertainty, we use three alternative values (5, 10, and 15 km). This seismogenic (or elastic) thickness is the average thickness over which a region's principal faults store and release seismic energy (Ward, 1998a). The thickness considered in the literature usually varies between 10 and 15km. Pancha, 2006 used a fixed seismogenic thickness of 15km throughout the Basin and Range region in Western US. D'Agostino, 2014 applied a thickness of 10 ± 2.5km throughout the Apennines in Italy, whereas Stevens and Avouac, 2021 considered 15km in the India-Asia collision zone. In a study extending over Canada, Ojo et al., 2021 constrained the crustal thickness inferred from ambient seismic noise tomography.

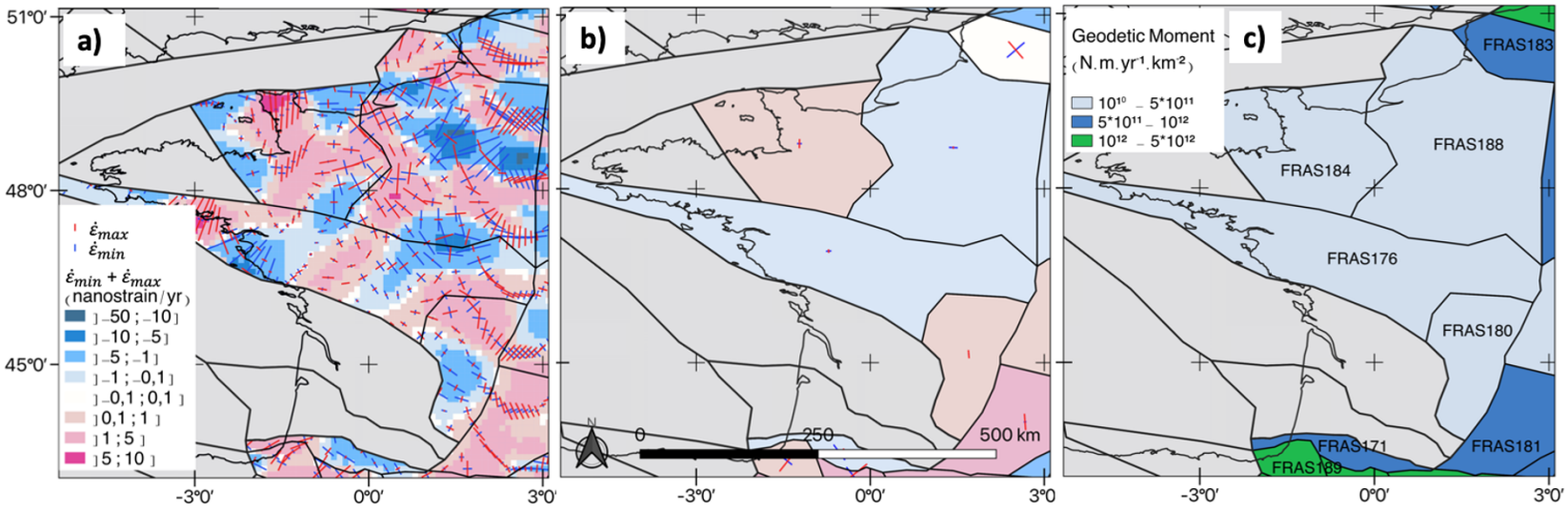

Fig. 3.8: Scalar geodetic moment computed from a mean strain tensor, example for the source zones in Northwestern France. a) Horizontal strain rate tensor from Piña-Valdés et al., 2022 best model, for each grid cell : principal components of the strain rate tensor ($\dot{\varepsilon}_{min}$ in red; $\dot{\varepsilon}_{max}$ in blue) and deformation style ($\dot{\varepsilon}_{min} + \dot{\varepsilon}_{max}$, red : extension, blue : compression). b) Mean strain rate tensor per source zone, mean principal components in the source zone ($\bar{\dot{\varepsilon}}_{min}$ and $\bar{\dot{\varepsilon}}_{max}$) (Equation 2.23, 2.24). c) One estimate for the geodetic moment rate within the source zone, using the strain rate best model of Piña-Valdés et al., 2022 and considering a depth of 10km, a shear modulus of $\mu = 3.3 * 10^{10} N.m^{-2}$, the equation from Savage and Simpson, 1997, and a geometric coefficient C_g equal to 2. Acronyms of ESHM20 area source zones are indicated.

A geodetic moment rate distribution per area source zone

The aim is to obtain a distribution for the moment rate within an area source, that is representative of the uncertainties. Figure 3.9 displays the exploration tree set up to combine 12 different selections of GNSS stations (choice on the class and on the radius applied to identify outliers), with 12 different regularizations of the GNSS velocities inversion to determine strain rates (choice of the distance and spatial weighting scheme, choice of the weighting threshold) and with finally 36 different parametrizations to calculate the moment rate from the strain rates. For a given source zone area, we obtain 5184 alternative moment rate estimates ($12 * 12 * 26$). Figure 3.9b displays the distribution obtained for the area source zone hosting Paris in France. The variability of the moment rate is significant, the value corresponding to the percentile 84^{th} is three times larger than the value corresponding to the percentile 16^{th}.

To understand which parameters, or decision, control the most the overall variability on the geodetic moment, different parts of the tree are explored (Figure 3.10, see Mariniere et al., 2021). The analysis is led in 3 example area source zones characterized by different seismic activity: southern Brittany in France, located in an intracontinental area and characterized by a low seismic activity, a large source zone in Fennoscandia in a very low seismicity region, and northern Tuscany in Italy, a moderate seismic area (see Fig. 3.11 for locations). For every parameter choice, the entire tree is explored keeping fixed the other parameters, then from the distribution obtained the mean as well as the percentiles 16^{th} and 84^{th} are estimated. For example, exploring separately the alternative branches corresponding to the three different selections of GPS stations yields 3 distributions, made of 1728 moment estimates each (in green). Exploring separately the branches based on the 2 alternative spatial weighting schemes yields 2 alternative distributions, made of 2592 moment estimates each (in pink). The larger is the dispersion obtained between the alternative mean values of the distributions, the larger is the contribution of this parameter uncertainty to the overall moment variability.

The results show that the uncertainty on the seismogenic thickness controls the overall moment variability, for all area source zones. The geodetic moment exhibits a linear variation with both the seismogenic thickness and the shear modulus. Except for the shear modulus for which a limited range of values is explored, all other parameters' uncertainties also contribute to the overall variability. It is interesting to note that the exact selection of GNSS stations has an influence on the moment rate estimates only in low seismicity areas (Fennoscandia and Southern Brittany), but no impact in the moderate to high seismicity areas (such as northern

Tuscany). This phenomenon can be attributed to the dominance of strong strains in high-deformation zones, where even lower-quality stations provide accurate measurements at a first-order approximation. Conversely, in low-deformation areas, the measured signal is close to the noise level. Consequently, the exclusion or inclusion of one or more stations has a substantial impact.

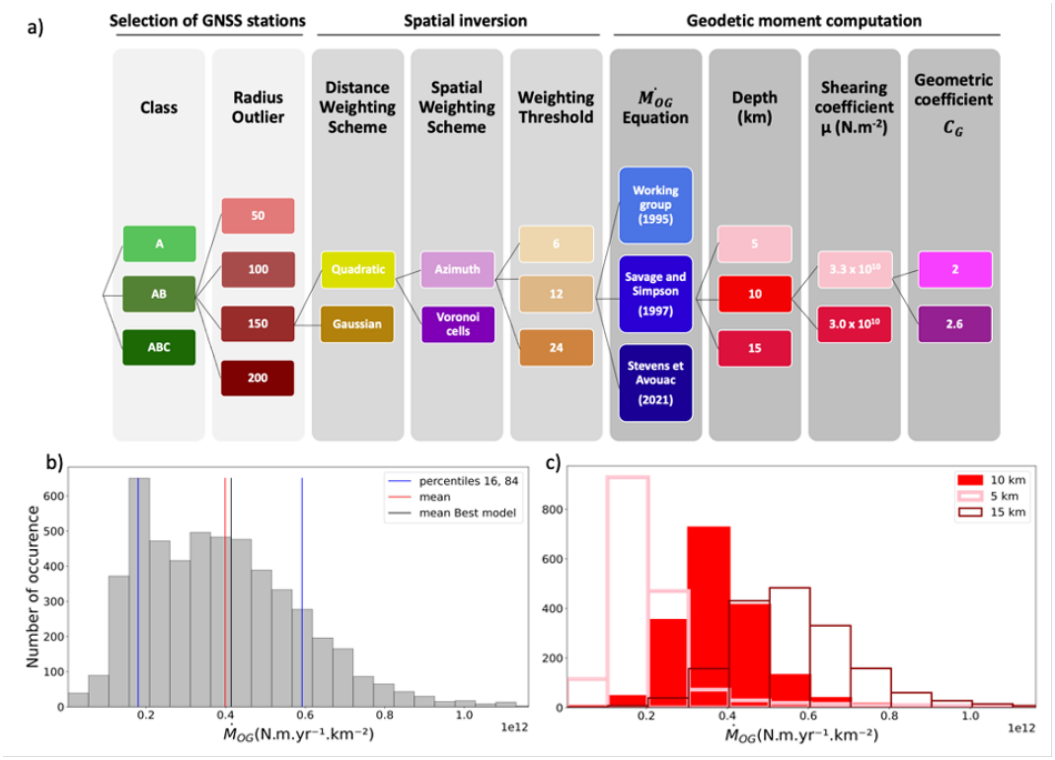

Fig. 3.9: Determination of a distribution for the moment rate per area source zone, taking into account the uncertainties on the different steps. a) Exploration tree to account for the uncertainty on the exact set of GNSS stations used, on the technique applied to infer strain rates from the geodetic velocities, and on the parameters used to calculate the moment rate within an area source. b) distribution of the geodetic moment rate estimates (5184 values) obtained for the example source zone Parisian Basin in France (FRAS188 in ESHM20), mean value (red) and percentiles 16^{th} and 84^{th} (blue). c) Three alternative distributions for the moment rate estimates, depending on the choice of the seismogenic depth, example source zone Parisian Basin in France

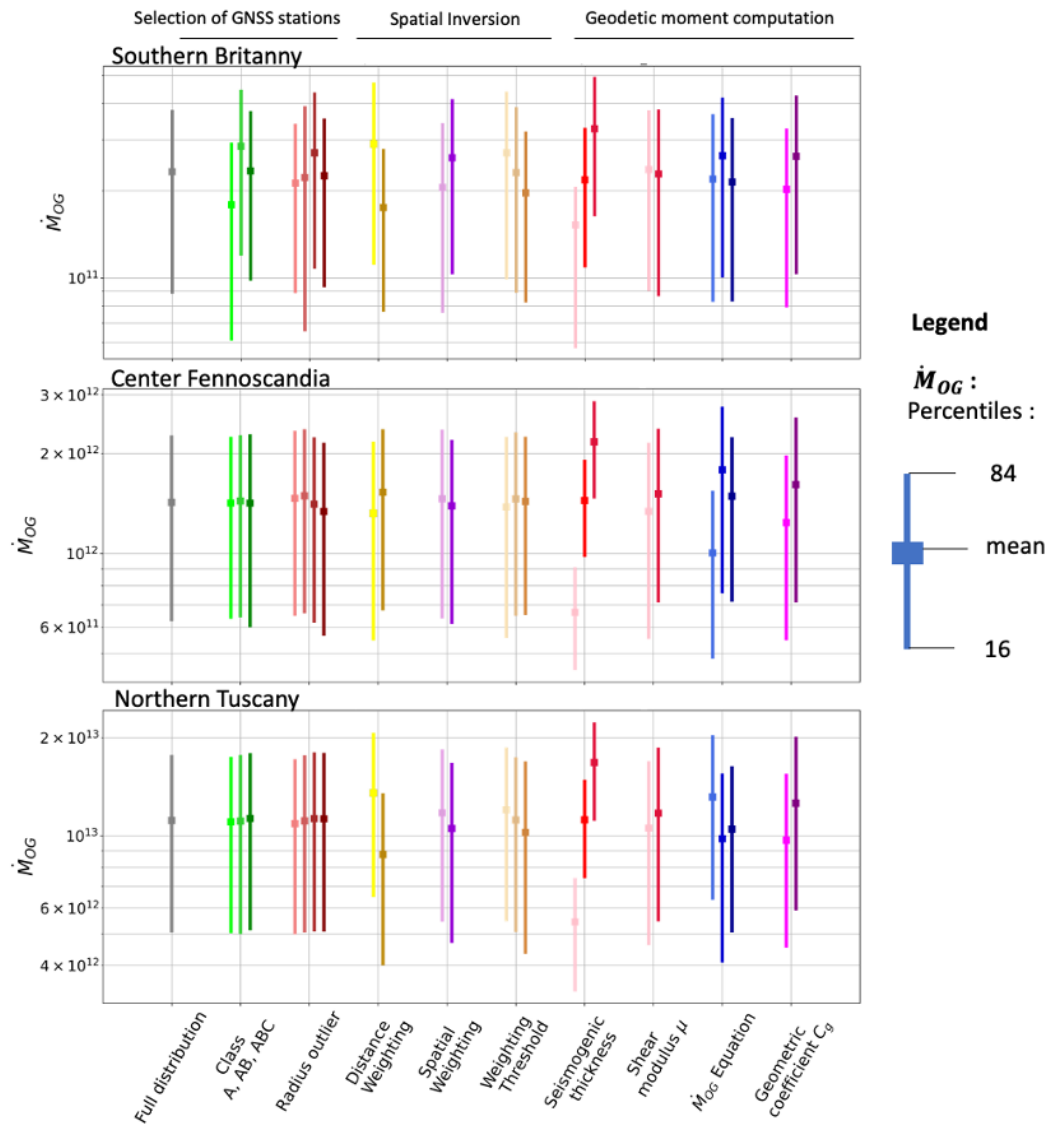

Fig. 3.10: Distribution for the geodetic moment rate ($\dot{M}_{0G}$) and identification of controlling parameters, in 3 example source zones: southern Brittany (FRAS176), Fennoscandia (SEAS410), and Northern Tuscany in Italy (ITAS335), see location in Figure 3.11). Mean value (square), as well as 16^{th} and 84^{th} percentiles (vertical bar). "Full": full exploration of the tree (5184 branches' combination and moment values). "Class A, AB, ABC": 3 different sets of GNSS stations, according to quality (1728 values each). "Radius outlier": choice of the spatial radius for discarding outliers (50, 100, 150, 200 km, from salmon to dark red, 1296 values each). "Distance weighting scheme": choice of the decay function used for interpolation, whether Gaussian or Quadratic (2592 values each). "Spatial weighting scheme": choice of the method for spatial inversion, whether Azimuth or Voronoi. "Weighting Threshold": Choice of the threshold value on the distance weighting function (6,12, 24, increasing smoothing, beige to brown, 1728 values each). "Seismogenic depth": elastic depth (5, 10 and 15 km, pink to red, 1728 values each). "μ": choice of shear modulus value ($3.3 * 10^{10} N.m$ (pink), $3 * 10^{10} N.m$ (red)). "$\dot{M}_{0G}$ equation": choice of the geodetic moment equation, see the text. "C_g". Choice of the geometric coefficient parameter, 2 (pink) or 2.6 (purple)

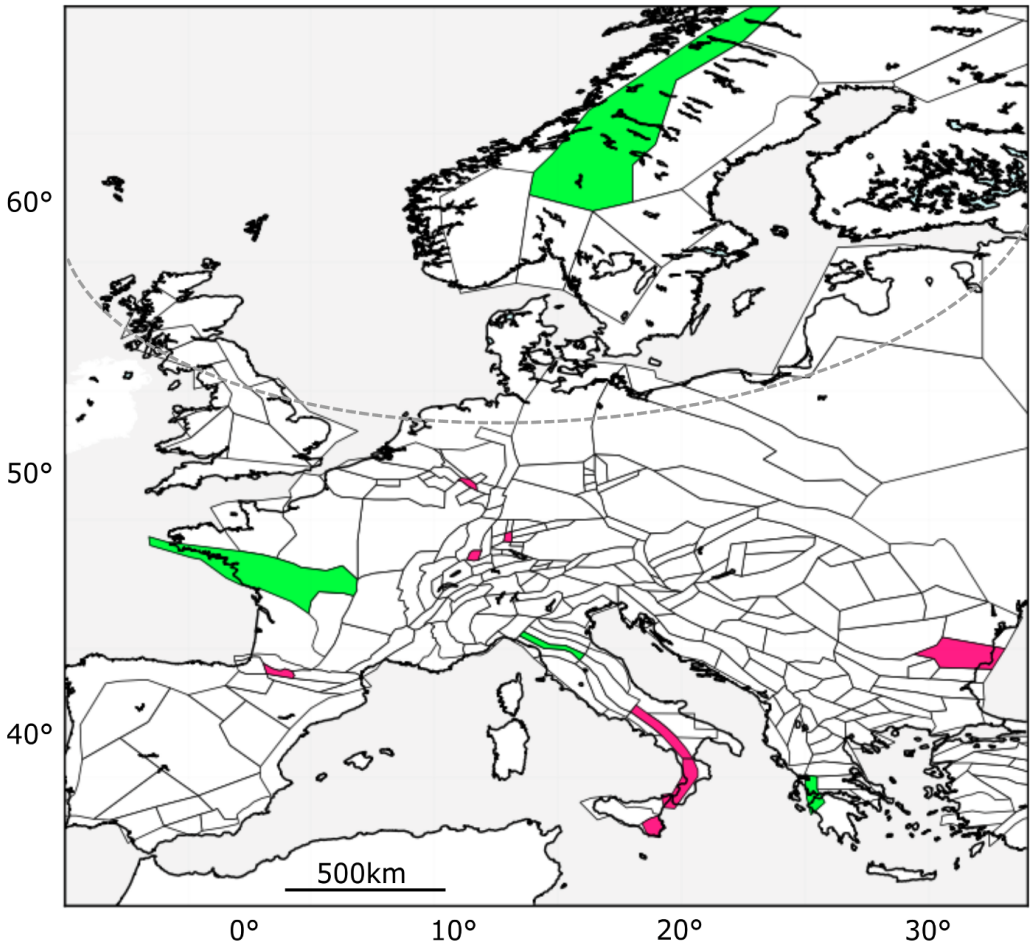

Fig. 3.11: Area source zones mentioned throughout the manuscript. In green: example source zones in section 3.2.3: FRAS176 in Southern Brittany in France, SEAS410 in Fennoscandia, ITAS335 in northern Italy, as well as GRAS257 in Greece in section 3.2.4. In pink : the eight source zones where the geodetic moment estimates is much lower than the seismic moment estimates (section 3.2.4 and Fig. 3.15). The grey dashed line represents the zones considered affected by the Scandinavian GIA, including those intersecting this line and those located to the north. The selection is based on the vertical velocity signal (Piña-Valdés et al., 2022) and includes 18 zones.

3.2.4 Is ESHM20 earthquake forecast consistent with the tectonic loading measured by geodesy?

Our aim is to compare the moment rate corresponding to the long-term ESHM20 source model with the geodetic moment rate. We acknowledge that the comparison between deformation measurements performed over a few decades and a source model built for hazard assessment must be done with caution. The ESHM20 earthquake forecast relies on earthquake catalogs extending over several centuries. The recurrence model is in general anchored on the observed seismic rates extrapolated up to magnitudes that correspond to the largest possible events in the area sources. The model thus relies on past seismic rates as well as on a wider analysis of the seismogenic potential of the area. The model also includes our current knowledge about active faults (fault traces, segmentation, extension at depth). Geodetic information has been used in some cases for estimating the deformation accumulating along these faults (Basili et al. in press). The strain model thus is not strictly independent from the source model, however GNSS velocities have not been directly used to build the ESHM20 source model. The strain rate model can be used to test the ESHM20 source model and evaluate how realistic the model is.

Correlation between geodetic and seismic moment rates at the scale of Europe

The geodetic moment rate quantifies the ground surface deformation, that encompasses both seismic and aseismic processes. The mean moment estimates obtained in every area source zone are displayed in Figure 3.12. Overall, geodetic moment rates appear larger or equal to seismic moment rates, similarly to the findings of many previous studies (e.g. Ward, 1998a; Jenny et al., 2004; Mazzotti et al., 2011). Largest geodetic and seismic rates are found in Greece, in Italy and in the Balkans. The distribution in space of the geodetic moment rate is much more smoothed than the seismic moment rate. One explanation could be that the deformation measured by geodesy is more representative of long-term processes than the earthquake catalogs. If earthquake catalogs of much longer time windows were available (e.g. 100,000 years), would the spatial distribution of the seismic moment rates be more alike the spatial distribution of the geodetic moment rates? Another explanation could be that the geodetic moment rate has a lower resolution in space than the seismic moment rate inferred from the modeling of earthquake recurrence. Indeed, because of the smoothing procedure applied to derive the strain rates, the geodetic moment is strongly correlated spatially. Besides, we observe that in low-seismicity regions,

geodetic moment rates reach a plateau (in green, in mainland Spain, northern Europe and Fennoscandia) most probably because of a sensitivity threshold of the velocities measured by GNSS, whereas the seismic moment rates go down to much lower values.

Figure 3.13 demonstrates a remarkable linear correlation between the geodetic and seismic moment rates above $\sim 2.10^{11} N.m.yr^{-1}.km^{-2}$. In general, in the most active regions in Southern Europe, the geodetic moment rates are well correlated with the seismic moment rates. On the contrary, in the less active regions in northern Europe, above $\sim 50°$ latitude, the geodetic moment appears completely decorrelated from the seismic moment. Seismic moment rates decrease to levels as low as $10^9 - 10^{10} N.m.yr^{-1}.km^{-2}$, whereas geodetic moment rates reach a plateau around $10^{12} N.m.yr^{-1}.km^{-2}$. The deformation measured in Fennoscandia and surrounding regions might be mostly related to the post-glacial rebound and only a very small part of it might be tectonic deformation (Keiding et al., 2015; Craig et al., 2016).

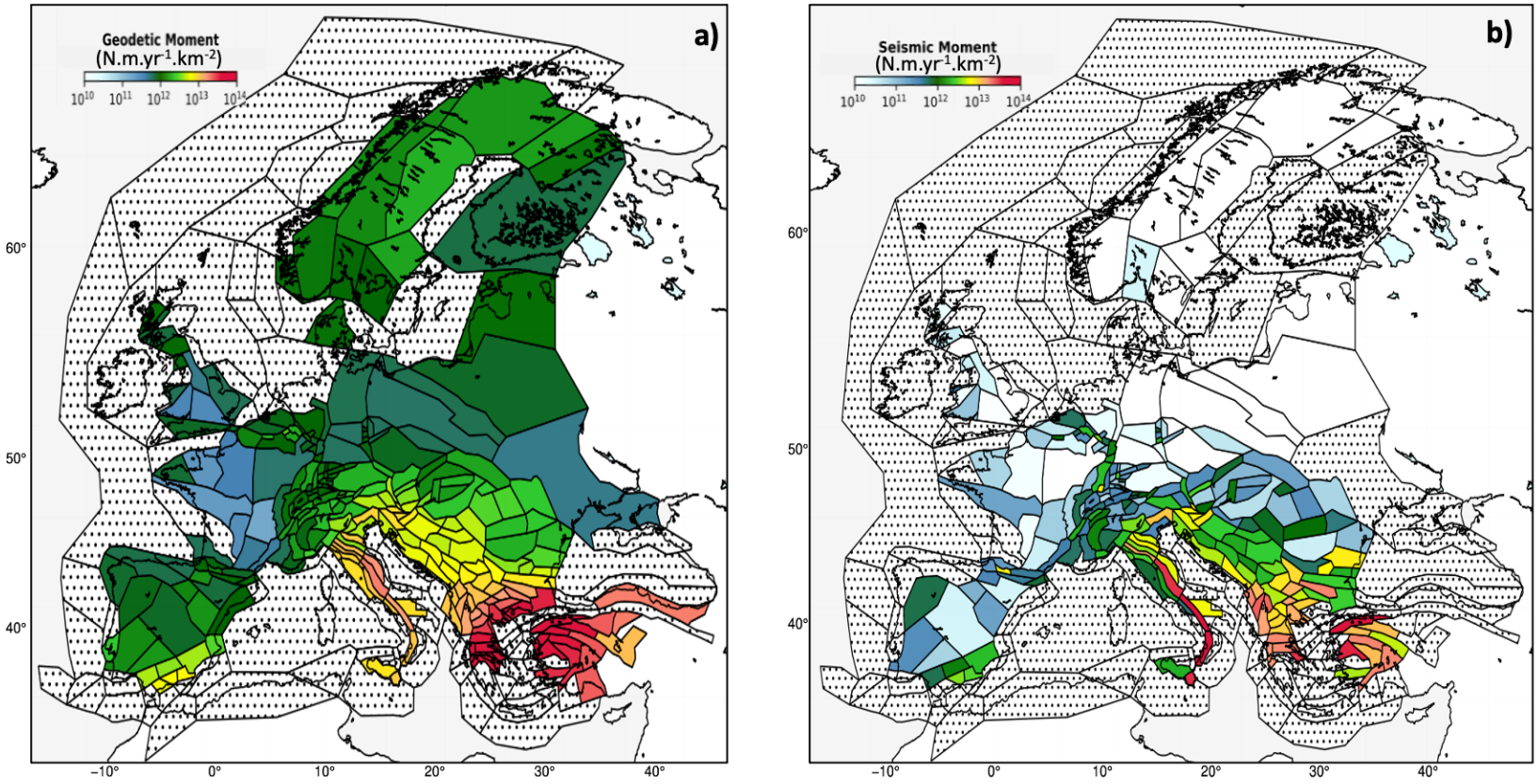

Fig. 3.12: Mean geodetic and seismic moment rates within the ESHM20 area source zones. a) Mean geodetic moment ($\dot{M}_{0G}$) based on the strain rates, mean of the distribution obtained by exploring uncertainties; b) Mean seismic moment ($\dot{M}_{0S}$) estimated from the ESHM20 source model logic tree. Area sources with more than 35% of surface off-shore, or where the density of GNSS station is too low (≤ 1 station per $100000 km^2$) are discarded.

Comparison of the moment rates distributions

Rather than comparing only mean values of distributions, the comparison of the full distributions can be more instructive as the uncertainties are accounted for. For a given area source zone, the distribution for the geodetic moment rate relies on 5184 alternative values (see Section 3.2.3), whereas the distribution for the seismic moment is built from the 21 alternative branches in the ESHM20 source model logic tree, taking into account the weights associated to each branch. To achieve parity in the number of data points with the geodetic moment rate distribution, we multiplied the seismic moment associated with each branch by its weighting coefficient. Subsequently, we duplicated this distribution to align the number of elements in the two datasets.

In Fennoscandia, the geodetic moment estimates are on average one hundred to three hundred higher than the seismic moment estimates ($log_{10}(\dot{M}_{0S}/\dot{M}_{0G})$ varies between -2 and -2.5, in red in Fig. 3.13). The uncertainty on the geodetic moment is large, but still there is no overlap between the two distributions (example source zone SEAS410, Fig. 3.14). In most area sources below latitude 52°, geodetic moment estimates are larger or equal to seismic moment rates, up to five times higher on average than seismic moment rates ($log_{10}(\dot{M}_{0S}/\dot{M}_{0G})$ varies between 0 and -0.7, in green and yellow in Fig. 3.13). In some area sources such as GRAS257 in Greece, the mean geodetic moment rate results five times higher than the seismic moment rate and the two distributions only partially overlap. In other sources, such as FRAS176 in France or ITAS335 in Italy, the seismic and geodetic distributions are very consistent.

We quantify the overlap between the geodetic and the seismic distributions, for all area sources (Fig. 3.15). As the distributions are mostly unimodal (one mode only), the overlap between the distributions is usually increasing with closer mean moment values. In the most seismically active regions in Europe, i.e. in Greece, Italy, the Balkans, as well as in some parts of France and Switzerland, the seismic and geodetic moment estimates are rather consistent (overlap between 35 and 80%, in blue); whereas elsewhere the fit is quite poor (overlap lower than 30%, in red).

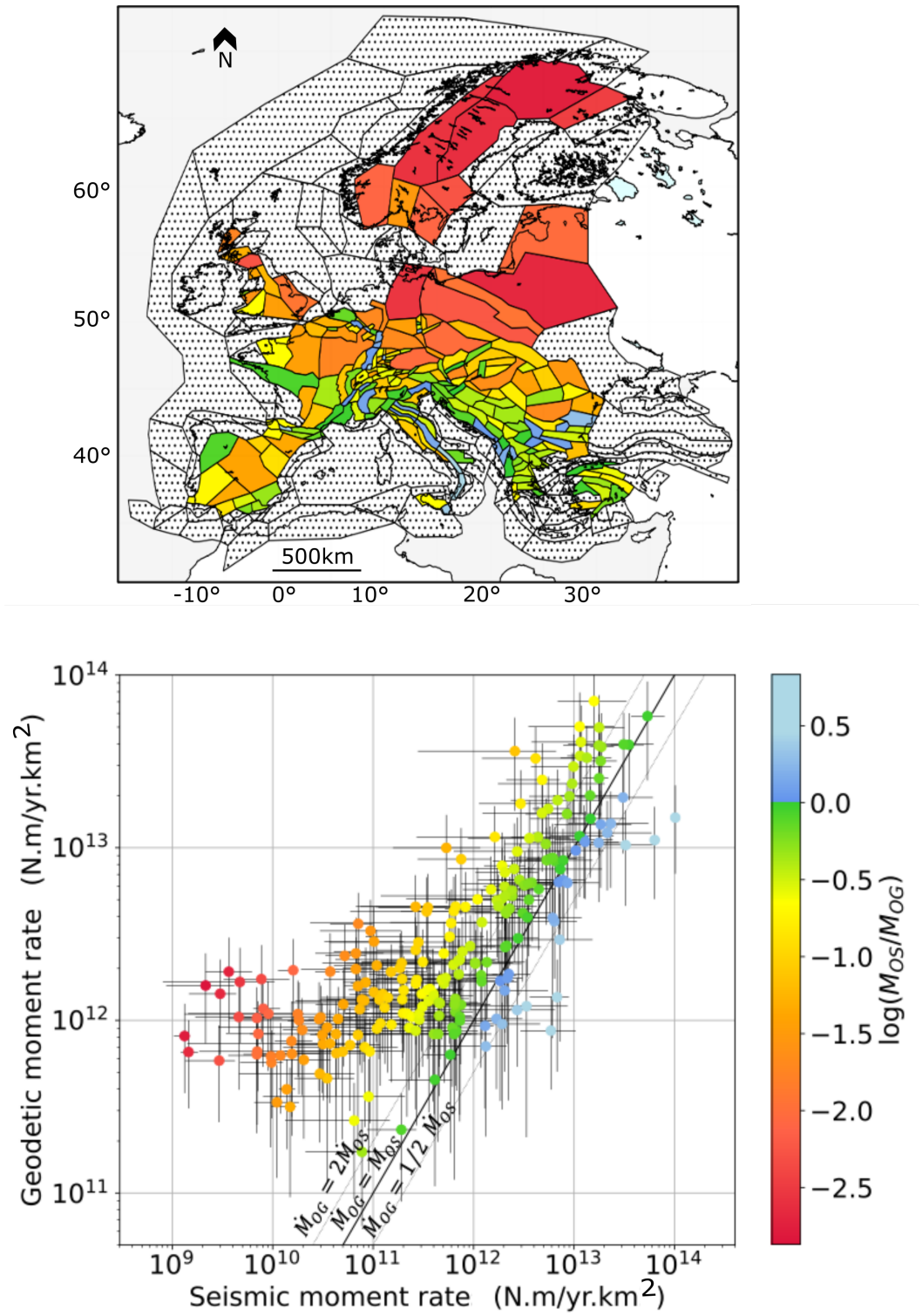

Fig. 3.13: Comparison between geodetic and seismic moment in Europe at the scale of the ESHM20 source zone : mean $\dot{M}_{0G}$ versus mean $\dot{M}_{0S}$ at the scale of the source zone (uncertainty range 16^{th} to 84^{th} percentile indicated). Sources zones locations are indicated : 1: FRAS176 (southern Britanny) ; 2 : FRAS188 (Parisian Basin) ; 3 : ITAS323 (Northern Tuscany) ; 4 : SEAS410 ; 5 : GRAS257 ; 6 : ITAS335 ; 7 : FRAS164 ; 8 : CHAS071 ; 9 : DEAS113 ; 10 : DEAS109 ; 11 : ITAS339 ; 12 : BGAS043 ; 13 : ITAS331 ; 14 : ITAS308.

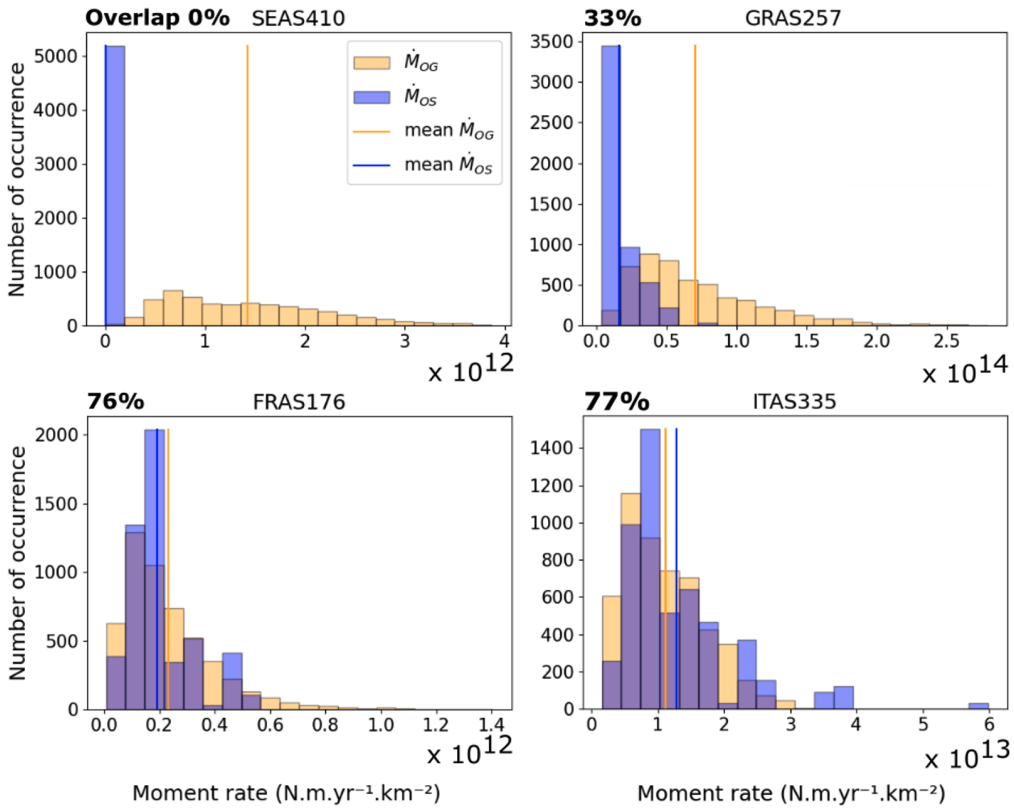

Fig. 3.14: Comparison of seismic and geodetic moment rate distributions, for 4 example source zone in Fennoscandia (SEAS410), Greece (GRAS257), France (FRAS176) and Italy (ITAS335), source zones in Fig. 3.11. The overlap is computed as : 0 if $MIN(\dot{M}_{0G}) > MAX(\dot{M}_{0S})$ or if $MIN(\dot{M}_{0S}) > MAX(\dot{M}_{0G})$ and as $\sum_{bins} MIN(\dot{M}_{0G}, \dot{M}_{0S})$/ number element($\dot{M}_{0G}$).

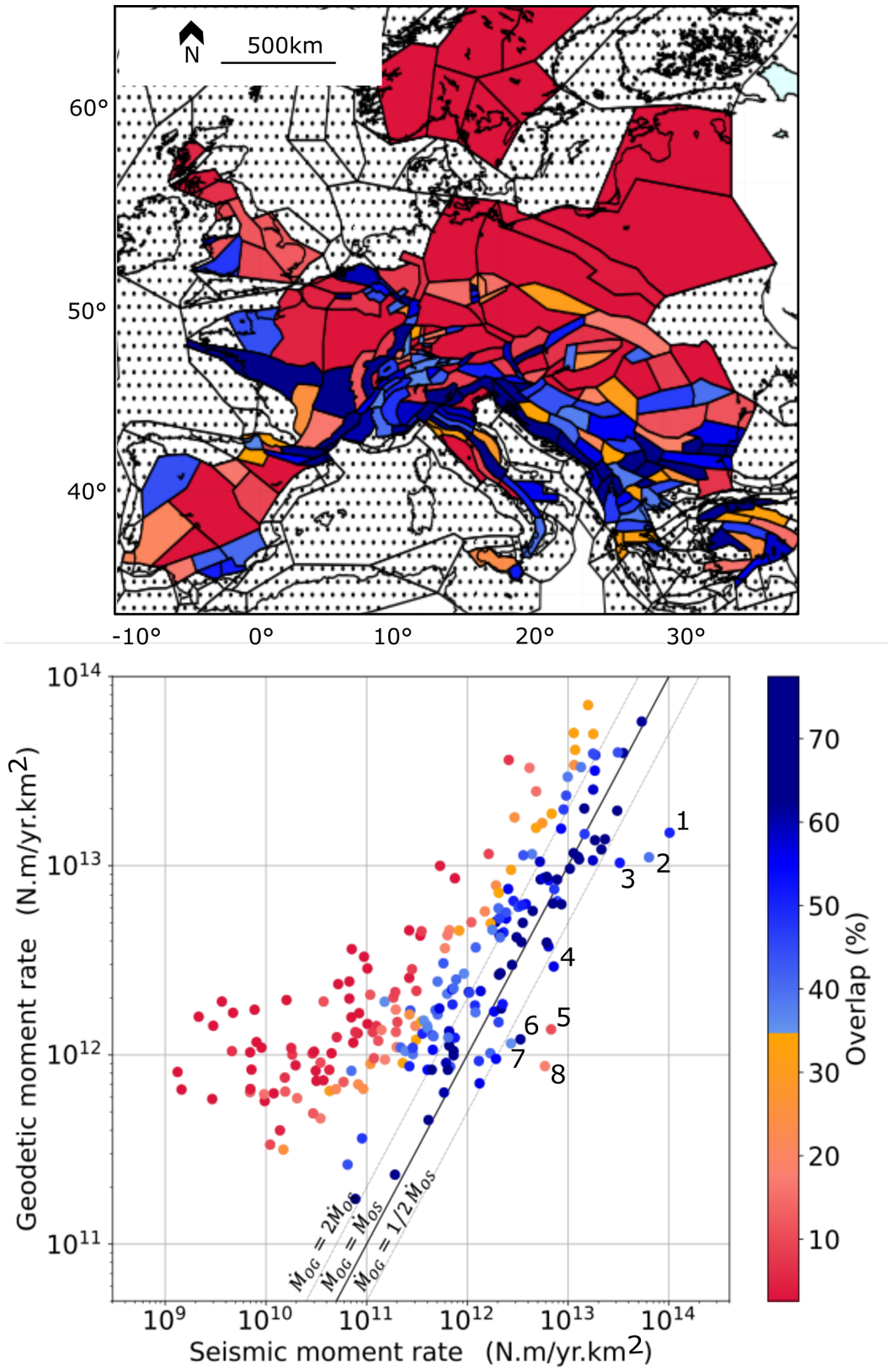

Fig. 3.15: Comparison between geodetic and seismic moment rate mean estimates, within the ESHM20 area source zones (227 source zones considered), estimates for the overlap between the seismic and geodetic distributions. Area source zones where the geodetic moment rate is much lower than the seismic moment rate : 1 : ITAS308 , 2 : ITAS331 ; 3: ITAS339 , 4 : BGAS043 , 5: FRAS164, 6: DEAS113, 7: DEAS109, 8: CHAS071 (see the text and Fig. 3.11).

Potential inconsistencies revealed in the ESHM20 source model

Let's have a closer look at the eight area sources where the geodetic moment rate results on average significantly lower than the seismic moment rate (data points that are below the straight line $\dot{M}_{0G} = \dot{M}_{0S}/2$ in Fig. 2.9). Are these seismic moment rates abnormally high ? Based on this observation, should we conclude that the seismic rates are most probably over-estimated ?

These area sources fall in three categories:

1. Small size area, below the resolution of the geodetic signal (FRAS164, CHAS071, DEAS113, DEAS109). The source zone FRAS164 in Western Pyrenees is a small area with high seismic activity in comparison with the neighboring area zones. The geodetic signal has a too large spatial wavelength to capture these rapid spatial changes. The source zones CHAS071, DEAS113 and DEAS109 are not as active, but they are also small size area sources. In these cases, the difference between the geodetic and the seismic moment estimates is expected and does not question the validity of earthquake recurrence model.

2. Areas where the ESHM20 recurrence model was anchored on the upper magnitude range rates, predicting in the moderate magnitude range much larger seismic rates than what has been observed in the past (ITAS339, BGAS043) In this case, the earthquake recurrence model might be over-estimating seismic rates.

3. Areas where unusual earthquake recurrence models have been proposed to account for two different slopes observed in the Gutenberg-Richter model (area model, ITAS331, ITAS308)

In both area sources, the slope of the recurrence model in the upper magnitude range (mostly historical period) is lower than the slope in the moderate magnitude range (mostly instrumental period). This is quite unusual and contradicts the universality of the Gutenberg-Richter model characterized by a unique b-value. It is interesting to note that the fault model branches overall provide a moment range that is consistent with the geodetic moment range, whereas the area model branches lead to much higher moment estimates (Fig. 3.16). The present results could constitute an argument for fitting the recurrence model on the moderate magnitude rates only.

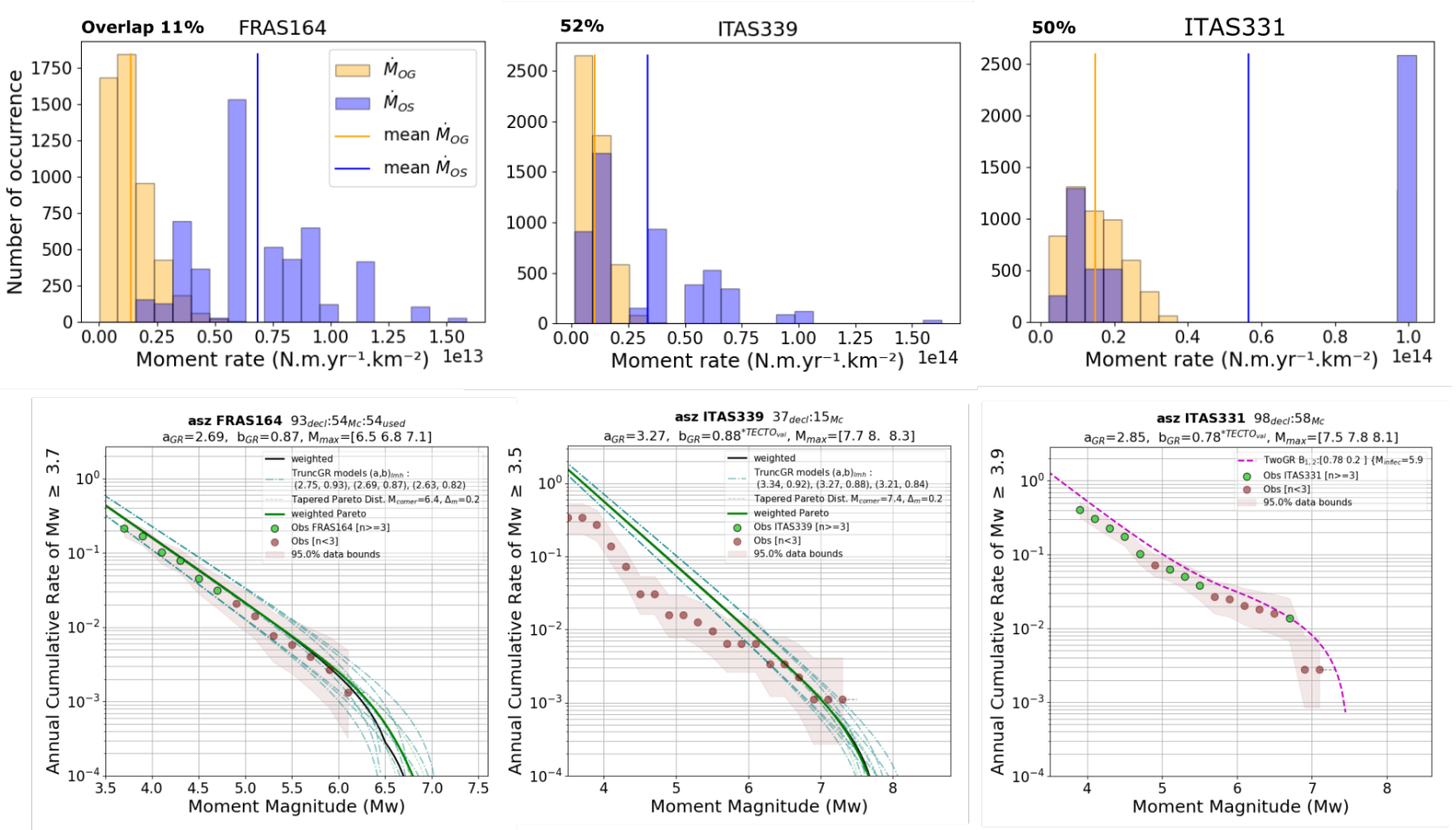

Fig. 3.16: Distributions of geodetic (orange) and seismic moment rates (blue) for three of the source zones, and the associated Magnitude Frequency Distributions taken from Danciu et al., 2021. Sources zones located on Figure 3.11.

The consistency between the geodetic and seismic moments depends on the activity level, the spatial scale, and the source model

Figure 3.17 provides an overall view on the comparison between geodetic and seismic moment estimates at the scale of Europe, and how this comparison varies when subsets of the data are selected. Area source zones are grouped according to the level of the geodetic moment estimates (dark and light green, red), showing that the consistency systematically improves with increasing deformation.

In area source zones affected by the glacial isostatic adjustment (18 zones, selected based on the vertical velocity signal (Piña-Valdés et al., 2022)), both the geodetic and the seismologic moments are low. But a noticeable feature is that the moment estimate based on modeled earthquake recurrence distributions is two orders of magnitude lower than the geodetic moment. This indicates that the deformation processes involved are mostly aseismic, which is compatible with the processes involved in glacial isostatic adjustment that result in a viscous asthenospheric flow and a large scale bending of the overlying lithosphere. In those areas, the surface deformation measured by geodesy is not a good proxy for the seismic activity and can not be used directly to constrain seismic hazard models.

Considering area sources with the best constrained recurrence models (at least 30 events used, see Danciu et al., 2021), the consistency between both moment rate estimates is strongly improved.

Considering only the ESHM20 model branch based on smoothed seismicity and faults, the seismic moment rate estimates are overall less consistent with the geodetic estimates (‘2)’ in left column, Fig. 3.17). We group the area zones that include faults on one side, and the area zones that do not include any fault in the model on the other side. We observe that the geodetic and seismic moment rates are much better correlated in the first group, as the faults have mostly been characterized in the seismically active parts of Europe. This also confirms that the inclusion of fault slip rates are a valuable constraint in addition to the seismic catalogue to assess the recurrence interval. In figure 3.24, we can observe that the inclusion of faults improves the consistency with geodetic estimates even in slowly deforming areas. This suggests that the identification of active faults in slowly deforming areas may strengthen the estimate of the recurrence interval in areas that are characterized by both a slow deformation rate and rare seismic events. This may also suggest that the discrepancy between seismic moment rate and geodetic moment rate in slowly deforming areas may be due to missing events in the seismic catalogue or a too short

observational time range, ending in an underestimated seismic moment that is not representative of the long term activity of the area.

At last, we check if the fit between geodetic and seismic moment rates varies with the model selected to extrapolate earthquake rates in the upper magnitude range (area branch). The fit results slightly better using the classical Anderson and Luco, 1983 form 2 than the Pareto distribution. This result is expected, as the Pareto distribution implies a stronger decrease of seismic rates in the upper magnitude range with respect to Anderson and Luco distribution (therefore a lower seismic moment rate).

As the size of some source zones is too small for the comparison to be meaningful (see Section 3.2.4), we also perform the comparison at the scale of the macrozones. Macrozones are used at different levels in the building of the ESHM20 source model, here we use the macrozones named 'TECTO' which corresponds to the merging of several area source zones according to tectonic criteria (Fig. 3.7). Danciu et al., 2021 used these macrozones to evaluate the b-value for poorly constrained area source zones. As expected, at the scale of Europe, the correlation between the seismic and geodetic moment rates is slightly improved when considering the macrozones, that cover a much larger spatial region than the individual area source zones (right column in Fig. 3.7, mean values of distributions tend to be closer to 0). Performing the comparison at the scale of the macrozones, a rather good fit is obtained for the whole Euro-Mediterranean region, except in Spain (Fig. 3.18).

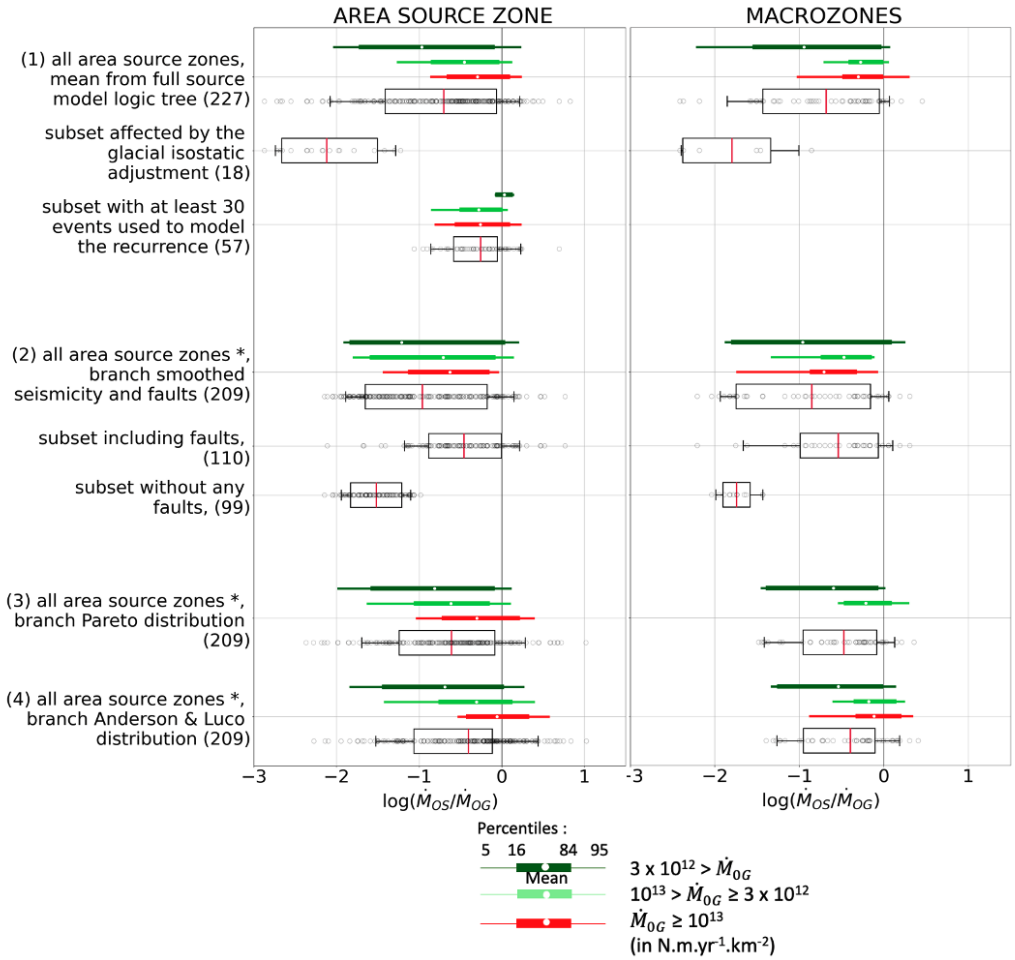

Fig. 3.17: Comparison of the correlation between $\dot{M}_{0S}$ and $\dot{M}_{0G}$ for the area source zone and for the macrozone depending on geodetic and seismic activity, and ESHM20 source model logic tree. The figures depict $log_{10}(\dot{M}_{0S}/\dot{M}_{0G})$. The black whisker plot illustrates the distribution of all zones in the studied subset. The red, light green, and green whisker plots respectively represent subsets of zones with geodetic moments below $3 * 10^{12} N.m.yr^{-1}.km^{-2}$, between $3 * 10^{12}$ and $10^{13} N.m.yr^{-1}.km^{-2}$, and $10^{13} Nm.yr^{-1}.km^{-2}$, reflecting zones with low, moderate, and high deformation. The star (*) indicates that zones affected by the Fennoscandian Glacial Isostatic Adjustment (GIA) are not represented, defined in figure 3.11. (1) The first line presents the distribution of all source zones (227) and all macrozones (51) studied, along with the subset of zones affected by GIA and with at least 30 events used to compute the recurrence model, (2), (3), (4) present a comparison between $\dot{M}_{0S}$ and $\dot{M}_{0G}$ computed from different branches of the logic tree ESHM20.

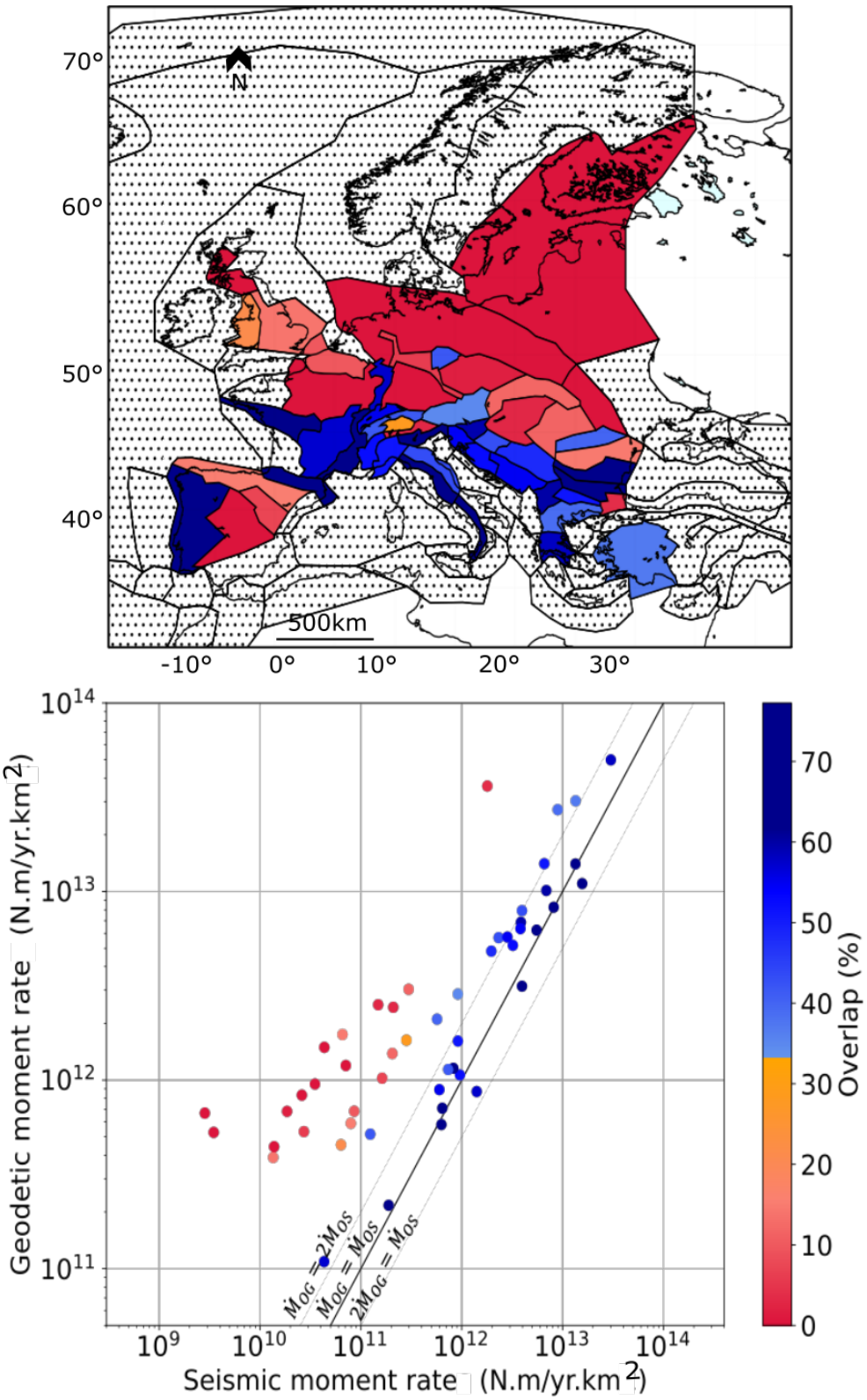

Fig. 3.18: Comparison between geodetic and seismic moment rate mean estimates, within the ESHM20 'TECTO' macrozones (51 macrozones considered), the overlap between the seismic and geodetic distributions is indicated

3.2.5 Focus in Italy

Figure 3.19a presents a magnified view of figure 3.13a in the central Apennines. As highlighted previously, the central zone (ITAS317) demonstrates a mean seismic moment ($\dot{M}_{0S}$) exceeding the mean geodetic moment ($\dot{M}_{0G}$) (Log($\dot{M}_{0S}/\dot{M}_{0G}$) > 0). Conversely, the surrounding zones exhibit a geodetic moment significantly higher than the seismic moment ($log_{10}(\dot{M}_{0S}/\dot{M}_{0G}) \sim -1$, overlap $< 20\%$).

However, as seen at the scale of macrozones (Fig. 3.18), this divergence is smoothed at a larger scale. What is the impact of the scale at which we compare seismic and geodetic moments on the result? In this section, we aim to assess this impact at a smaller scale than previously considered, along a profile A, B passing through Rome (as illustrated in figure 3.13b). Given our objective to examine the evolution of seismic and geodetic moments along the profile, we will employ the Fault + smoothed seismicity branch of ESHM20 model for comparison with the average geodetic strain rate solution plotted on the same grid scale.

Figure 3.19c presents a comparison between the estimated $\dot{M}_{0G}$ and $\dot{M}_{0S}$ at the scale of source zones along the cross-section AB. $\dot{M}_{0G}$ consistently exceeds the mean $\dot{M}_{0S}$ in all source zones (5 to 10 times larger), except in the central source zone, which is the most seismically active and encompasses several faults. In this particular source zone, named ITAS317, $\dot{M}_{0S}$ represents approximately two-thirds of the geodetic moment estimated from strain rates. On the other hand, the seismic moment computed as the weighted mean of all model is higher than the geodetic moment rate in this zone (as highlighted in figure 3.17a).

To obtain values at a smaller scale, we calculate the summation of $\dot{M}_{0S}$ and $\dot{M}_{0G}$ within the grid cells that belong to polygons approximately 14 km thick and 50 km long (the polygons in figure 3.19b indicate the edges of all considered slices), as illustrated in figure 3.19d. This comparison reveals that the seismic moment is concentrated in fault zones (marked with small blue arrows) and exhibits a sharp decrease moving away from the fault zone. On the other hand, the geodetic moment rates reach their maximum ($4 * 10^{13} N.m.yr^{-1}.km^{-2}$) when crossing the eastern fault (at the same location as the maximum observed for $\dot{M}_{0S}$). However, this time, the decrease is not sharp but descends slowly toward the coast.

Several propositions can be put forth to explain this phenomenon.

Firstly, we may question whether the application of a smoothing step between GPS data recording and strain map generation could lead to the solution being smoothed. Secondly, another possible explanation is that, in areas dominated by large faults, the

elastic rebound theory states that faults accumulate elastic strain that is then released into earthquakes. During the interseismic period, the deformation associated with the loading is usually modeled as a fault locked down to a given locking depth and creeping at the loading rate below. This generates a smoothed deformation pattern. The deeper the locking, the wider the deformation across the fault. In elastic rebound theory, the slip deficit accumulated during the loading phase is then released into earthquakes located on the fault plane. In areas where the deformation mechanism is dominated by the seismic cycle on faults, the approach consisting in comparing $\dot{M}_{0S}$ and $\dot{M}_{0G}$ reaches strong limitations, and a proper modelling of the interseismic coupling on the faults would be better adapted.

From all this, we can conclude that the scale at which deformation is observed is a crucial criterion for analyzing the compatibility between seismic and geodetic moments. Therefore, in places where source zones are centered around fault zones or areas with high seismic activity, a good practice for using geodesy as a proxy for seismicity would be to work at a larger scale.

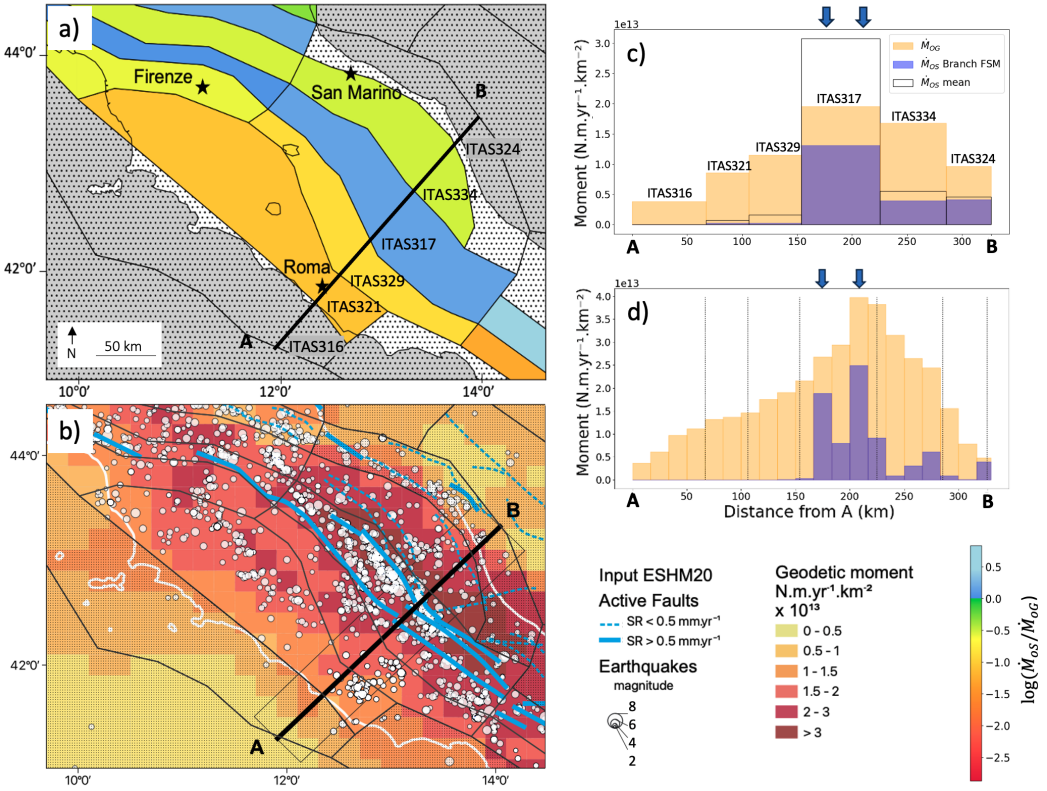

Fig. 3.19: Spatial variability of geodetic deformation and seismic release in the central Apennines. a) mean $\dot{M}_{0G}$ versus mean $\dot{M}_{0S}$ at the scale of the source zone (zoom of Fig 8.a.) b) Geodetic moment inferred from strain rates is shown as a colored map;grey dots represent earthquakes in the ESHM20 catalog; blue lines represent the active faults in the ESHM20 fault model. c and d) Geodetic ($\dot{M}_{0G}$) and seismic ($\dot{M}_{0S}$ moment rate per kilometer along the cross-section AB : averaged within the source zones (c), or averaged within bins of 14km along the swath profile (thin grey rectangle) (d). The blue arrows indicate the intersection with the two main faults systems along AB.

3.2.6 Focus in France

The figure 3.20 illustrates the locations of different zones in France, color-coded based on the overlap. Meanwhile, the figure below displays the distributions of geodetic and seismic moments obtained for each zone. These zones are categorized by the number of earthquakes used to constrain the recurrence models in ESHM20 area source zones. It is evident that in zones with fewer than 10 earthquakes used to constrain the recurrence models, the distribution of seismic moment ($\dot{M}_{0S}$) is consistently lower than the distribution of geodetic moment ($\dot{M}_{0G}$). However, as the number of earthquakes used increases to 18, the distributions tend to overlap more. This trend continues until they become almost consistently superimposed when the number of events in the zone exceeds 30 (starting from FRAS174), except for the Lourdes area, FRAS164, which was previously detailed in more depth.

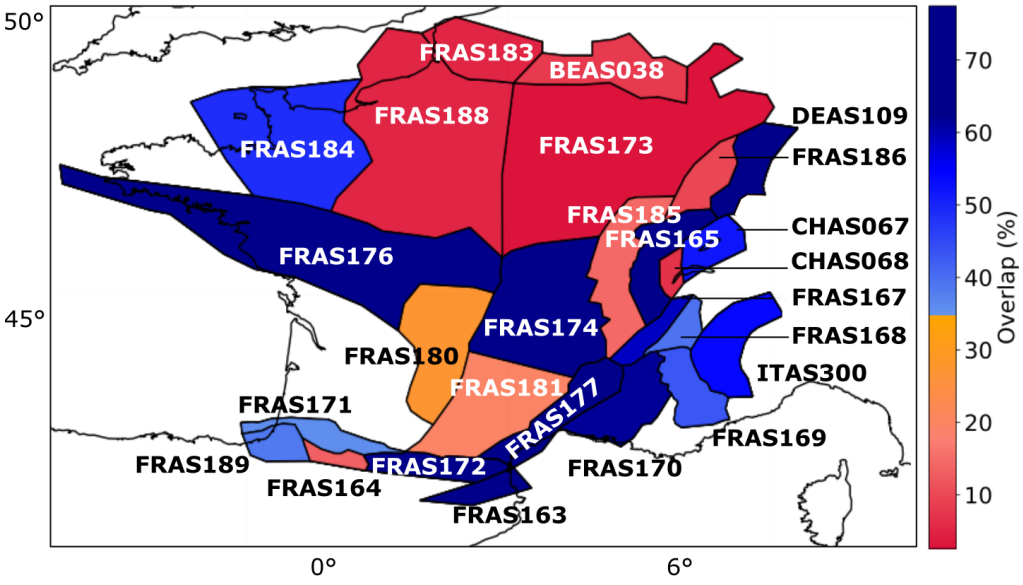

Fig. 3.20: Percentage of overlap between $\dot{M}_{0G}$ and $\dot{M}_{0S}$ distributions in France. ESHM20 denominations are indicated.

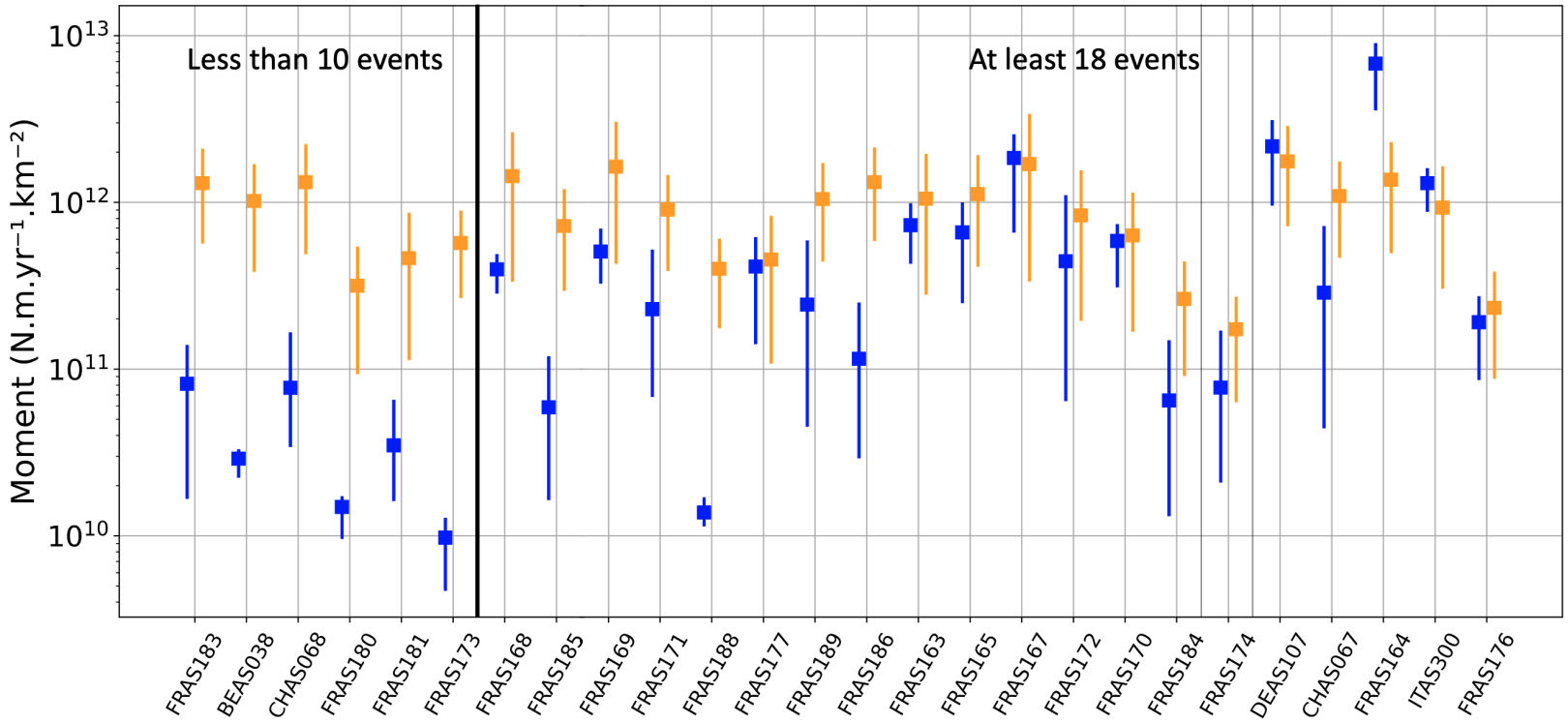

Fig. 3.21: For area source zones in France or at the border, distribution for the geodetic moment rate (orange) and distribution for the seismic moment rate (blue, inferred from the ESHM20 earthquake recurrence model). Mean values and percentiles 16^{th} and 84^{th}. The order from left to right correspond to an increasing number of events used for establishing the earthquake recurrence model, less than 10 events for sources FRAS183 to FRAS173, and 30 to 78 events for sources FRAS174 to FRAS176

3.2.7 Conclusion

We compared the consistency between seismic and geodetic moment rates at the scale of Europe based on strain models (Piña-Valdés et al., 2022) and earthquake recurrence models from the ESHM20 source model (Danciu et al., 2021). We observed that in moderate to high seismic activity zones such as the Apennines, Greece, the Balkans and the Betics, the overlap between the distributions of seismic and geodetic moment rates was sufficient to demonstrate a first-order compatibility. However, local differences between the two distributions were observed when seismicity was concentrated in areas with small characteristic distances (i.e., small areas/faults). This suggests that in some cases, the scale of the source zones is not suitable for comparing seismic moment rate and and geodetic moment rate. As expected, considering larger spatial scale conducting the same analysis at the macrozone scale yielded improved consistency.

In low activity zones, two cases can be distinguished. First, in regions where the geodetic signal is dominated by isostatic rebound, such as in Fennoscandia, the two estimates (seismic and geodetic) are not compatible, with a geodetic moment much larger than the seismic moment. Second, in other areas south of Fennoscandia (e.g., France, Germany, Spain), it can be hypothesized that geodesy represents the current horizontal tectonic stresses. In these cases, either compatibility between seismic and geodetic moments is observed, or the geodetic moment is much larger than the seismic moment. In zones where the ESHM20 recurrence models are well constrained (with >20 earthquakes used to constrain the models), we observed that the distributions of seismic and geodetic moments tend to overlap. This gives us hope for the integration of geodetic data, even in regions with low deformation.

3.3 Additional analyses

In this section, we will explore some interesting results that were not included in the article presented in section 3.2. Building upon Figure 3.10, our initial inquiry will delve into the variability of geodetic moment uncertainty across the studied parameters for all area source zones. Subsequently, we will compare the overlap between geodetic moment rates computed from a non-combined GNSS solution (Socquet et al., 2019) with the combined GNSS solution we used before (Piña-Valdés et al., 2022). Lastly, we will examine how the ratio $\dot{M}_{0S}/\dot{M}_{0G}$ is influenced by the density of earthquakes used to constrain the recurrence model and the inclusion of active faults in the studied zones.

3.3.1 Assessing geodetic moment uncertainty: variability across studied parameters for all area source zones

The presented figure 3.22 illustrates the variability (standard deviation/mean) of the distribution of mean moments across studied parameters for geodetic moment uncertainty assessment. The objective is to examine the impact of parameters on the variability of geodetic moments across different zones: a parameter with higher variability contributes more significantly to the variability of the geodetic moment rate.

The figure indicates that the considered seismogenic thickness has a relatively constant impact across zones (approximately 0.45) and exhibits higher variability than other parameters in the majority of zones. Additionally, certain parameters demonstrate negligible variability compared to the contribution of seismogenic depth, consistently remaining below 0.2 across all zones. This is observed for the geometric coefficient (C_g), shear modulus (μ), as well as, to a slightly lesser extent, the spatial weighting scheme (with one exception), Class, and radius outlier (within less than 10 zones). Notably, for the latter three parameters, zones with variability exceeding 0.2 are situated in regions characterized by low deformation rates ($\dot{M}_{0G} \leq 10^{12} N.m.yr^{-1}$ůkm^{-2}).

Furthermore, some parameters exhibit intermediate behavior, with variability less than 0.25 in the majority of zones, significantly lower than that of seismogenic thickness. However, more than 10 zones for these parameters show variability surpassing 0.2. Examples include the equation used for geodetic moment calculation, weighting threshold, and distance weighting scheme. Concerning the weighting

threshold, zones with variability exceeding 0.25 are associated with geodetic moment rates below $3 * 10^{12} N.m.yr^{-1}.km^{-2}$. For this parameter, variability remains strictly below 0.45 for all zones. Regarding the distance weighting scheme, the variability of this parameter reaches maximum values (up to 0.7), occasionally surpassing that of seismogenic depth. All zones except five, with variability surpassing seismogenic thickness, correspond to regions with low to moderate deformation characterized by geodetic moment rates $\leq 2 * 10^{12} N.m.yr^{-1}.km^{-2}$.

We observed that the parameters distance weighting and weighting threshold (and to a much lesser extent, station class and radius outlier), had an impact on the uncertainty of the geodetic moment rate, primarily in low-deformation zones. This can be explained by the fact that in areas with less deformation, higher-quality stations are required, outliers need to be well-identified, and more significant smoothing is necessary due to the proximity to the noise limit. Hence, it is normal to observe substantial variability in these parameters in low-deformation zones. Additionally, we did not identify a clear trend in the impact of the geodetic moment rate equation, which can be attributed to the fact that this parameter largely depends on tectonic style. Therefore, there is no apparent reason to observe a trend with the seismic moment rate equation concerning the geodetic moment.

In conclusion, seismogenic depth is the primary control parameter for the variability of geodetic moment rates across all zones. However, other parameters, such as the weighting threshold, distance weighting scheme, and the moment equation used, can also impact geodetic moment variability. Particularly for zones with low deformation ($\dot{M}_{0G} \leq 2 * 10^{12} N.m.yr^{-1}.km^{-2}$), the distance weighting scheme may be the predominant parameter influencing geodetic moment variability.

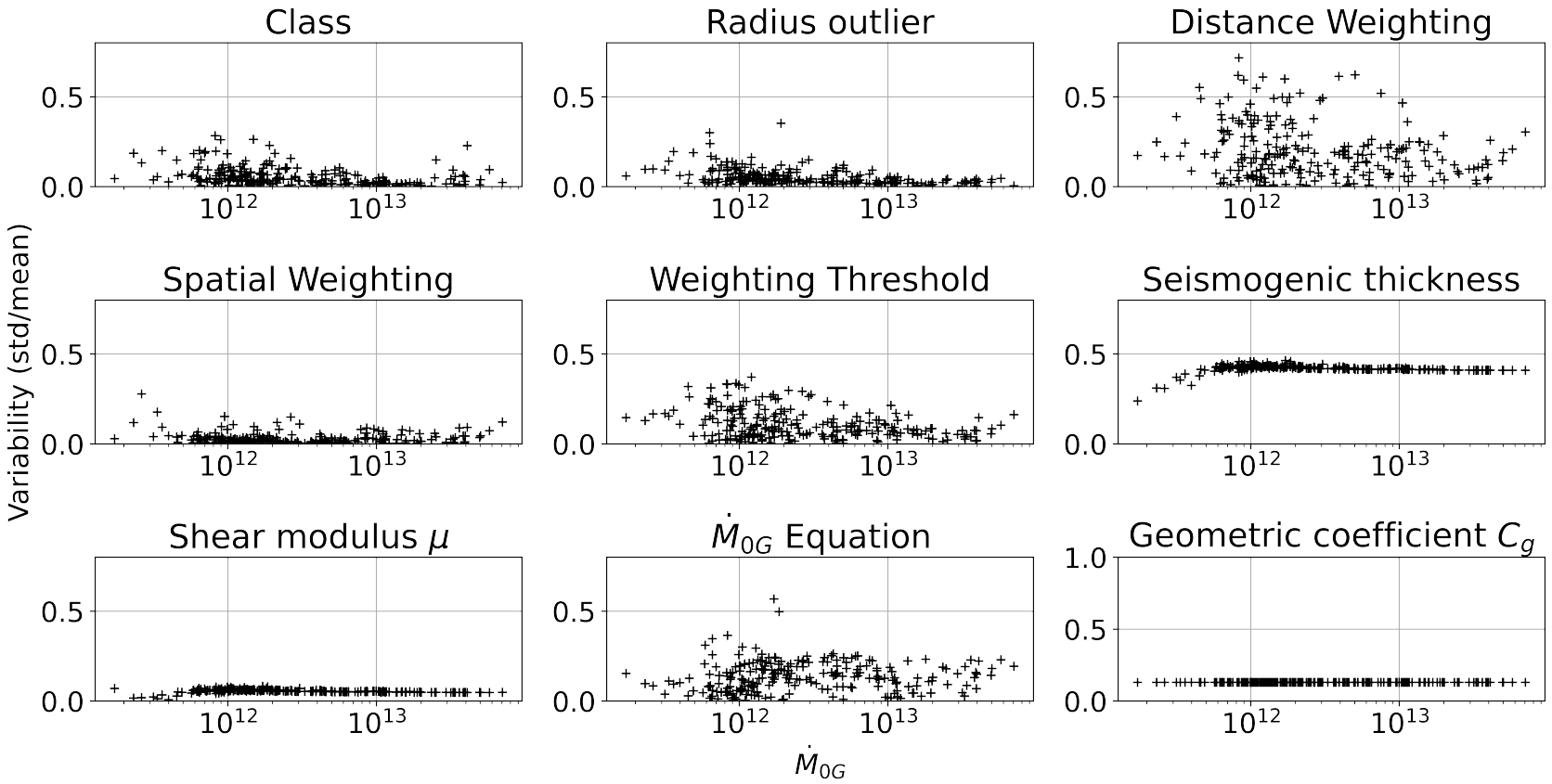

Fig. 3.22: Variability (standard deviation/mean) of the distribution of mean moments across studied parameters (presented in figure 3.9) for geodetic moment uncertainty assessment. The first line includes 'Class' (A, AB, ABC): three different sets of GNSS stations based on quality (1728 values each), 'Radius Outlier': spatial radius choices for discarding outliers (50, 100, 150, 200 km, 1296 values each), and 'Distance Weighting Scheme': choices of decay functions for interpolation, either Gaussian or Quadratic (2592 values each). The second line comprises 'Spatial Weighting Scheme': methods for spatial inversion, either Azimuth or Voronoi, and 'Weighting Threshold': threshold values on the distance weighting function (6, 12, 24, 1728 values each). The third line includes 'Seismogenic Thickness': choices of thickness (5, 10, and 15 km, 1728 values each), 'Shear modulus, μ': choices of shear modulus values ($3.3 \times 10^{10}, \mathrm{N} \cdot \mathrm{m}$ in pink, $3 \times 10^{10}, \mathrm{N} \cdot \mathrm{m}$ in red), '$\dot{M}_{0G}$ Equation': choices of the geodetic moment equation, as described in the text, and 'Geometric coefficient C_g': choices of the geometric coefficient parameter, either 2 or 2.6.

3.3.2 Impact of the GNSS solution

The combined velocity solution we have utilized thus far has been derived from ten GNSS solutions in Europe. Piña-Valdés et al., 2022 conducted a series of steps to create this common solution, which involved transforming the solutions into a common reference scale, weighting the different solutions, harmonizing uncertainties, and removing some stations. We are interested in examining the impact of this process, on the overlap between the distributions of $\dot{M}_{0S}$ and $\dot{M}_{0G}$ in areas of low to moderate activity by taking the example of France, by comparing with a GNSS solution centered in France, proposed by Socquet et al., 2019.

To begin, we calculated the distribution of geodetic moment from the non-combined French solution (Socquet et al., 2019) as we did previously with Piña-Valdés et al., 2022 solution. Subsequently, we assessed its overlap with the distribution of seismic moment. Figure 3.23 provides a comparison between the overlap with seismic moment of the geodetic moment based on the non-combined solution on the one hand, and based on the European common solution in the other hand. We observed that in certain areas where $\dot{M}_{0G} > \dot{M}_{0S}$, transitioning to a non-combined solution resulted in a decrease in geodetic moment and improved overlap. However, this behavior is not consistently observed throughout the study area.

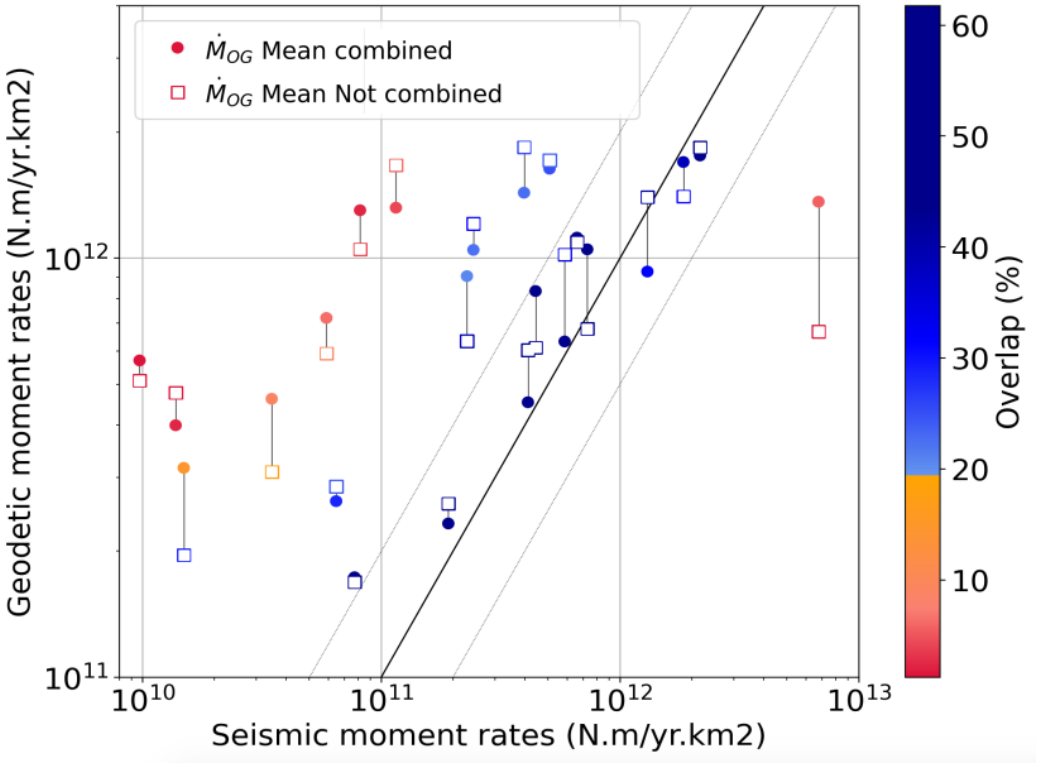

Fig. 3.23: Comparison between the overlap with seismic moment of the geodetic moment based on the non-combined solution on the one hand Masson et al., 2019, and based on the European common solution in the other hand Piña-Valdés et al., 2022.

3.3.3 Interplay between seismic and geodetic moment rates with earthquake and fault densities

Figure 3.24 illustrates the logarithm (base 10) of the ratio between the mean seismic moment rate ($\dot{M}_{0S}$) and the mean geodetic moment rate ($\dot{M}_{0G}$) per source zone. Below, we will delineate zones where $log_{10}(\dot{M}_{0S}/\dot{M}_{0G})$ falls within the range of -1 to 1, indicating seismic moments rates 10 times higher or lower than geodetic moments rates, as well as zones where the $log_{10}(\dot{M}_{0S}/\dot{M}_{0G})$ ratio is between -0.5 and 0.5, signifying seismic moments rates approximately 3 times lesser to 3 times greater than geodetic moments rates.

Increasing the earthquake density used to constrain recurrence models causes $log_{10}(\dot{M}_{0S}/\dot{M}_{0G})$ to tend towards 0, suggesting convergence between $\dot{M}_{0S}$ and $\dot{M}_{0G}$. Except for five zones, all areas with a density surpassing $5 * 10^{-9}$ earthquakes used to constrain recurrence models per km^2 have a $log_{10}(\dot{M}_{0S}/\dot{M}_{0G})$ between -0.5 and 0.5.

The figure also highlights the impact of active fault density on the consistency between geodetic moment rates. Active fault density for each zone is defined as the length of faults with a slip rate exceeding 0.1 mm/yr, divided by the zone's area (expressed in km^{-1}). Zones with a density above $4 * 10^{-5} km^{-1}$ display a $log_{10}(\dot{M}_{0S}/\dot{M}_{0G})$ between -1 and 1, with the majority falling within -0.5 and 0.5. Higher active fault density tends to enhance compatibility between $\dot{M}_{0S}$ and $\dot{M}_{0G}$.

Consistent with findings in figure 3.17, zones with higher geodetic moment exhibit better consistency between $\dot{M}_{0S}$ and $\dot{M}_{0G}$ (all zones with $\dot{M}_{0G} \geq 10^{13} N.m.yr^{-1}.km^{-2}$, in red, fall within the $log_{10}(\dot{M}_{0S}/\dot{M}_{0G})$ interval of -1 to 1). Notably, in zones with lower activity ($\dot{M}_{0G} \leq 3 * 10^{12} N.m.yr^{-1}.km^{-2}$), increasing seismic or fault density brings the $log_{10}(\dot{M}_{0S}/\dot{M}_{0G})$ closer to 0. Zones with $log_{10}(\dot{M}_{0S}/\dot{M}_{0G})$ below -1 are all characterized by a low earthquake density ($\leq 0.5 * 10^{-8}$ events.km^{-2}) and a minimum fault density ($\leq 2 * 10^{-5} km^{-1}$).

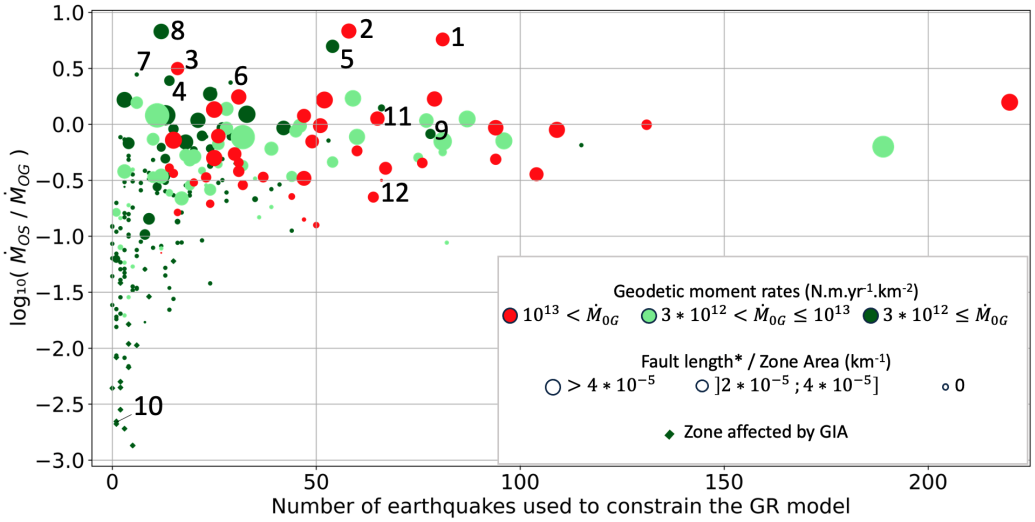

Fig. 3.24: Mean $log_{10}(\dot{M}_{0S}/\dot{M}_{0G})$ for all source zones in Europe, as a function of the number of earthquakes used to constrain the earthquake recurrence model ($M_W \geq 3.5$). The color represents the mean geodetic moment of the source zone area, and the size of the symbol is proportional to the density of the faults, which slip rates is higher than 0.1mm/yr (*), in the ESHM20 fault model. Compatibility between geodetic and seismic moment rates increases with the geodetic moment rates, the number of earthquakes used to constrain the earthquake recurrence model, and the fault density. Shallow area source zones where the geodetic moment rate is much lower than the seismic moment rate : 1 : ITAS308 , 2 : ITAS331 ; 3: ITAS339 , 4 : BGAS043 , 5: FRAS164, 6: DEAS113, 7: DEAS109, 8: CHAS071 and example source zones in section 3.2.3 : 9: FRAS176, 10: SEAS410, 11: ITAS335, 12: GRAS257 (see the text and Fig. 3.11).

4

Assessing the adequacy of earthquake catalog sampling for long-term seismicity in low-to-moderate seismic regions: A geodetic perspective

This article is currently in development, undergoing revision with the aim of submission to the special issue of Seismological Research Letters of November 2024 in the coming months (submission deadline on the 4th of May 2024). It has been collaboratively crafted with the contributions of David Marsan from ISTerre Chambéry, along with Anne Socquet.

4.1 Introduction

The incorporation of geodetic data into probabilistic seismic hazard assessment (PSHA) has emerged as a promising trend in recent geophysical research. These datasets offer valuable insights into the interseismic periods of seismic cycles, deemed representative for hazard assessment. Over the past decades, numerous studies have endeavored to compare geodetic and seismic-derived strain rates within various geodynamic contexts. To facilitate the integration of this emerging dataset into hazard assessments, researchers have undertaken moment budget computations at different scales. A consistent finding in these investigations is that, in regions of high seismic activity, geodetic and seismic moment rates are often in the same range, providing constraints on magnitude-frequency distributions and maximum magnitude (Kreemer and Young, 2022; D'Agostino, 2014; Mohapatra et al., 2014; Middleton et al., 2018). However, in low-to-moderate activity regions, geodetic moment rates have frequently surpassed seismic moment rates. (for example Ojo et al., 2021, Sparacino et al., 2020 in most of the zones considered in Maghreb,

Ward, 1998a in Turkey, Chousianitis et al., 2015 for most of the Aegean zone, Clarke et al., 1997, Masson et al., 2004 for southern Iran, Mazzotti et al., 2011 for Western Canada). An often-discussed hypothesis to account for this phenomenon suggests that a large part of the energy accumulated in the crust, as captured by geodetic measurements, may be released aseismically. Depending on the seismotectonic context, another explanation is that available earthquake catalogs in such low-activity regions are too short to sample the long-term characteristics of seismicity.

Nevertheless, recent work by Donniol Jouve et al. (in preparation, see section 3) has shown that in certain low-to-moderate seismic activity regions where Glacial Isostatic adjustment can be neglected, such as Southern Britanny in France, geodetic moment rate estimates can serve as a reliable proxy for seismic moment rates. Their research also indicates that the consistency between these two quantities may depend on the number of earthquakes employed to constrain parameters in magnitude-frequency distributions. Additionally, magnitude-frequency distributions are often based on declustered catalogs where aftershocks are excluded. However, even though certain studies as Beauval et al., 2006 have quantified the contribution of aftershocks to seismic hazard in some regions and found it can be neglected, Rollins and Avouac, 2019 argue that ignoring aftershocks may affect the inferred long-term model. This concern has also been raised by Stein and Liu, 2009, who demonstrated that in intracontinental areas, a substantial portion of intracontinental earthquakes may constitute aftershock sequences initiated by events occurring centuries ago.

In light of these considerations, this study attempts to address a fundamental question: Does the existing earthquake catalog encompass a sufficiently long-time span to adequately sample long-term seismicity in low-to-moderate seismic regions ? To do so, we first calculate geodetic moment rate estimates based on the methodology of Donniol Jouve et al. (see section 3) using the ESHM20 macrozones. We then generate synthetic earthquake catalogs rooted in the highest magnitude range possible to represent the long-term seismicity of the region, ensuring moment balance according to the Marsan and Tan, 2020 model. Some of the model parameters are difficult to constrain by the existing data, as will be shown here, rendering the practical use of this approach doubtful. However, the goal is rather to show that we can propose realistic simulations that allow a first-order examination of this sampling issue. Our investigation seeks to perform a sanity check by examining the consistency of our results with the observed maximum magnitude and the temporal clustering characteristics of the actual catalog. Additionally, we also compare the resulting synthetic earthquake catalogs with the long-term recurrence models proposed by ESHM20 (Danciu et al., 2021). These recurrence models are constructed using two types of models. The first set of models is defined at the scale of polygons,

and relies on a harmonized declustered catalog created for Europe. These models encompass various possibilities regarding the shape of recurrence models, along with an uncertainty range for the associated parameters (a, b, and a parameter controlling the maximum magnitude). On the other hand, the second set of models is based on a fault and smoothed seismicity model, defined on a grid. In areas where faults are defined, the frequency-magnitude distribution relies on fault geometries and slip rates. In cells without defined faults, the frequency-magnitude distribution is based on the earthquake catalog.

4.2 Methods

4.2.1 Selection of the studied areas

We have opted to base our comparison on ESHM20 macrozones (called TECTO-zones in ESHM20) for several reasons. Firstly, as outlined by (Danciu et al., 2021), these macrozones were deliberately designed to represent tectonic regions. Secondly, they encompass a sufficient number of earthquakes, making it possible to compute the b-value of the Gutenberg-Richter law even in areas with low deformation. Additionally, as per the findings of Donniol Jouve et al. (see section 3), conducting comparisons of geodetic and seismic moment rates at the scale of ESHM20 macrozones yields better consistency than at smaller scales.

In the initial phase of our investigation, our focus will be on Brittany (TSZ056) to detail and illustrate the methodology. This particular area has been chosen due to its comparability in geodetic and seismic moment rates distributions, coupled with the abundance of available data. Subsequently, our examination will extend to a second macrozone characterized by significantly higher geodetic moment rates than seismic moment rate estimates. For this second analysis, we have selected the region TSZ089 in southeastern Switzerland. This region offers a double advantage, featuring a robust density of GNSS stations and a substantial number of earthquakes, providing a solid foundation for anchoring our statistical analyses. The geographical locations of these exemplary zones and the dataset utilized for this article are depicted in Figure 4.1. In Figure 4.2, the distributions of geodetic and seismic moment rates for these two macrozones are presented.

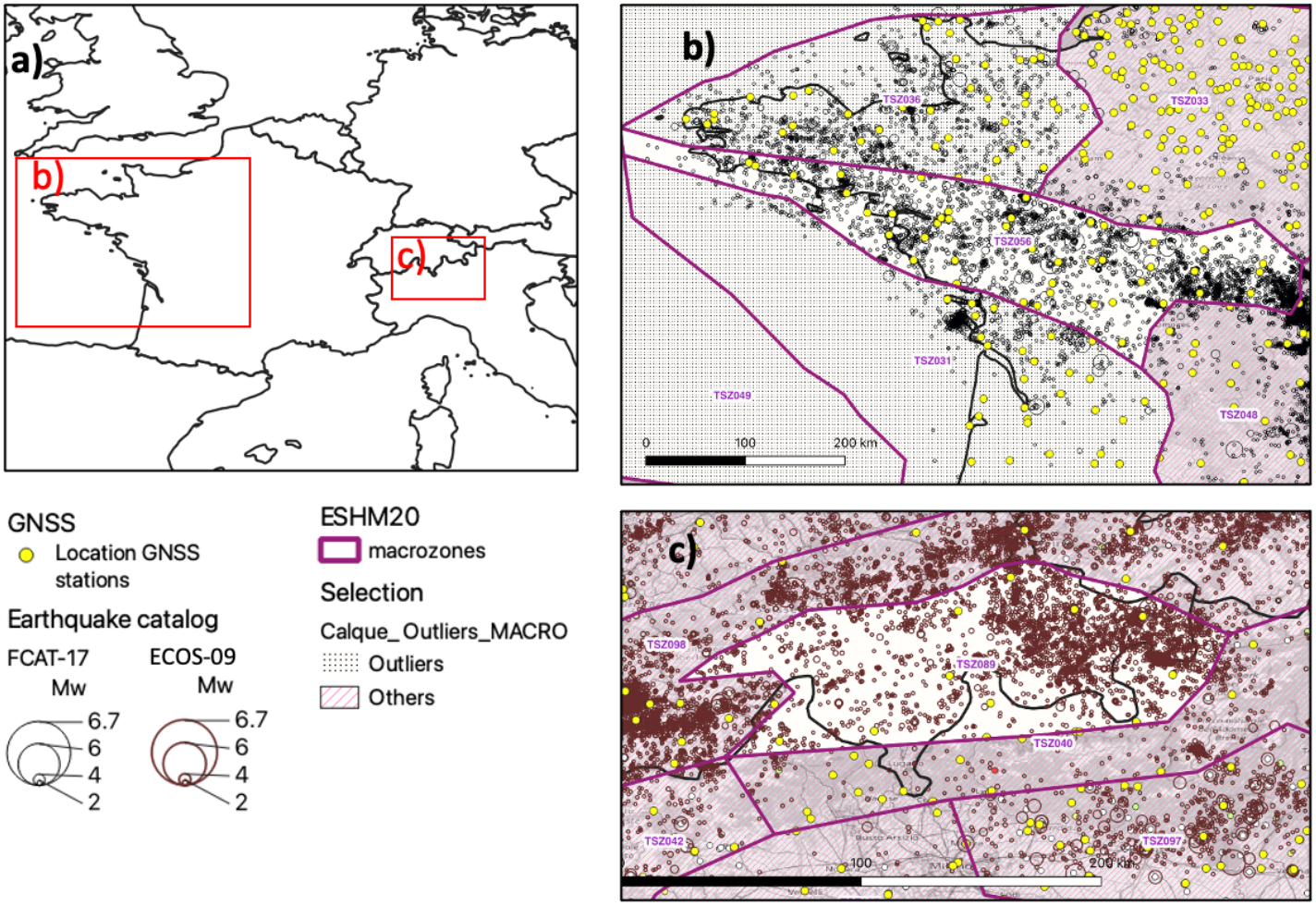

Fig. 4.1: Geographical representation of the two designated macrozones under investigation and the corresponding datasets. a) Depiction of the region highlighted in the zoomed-in figures b) and c). b) Geographical location of macrozone TSZ056. The earthquake catalog used (FCAT-17) is depicted in black. c) Geographical location of macrozone TSZ089 in Switzerland. The earthquake catalog employed (ECOS-09) is represented in maroon. The GNSS (Global Navigation Satellite System) stations, shown in yellow, were employed for the computation of geodetic moment rates within each zone. The national borders are delineated in black. The color information is optimized for the electronic version of this figure.

4.2.2 Geodetic moment computation

To tackle uncertainties in geodetic moment computations, we employed the geodetic moment distributions over the relevant polygons, computed by Donniol Jouve et al (in preparation; see Section 3 for the methodology). These distributions were derived from Piña-Valdés et al., 2022, strain rates maps, computed at the scale of Europe using VISR software (Shen et al., 2015).

In Figure 4.2, we compare this distribution with the seismic moment rates from ESHM20 that have been computed by Donniol Jouve et al. in prep (see section 3.2).

Our analysis reveals two significant observations. Firstly, the geodetic and seismic moment distributions exhibit well-defined patterns, albeit with inherent variability. By computing their mean values, we inevitably lose valuable information encapsulated within these distributions. Secondly, the adequacy between these moment rate distributions varies depending on the macrozone under consideration. As emphasized in the upcoming study by Donniol Jouve et al. (section 3), the Brittany macrozone (TSZ056) exhibits a notably strong similarity between geodetic and seismic moment estimates, both in terms of the mean values and the overlap between the two distributions. In the Swiss macrozone (TSZ089), these distributions exhibit a weak overlap. Moreover, the mean geodetic moment rate is approximately six times higher than the mean seismic moment rate, indicating significant disparity between these two quantities. Our study aims at evaluating whether this disparity could be owed to the limited sampling provided by the available seismicity dataset.

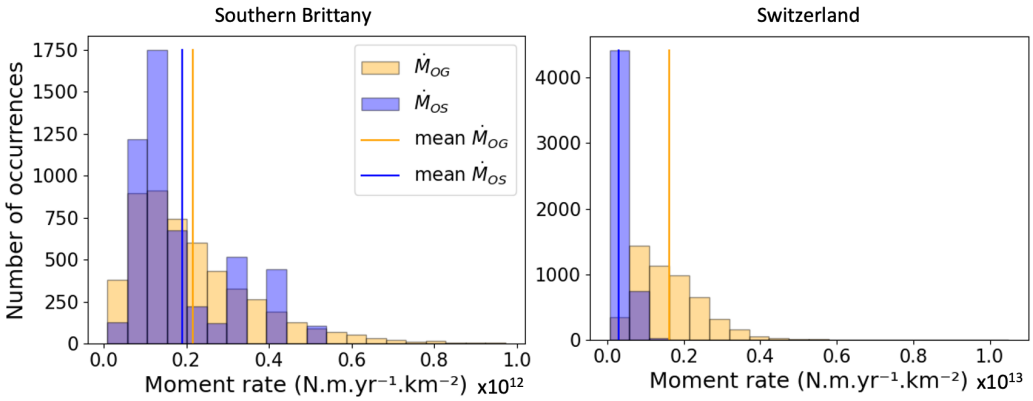

Fig. 4.2: The distributions of geodetic $\dot{M}_{0G}$(orange) and seismic $\dot{M}_{0S}$ moment rates computed from ESHM20 models (blue), for the two macrozones under investigation. Vertical lines denote the mean of each respective distribution. The Southern Brittany region (on the left) exhibits a commendable concordance between the two distributions, whereas the Switzerland macrozone (on the right) manifests a distinct prevalence of geodetic moment rates over seismic moment rates. Locations are referenced in Figure 4.2. Color representation optimized for the electronic version.

4.2.3 Methodological Development Illustrated: The Case Study of Southern Brittany

Description of the catalog

We used the FCAT-17 catalog (Manchuel et al., 2018) (Figure 4.3a) for our analysis, restricting our focus to earthquakes with hypocenters located at depths lower than 30 km confined within the polygon of southern Brittany shown in Figure 4.1. The magnitudes of completeness were taken from (Drouet et al., 2020). The values $M_W \geq 3$, 3.5, 4, 4.5, 5, 5.5 are linked to the corresponding years of completeness, which are 1950, 1850, 1850, 1700, 1600, and 1500, respectively.

Our objective was to identify a magnitude interval with the longest completeness period possible, allowing us to assemble a representative sample spanning the greatest duration. As depicted in Figure 4.3a, the number of earthquakes with magnitudes below 5 exhibits significant temporal variation, notably increasing over the past 200 years. This upward trend is less pronounced for earthquakes with magnitudes of M_W5 and above. Therefore, we focused on this magnitude range.

Drouet et al., 2020 defined the magnitude of completeness for this interval as 1600 ± 100 years. The annual earthquake rate for this magnitude interval is 0.01 per year. In Figure 4.3c, we present the annual rates of exceedance with respect

to magnitude (in the magnitude of completeness range according to Drouet et al., 2020. The b-value was computed as the slope of this distribution (Fig4.3c), yielding a result of 0.9.

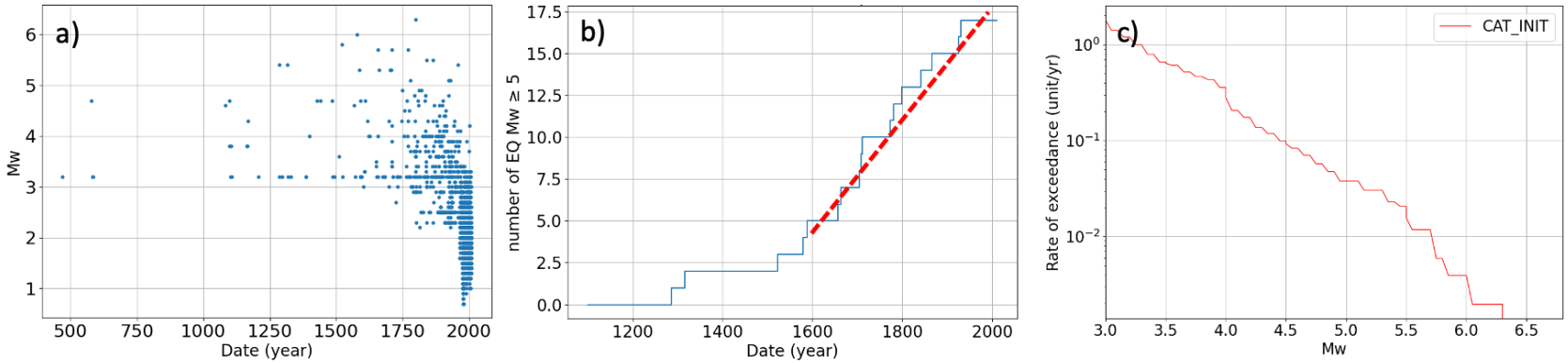

Fig. 4.3: Description of the considered catalog. a: Catalog, each point represents an earthquake. M_W vs time. b: cumulative number of earthquakes $M_W \geq 5$ as a function of time. Data (blue) can be fitted by a linear relationship (pink line) in the completeness period (from 1600 according to Drouet et al. 2020). c: rate of exceedence vs M_W for the considered catalog, taking into account the evolution over time of the completeness magnitude (Drouet et al., 2020)

Generation of Synthetic Catalogs

For the generation of synthetic catalogs, we employed the (Marsan and Tan, 2020) model and methodology, aiming to create catalogs that are constrained to replicate the mean geodetic moment of energy release. This model amounts to an Epidemic Aftershock Sequence (ETAS) model that dynamically limits the maximum magnitude of the Gutenberg-Richter law to yield a seismic moment release equal to stored seismic moment. This ensures that the total seismic moment released by all earthquakes equals the total geodetic moment accumulated within the tectonic region, over long time scales (1 Myrs).

Marsan and Tan, 2020 model is based on the simplest version of the ETAS model (Ogata, 1998) that describes the earthquake rate as :

$$\lambda_t = \mu + \sum_{i,t_i<t} n_0 \exp^{\alpha(m_i - m_0)} \frac{p-1}{c} \left(1 + \frac{t - t_i}{c}\right)^{-p} \tag{4.1}$$

with μ the background earthquake rate (per year), m_0 the minimum magnitude considered, n_0 the mean number of aftershocks generated by a m_0 magnitude mainshock, α the productivity exponent, p and c from Omori's law.

This model involves making assumptions as detailed below. We constrain as much as we can the model parameters to yield simulations that mimic the statistical characteristics of the FCAT-17 catalog.

The following choices and assumptions were made:

1. **Choice of Magnitude Cutoff (m_0):** We selected $m_0 = 3$ in order to maintain a magnitude sufficiently below $M_W = 5$.

2. **Omori Law Parameter (p):** We adopted $p = 1.1$. The temporal clustering and sampling variability of the model output strongly depend on the choice of this value, as will be described below. This $p = 1.1$ value is here intended for illustration. A proper sensitivity study will be conducted below.

3. **Background earthquake rate (μ):** It was assumed negligible. This amounts to assuming a branching ratio very close to 1. There exists a wide scatter of estimates for the branching ratio, depending on the region studied, the methodological approach, and the size of the available dataset. It was however argued by Marsan and Tan (2020) that the limit $\mu \to 0$ is plausible in the framework of an ETAS model with seismic moment budget as used here.

The parameters used for the computation of the synthetics are detailed in Table 4.1, and a comprehensive description of the calculations and rationale for all parameter's choices is presented hereafter.

In the geodetic zone, the geodetic moment is selected as the moment that can be released. Therefore:

$$\dot{M}_0 = \dot{M}_{0G} = 1.52\ 10^{16}\text{N.m/yr} \tag{4.2}$$

We estimated $b = 0.9$ in Section 4.2.3, thus $\beta = b\ln(10) = 2.07$. We further assume $\alpha = \beta$. Equalling these two parameters amounts to ensure self-similarity of the model, e.g., zooming on the aftershock sequence of a $M_W = 4$ mainshock and its $M_W \geq 1$ aftershocks is statistically indistinguishable from looking at a $M_W = 8$ mainshock and its $M_W \geq 5$ aftershocks, in terms of number, temporal decay and spatial pattern (after zooming in). This $\alpha = \beta$ equality is suggested by several studies on the scaling of aftershock productivity (Console et al., 2003; Helmstetter and Sornette, 2003; Saichev and Sornette, 2005; Holliday et al., 2008; Davidsen and Baiesi, 2016).

We choose m_0, the cutoff magnitude, to be 3, in order to be sufficiently below $M_W 5$ to provide an overall view without requiring too long computation times. We have also estimated that the number of earthquakes with magnitude ≥ 5, λ_5, is 0.032 earthquake per year (cf. Figure 4.3), which implies that the mean earthquake annual rate for magnitude m_0, $\bar{\lambda}_{m_0}$, is $\lambda_5 \times 10^{(b\times(5-m_0))} = 2.0$. The branching ratio is given by:

$$\bar{n} = 1 - \frac{\mu}{\bar{\lambda}_{m_0}} \tag{4.3}$$

Other model parameters depend on these initial ones according to Marsan and Tan, 2020. We have: The average seismic moment of an earthquake with magnitude $\geq m_0$:

$$\bar{M}_0 = \frac{\dot{M}_{0G}}{\bar{\lambda}_{m_0}} = 7.6 \times 10^{15}\text{N.m/yr} \tag{4.4}$$

Moreover, direct calculation using the Gutenberg-Richter law implies that,

$$\bar{M}_0 = M_0(m_0)\frac{\beta}{\gamma - \beta}\exp^{(\gamma-\beta)(\Omega-m_0)} \tag{4.5}$$

Therefore,

$$\Omega = \ln\left(\frac{\bar{M}_0}{M_0(m_0)\frac{\beta}{\gamma-\beta}}\right)\frac{1}{\gamma-\beta} + m_0 \tag{4.6}$$

with $\gamma = 1.5\ln(10)$ and $M_0(m_0) = M_0(3) = 10^{1.5\ 3+9.1}$ from Hanks and Kanamori, 1979.

Hence $\Omega = 6.5$. This value corresponds to the maximum magnitude that can occur when averaging over long time scales, and is in this model the average seismic moment stored in the system at any time, translated into magnitude. It can be viewed as the equivalent of the long term maximum magnitude M_{max}.

Further considerations lead to the determination of n_0, i.e., the average number of aftershocks triggered by a mainshock of magnitude m_0:

$$n_0 = \frac{\bar{n}}{\beta(M_{\text{max}} - m_0)} \tag{4.7}$$

In our case, $n_0 = 0.14$.

Therefore, the parameters obtained for this initial run are:

Parameter		Chosen value
b	b value	0.9
β	β = b * ln(10)	2.07
α	productivity exponent (taken = β)	2.07
μ	background earthquake rate (per year)	10^{-6}
n_0	mean number of aftershocks generated by a m_0 magnitude mainshock	0.14
m_0	minimum magnitude considered	3
p	p (Omori's law)	1.1
c	c (Omori's law) (yr)	10^{-7}
t_{max}	Simulation duration	1 million years
$\dot{M}_{0G}$	Geodetic moment rate	1.52×10^{16} N.m/yr
$\bar{M}_0$	Mean seismic moment for any random earthquake	7.6×10^{15} N.m
λ_{m_0}	Annual rates of earthquakes with magnitude $\geq m_0$	2.0
Ω	Time-averaged seismic moment stored in the system (in magnitude scale)	6.5

Tab. 4.1: Model parameters used for the french zone TSZ056

Synthetic catalog analysis

In Figure 4.4, we present a zoom on the last 20000 yrs of the synthetic earthquake catalog computed for the parameters listed in Table 4.1, that spans a total duration of

one million years. The analysis of interevent times for earthquakes with magnitude greater than 5 reveals significant aftershock clusters, such as the one around the year 10000. Seismic activity tends to concentrate within these clusters, characterized by both high magnitudes (higher than 6 in this instance) and a larger number of earthquakes with higher magnitudes. This strong clustering is due to both the branching ratio close to 1 and the p value ($p = 1.1$) that sufficiently departs from 1, as explained below. Conversely, this configuration also leads to extended periods during which fewer high-magnitude earthquakes occur. An illustrative example of such a period occurs around the year 5000. This intermittency implies that any short period sampling is likely not to reflect the overall seismicity activity.

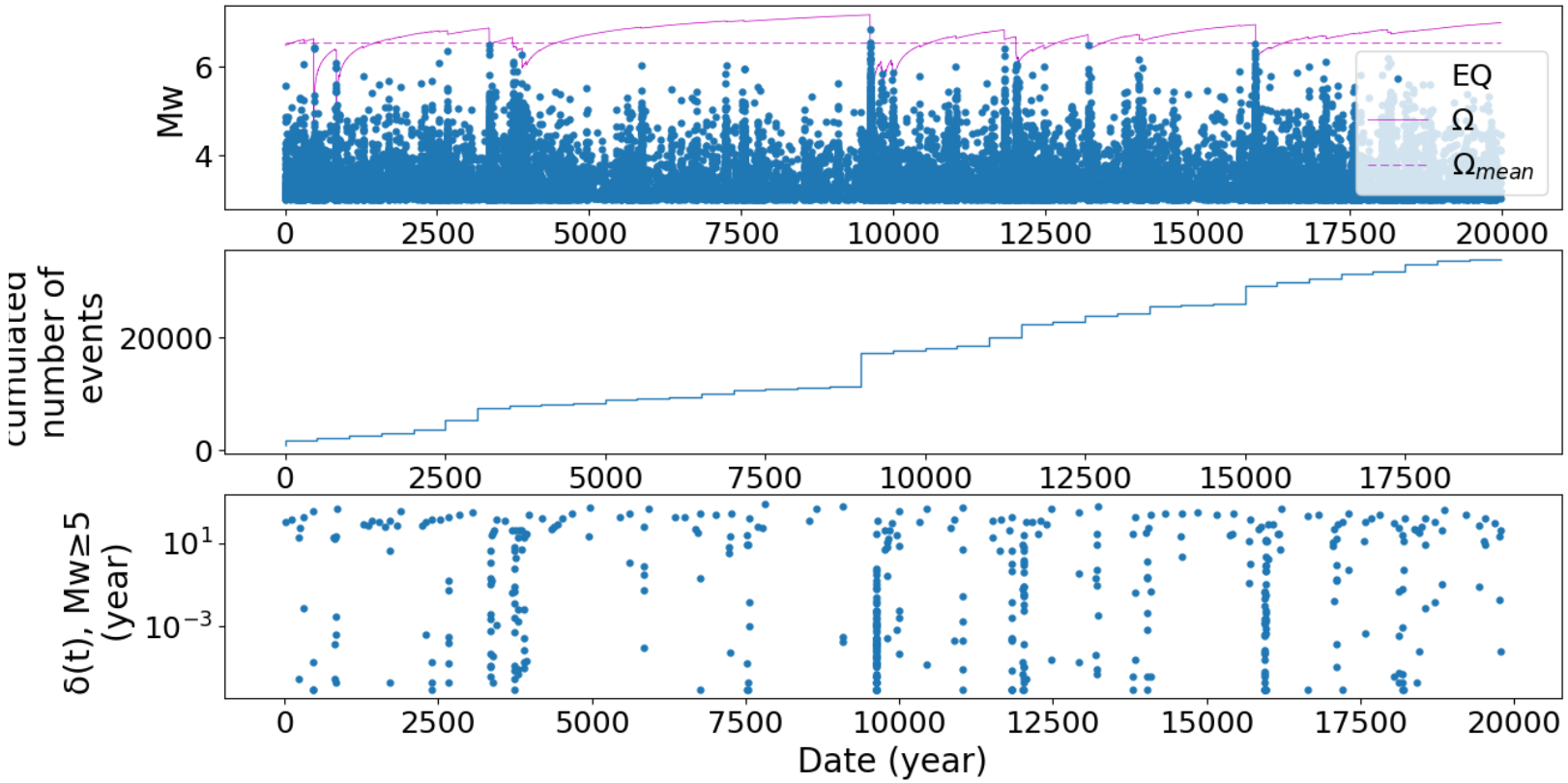

Fig. 4.4: Synthetic catalog, for southern Brittany (TSZ056) resulting from Run 1 (refer to Table 4.1) spanning one million years. Parameters include $p = 1.1$, negligible μ, and a rate of 2.0 earthquakes with $M_W \geq 3$ occurring annually. a) The synthetic catalog, where each blue dot represents an earthquake. $\Omega(t)$ is the seismic moment that the system can release at time t (in magnitude scale), and Ω_{mean} is the mean of $\Omega(t)$, chosen as a proxy for the maximum magnitude in the subsequent point (here $\Omega_{mean} = 6.5$). b) Cumulative number of events over time. c) Interevent time for earthquakes with $M_W \geq 5$, in years. The most significant aftershock sequences are discernible and characterized by rapid successions of events (e.g., observed not long before year 10000 for example).

We computed the total seismic moment cumulated over 410-year periods (representing the duration of completeness for magnitude 5+ earthquakes) by summing all the moments of earthquakes within each respective time span. The resulting distribution is shown in Figure 4.5.

Importantly, a substantial portion of the seismic moment rates falls within the range proposed by ESHM20. Specifically, seismic moment rates computed from the actual catalog (depicted in green) fall within the 16^{th} and 84^{th} percentiles of the synthetic seismic moment distribution, demonstrating a robust consistency between the two sets of results.

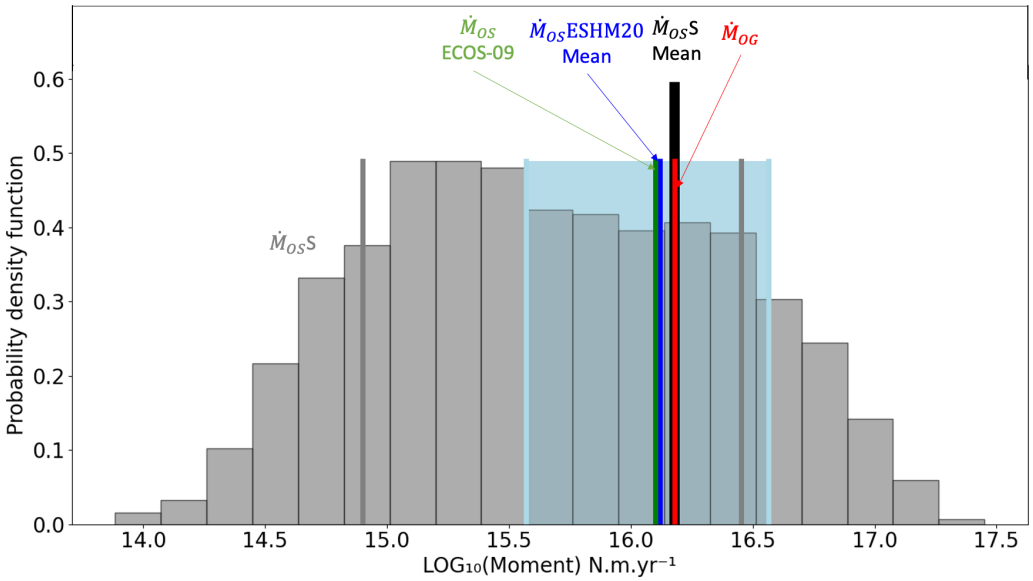

Fig. 4.5: Histogram (in grey) of the distribution of log_{10} of the seismic moment rate (N·m/yr), calculated as the sum of moments of all earthquakes in samples of 410 years of the synthetic catalog divided by 410 years, for southern Brittany (TSZ056). The grey and black bars denote the 16^{th}, 84^{th} percentiles, and the mean of the distribution. The green bar is the seismic moment rate of the actual catalog, while the blue bars give the seismic moment rates computed from ESHM20 magnitude-frequency distributions (refer to Section 3 for details), indicating the 16^{th} and 84^{th} percentiles and the weighted mean. The red bar shows the geodetic moment.

Figure 4.6 offers an insightful perspective as it juxtaposes the magnitude-frequency distributions across the entire dataset. In this representation, the distributions proposed by ESHM20 for both the Pareto and Gutenberg-Richter branches are depicted in green and blue, respectively. The red curve represents the actual catalog (as seen in Fig 4.3c), while the black and grey curves represent the synthetic catalog, both in terms of the overall distribution and the 410-year segments within the synthetic catalog. Notably, this analysis reveals that when utilizing this model,

the cumulative annual rates exhibit a strong consistency with both ESHM20 and the actual catalog in all the magnitude ranges. This shows that the earthquake activity over any random 410 year period can indeed be widely varying. We here simply measure this variability using the coefficient of variation COV_{M_0}, namely, the standard deviation of the log of the seismic moment rate normalized by its mean, cf. Figure 4.8. The sample variability is mostly controlled by the p exponent of the Omori's law: as $p \to 1$, the variability as measured by COV_{M_0} becomes vaninshingly small, i.e., all 410 year samples are characterized by the same typical earthquake activity. The release of seismic moment becomes increasingly intermittent as p departs from 1. We must emphasize that even at $p = 1.1$ the intermitency is significant, implying a high sensitivity to small excursions of p. In contrast, variations in the branching ratio are found to little affect this sampling variability.

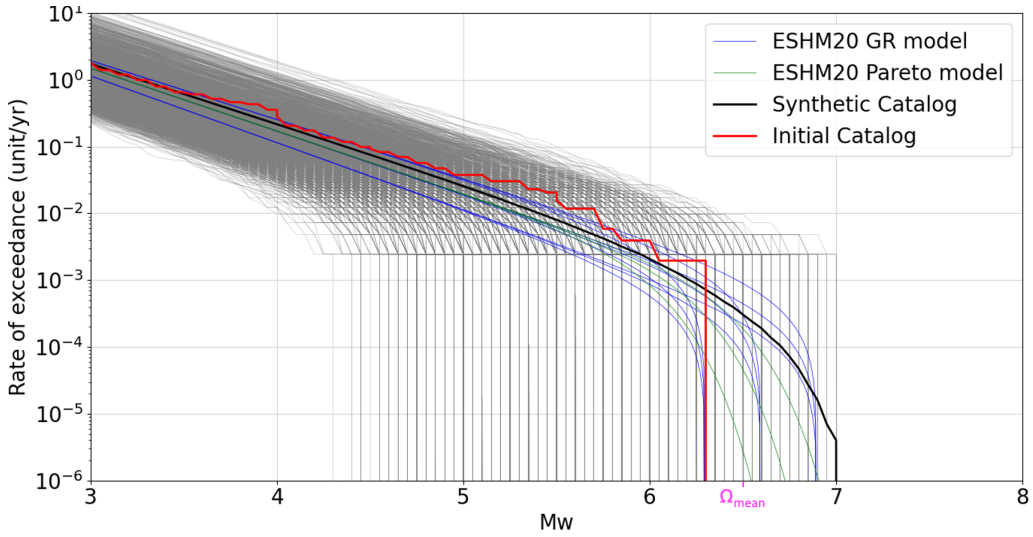

Fig. 4.6: Magnitude-frequency distribution for the macrozone of southern Britanny (TSZ056) from earthquake catalogs : Synthetic-catalog total and 410 year long samples (black and grey lines), the FCAT-17 catalog (red line) and the recurrence models proposed by ESHM20 (with varying shapes in the highest magnitude range to account for the uncertainties) (in blue and green). The value of Ω_{mean} is also indicated.

Sanity check

In order to evaluate the consistency of the synthetic earthquake catalog with the properties of the FCAT-17 catalog, we conducted two distinct sanity checks with the following objectives:

1. **Temporal Clustering Analysis:** Our first objective is to gauge the temporal clustering within the synthetic catalog in comparison to the original FCAT-17 catalog. After selecting events with a magnitude equal to or greater than 5 ($M_W \geq 5$), we calculate the coefficient of variation (COV) for the time intervals between successive earthquakes. The COV is determined as the ratio of the standard deviation to the mean of these time intervals. A COV of 0 implies cyclic seismicity, COV = 1 suggests random seismicity, and COV > 1 indicates an intermittent behavior. The analysis is carried out over 410-year periods, specifically when the number of earthquakes with magnitude greater than 5 exceeds 5, ensuring meaningful COV values. The resulting distribution, presented in Figure 4.7a, indicates that the COV value computed for the actual catalog is consistent with those obtained from the synthetic earthquake catalog. However, it falls outside the 16th - 84th percentile interval, indicating that the actual catalog is not one of the most likely 410-year earthquake catalog corresponding to the seismicity described by our model as it is currently parameterized.

2. **Maximum Magnitude Consistency:** Our second objective is to assess whether different models lead to observed maximum magnitudes that align with those of the actual catalog. We compare the maximum magnitude observed in each 410-year interval in the synthetic earthquake catalog, as illustrated in Figure 4.7.b. The analysis reveals that the observed maximum magnitude ($M_W = 6.3$) is consistent with the distribution obtained for the synthetic catalog.

In conclusion, our analyses support the notion that the synthetic earthquake catalog can be considered representative of the observed seismicity in the FCAT-17 catalog. Moreover, the comparison of the long-term behavior in the maximum magnitude range with the ESHM20 model reveals a high degree of agreement. This is evident when observing that the synthetic catalog (depicted in black) falls within the bounds of the 12 area models proposed by ESHM20 in green and blue in Figure 4.6. We use Ω_{mean} as a proxy for M_{max} for the synthetic catalog, so to compare it to the M_{max} values proposed by ESHM20 (depicted in blue and green in Figure 4.7). This streamlined comparison provides a rapid means of assessing the agreement between the long term synthetic earthquake catalog and expert-derived models. In

the present case of Brittany, $\Omega_{mean} = 6.45$ indeed falls in the $6.3 \leq M_{max} \leq 6.9$ interval proposed by ESHM20.

We note that a maximum likelihood approach could be used to infer the most likely p and $\bar{n}$ parameters given COV and M_{max} of the actual catalog. However, this would amount to assuming that the only 410 year sample we know (i.e., the actual catalog) is representative of all the 410 year samples over a long time scale, which is precisely what we would like to asses here.

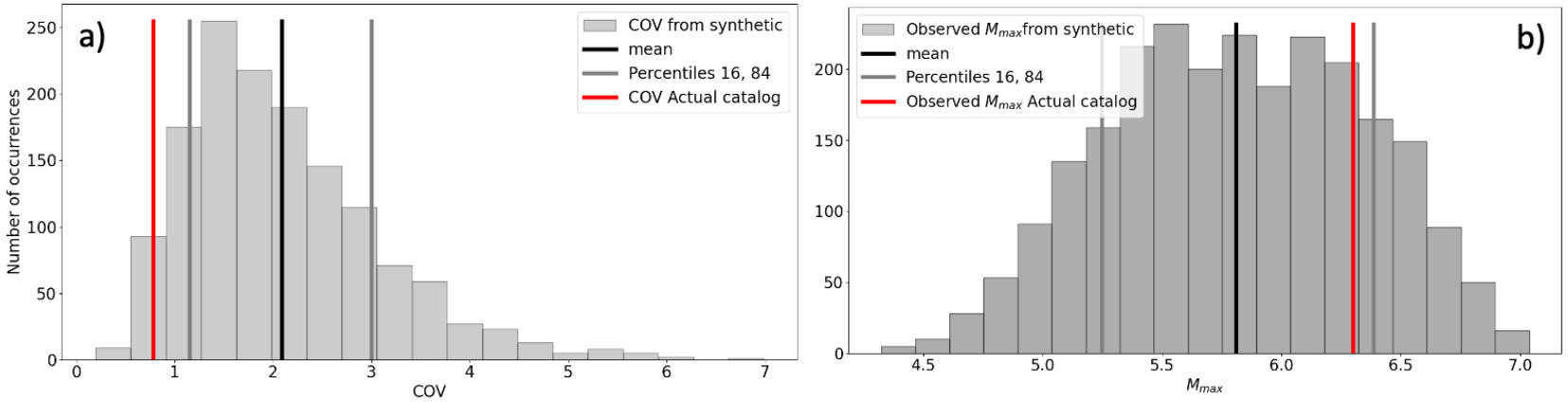

Fig. 4.7: Sanity check comparing synthetic and actual catalogs. a) Histogram of the distribution of COV for magnitudes ≥ 5 calculated over 410 years from the synthetic catalog. The red bar represents the COV of the FCAT17 catalog on TSZ056 for the same magnitude interval. b) Histogram of the distribution of observed Maximum Magnitudes over 410 years from the synthetic catalog. The red bar represents the maximum magnitude observed for the FCAT17 catalog on TSZ056.

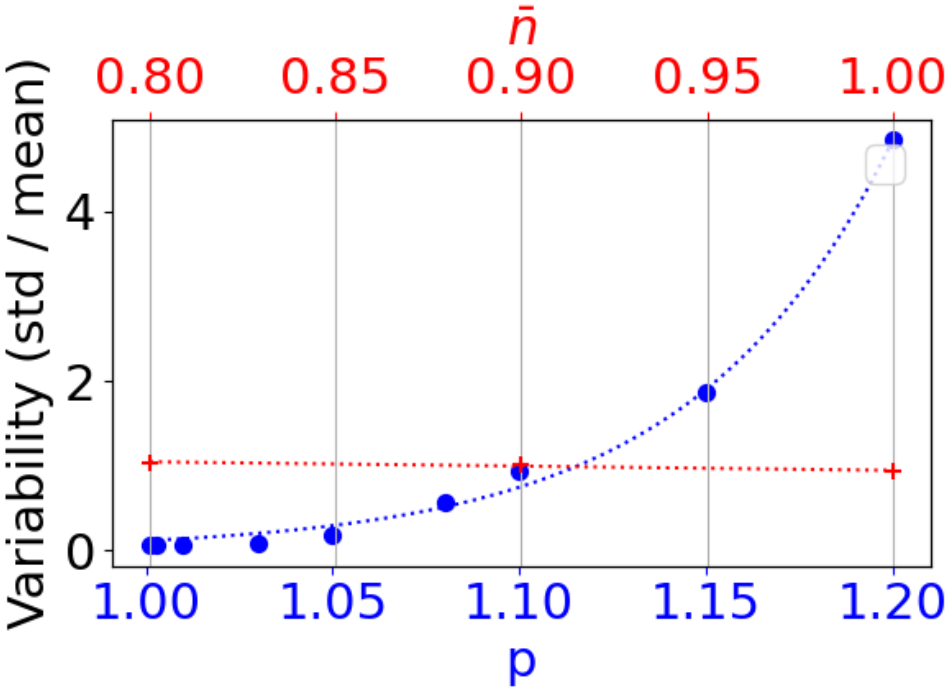

Fig. 4.8: **Sensitivity analysis for southern Brittany (TSZ056)**: Variability of the synthetic catalog (std/mean) concerning varying parameters. In blue, for these points, we computed 8 synthetic catalogs with parameters from Table 4.1 except for varying p. The data points exhibit a pattern that can be interpolated by an exponential function, given by the equation $y = 8.7 \times 10^{-10} \cdot \exp(19x)$. In red, we generated 3 different synthetic catalogs with parameters from Table 4.1 but varying $\bar{n}$. The points can be fitted with an affine equation: $y = -0.5x + 1.4$.

4.3 Can the analysis of the synthetic catalog provide a potential explanation for the observed disparity between geodetic and seismic moments distribution in TSZ089 ?

4.3.1 Description of the earthquake catalog used and generation of synthetic catalogs

We conducted a similar analysis for the swiss macrozone considered. We utilized the event of ECOS-09 catalog (Fäh et al., 2011) (Figure 4.9a), specifically focusing on hypocenters located at depths less than 30 km, for our analysis. As we were unable to find an estimate of the completeness period specifically centered in our study region, we determined it using the Weichert, 1980 methodology. (Refer to Annex 4.6.1 for the corresponding plots).

Similar to Section 4.2.1, our aim was to identify a magnitude interval with the longest completeness period possible, enabling the assembly of a representative sample spanning the greatest duration. We selected the $M_W \geq 4$ magnitude range. For this interval, we defined the period of completeness as starting in year 1890. The annual earthquake rate within this magnitude interval is 0.11 per year. In Figure 4.9c, we present the annual rates of exceedance concerning magnitude (specifically for $M_W \geq 3$, 3.5, 4, 4.5, 5 with corresponding completeness periods starting in year 2000, 1967, 1890, 1800 and 1500, respectively). The b-value was computed as the slope of this distribution (Fig. 4.9c), yielding $b = 1.1$.

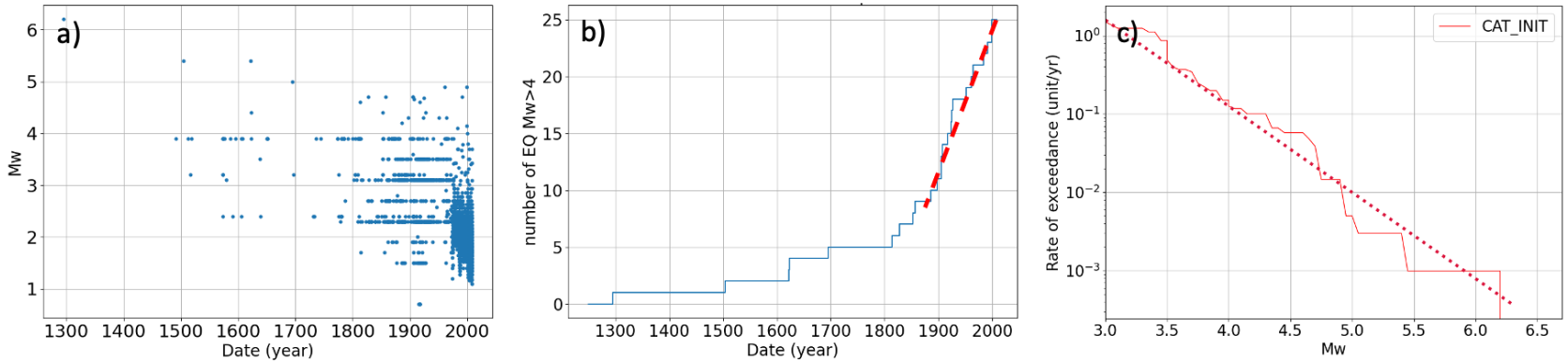

Fig. 4.9: Description of the considered catalog. a: Catalog, each point represents an earthquake. M_W vs time. b: cumulative number of earthquakes $M_W \geq 4$ as a function of time. Data (blue) can be interpolated by a linear relationship (crimson line) in the completeness period (from 1890). C: rate of exceedance vs M_W for the considered catalog, taking into account the difference in completeness periods (see annex 4.6.1

In the preceding section, we made several assumptions regarding the parameters of the Marsan and Tan, 2020 model. We will now systematically vary these parameters to assess their impact on the resulting synthetic catalog, on top of the sensitivity study already performed with Figure 4.8. Our objective is to identify a set of parameters that validate the conditions outlined in the sanity checks detailed in section 4.2.3.

We generated a total of 18 synthetic earthquake catalogs by systematically varying the parameters as shown in Figure 4.10 (3 values of p, 2 values of μ, and 3 values of annual rates). The parameters used for the runs are detailed in annex 4.6.2.

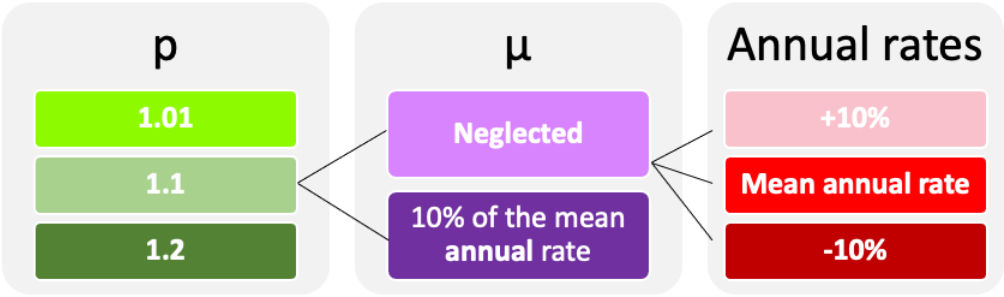

Fig. 4.10: Sets of parameters of the Marsan and Tan, 2020's model. $\mu = 0$ and $\mu = 10\%$ of the mean annual rate are equivalent to a branching ratio $\bar{n}$ of 1 and 0.9, respectively.

4.3.2 Evaluation of Parameter Choices on the Results and Selection of an Optimal Synthetic Catalog

In Figure 4.11a, we present the overall distribution of moment values computed for each set of fixed parameters. Similar to the approach detailed in section 4.2.3, the plotted moment values result from aggregating all earthquakes within all the 118-year time intervals (the completeness period for $M_W \geq 4$) in the synthetic catalog. For instance, the light green distribution corresponds to the aggregation of samples from 6 models that share the p value 1.01 (i.e., the two values of μ and the three values of annual rates). The greater the spread observed between the alternative median values of these distributions, the larger the impact of parameter uncertainty on the overall variability of moments. A similar analysis is conducted for COV values in Figure 4.11c and for the observed maximum magnitude in Figure 4.11b.

Over 84^{th} percentile of the seismic moment distributions from synthetics with a p value of 1.01 fall within or below the seismic moment range proposed by ESHM20,

with higher p values leading to a translation of this range towards lower moment values and a higher dispersion. Similarly, μ significantly influences the distribution shape (the lower value implies a more dispersed distribution), while the effect of λ appears less pronounced.

Among the three distributions depending on p, the one yielding observed M_{max} ranges closest to those in the actual catalog occurs at $p = 1.01$, with the actual M_{max} observed between the 5^{th} and 95^{th} percentiles of the distribution. The corollary is that a synthetic catalog with a p-value of 1.01 is more likely to generate an actual catalog with the same M_{max} as observed.

Turning our attention to the coefficient of variation (COV), once again, p proves to be the most influential parameter. Interestingly, this time the COV value of the actual catalog falls within the 16^{th} to 84^{th} percentile range for each p-value, even as dispersion increases with p. Distributions centered on $p = 1.01$ and negligible μ exhibit the most alignment with these COV values, with λ showing minimal influence.

In conclusion, our findings suggest that a synthetic catalog generated using a value of $p = 1.01$, negligible μ, $\lambda = \lambda_{mean}$, and incorporating both seismic and geodetic data, is closest to the actual, observed catalog. A systematic search by likelihood maximization over the parameter space could eventually be conducted, although we did not perform this here. Again, this would assume that the available sample is representative of the long-term activity, which is the question we aim to address here.

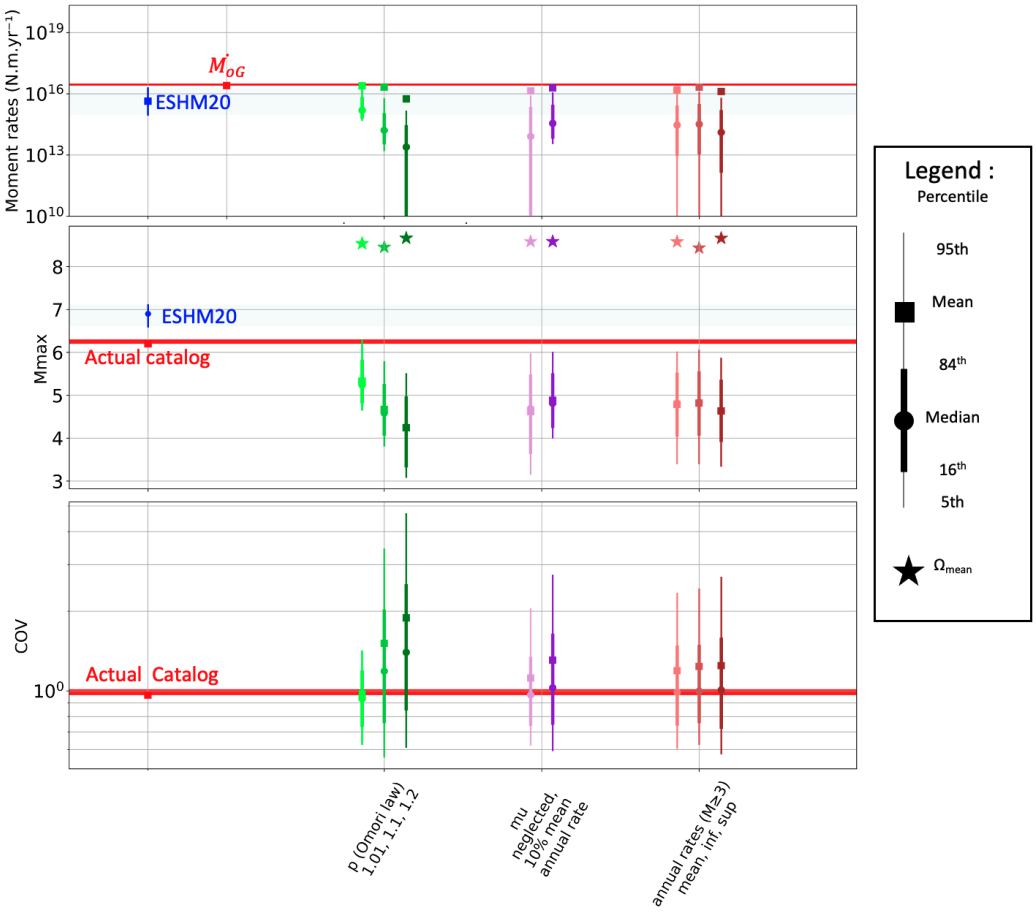

Fig. 4.11: Impact of the model parameters on a) the moment rates estimate, b) M_{max} and c) the COV, for 118 year-long samples.

4.3.3 Results

In this study, seismic moments were computed over 118-year periods, representing the duration of completeness for magnitude 4+ earthquakes. The methodology involved summing the moments of earthquakes within each respective time span. The resulting distribution of seismic moments over the 1 million-year synthetic catalog generated using a value of $p = 1.01$, negligible μ, $\lambda = \lambda_{mean}$, is illustrated in grey in Figure 4.12. The seismic moment rates obtained from ESHM20 models are depicted in blue, the seismic moment rate from the actual catalog is presented in green, and the geodetic moment rate is represented by the red line. The analysis reveals that the majority (over 84^{th} percentile) of the distribution of seismic moments in the synthetic catalog falls within the interval proposed by ESHM20 for long-term seismicity. Additionally, the green bar falls within the $16^{th} - 84th$ percentile interval, indicating that the synthetic catalog has a high likelihood of producing a catalog with a seismic moment similar to the observed catalog. This goes on to demonstrate that our model can explain why random samples of 118 years can have a low seismic moment rate (i.e., significantly lower than the geodetic rate), coherent with the estimation of ESHM20, even though the long term moment rate equals the geodetic one. In essence, this implies that the observed disparity between seismic and geodetic moments can simply be due to sampling biases.

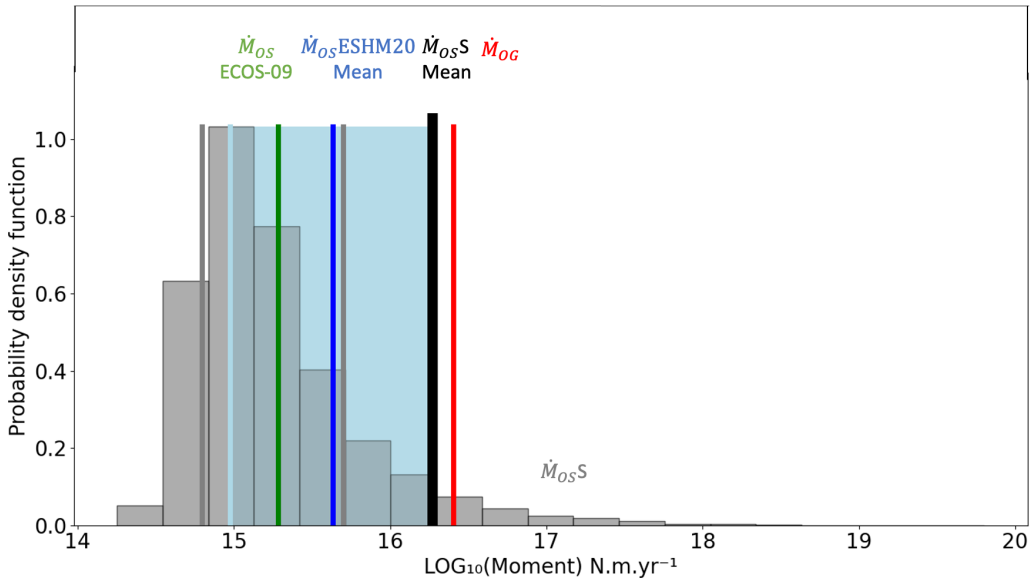

Fig. 4.12: Histogram of the distribution of log10 seismic moment rates(N·m/yr) calculated as the sum of moments from earthquakes within 118-year periods of the synthetic catalog, divided by 118 years. The bars show (in green) the seismic moment of the actual catalog and (in blue) in ESHM20 macrozone, and (in red) the geodetic moment.

4.4 Discussion: integrating this result into PSHA Models ?

Examining the findings presented in Figure 4.11, it becomes apparent that the proposed value of Ω_{mean} consistently surpasses the maximum M_{max} values recommended by ESHM20 by more than an order of magnitude. Specifically, Ω_{mean} averages around 8.3, in contrast to ESHM20's maximum M_{max} of 7.1. It is crucial to note that Ω_{mean} represents the long-term average seismic moment stored in the system, indicating the presence of sufficient energy for a potentially significant rupture event, albeit such occurrences are unlikely within the 118-year timeframe considered. This disparity suggests that the long-term seismic activity envisioned by domain experts does not align with the synthetic catalog's long-term seismicity.

The range of maximum magnitudes proposed by domain experts serves as a reference, considered the most reliable. Consequently, it prompts inquiry into alternative hypotheses that could elucidate the variance between these M_{max} ranges.

Primarily, we acknowledge this challenge and recognize the absence of a straightforward resolution. A plausible hypothesis suggests that the contribution of aseismic deformation in these regions cannot be disregarded when constraining magnitude-frequency distributions. Figure 4.13 illustrates a potential method for estimating this parameter within our study. This approach involves selecting the optimal model (in this case, the synthetic catalog generated using $p = 1.01$, negligible μ, and $\lambda = \lambda_{mean}$), then adjusting the input geodetic moment by an aseismic coefficient until it aligns with the M_{max} proposed by experts, provided it is well-constrained. In our scenario, over 70 percent of deformation would need to occur aseismically for the mean Ω value to fall within ESHM20's proposed range.

Aseismic deformation is one hypothesis to explain this discrepancy, yet it is pertinent to note other significant hypotheses. The disparity between seismic and geodetic moments may also stem from the inability to overlook the geodetic signal associated with post-glacial isostatic rebound in the Alps. The phenomenon of Glacial Isostatic Adjustment (GIA) represents a distinct seismotectonic context often characterized by a persistent prevalence of geodetic moment over seismic moment. This disparity, documented in various studies across different regions including Canada (Ojo et al., 2021, Mazzotti et al., 2005), the western United States (Mazzotti et al., 2011), North America (James and Bent, 1994), and Scandinavia (Keiding et al., 2015), can be attributed to several factors.

Firstly, the rapid and cyclical nature of post-glacial loading and unloading triggers crustal yielding under significant strains over prolonged periods. Secondly, the orientation of strains induced by GIA may not align to amplify the observed deviatoric stress field (James and Bent, 1994). Thirdly, contemporary seismicity in some regions may release both elastic strain from postglacial relaxation and ongoing tectonic strain, leading to misalignment between the modern geodetic strain rate tensor and accumulated elastic strain available for seismic release (Keiding et al., 2015 and Craig et al., 2016). Additionally, the lithosphere's viscoelastic response to postglacial rebound may contribute to aseismic strain (Mazzotti et al., 2011) .

One approach to address this phenomenon involves isolating the glacio-isostatic adjustment component of deformation to evaluate if the remaining long-term tectonic loading aligns with seismic observations. Furthermore, other viscoelastic processes in the Alps, such as erosion and slab detachment, may also influence geodetic and seismic moment rate estimates, potentially leading to overestimations of maximum magnitude estimates.

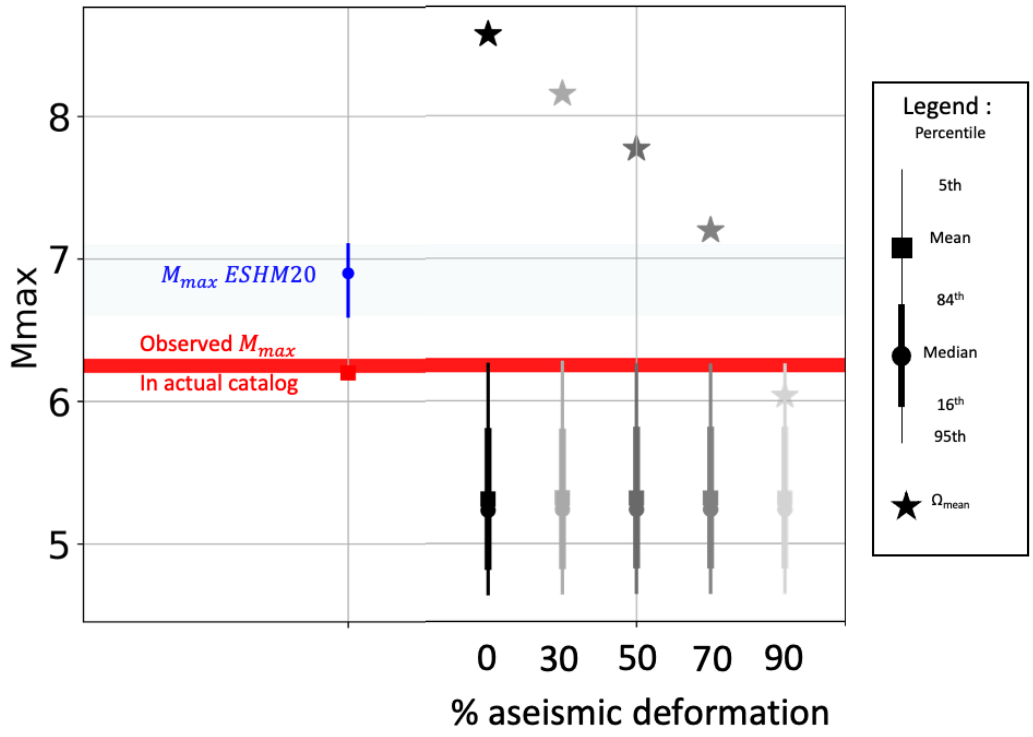

Fig. 4.13: Influence of the percentage of aseismic deformation on the synthetic catalog's behavior: Analysis of both the distribution of maximum magnitude observed in the synthetic catalog (segmented into bins of 118 years) and the long-term behavior represented by Ω_{mean}. The range of maximum magnitude proposed in ESHM20 is depicted in blue, while the maximum observed magnitude in the actual catalog is highlighted in red.

4.5 Conclusion

Essentially, what we have developed here is a robust methodology for estimating moment-balanced seismicity catalogs based on earthquake occurrence rates. By extending the data considerations to include properties of temporal clustering in catalogs and observed maximum magnitudes, we have been able to parameterize ETAS models that could be seen as representative of the long term seismicity (in terms of number of earthquakes, and of the temporal clustering of earthquakes and associated intermittency of the release of stored seismic moment). We observe that in regions where geodetic moment significantly exceeds seismic moment, our model demonstrates that it is highly probable to mimic the actual catalog over the historical period of completeness (typically one to a few centuries) with regards to the released seismic moment and the observed maximum magnitudes. In essence, this suggests that the difference between seismic and geodetic moments in these low-deformation regions, such as southwestern Switzerland, could be explained by limited time range of the observed catalog, missing very rare events that would balance seismic and geodetic moments. However, it is important to note that the magnitude ranges of these very rare events appear unrealistic in light of our understanding of the seismotectonics of this region. Therefore, this hypothesis alone cannot explain the predominance of the geodetic moment over the seismic moment but must be supplemented with other research hypotheses, such as the impact of aseismic deformation, the necessity to consider the effects of post-glacial isostatic rebound, or the inclusion of a GNSS solution with less uncertainty, featuring longer time series and a greater number of stations.

4.6 Annex

4.6.1 Determination of periods of completeness for TSZ089

To determine completeness periods for the Swiss zone TSZ089, a thorough literature review was conducted, but no completeness periods specifically developed for this source zone using the same seismic catalog were found. While ESHM20 provided completeness periods, it relied on a different catalog (declustered and harmonized at the European scale). In Figure 4.14, we illustrate the methodology employed to calculate completeness periods for various magnitude intervals with a sufficient number of earthquakes ($M_W 3, 3.5, 4, 4.5$). Specifically, we identified breakpoints in the curve representing the cumulative seismic rate for each target magnitude to

ascertain completeness periods (according to Weichert, 1980). However, our catalog only contained three earthquakes above $M_W 5$, posing challenges in obtaining well-constrained completeness periods for higher magnitudes. Consequently, for moment magnitudes exceeding 5, we opted to adopt the completeness periods proposed by ESHM20, namely 1510 for moment magnitudes greater than 5 and 1200 for moment magnitudes exceeding 5.9.

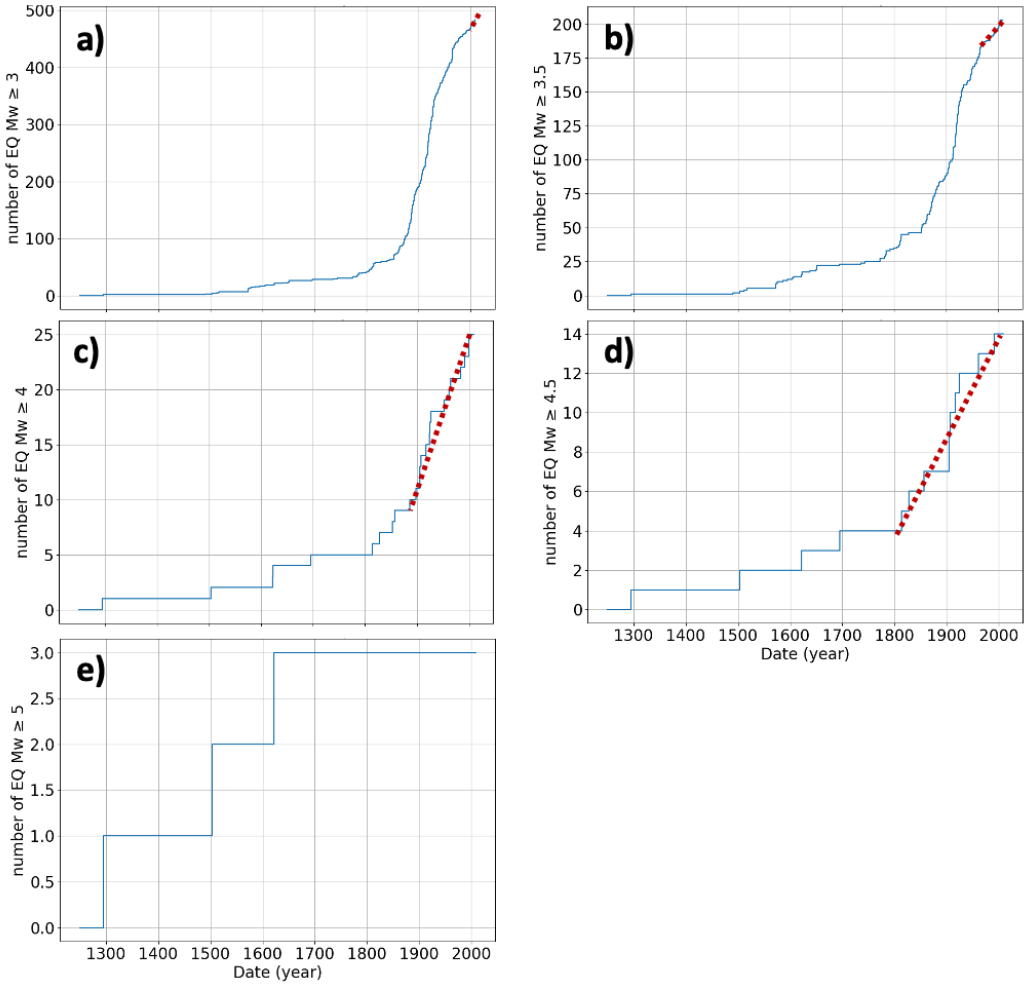

Fig. 4.14: Determination of completeness periods according to the Weichert, 1980 methodology in the Swiss macrozone TSZ089. Panels (a) to (e) depict the cumulated annual rates of events in blue for $M_W \geq 3, 3.5, 4, 4.5$ and 5, respectively. The red lines represent linear regressions observed in the most recent part of the catalog. The determined periods of completeness are 2000, 1967, 1890, 1800, and 1510 for the respective magnitude ranges. It is noteworthy that the limited number of events in the actual catalog for magnitudes higher than 5 adds complexity to the analysis. Consequently, we selected the year 1510, aligning with the completeness period proposed by ESHM20 (Danciu et al., 2021) for the magnitudes higher than 5 and 1200 for magnitude higher than 5.9.

4.6.2 Parameters used to compute the synthetic catalogs for Switzerland (TSZ089)

Here are the parameters employed in computing the synthetic catalogs for the TSZ089 region. These correspond to the exploration depicted in Figure 4.10, utilizing the detailed equations outlined in Section 4.2.3.

Parameter	Chosen value																	
b	1.1																	
β	2.5																	
α	2.5																	
μ	10^{-6}	10^{-6}	10^{-6}	0.14	10^{-6}	0.14	0.14	0.14	0.14	10^{-6}	0.14	10^{-6}	10^{-6}	0.14	10^{-6}	0.14	10^{-6}	0.14
n_0	0.07	0.07	0.07	0.07	0.07	0.06	0.07	0.07	0.07	0.07	0.06	0.07	0.07	0.06	0.07	0.06	0.07	0.06
m_0	3																	
p	1.01	1.01	1.1	1.01	1.2	1.2	1.1	1.2	1.1	1.2	1.1	1.01	1.1	1.2	1.2	1.01	1.1	1.01
c	10^{-7}																	
t_{max} (year)	1 million																	
$\dot{M}_{0G}$ (N.m/yr)	$2.53 * 10^{16}$																	
$\bar{M}_0$ (N.m) $(*10^{16})$	1.6	1.8	1.6	1.6	1.6	2.0	2.0	1.6	1.6	1.8	1.8	2.0	1.8	1.8	2.0	1.8	2.0	2.0
λ_{m_0}	1.6	1.4	1.6	1.6	1.6	1.3	1.3	1.6	1.6	1.4	1.4	1.3	1.4	1.4	1.3	1.4	1.3	1.3
Ω	8.5	8.6	8.7	8.5	8.6	8.8	8.4	8.2	8.1	8.8	8.7	8.5	8.1	8.8	8.8	8.6	8.8	8.5

Tab. 4.2: Model parameters used for the swiss zone TSZ089

5 General conclusions

The thesis has centered around a pivotal question: to what extent can geodetic moment serve as a reliable proxy for seismic moment in Europe, spanning from high-deformation zones to regions with low to moderate deformation? The exploration through the chapters has been guided by this fundamental question. In this concluding section, I will initially provide a summary of the findings from each chapter. Subsequently, I will delve into the issues addressed in my study and suggest potential perspectives.

Conclusions

First we scrutinized the compatibility between seismic and geodetic moment rates across Europe. Epistemic uncertainties associated with geodetic moment rates have been thoroughly investigated and considered in the analysis. The parameter identified as controlling these uncertainties is the seismogenic thickness, which is taken into account in the computation of geodetic moment rates. In high-activity zones, a first-order compatibility was observed. Nevertheless, local variations between the seismic and geodetic moment rates became evident when seismicity was focalized in regions with small characteristic distances (i.e., small areas/faults). This suggests that, in certain instances, the size of the source zones may not be appropriate for comparing seismic moment rates and geodetic moment rates. As anticipated, expanding the spatial scale to the macrozone level enhanced the overall consistency. In low-to-moderate activity zones, discrepancies emerged. In regions dominated by glacial isostatic adjustment in the geodetic signal, the two models (seismic and geodetic) were found to be incompatible, with a clear predominance of the geodetic moment over the seismic moment. This discrepancy has been noted in the scientific literature within this tectonic context and can be attributed to several factors. These include the rapid and cyclical nature of post-glacial loading and unloading, as well as the concurrent release of both elastic strain from post-glacial relaxation and ongoing tectonic strain during contemporary seismic events. Additionally, the viscoelastic relaxation of the upper mantle can causes extensive large-scale aseismic deformation. In zones characterized by a high density of active faults or well-constrained ESHM20 recurrence models (with >20 earthquakes used to constrain the recurrence models), we observed a tendency for the distributions of seismic and geodetic moments to

overlap. This observation offers hope for the integration of geodetic data even in regions with low deformation.

In the final chapter, we explored the possibility that the divergence between seismic and geodetic moments may be attributed to potential sampling biases in seismicity catalogs, which are used to constrain recurrence models. This consideration arises from the fact that seismic cycles in low-deformation zones exhibit significantly longer durations compared to those in active zones. To address this issue, we have established a robust methodology to estimate moment-balanced seismicity catalogs based on earthquake occurrence rates, leveraging the work by Marsan and Tan, 2020. By expanding the scope of data considerations to encompass temporal clustering properties in catalogs and observed maximum magnitudes, we have been able to parameterize ETAS models that can be considered representative of long-term seismicity. By taking the example of southwestern Switzerland, a region characterized by low deformation, our study showed that in regions where geodetic moment significantly surpasses seismic moment, our model has a high likelihood of mimicking the actual catalog over the historical period of completeness (typically one to a few centuries) in terms of released seismic moment, observed maximum magnitudes and temporal clustering. Essentially, the discrepancy between seismic and geodetic moments in low-deformation regions, like southwestern Switzerland, may be attributed to the limited time range of the observed catalog. This limitation could result in the omission of very rare events that would otherwise balance seismic and geodetic moments. However, it is important to note that the magnitude ranges of these very rare events appear unrealistic in light of our understanding of the seismotectonics of this region. Therefore, this hypothesis alone cannot explain the predominance of the geodetic moment over the seismic moment but must be supplemented with other research hypotheses, such as the impact of aseismic deformation, the necessity to consider the effects of post-glacial isostatic rebound, or the inclusion of a GNSS solution with less uncertainty, featuring longer time series and a greater number of stations.

Perspectives

This thesis is positioned within the overarching goal of introducing a supplementary approach to seismic catalogs and fault datasets for the development of PSHA source models. The study conducted by Hodge et al., 2015 in Malawi serves as a compelling illustration of this approach. In their research area, they demonstrated that the extrapolation of the highest recorded magnitude to the upper magnitude range, as done in the last PSHA source model, did not align with the geomorphological evidence in the Malawi Rift. Consequently, they proposed a new PSHA source model, incorporating geodetic and geomorphological data, as a valuable alternative to the existing model.

In the perspective to develop regional PSHA source models incorporating geodetic data, our work highlights new avenues for research.

Firstly, when we explored the geodetic moment rates uncertainties, we observed that the seismogenic thickness exerted the greatest control over the uncertainty of the geodetic moment. This result underscores the importance of integrating reliable seismogenic thickness models into these studies. Although not directly addressed in our work, a prospective avenue for research in this context would be to develop a methodology for locally (and perhaps jointly) calculating parameters which describe the behavior of the crust (the seismogenic thickness and the shear modulus) that are not solely based on statistics related to earthquake depths or average at the scale of continental upper crust, thereby incorporating local variations in rock rheology.

Furthermore, we also observed that the scale at which we integrated the geodetic moment played a pivotal role in achieving moment equality. It is essential to consider zones with a sufficiently large size for the comparison to be meaningful. It would be beneficial to continue investigating this aspect to establish a set of best practices for defining seismic source zones that make sense from a seismotectonic perspective and are well-suited for incorporating geodetic strain rates.

In this thesis, we addressed epistemic uncertainties stemming from the computation of strains, specifically those calculated using the method employed by Piña-Valdés et al., 2022 and the geodetic moment calculation. Within this uncertainty framework, we integrated various choices provided by the VISR software by Shen et al., 2015 for spatial inversion of velocities. I believe it would be valuable to perform a bechmark of different methods to derive the strain rates in order to obtain a value of the variability of strain rate computation depending on the different methods. Regarding this aspect, leveraging the work by Maurer and Materna, 2023 could be particularly insightful. In their study, they presented a methodology to estimate epistemic

uncertainty related to the selection of spatial inversion models. The researchers specifically examined five inversion models, including VISR. Their findings, based on a study in California, indicate that the total variability among these five deformation rate models is approximately 40%. Applying their method in this study on Europe could shed light on the impact of the spatial inversion method on the distributions of geodetic moments. Overall, considering the computation of strain inversion methodology on epistemic uncertainties in geodetic moment calculations to constrain seismic source models for PSHA can be crucial.

Subsequently, we observed that in certain regions of low to moderate deformation in Europe, the moment conservation theorem could be extended. However, in the majority of zones, this is not the case, and geodetic moment rates are significantly higher than seismic moment rates. As a future perspective, it might be worthwhile to revisit this study over a more extended period to assess whether acquiring new GNSS data would yield improved results. Indeed, the work of Walpersdorf et al., 2015 suggests that a prolonged acquisition period may be necessary to stabilize the signal over time. In their study, they demonstrated that sub-millimeter velocities in the southwestern Alps converged after a 15-year acquisition period. A longer acquisition period for existing stations, coupled with increased station density, could lead to better-constrained strain maps.

Dovetailing with this perspective, it is noteworthy to mention a recent trend in the literature, where researchers compile strain rates maps inverted from large-scale InSAR and GPS data. These findings are highly compelling and have the potential to yield even better-constrained results rapidly. A notable study by Weiss et al., 2020 developed an innovative method for generating strain rate maps through a joint inversion of InSAR and GPS data over a five-year period on a national scale in Turkey. They claim that their resulting maps provide a more detailed view of surface deformation. When comparing strain maps obtained using each of the two methods, they discern more precise deformation patterns, particularly along fault zones, with the GNSS + InSAR method compared to GNSS alone. In our study, it would be interesting to explore the application of their method on a European scale. More broadly, I believe this novel use of InSAR data has the potential to swiftly deliver usable strain maps, even in regions with sparse GNSS station density.

Bibliography

Ader, Thomas, Jean-Philippe Avouac, Jing Liu-Zeng, et al. (2012). “Convergence rate across the Nepal Himalaya and interseismic coupling on the Main Himalayan Thrust: Implications for seismic hazard”. In: *Journal of Geophysical Research: Solid Earth* 117 (B4). _eprint: https://onlinelibrary.wiley.com/doi/pdf/10.1029/2011JB009071 (Cited on page 39).

Adly, Ashraf, Laurentiu Danciu, Donat Fäh, et al. (Dec. 2018). “Probabilistic seismic hazard model for Cairo, Egypt: estimates and uncertainties”. In: *Bulletin of Earthquake Engineering* 16.12. Number: 12, pp. 5697–5733 (Cited on page 27).

Amelung, Falk and Geoffrey King (1997). “Large Scale Tectonic deformation inferred from small earthquake”. In: *Nature* 386, p. 4 (Cited on page 51).

Anderson, John G. and J. Enrique Luco (Apr. 1, 1983). “Consequences of slip rate constraints on earthquake occurrence relations”. In: *Bulletin of the Seismological Society of America* 73.2, pp. 471–496 (Cited on pages 16, 17, 57, 79, 82, 101).

Angelica, Carmelo, Alessandro Bonforte, Giovanni Distefano, Enrico Serpelloni, and Stefano Gresta (Nov. 2013). “Seismic potential in Italy from integration and comparison of seismic and geodetic strain rates”. In: *Tectonophysics* 608, pp. 996–1006 (Cited on page 67).

Aristizabal, Claudia (2018). “Integration of Site Effects into Probabilistic Seismic Hazard Assessment.Integration of site effects into probabilistic seismic hazard methods.” In: (Cited on page 9).

Arvidsson, Ronald (Nov. 1996). “Fennoscandian Earthquakes: Whole Crustal Rupturing Related to Postglacial Rebound”. In: *Science* 274.5288, pp. 744–746 (Cited on page 51).

Avouac, Jean-Philippe (May 30, 2015). “From Geodetic Imaging of Seismic and Aseismic Fault Slip to Dynamic Modeling of the Seismic Cycle”. In: *Annual Review of Earth and Planetary Sciences* 43.1, pp. 233–271 (Cited on pages 16, 34–36, 57, 76).

Avouac, Jean-Philippe, Lingsen Meng, Shengji Wei, Teng Wang, and Jean-Paul Ampuero (Sept. 2015). “Lower edge of locked Main Himalayan Thrust unzipped by the 2015 Gorkha earthquake”. In: *Nature Geoscience* 8.9. Number: 9 Publisher: Nature Publishing Group, pp. 708–711 (Cited on page 39).

Barani, Simone, Davide Scafidi, and Claudio Eva (2010). “Strain rates in northwestern Italy from spatially smoothed seismicity”. In: *Journal of Geophysical Research: Solid Earth* 115 (B7). _eprint: https://agupubs.onlinelibrary.wiley.com/doi/pdf/10.1029/2009JB006637 (Cited on page 49).

Barba, Salvatore, Debora Finocchio, Elena Sikdar, and Pierfrancesco Burrato (June 2013). “Modelling the interseismic deformation of a thrust system: seismogenic potential of the Southern Alps”. In: *Terra Nova* 25.3, pp. 221–227 (Cited on page 69).

Beauval, C., J. Marinière, H. Yepes, et al. (Apr. 3, 2018). “A New Seismic Hazard Model for Ecuador”. In: *Bulletin of the Seismological Society of America* 108.3, pp. 1443–1464 (Cited on pages 4, 12, 75).

Beauval, Céline, Sebastian Hainzl, and Frank Scherbaum (Mar. 1, 2006). “Probabilistic seismic hazard estimation in low-seismicity regions considering non-Poissonian seismic occurrence”. In: *Geophysical Journal International* 164.3, pp. 543–550 (Cited on pages 52, 118).

Beauval, Céline, Hugo Yepes, Laurence Audin, et al. (Oct. 22, 2014). “Probabilistic Seismic-Hazard Assessment in Quito, Estimates and Uncertainties”. In: *Seismological Research Letters* 85.6, pp. 1316–1327 (Cited on pages 17, 56).

Beavan, John and John Haines (Jan. 10, 2001). “Contemporary horizontal velocity and strain rate fields of the Pacific-Australian plate boundary zone through New Zealand”. In: *Journal of Geophysical Research: Solid Earth* 106 (B1), pp. 741–770 (Cited on page 26).

Behr, Whitney M. and Roland Bürgmann (Mar. 22, 2021). “What’s down there? The structures, materials and environment of deep-seated slow slip and tremor”. In: *Philosophical Transactions of the Royal Society A: Mathematical, Physical and Engineering Sciences* 379.2193, p. 20200218 (Cited on page 49).

Bevis, Michael and Abel Brown (Mar. 1, 2014). “Trajectory models and reference frames for crustal motion geodesy”. In: *Journal of Geodesy* 88.3, pp. 283–311 (Cited on page 21).

Bilham, Roger (Jan. 2019). “Himalayan earthquakes: a review of historical seismicity and early 21st century slip potential”. In: *Geological Society, London, Special Publications* 483.1, pp. 423–482 (Cited on page 39).

Bilham, Roger, Vinod K. Gaur, and Peter Molnar (2001). “Himalayan Seismic Hazard”. In: *Science* 293.5534, pp. 1442–1444 (Cited on page 39).

Bilham, Roger, Kristine Larson, and Jeffrey Freymueller (Mar. 1997). “GPS measurements of present-day convergence across the Nepal Himalaya”. In: *Nature* 386.6620, pp. 61–64 (Cited on page 39).

Bird, P. (Dec. 1, 2004). “Plate-Tectonic Analysis of Shallow Seismicity: Apparent Boundary Width, Beta, Corner Magnitude, Coupled Lithosphere Thickness, and Coupling in Seven Tectonic Settings”. In: *Bulletin of the Seismological Society of America* 94.6, pp. 2380–2399 (Cited on pages 29, 49, 60).

Bird, P., D. D. Jackson, Y. Y. Kagan, C. Kreemer, and R. S. Stein (Oct. 2015). “GEAR1: A Global Earthquake Activity Rate Model Constructed from Geodetic Strain Rates and Smoothed Seismicity”. In: *Bulletin of the Seismological Society of America* 105.5, pp. 2538–2554 (Cited on page 62).

Bird, P., C. Kreemer, and W. E. Holt (Mar. 1, 2010). “A Long-term Forecast of Shallow Seismicity Based on the Global Strain Rate Map”. In: *Seismological Research Letters* 81.2, pp. 184–194 (Cited on page 49).

Bird, P. and Z. Liu (Jan. 1, 2007). “Seismic Hazard Inferred from Tectonics: California”. In: *Seismological Research Letters* 78.1, pp. 37–48 (Cited on pages 31, 49, 60, 61, 85).

Bird, Peter (2003). “An updated digital model of plate boundaries”. In: *Geochemistry, Geophysics, Geosystems* 4.3 (Cited on pages 60, 61).

– (Nov. 2009). “Long-term fault slip rates, distributed deformation rates, and forecast of seismicity in the western United States from joint fitting of community geologic, geodetic, and stress direction data sets: FAULT SLIP AND DEFORMATION IN WESTERN UNITED STATES”. In: *Journal of Geophysical Research: Solid Earth* 114 (B11) (Cited on page 60).

Bird, Peter and Corné Kreemer (Feb. 2015). “Revised Tectonic Forecast of Global Shallow Seismicity Based on Version 2.1 of the Global Strain Rate Map”. In: *Bulletin of the Seismological Society of America* 105.1, pp. 152–166 (Cited on pages 29, 49).

Blewitt, Geoffrey, Corné Kreemer, William C. Hammond, and Julien Gazeaux (2016). “MIDAS robust trend estimator for accurate GPS station velocities without step detection”. In: *Journal of Geophysical Research: Solid Earth* 121.3. doi/10.1002/2015JB012552, pp. 2054–2068 (Cited on page 21).

Burov, Evgene B. (Aug. 2011). “Rheology and strength of the lithosphere”. In: *Marine and Petroleum Geology* 28.8, pp. 1402–1443 (Cited on pages 27, 29, 48).

Carafa, M. M. C., V. Kastelic, P. Bird, F. E. Maesano, and G. Valensise (Feb. 28, 2018). “A “Geodetic Gap” in the Calabrian Arc: Evidence for a Locked Subduction Megathrust?” In: *Geophysical Research Letters* 45.4, pp. 1794–1804 (Cited on page 69).

Carafa, Michele M. C., Gianluca Valensise, and Peter Bird (Jan. 11, 2017). “Assessing the seismic coupling of shallow continental faults and its impact on seismic hazard estimates: a case-study from Italy”. In: *Geophysical Journal International*, ggx002 (Cited on pages 29, 49, 60, 69).

Cheloni, D., N. D’Agostino, and G. Selvaggi (May 2014). “Interseismic coupling, seismic potential, and earthquake recurrence on the southern front of the Eastern Alps (NE Italy)”. In: *Journal of Geophysical Research: Solid Earth* 119.5, pp. 4448–4468 (Cited on page 69).

Chen, Wang-Ping and Peter Molnar (1977). “Seismic moments of major earthquakes and the average rate of slip in central Asia”. In: *Journal of Geophysical Research (1896-1977)* 82.20. _eprint: https://agupubs.onlinelibrary.wiley.com/doi/pdf/10.1029/JB082i020p02945, pp. 2945–2969 (Cited on page 39).

Chlieh, M., J. P. Avouac, K. Sieh, D. H. Natawidjaja, and John Galetzka (May 13, 2008). “Heterogeneous coupling of the Sumatran megathrust constrained by geodetic and paleogeodetic measurements”. In: *Journal of Geophysical Research* 113 (B5), B05305 (Cited on page 41).

Chlieh, M., J. B. De Chabalier, J. C. Ruegg, et al. (Aug. 2004). “Crustal deformation and fault slip during the seismic cycle in the North Chile subduction zone, from GPS and InSAR observations”. In: *Geophysical Journal International* 158.2, pp. 695–711 (Cited on page 41).

Chlieh, Mohamed, Hugo Perfettini, Hernando Tavera, et al. (Dec. 17, 2011). “Interseismic coupling and seismic potential along the Central Andes subduction zone”. In: *Journal of Geophysical Research* 116 (B12), B12405 (Cited on page 41).

Chousianitis, Konstantinos, Athanassios Ganas, and Christos P. Evangelidis (2015). "Strain and rotation rate patterns of mainland Greece from continuous GPS data and comparison between seismic and geodetic moment release". In: *Journal of Geophysical Research: Solid Earth* 120.5. doi/10.1002/2014JB011762, pp. 3909–3931 (Cited on pages 6, 47, 48, 73, 118).

Chéry, Jean, Sébastien Carretier, and Jean-François Ritz (Dec. 30, 2001). "Postseismic stress transfer explains time clustering of large earthquakes in Mongolia". In: *Earth and Planetary Science Letters* 194.1, pp. 277–286 (Cited on page 51).

Clarke, P. J., R. R. Davies, P. C. England, et al. (June 1, 1997). "Geodetic estimate of seismic hazard in the Gulf of Korinthos". In: *Geophysical Research Letters* 24.11, pp. 1303–1306 (Cited on pages 6, 47, 71, 118).

Console, Rodolfo, Anna Maria Lombardi, Maura Murru, and David Rhoades (Feb. 2003). "Båth's law and the self-similarity of earthquakes". In: *Journal of Geophysical Research: Solid Earth* 108 (B2), 2001JB001651 (Cited on page 126).

Cornell, C. Allin (Oct. 1, 1968). "Engineering seismic risk analysis". In: *Bulletin of the Seismological Society of America* 58.5, pp. 1583–1606 (Cited on page 9).

Craig, T. J., E. Calais, L. Fleitout, L. Bollinger, and O. Scotti (July 16, 2016). "Evidence for the release of long-term tectonic strain stored in continental interiors through intraplate earthquakes: RELEASE OF LONG-TERM STRAIN". In: *Geophysical Research Letters* 43.13, pp. 6826–6836 (Cited on pages 51, 54, 73, 92, 143).

Cross, Ryan S. and Jeffrey T. Freymueller (2007). "Plate coupling variation and block translation in the Andreanof segment of the Aleutian arc determined by subduction zone modeling using GPS data". In: *Geophysical Research Letters* 34.6. doi/10.1029/2006GL028970 (Cited on page 41).

D'Agostino, N. (2014). "Complete seismic release of tectonic strain and earthquake recurrence in the Apennines (Italy)". In: *Geophysical Research Letters* 41.4, pp. 1155–1162 (Cited on pages 6, 16, 27, 29, 31, 67, 68, 85, 117).

D'Agostino, N., S. Mantenuto, E. D'Anastasio, et al. (2009). "Contemporary crustal extension in the Umbria–Marche Apennines from regional CGPS networks and comparison between geodetic and seismic deformation". In: *Tectonophysics*. Ten years after the Umbria-Marche earthquake, Central Italy 476.1, pp. 3–12 (Cited on pages 27, 28, 47, 65).

Damon, Adrien, Stephane Mazzotti, Philippe Vernant, et al. (Sept. 1, 2022). *Impact of far-field glacially induced stresses on fault stability in the eastern Paris basin* (Cited on page 49).

Danciu, Laurentiu, Shyam Nandan, Celso Reyes, et al. (2021). *ESHM20 - EFEHR Technical ReportThe 2020 update of the European Seismic Hazard Model - ESHM20: Model Overview*. EFEHR European Facilities of Earthquake Hazard and Risk (Cited on pages 5, 6, 8, 10, 12, 13, 75, 76, 78–81, 99–101, 109, 118, 119, 145).

Davidsen, Jörn and Marco Baiesi (Aug. 23, 2016). "Self-similar aftershock rates". In: *Physical Review E* 94.2, p. 022314. arXiv: `1606.03958[cond-mat,physics:physics]` (Cited on page 126).

DeMets, C., R. G. Gordon, D. F. Argus, and S. Stein (May 1, 1990). “Current plate motions”. In: *Geophysical Journal International* 101.2, pp. 425–478 (Cited on page 5).

Drouet, Stéphane, Gabriele Ameri, Kristell Le Dortz, Ramon Secanell, and Gloria Senfaute (Mar. 1, 2020). “A probabilistic seismic hazard map for the metropolitan France”. In: *Bulletin of Earthquake Engineering* 18.5, pp. 1865–1898 (Cited on pages 122–124).

Dziewonski, Adam M. and Don L. Anderson (June 1981). “Preliminary reference Earth model”. In: *Physics of the Earth and Planetary Interiors* 25.4, pp. 297–356 (Cited on pages 27, 29, 85).

Déprez, Aline, Cécile Doubre, Frédéric Masson, and Patrice Ulrich (June 1, 2013). “Seismic and aseismic deformation along the East African Rift System from a reanalysis of the GPS velocity field of Africa”. In: *Geophysical Journal International* 193.3, pp. 1353–1369 (Cited on pages 46, 48).

Ekström, Göran and Philip England (Aug. 10, 1989). “Seismic strain rates in regions of distributed continental deformation”. In: *Journal of Geophysical Research: Solid Earth* 94 (B8), pp. 10231–10257 (Cited on page 49).

Elliott, J. R., R. J. Walters, and T. J. Wright (Dec. 22, 2016). “The role of space-based observation in understanding and responding to active tectonics and earthquakes”. In: *Nature Communications* 7.1. Number: 1 Publisher: Nature Publishing Group, p. 13844 (Cited on pages 1, 2, 43, 48, 53, 55).

Esteva, Luis (1967). “Criteria for the construction of spectra for seismic design”. In: *Third Panamerican Symposium on Structures, Caracas, Venezuela*. Vol. 1082 (Cited on page 9).

Field, E. H., R. J. Arrowsmith, G. P. Biasi, et al. (June 1, 2014). “Uniform California Earthquake Rupture Forecast, Version 3 (UCERF3)–The Time-Independent Model”. In: *Bulletin of the Seismological Society of America* 104.3, pp. 1122–1180 (Cited on pages 4, 12, 56, 57, 75).

Field, Edward H, David D Jackson, and James F Dolan (1999). “A Mutually Consistent Seismic-Hazard Source Model for Southem California”. In: (Cited on pages 45, 56).

Frank, F. C. (Feb. 1, 1966). “Deduction of earth strains from survey data”. In: *Bulletin of the Seismological Society of America* 56.1, pp. 35–42 (Cited on page 26).

Fäh, D., D. Giardini, P. Kästli, and N. Deichmann (2011). *ECOS-09* (Cited on page 136).

Grunewald, Elliot D. and Ross S. Stein (2006). “A new 1649–1884 catalog of destructive earthquakes near Tokyo and implications for the long-term seismic process”. In: *Journal of Geophysical Research: Solid Earth* 111 (B12). doi/10.1029/2005JB004059 (Cited on page 46).

Gutenberg, B. and C. F. Richter (Oct. 1944). “Frequency of earthquakes in California”. In: *Bulletin of the Seismological Society of America* 34.4. Number: 4 Publisher: Seismological Society of America, pp. 185–188 (Cited on pages 4, 10, 16, 17, 79).

Hanks, T. C. (June 1, 2002). “A Bilinear Source-Scaling Model for M-log A Observations of Continental Earthquakes”. In: *Bulletin of the Seismological Society of America* 92.5, pp. 1841–1846 (Cited on page 19).

Hanks, Thomas C. and William H. Bakun (Feb. 1, 2008). “M-logA Observations for Recent Large Earthquakes”. In: *Bulletin of the Seismological Society of America* 98.1, pp. 490–494 (Cited on page 19).

Hanks, Thomas C. and Hiroo Kanamori (1979). “A moment magnitude scale”. In: *Journal of Geophysical Research* 84 (B5), p. 2348 (Cited on pages 15, 16, 82, 127).

Harris, Ruth A. and Paul Segall (1987). “Detection of a locked zone at depth on the Parkfield, California, segment of the San Andreas Fault”. In: *Journal of Geophysical Research* 92 (B8), p. 7945 (Cited on page 38).

Heki, Kosuke and Yuta Mitsui (Feb. 1, 2013). “Accelerated pacific plate subduction following interplate thrust earthquakes at the Japan trench”. In: *Earth and Planetary Science Letters* 363, pp. 44–49 (Cited on page 5).

Helmstetter, Agnès and Didier Sornette (Oct. 2003). “Båth’s law derived from the Gutenberg-Richter law and from aftershock properties”. In: *Geophysical Research Letters* 30.20, 2003GL018186 (Cited on page 126).

Hodge, Michael, Juliet Biggs, Katsuichiro Goda, and Willy Aspinall (Apr. 1, 2015). “Assessing infrequent large earthquakes using geomorphology and geodesy: the Malawi Rift”. In: *Natural Hazards* 76.3, pp. 1781–1806 (Cited on pages 28, 29, 57, 151).

Holliday, James R., Donald L. Turcotte, and John B. Rundle (Feb. 1, 2008). “Self-similar branching of aftershock sequences”. In: *Physica A: Statistical Mechanics and its Applications* 387.4, pp. 933–943 (Cited on page 126).

Hornblow, S., M. Quigley, A. Nicol, R. Van Dissen, and N. Wang (Dec. 10, 2014). “Paleoseismology of the 2010 Mw 7.1 Darfield (Canterbury) earthquake source, Greendale Fault, New Zealand”. In: *Tectonophysics* 637, pp. 178–190 (Cited on pages 5, 75).

Hsu, Ya-Ju, Shui-Beih Yu, John P. Loveless, et al. (2016). “Interseismic deformation and moment deficit along the Manila subduction zone and the Philippine Fault system”. In: *Journal of Geophysical Research: Solid Earth* 121.10. doi/10.1002/2016JB013082, pp. 7639–7665 (Cited on page 41).

Hyndman, R. D., S. Mazzotti, D. Weichert, and G. C. Rogers (2003). “Frequency of large crustal earthquakes in Puget Sound–Southern Georgia Strait predicted from geodetic and geological deformation rates”. In: *Journal of Geophysical Research: Solid Earth* 108 (B1). _eprint: https://agupubs.onlinelibrary.wiley.com/doi/pdf/10.1029/2001JB001710 (Cited on pages 29, 45).

James, Thomas S. and Allison L. Bent (1994). “A comparison of eastern North American seismic strain-rates to glacial rebound strain-rates”. In: *Geophysical Research Letters* 21.19. _eprint: https://agupubs.onlinelibrary.wiley.com/doi/pdf/10.1029/94GL01854, pp. 2127–2130 (Cited on pages 54, 142, 143).

Jenny, S., S. Goes, D. Giardini, and H. G. Kahle (Mar. 27, 2006). “Seismic potential of Southern Italy”. In: *Tectonophysics* 415.1, pp. 81–101 (Cited on page 67).

Jenny, Sarah, Saskia Goes, Domenico Giardini, and Hans-Gert Kahle (June 2004). “Earthquake recurrence parameters from seismic and geodetic strain rates in the eastern Mediterranean”. In: *Geophysical Journal International* 157.3, pp. 1331–1347 (Cited on pages 12, 31, 44, 51, 75, 76, 85, 91).

Kagan, Yan and Leon Knopoff (Oct. 1, 1978). “Statistical study of the occurrence of shallow earthquakes”. In: *Geophysical Journal International* 55.1, pp. 67–86 (Cited on page 15).

Kagan, Yan Y. (June 2002). “Seismic moment distribution revisited: II. Moment conservation principle: Seismic moment distribution revisited: II”. In: *Geophysical Journal International* 149.3, pp. 731–754 (Cited on pages 17, 79).

Kaneko, Yoshihiro, Jean-Philippe Avouac, and Nadia Lapusta (Apr. 25, 2010). “Towards inferring earthquake patterns from geodetic observations of interseismic coupling”. In: 3, 363–U24 (Cited on page 39).

Kastelic, Vanja, Michele M.C. Carafa, and Francesco Visini (June 1, 2016). “Neotectonic deformation models for probabilistic seismic hazard: a study in the External Dinarides”. In: *Geophysical Journal International* 205.3, pp. 1694–1709 (Cited on pages 57, 70).

Keiding, M., C. Kreemer, C.D. Lindholm, et al. (Aug. 1, 2015). “A comparison of strain rates and seismicity for Fennoscandia: depth dependency of deformation from glacial isostatic adjustment”. In: *Geophysical Journal International* 202.2, pp. 1021–1028 (Cited on pages 54, 73, 92, 142, 143).

Koravos, G., I. G. Main, T. M. Tsapanos, and R. M. W. Musson (Jan. 1, 2003). “Maximum earthquake magnitudes in the Aegean area constrained by tectonic moment release rates”. In: *Geophysical Journal International* 152.1, pp. 94–112 (Cited on page 57).

Kostrov, V. V. (1974). “Seismic moment and enengy of earthquakes, and the seismic flow of rock, Izv. Acad. Sci. USSR”. In: *Phys. Solid Earth* 1, pp. 23–44 (Cited on page 16).

Koulali, A., D. Ouazar, A. Tahayt, et al. (Aug. 2011). “New GPS constraints on active deformation along the Africa–Iberia plate boundary”. In: *Earth and Planetary Science Letters* 308.1, pp. 211–217 (Cited on page 64).

Kreemer, Corné and Zachary M. Young (Nov. 1, 2022). “Crustal Strain Rates in the Western United States and Their Relationship with Earthquake Rates”. In: *Seismological Research Letters* 93.6, pp. 2990–3008 (Cited on pages 6, 117).

Kulkarni, R. B., R. R. Youngs, and K. J. Coppersmith (1984). “Assessment of confidence intervals for results of seismic hazard analysis”. In: *Proceedings of the eighth world conference on earthquake engineering*. Vol. 1. San Francisco, pp. 263–270 (Cited on page 11).

Leonard, Mark (Nov. 2015). “Comment on “Reassessment of the Maximum Fault Rupture Length of Strike-Slip Earthquakes and Inference on M_{max} in the Anatolian Peninsula, Turkey” by Arnaud Mignan, Laurentiu Danciu, and Domenico Giardini”. In: *Seismological Research Letters* 86.6, pp. 1690–1691 (Cited on page 80).

Lotfi, A., H. Zafarani, and A. Khodaverdian (Oct. 1, 2022). “A probabilistic deformation-based seismic hazard model for Iran”. In: *Bulletin of Earthquake Engineering* 20.13, pp. 7015–7046 (Cited on pages 50, 57).

Loveless, John P. and Brendan J. Meade (2011). “Spatial correlation of interseismic coupling and coseismic rupture extent of the 2011 MW = 9.0 Tohoku-oki earthquake”. In: *Geophysical Research Letters* 38.17. doi/10.1029/2011GL048561 (Cited on page 39).

Lundgren, P., M. Protti, A. Donnellan, et al. (1999). “Seismic cycle and plate margin deformation in Costa Rica: GPS observations from 1994 to 1997”. In: *Journal of Geophysical Research: Solid Earth* 104 (B12). doi/10.1029/1999JB900283, pp. 28915–28926 (Cited on page 41).

Main, Ian, Duncan Irving, Roger Musson, and Anya Reading† (1998). “Constraints on the frequency-magnitude relation and maximum magnitudes in the UK from observed seismicity and glacio-isostatic recovery rates: Maximum magnitudes in the UK”. In: *Geophysical Journal International* 137.2, pp. 535–550 (Cited on pages 16, 17, 56).

Manchuel, K., P. Traversa, D. Baumont, et al. (2018). “The French seismic CATalogue (FCAT-17)”. In: *Bulletin of Earthquake Engineering* 16.6, pp. 2227–2251 (Cited on page 122).

Marill, Lou, David Marsan, Anne Socquet, et al. (Nov. 2021). “Fourteen-Year Acceleration Along the Japan Trench”. In: *Journal of Geophysical Research: Solid Earth* 126.11, e2020JB021226 (Cited on pages 5, 21).

Mariniere, Judith (Oct. 8, 2020). “Improving earthquake forecast models for PSHA with geodetic data, applied on Ecuador”. PhD thesis. Université Grenoble Alpes [2020-....] (Cited on pages 9–11, 16, 20).

Mariniere, Judith, Céline Beauval, Jean-Mathieu Nocquet, Mohamed Chlieh, and Hugo Yepes (June 1, 2021). “Earthquake Recurrence Model for the Colombia–Ecuador Subduction Zone Constrained from Seismic and Geodetic Data, Implication for PSHA”. In: *Bulletin of the Seismological Society of America* 111.3, pp. 1508–1528 (Cited on pages 17, 41, 52, 56, 57, 76, 82, 87).

Marsan, David and Yen Joe Tan (Apr. 1, 2020). “Maximum Earthquake Size and Seismicity Rate from an ETAS Model with Slip Budget”. In: *Bulletin of the Seismological Society of America* 110.2, pp. 874–885 (Cited on pages 8, 15, 52, 118, 125, 126, 138, 150).

Masson, Christine, Stephane Mazzotti, Philippe Vernant, and Erik Doerflinger (Nov. 8, 2019). “Extracting small deformation beyond individual station precision from dense Global Navigation Satellite System (GNSS) networks in France and western Europe”. In: *Solid Earth* 10.6. Publisher: Copernicus GmbH, pp. 1905–1920 (Cited on pages 20, 114).

Masson, F., J. Chéry, D. Hatzfeld, et al. (Dec. 21, 2004). “Seismic versus aseismic deformation in Iran inferred from earthquakes and geodetic data: Seismic versus aseismic deformation in Iran”. In: *Geophysical Journal International* 160.1, pp. 217–226 (Cited on pages 6, 16, 29, 44, 47–49, 51, 118).

Mathey, Marguerite (Dec. 17, 2020). “Quantification haute résolution du champ de déformation 3D des Alpes occidentales : interprétations tectoniques et apports à l’aléa sismique”. PhD thesis. Université Grenoble Alpes [2020-....] (Cited on page 9).

Mathey, Marguerite, Andrea Walpersdorf, Stéphane Baize, et al. (Apr. 1, 2018). “3D deformation in the South-Western European Alps (Briançon region) revealed by 20 years of geodetic data”. In: Conference Name: EGU General Assembly Conference Abstracts ADS Bibcode: 2018EGUGA..2010415M, p. 10415 (Cited on page 75).

Maurer, Jeremy and Kathryn Materna (Apr. 27, 2023). “Quantification of geodetic strain rate uncertainties and implications for seismic hazard estimates”. In: *Geophysical Journal International* 234.3, pp. 2128–2142 (Cited on page 151).

Mavrommatis, Andreas P., Paul Segall, and Kaj M. Johnson (2014). “A decadal-scale deformation transient prior to the 2011 Mw 9.0 Tohoku-oki earthquake”. In: *Geophysical Research Letters* 41.13. doi/10.1002/2014GL060139, pp. 4486–4494 (Cited on page 5).

Mazzotti, S., A. Lambert, J. Henton, T. S. James, and N. Courtier (Dec. 28, 2011). “Absolute gravity calibration of GPS velocities and glacial isostatic adjustment in mid-continent North America: AG CALIBRATION OF GPS AND PGR”. In: *Geophysical Research Letters* 38.24, n/a–n/a (Cited on pages 6, 28, 29, 47, 48, 51, 54, 91, 118, 142, 143).

Mazzotti, Stéphane and John Adams (2005). “Rates and uncertainties on seismic moment and deformation in eastern Canada”. In: *Journal of Geophysical Research: Solid Earth* 110 (B9). _eprint: https://agupubs.onlinelibrary.wiley.com/doi/pdf/10.1029/2004JB003510 (Cited on pages 28–30).

Mazzotti, Stéphane, Thomas S. James, Joe Henton, and John Adams (2005). “GPS crustal strain, postglacial rebound, and seismic hazard in eastern North America: The Saint Lawrence valley example”. In: *Journal of Geophysical Research: Solid Earth* 110 (B11). _eprint: https://onlinelibrary.wiley.com/doi/pdf/10.1029/2004JB003590 (Cited on pages 16, 45, 47, 54, 57, 142).

Mazzotti, Stéphane, Xavier Le Pichon, Pierre Henry, and Shin-Ichi Miyazaki (June 10, 2000). “Full interseismic locking of the Nankai and Japan-west Kurile subduction zones: An analysis of uniform elastic strain accumulation in Japan constrained by permanent GPS”. In: *Journal of Geophysical Research: Solid Earth* 105 (B6), pp. 13159–13177 (Cited on page 41).

McCaffrey, Robert, Robert W. King, Suzette J. Payne, and Matthew Lancaster (Feb. 2013). “Active tectonics of northwestern U.S. inferred from GPS-derived surface velocities”. In: *Journal of Geophysical Research: Solid Earth* 118.2, pp. 709–723 (Cited on page 26).

Meade, B. J., Y. Klinger, and E. A. Hetland (Oct. 1, 2013). “Inference of Multiple Earthquake-Cycle Relaxation Timescales from Irregular Geodetic Sampling of Interseismic Deformation”. In: *Bulletin of the Seismological Society of America* 103.5, pp. 2824–2835 (Cited on page 50).

Meade, Brendan J. and John P. Loveless (Dec. 1, 2009). “Block Modeling with Connected Fault-Network Geometries and a Linear Elastic Coupling Estimator in Spherical Coordinates”. In: *Bulletin of the Seismological Society of America* 99.6, pp. 3124–3139 (Cited on page 56).

Meghraoui, M., R. Toussaint, and M. E. Aksoy (Mar. 1, 2021). “The slip deficit on the North Anatolian Fault (Turkey) in the Marmara Sea: insights from paleoseismicity, seismicity and geodetic data”. In: *Mediterranean Geoscience Reviews* 3.1, pp. 45–56 (Cited on page 73).

Mey, Jürgen, Dirk Scherler, Andrew D. Wickert, et al. (Nov. 10, 2016). “Glacial isostatic uplift of the European Alps”. In: *Nature Communications* 7.1. Number: 1 Publisher: Nature Publishing Group, p. 13382 (Cited on page 55).

Michel, Sylvain, Romain Jolivet, Chris Rollins, Jorge Jara, and Luca Dal Zilio (2021). “Seismogenic Potential of the Main Himalayan Thrust Constrained by Coupling Segmentation and Earthquake Scaling”. In: *Geophysical Research Letters* 48 (Cited on page 39).

Middleton, Timothy A, Barry Parsons, and Richard T Walker (Feb. 1, 2018). “Comparison of seismic and geodetic strain rates at the margins of the Ordos Plateau, northern China”. In: *Geophysical Journal International* 212.2, pp. 988–1009 (Cited on pages 6, 45, 49, 117).

Mohapatra, Alok K., William K. Mohanty, and Akhilesh K. Verma (June 2014). “Estimation of maximum magnitude (M max): Impending large earthquakes in northeast region, India”. In: *Journal of the Geological Society of India* 83.6, pp. 635–640 (Cited on pages 6, 57, 117).

Molnar, Peter (Feb. 1, 1979). “Earthquake recurrence intervals and plate tectonics”. In: *Bulletin of the Seismological Society of America* 69.1, pp. 115–133 (Cited on pages 37, 56).

Moreno, Marcos, Matthias Rosenau, and Onno Oncken (Sept. 2010). “2010 Maule earthquake slip correlates with pre-seismic locking of Andean subduction zone”. In: *Nature* 467.7312. Number: 7312 Publisher: Nature Publishing Group, pp. 198–202 (Cited on pages 39, 40).

Métois, M., A. Socquet, C. Vigny, et al. (Sept. 1, 2013a). “Revisiting the North Chile seismic gap segmentation using GPS-derived interseismic coupling”. In: *Geophysical Journal International* 194.3, pp. 1283–1294 (Cited on page 41).

Métois, M., C. Vigny, and A. Socquet (2016). “Interseismic Coupling, Megathrust Earthquakes and Seismic Swarms Along the Chilean Subduction Zone (38°–18°S)”. In: *Pure and Applied Geophysics* 173.5, pp. 1431–1449 (Cited on page 39).

Métois, Marianne, Anne Socquet, and Christophe Vigny (Mar. 1, 2012). “Interseismic coupling, segmentation and mechanical behavior of the Central Chile subduction zone”. In: *Journal of Geophysical Research* 117 (Cited on page 41).

Métois, Marianne, Christophe Vigny, Anne Socquet, et al. (Nov. 7, 2013b). “GPS-derived interseismic coupling on the subduction and seismic hazards in the Atacama region, Chile”. In: *Geophysical Journal International* 196 (Cited on page 41).

Nemcok, M., L. Pospisil, J. Lexa, and R. A. Donelick (Oct. 15, 1998). “Tertiary subduction and slab break-off model of the Carpathian–Pannonian region”. In: *Tectonophysics* 295.3, pp. 307–340 (Cited on page 55).

Nocquet, J.-M. and E. Calais (Mar. 1, 2004). “Geodetic Measurements of Crustal Deformation in the Western Mediterranean and Europe”. In: *Pure and Applied Geophysics* 161.3, pp. 661–681 (Cited on page 64).

Nocquet, Jean-Mathieu (2005). “Geodetic constraints on glacial isostatic adjustement in Europe”. In: p. 6 (Cited on pages 54, 73).

– (Dec. 2012). “Present-day kinematics of the Mediterranean: A comprehensive overview of GPS results”. In: *Tectonophysics* 579, pp. 220–242 (Cited on pages 64–66, 70–72).

Ogata, Yosihiko (1998). “Space-Time Point-Process Models for Earthquake Occurrences”. In: *Annals of the Institute of Statistical Mathematics* 50.2, pp. 379–402 (Cited on pages 15, 125).

– (Mar. 1988). “Statistical Models for Earthquake Occurrences and Residual Analysis for Point Processes”. In: *Journal of the American Statistical Association* 83.401, pp. 9–27 (Cited on pages 4, 15).

Ojo, Adebayo Oluwaseun, Honn Kao, Yan Jiang, Michael Craymer, and Joseph Henton (Apr. 2021). “Strain Accumulation and Release Rate in Canada: Implications for Long-Term Crustal Deformation and Earthquake Hazards”. In: *Journal of Geophysical Research: Solid Earth* 126.4 (Cited on pages 6, 16, 26, 28, 29, 47, 51, 52, 54, 85, 117, 142).

Pagani, Colin (Oct. 14, 2021). “Quantification probabiliste des taux de déformation crustale par inversion bayésienne de données GPS”. PhD thesis. Université de Lyon (Cited on pages 20, 26).

Pagani, M, V Silva, A Rao, M Simionato, and K Johnson (2023). “OpenQuake Engine Manual”. In: (Cited on pages 10, 17).

Palano, Mimmo, Paola Imprescia, Amotz Agnon, and Stefano Gresta (Apr. 1, 2018). “An improved evaluation of the seismic/geodetic deformation-rate ratio for the Zagros Fold-and-Thrust collisional belt”. In: *Geophysical Journal International* 213.1, pp. 194–209 (Cited on pages 16, 29, 46, 48, 52).

Pancha, A. (Feb. 1, 2006). “Comparison of Seismic and Geodetic Scalar Moment Rates across the Basin and Range Province”. In: *Bulletin of the Seismological Society of America* 96.1, pp. 11–32 (Cited on pages 16, 29, 46, 53, 57, 84, 85).

Pandey, M. R., R. P. Tandukar, J. P. Avouac, J. Lavé, and J. P. Massot (Apr. 1, 1995). “Interseismic strain accumulation on the Himalayan crustal ramp (Nepal)”. In: *Geophysical Research Letters* 22.7, pp. 751–754 (Cited on page 39).

Papastamatiou, Dimitri (1980). “INCORPORATION OF CRUSTAL DEFORMATION TO SEISMIC HAZARD ANALYSIS”. In: (Cited on page 56).

Parsons, Tom (Mar. 2006). “Tectonic stressing in California modeled from GPS observations”. In: *Journal of Geophysical Research: Solid Earth* 111 (B3), 2005JB003946 (Cited on page 26).

Peltzer, Gilles, Fréderic Crampé, Scott Hensley, and Paul Rosen (2001). “Transient strain accumulation and fault interaction in the Eastern California shear zone”. In: *Geology* 29.11, p. 975 (Cited on page 50).

Petersen (2014). *Geodesy- and Geology-Based Slip-Rate Models for the Western United States (Excluding California) National Seismic Hazard Maps*. Open-File Report. Series: Open-File Report (Cited on page 56).

Piña-Valdés, Jesús, Anne Socquet, Céline Beauval, et al. (2022). “3D GNSS Velocity Field Sheds Light on the Deformation Mechanisms in Europe: Effects of the Vertical Crustal Motion on the Distribution of Seismicity”. In: *Journal of Geophysical Research: Solid Earth* 127.6. _eprint: https://onlinelibrary.wiley.com/doi/pdf/10.1029/2021JB023451, e2021JB023451 (Cited on pages 6–8, 20, 26, 65, 76, 78, 82, 83, 86, 90, 100, 109, 110, 113, 114, 121, 151, 176).

Protti, Marino, Victor González, Andrew V. Newman, et al. (Feb. 2014). “Nicoya earthquake rupture anticipated by geodetic measurement of the locked plate interface”. In: *Nature Geoscience* 7.2, pp. 117–121 (Cited on page 39).

Reid (1910). “The mechanism of the earthquake, The California earthquake of April 18, 1906”. In: *Report of the Research Senatorial Commission, Carnegie Institution, Washington, D. C.* 2, pp. 16–18 (Cited on pages 3, 32, 37).

Reiter, L. (Leon) (1990). “Earthquake hazard analysis : issues and insights”. In: *Colombia University Press.* (Cited on page 10).

Reverso, Thomas (Dec. 16, 2015). “Sismogenèse dans les zones de déformations transitoires”. PhD thesis. Université Grenoble Alpes (Cited on pages 14, 32).

Rollins, Chris and Jean-Philippe Avouac (Mar. 28, 2019). “A Geodesy- and Seismicity-Based Local Earthquake Likelihood Model for Central Los Angeles”. In: *Geophysical Research Letters* 46.6, pp. 3153–3162 (Cited on pages 52, 57, 58, 118).

Rong, Y., P. Bird, and D.D. Jackson (Apr. 1, 2016). “Earthquake potential and magnitude limits inferred from a geodetic strain-rate model for southern Europe”. In: *Geophysical Journal International* 205.1, pp. 509–522 (Cited on pages 29, 49, 60, 63).

Rong, Yufang, M Eeri, Xiwei Xu, et al. (2020). “A probabilistic seismic hazard model for Mainland China”. In: *Earthquake Spectra*, p. 29 (Cited on page 57).

Rontogianni, Sofia (Dec. 1, 2010). “Comparison of geodetic and seismic strain rates in Greece by using a uniform processing approach to campaign GPS measurements over the interval 1994–2000”. In: *Journal of Geodynamics* 50.5, pp. 381–399 (Cited on pages 49, 51, 71).

Rosen, P., C. Werner, E. Fielding, et al. (1998). “Aseismic creep along the San Andreas Fault northwest of Parkfield, CA measured by radar interferometry”. In: *Geophysical Research Letters* 25.6. _eprint: https://agupubs.onlinelibrary.wiley.com/doi/pdf/10.1029/98GL50495, pp. 825–828 (Cited on page 49).

Sagiya, Takeshi (Aug. 1, 1999). “Interplate coupling in the Tokai District, central Japan, deduced from continuous GPS data”. In: *Geophysical Research Letters* 26.15, pp. 2315–2318 (Cited on page 41).

Saichev, A. and D. Sornette (May 31, 2005). “Distribution of the Largest Aftershocks in Branching Models of Triggered Seismicity: Theory of the Universal Bath’s law”. In: *Physical Review E* 71.5, p. 056127. arXiv: `physics/0501102` (Cited on page 126).

Savage, J. C. (1983). “A dislocation model of strain accumulation and release at a subduction zone”. In: *Journal of Geophysical Research: Solid Earth* 88 (B6), pp. 4984–4996 (Cited on page 38).

Savage, J. C. and R. W. Simpson (Oct. 1, 1997). “Surface strain accumulation and the seismic moment tensor”. In: *Bulletin of the Seismological Society of America* 87.5, pp. 1345–1353 (Cited on pages 27, 31, 85, 86).

Serpelloni, E., G. Vannucci, S. Pondrelli, et al. (June 2007). “Kinematics of the Western Africa-Eurasia plate boundary from focal mechanisms and GPS data”. In: *Geophysical Journal International* 169.3, pp. 1180–1200 (Cited on page 64).

Shen, Z.-K., D. D. Jackson, and Y. Y. Kagan (Jan. 1, 2007). "Implications of Geodetic Strain Rate for Future Earthquakes, with a Five-Year Forecast of M5 Earthquakes in Southern California". In: *Seismological Research Letters* 78.1, pp. 116–120 (Cited on pages 12, 44, 75).

Shen, Zheng-Kang and Peter Bird (Sept. 14, 2022). "NeoKinema Deformation Model for the 2023 Update to the U.S. National Seismic Hazard Model". In: *Seismological Research Letters* (Cited on pages 50, 59).

Shen, Zheng-Kang, David D. Jackson, and Bob X. Ge (Dec. 10, 1996). "Crustal deformation across and beyond the Los Angeles basin from geodetic measurements". In: *Journal of Geophysical Research: Solid Earth* 101 (B12), pp. 27957–27980 (Cited on page 26).

Shen, Zheng-Kang, Min Wang, Yuehua Zeng, and Fan Wang (Aug. 2015). "Optimal Interpolation of Spatially Discretized Geodetic Data". In: *Bulletin of the Seismological Society of America* 105.4, pp. 2117–2127 (Cited on pages 20, 22, 25, 26, 83, 84, 121, 151).

Silva, Vitor, Marco Pagani, John Schneider, and Paul Henshaw (2019). "Assessing Seismic Hazard and Risk Globally for an Earthquake Resilient World". In: (Cited on page 1).

Socquet, A., A. Deprez, and N. Cotte (2019). *GNSS position and velocity solutions in Europe*. In collab. with Anne.Socquet@Univ-Grenoble-Alpes.Fr, Gael.Janex@Univ-Grenoble-Alpes.Fr, Anne Socquet, et al. (Cited on pages 110, 113).

Soudarin, Laurent and Anny Cazenave (1995). "Large-scale tectonic plate motions measured with the DORIS Space Geodesy System". In: *Geophysical Research Letters* 22.4. _eprint: https://agupubs.onlinelibrary.wiley.com/doi/pdf/10.1029/94GL03382, pp. 469–472 (Cited on page 5).

Sparacino, Federica, Mimmo Palano, José Antonio Peláez, and José Fernández (Jan. 2020). "Geodetic Deformation versus Seismic Crustal Moment-Rates: Insights from the Ibero-Maghrebian Region". In: *Remote Sensing* 12.6. Number: 6 Publisher: Multidisciplinary Digital Publishing Institute, p. 952 (Cited on pages 6, 47, 48, 64, 117).

Steffen, Holger and Patrick Wu (Oct. 1, 2011). "Glacial isostatic adjustment in Fennoscandia—A review of data and modeling". In: *Journal of Geodynamics* 52.3, pp. 169–204 (Cited on page 73).

Stein, Seth and Mian Liu (Nov. 2009). "Long aftershock sequences within continents and implications for earthquake hazard assessment". In: *Nature* 462.7269. Number: 7269 Publisher: Nature Publishing Group, pp. 87–89 (Cited on pages 52, 118).

Stevens, V. L. and J. P. Avouac (2015). "Interseismic coupling on the main Himalayan thrust". In: *Geophysical Research Letters* 42.14. doi/10.1002/2015GL064845, pp. 5828–5837 (Cited on page 39).

Stevens, V L and J-P Avouac (Apr. 12, 2021). "On the relationship between strain rate and seismicity in the India–Asia collision zone: implications for probabilistic seismic hazard". In: *Geophysical Journal International* 226.1, pp. 220–245 (Cited on pages 28, 29, 31, 44, 51, 52, 57, 76, 85).

Stevens, V. L. and J.-P. Avouac (Dec. 2017). “Determination of Mmax from Background Seismicity and Moment Conservation”. In: *Bulletin of the Seismological Society of America* 107.6, pp. 2578–2596 (Cited on pages 16, 57).

– (2016). “Millenary $M_w > 9.0$ earthquakes required by geodetic strain in the Himalaya”. In: *Geophysical Research Letters* 43.3, pp. 1118–1123 (Cited on pages 16, 39).

Stevens, V. L., S. N. Shrestha, and D. K. Maharjan (Sept. 11, 2018). “Probabilistic Seismic Hazard Assessment of Nepal”. In: *Bulletin of the Seismological Society of America* 108.6, pp. 3488–3510 (Cited on page 57).

Stirling, M, Graeme Mcverry, Matthew Gerstenberger, et al. (Aug. 8, 2012). “National Seismic Hazard Model for New Zealand: 2010 Update”. In: *Bulletin of the Seismological Society of America* 102, pp. 1514–1542 (Cited on pages 4, 12, 75).

Szeliga, Walter, Roger Bilham, Din Kakar, and Sarosh Lodi (Aug. 8, 2012). “Interseismic strain along the western boundary of the Indian subcontinent”. In: *Journal of Geophysical Research (Solid Earth)* 117, p. 8404 (Cited on page 41).

Takeuchi, Christopher S. and Yuri Fialko (May 2012). “Dynamic models of interseismic deformation and stress transfer from plate motion to continental transform faults: MODELS OF INTERSEISMIC DEFORMATION”. In: *Journal of Geophysical Research: Solid Earth* 117 (B5), n/a–n/a (Cited on page 50).

Tarayoun, Alizia (Nov. 5, 2018). “Localisation de la déformation et de la sismicité en domaine intraplaque : réactivation des paléo-structures crustales et lithosphériques”. These de doctorat. Montpellier (Cited on page 20).

Thomas, Marion Y., Jean-Philippe Avouac, Johann Champenois, Jian-Cheng Lee, and Long-Chen Kuo (2014). “Spatiotemporal evolution of seismic and aseismic slip on the Longitudinal Valley Fault, Taiwan”. In: *Journal of Geophysical Research: Solid Earth* 119.6. _eprint: https://agupubs.onlinelibrary.wiley.com/doi/pdf/10.1002/2013JB010603, pp. 5114–5139 (Cited on page 41).

Turner, Jonathan (Nov. 1, 2002). “Turcotte, D. L. & Schubert, G. 2002. Geodynamics, 2nd ed.: xv + 456 pp. Cambridge, New York, Melbourne: Cambridge University Press. Price £75.00, US $110.00 (hard covers); £29.95, US $45.00 (paperback). ISBN 0521 66186 2; 0 521 66624 4 (pb). Geol. Mag. 139, 2002,” in: *Geological Magazine* 139.6, p. 719 (Cited on page 29).

Valensise, Gianluca, Daniela Pantosti, and Roberto Basili (July 1, 2004). “Seismology and Tectonic Setting of the 2002 Molise, Italy, Earthquake”. In: *Earthquake Spectra* 20.1. Publisher: SAGE Publications Ltd STM, pp. 23–37 (Cited on pages 5, 75).

Vernant, Philippe, Robert Reilinger, and Simon McClusky (Jan. 1, 2014). “Geodetic evidence for low coupling on the Hellenic subduction plate interface”. In: *Earth and Planetary Science Letters* 385, pp. 122–129 (Cited on page 71).

Walpersdorf, A., C. Sue, S. Baize, et al. (Apr. 1, 2015). “Coherence between geodetic and seismic deformation in a context of slow tectonic activity (SW Alps, France)”. In: *Journal of Geodynamics* 85, pp. 58–65 (Cited on pages 47, 152).

Wang, Kelin and Timothy Dixon (2004). ""Coupling" Semantics and science in earthquake research". In: *Eos, Transactions American Geophysical Union* 85.18, p. 180 (Cited on page 34).

Wang, Kelin, Yan Hu, Michael Bevis, et al. (2007). "Crustal motion in the zone of the 1960 Chile earthquake: Detangling earthquake-cycle deformation and forearc-sliver translation". In: *Geochemistry, Geophysics, Geosystems* 8.10. doi/10.1029/2007GC001721 (Cited on page 51).

Wang, Kelin, Yan Hu, and Jiangheng He (Apr. 2012). "Deformation cycles of subduction earthquakes in a viscoelastic Earth". In: *Nature* 484.7394. Number: 7394 Publisher: Nature Publishing Group, pp. 327–332 (Cited on page 51).

Ward, Steven N (1994). "A Multidisciplinary Approach to Seismic Hazard in Southern California". In: (Cited on pages 27, 50, 56).

Ward, Steven N. (July 1998a). "On the consistency of earthquake moment rates, geological fault data, and space geodetic strain: the United States". In: *Geophysical Journal International* 134.1, pp. 172–186 (Cited on pages 6, 16, 27, 29, 31, 45, 47, 53, 84, 85, 91, 118).

– (Dec. 1998b). "On the consistency of earthquake moment release and space geodetic strain rates: Europe". In: *Geophysical Journal International* 135.3, pp. 1011–1018 (Cited on pages 16, 27, 48, 63).

Weichert (1980). "Estimation of the earthquake recurrence parameters for unequal observation periods for different magnitudes". In: *Bulletin of the Seismological Society of America* 70.4, pp. 1337–1346 (Cited on pages 17, 52, 136, 145).

Weiss, Jonathan R., Richard J. Walters, Yu Morishita, et al. (Sept. 16, 2020). "High-Resolution Surface Velocities and Strain for Anatolia From Sentinel-1 InSAR and GNSS Data". In: *Geophysical Research Letters* 47.17, e2020GL087376 (Cited on page 152).

Wells, Donald L. and Kevin J. Coppersmith (Aug. 1, 1994). "New empirical relationships among magnitude, rupture length, rupture width, rupture area, and surface displacement". In: *Bulletin of the Seismological Society of America* 84.4, pp. 974–1002 (Cited on page 19).

Wesnousky, S. G. (Aug. 1, 2008). "Displacement and Geometrical Characteristics of Earthquake Surface Ruptures: Issues and Implications for Seismic-Hazard Analysis and the Process of Earthquake Rupture". In: *Bulletin of the Seismological Society of America* 98.4, pp. 1609–1632 (Cited on page 19).

Whitney, Beau B and James V Hengesh (2013). "Geological Constraints on Mmax values from Western Australia: Implications for Seismic Hazard Assessments". In: (Cited on page 19).

Williams, J N, M J Werner, K Goda, et al. (June 1, 2023). "Fault-based probabilistic seismic hazard analysis in regions with low strain rates and a thick seismogenic layer: a case study from Malawi". In: *Geophysical Journal International* 233.3, pp. 2172–2207 (Cited on page 57).

Woessner, Jochen, Danciu Laurentiu, Domenico Giardini, et al. (Dec. 1, 2015). “The 2013 European Seismic Hazard Model: key components and results”. In: *Bulletin of Earthquake Engineering* 13.12, pp. 3553–3596 (Cited on pages 63, 75).

Working Group on California Earthquake Probabilities (Apr. 1, 1995). “Seismic hazards in Southern California: Probable earthquakes, 1994 to 2024”. In: *Bulletin of the Seismological Society of America* 85.2, pp. 379–439 (Cited on pages 27, 29, 31, 49, 56, 84, 85).

Zeng, Yuehua, Mark D. Petersen, and Zheng-Kang Shen (2018). “Earthquake Potential in California-Nevada Implied by Correlation of Strain Rate and Seismicity”. In: *Geophysical Research Letters* 45.4. doi/10.1002/2017GL075967, pp. 1778–1785 (Cited on page 44).

Webpages

Calais (2023). *GPS Geodesy | . | Eric Calais*. URL: `https://www.geologie.ens.fr/~ecalais/teaching/gps-geodesy/` (visited on Dec. 20, 2023) (Cited on page 21).

USGS.gov | Science for a changing world (2023). URL: `https://www.usgs.gov/` (visited on Dec. 14, 2023) (Cited on pages 1, 3).

List of Figures

List of Tables

Colophon

This thesis was typeset with LaTeX 2_ε. It uses the *Clean Thesis* style developed by Ricardo Langner. The design of the *Clean Thesis* style is inspired by user guide documents from Apple Inc.

Download the *Clean Thesis* style at `http://cleanthesis.der-ric.de/`.